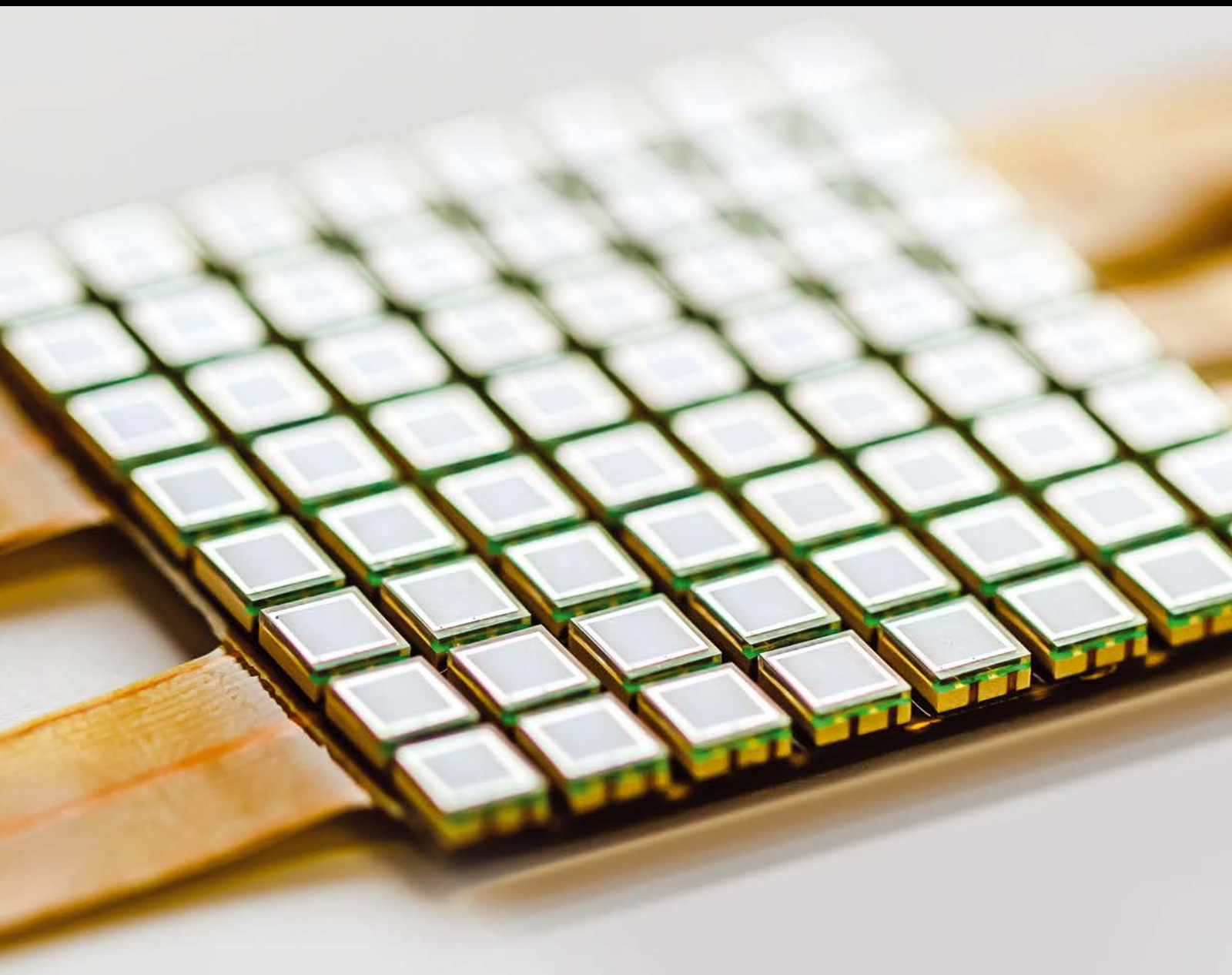


Embeddable Advanced Sensors for Harsh Environment Sensing Applications

Guest Editors: Lei Yuan, Yinan Zhang, Yan Lu, Xiaobei Zhang,
and Mengmeng Wang





Embeddable Advanced Sensors for Harsh Environment Sensing Applications

Embeddable Advanced Sensors for Harsh Environment Sensing Applications

Guest Editors: Lei Yuan, Yinan Zhang, Yan Lu, Xiaobei Zhang,
and Mengmeng Wang



Copyright © 2016 Hindawi Publishing Corporation. All rights reserved.

This is a special issue published in "Journal of Sensors." All articles are open access articles distributed under the Creative Commons Attribution License, which permits unrestricted use, distribution, and reproduction in any medium, provided the original work is properly cited.

Editorial Board

Harith Ahmad, Malaysia
Bruno Andò, Italy
Francisco J. Arregui, Spain
Francesco Baldini, Italy
Fernando Benito-Lopez, Ireland
Romeo Bernini, Italy
Shekhar Bhansali, USA
Wojtek J. Bock, Canada
Hubert Brändle, Switzerland
Davide Brunelli, Italy
Paolo Bruschi, Italy
Belén Calvo, Spain
Stefania Campopiano, Italy
Domenico Caputo, Italy
Sara Casciati, Italy
Gabriele Cazzulani, Italy
Chi Chiu Chan, Singapore
Nick Chaniotakis, Greece
Nicola Cioffi, Italy
Elisabetta Comini, Italy
Marco Consales, Italy
Jesus Corres, Spain
Andrea Cusano, Italy
Antonello Cutolo, Italy
Dzung Dao, Australia
Manel del Valle, Spain
Ignacio Del Villar, Spain
Francesco Dell'Olio, Italy
Utkan Demirci, USA
Nicola Donato, Italy
Junhang Dong, USA
Abdelhamid Errachid, France
Stephane Evoy, Canada
Vittorio Ferrari, Italy

Luca Francioso, Italy
Laurent Francis, Belgium
Wei Gao, Japan
Michele Giordano, Italy
Banshi D. Gupta, India
Clemens Heitzinger, Austria
María del Carmen Horrillo, Spain
Wieslaw Jakubik, Poland
Hai-Feng Ji, USA
Kouros Kalantar-Zadeh, Australia
Sher Bahadar Khan, KSA
Sang Sub Kim, Republic of Korea
Challa Kumar, USA
Laura M. Lechuga, Spain
Chengkuo Lee, Singapore
Chenzhong Li, USA
Eduard Llobet, Spain
Jaime Lloret, Spain
Yu-Lung Lo, Taiwan
Oleg Lupan, Moldova
Frederick Maily, France
Eugenio Martinelli, Italy
Jose R. Martinez-De-Dios, Spain
Yasuko Y. Maruo, Japan
Mike McShane, USA
Igor L. Medintz, USA
Fanli Meng, China
Aldo Minardo, Italy
Joan Ramon Morante, Spain
Lucia Mosiello, Italy
Masayuki Nakamura, Japan
Calogero M. Oddo, Italy
Marimuthu Palaniswami, Australia
Alberto J. Palma, Spain

Lucio Pancheri, Italy
Alain Pauly, France
Giorgio Pennazza, Italy
Michele Penza, Italy
Andrea Ponzoni, Italy
Biswajeet Pradhan, Malaysia
Ioannis Raptis, Greece
Armando Ricciardi, Italy
Christos Riziotis, Greece
Maria Luz Rodríguez-Méndez, Spain
Albert Romano-Rodriguez, Spain
Carlos Ruiz, Spain
Josep Samitier, Spain
Giorgio Sberveglieri, Italy
Luca Schenato, Italy
Michael J. Schöning, Germany
Andreas Schütze, Germany
Woosuck Shin, Japan
Pietro Siciliano, Italy
Vincenzo Spagnolo, Italy
Vincenzo Stornelli, Italy
Weilian Su, USA
Tong Sun, UK
Raymond Swartz, USA
Hidekuni Takao, Japan
Isao Takayanagi, Japan
Guiyun Tian, UK
Suna Timur, Turkey
Hana Vaisocherova, Czech Republic
Qihao Weng, USA
Matthew J. Whelan, USA
Hai Xiao, USA

Contents

Embeddable Advanced Sensors for Harsh Environment Sensing Applications

Lei Yuan, Yinan Zhang, Yan Lu, Xiaobei Zhang, and Mengmeng Wang
Volume 2016, Article ID 2897541, 2 pages

Location Fingerprint Extraction for Magnetic Field Magnitude Based Indoor Positioning

Wenhua Shao, Fang Zhao, Cong Wang, Haiyong Luo,
Tunio Muhammad Zahid, Qu Wang, and Dongmeng Li
Volume 2016, Article ID 1945695, 16 pages

An IFPI Temperature Sensor Fabricated in an Unstriped Optical Fiber with Self-Strain-Compensation Function

Yang Song, Liwei Hua, Jincheng Lei, Qi Zhang, Jie Liu, Lingyun Ye, and Hai Xiao
Volume 2016, Article ID 6419623, 7 pages

New Leakage Current Particulate Matter Sensor for On-Board Diagnostics

Jiawei Wang, Dong Tang, Songhua Wang, Zehong Zhu, Nan Li, and Lie Chen
Volume 2016, Article ID 5380646, 8 pages

Research on Fused Tapered Photonic Crystal Fiber Sensor Based on the Method of Intermittent Cooling

Guangwei Fu, Xinghu Fu, Peng Guo, Yushen Ji, and Weihong Bi
Volume 2016, Article ID 7353067, 7 pages

Characteristics of Eddy Current Distribution in Carbon Fiber Reinforced Polymer

Shaoni Jiao, Jian Li, Fei Du, Lei Sun, and Zhiwei Zeng
Volume 2016, Article ID 4292134, 8 pages

WildSense: Monitoring Interactions among Wild Deer in Harsh Outdoor Environments Using a Delay-Tolerant WSN

Junho Ahn, Akshay Mysore, Kati Zybko, Caroline Krumm, Sravan Thokala, Xinyu Xing, Ming Lian,
Richard Han, Shivakant Mishra, and Thompson Hobbs
Volume 2016, Article ID 1693460, 17 pages

Measurement of Circumferential Liquid Film Based on LIF and Virtual Stereo Vision Sensor

Ting Xue, Xiaokang Lin, and Liuxiangzi Yang
Volume 2016, Article ID 2872947, 5 pages

Research on Application of Wax Deposition Detection in the Nonmetallic Pipeline Based on Electrical Capacitance Tomography

Nan Li, Kui Liu, Xiangdong Yang, and Mingchen Cao
Volume 2016, Article ID 7390470, 10 pages

Compressed Sensing, Pseudodictionary-Based, Superresolution Reconstruction

Chun-mei Li, Ka-zhong Deng, Jiu-yun Sun, and Hui Wang
Volume 2016, Article ID 1250538, 9 pages

Evaluation of the Degradation on a COTS Linear CCD Induced by Total Ionizing Dose Radiation Damage

Zujun Wang, Baoping He, Wuying Ma, Zhibin Yao, Shaoyan Huang, Minbo Liu, and Jiangkun Sheng
Volume 2016, Article ID 9604042, 6 pages



Design and Fabrication of Air-Based 1-3 Piezoelectric Composite Transducer for Air-Coupled Ultrasonic Applications

Cunfu He, Yaoyao Wang, Yan Lu, Yuepeng Liu, and Bin Wu
Volume 2016, Article ID 4982616, 11 pages

Development of a Wireless Temperature Sensor Using Polymer-Derived Ceramics

Ran Zhao, Gang Shao, Ni Li, Chengying Xu, and Linan An
Volume 2016, Article ID 8624817, 5 pages

Editorial

Embeddable Advanced Sensors for Harsh Environment Sensing Applications

Lei Yuan,¹ Yinan Zhang,² Yan Lu,³ Xiaobei Zhang,⁴ and Mengmeng Wang⁵

¹Department of Electrical and Computer Engineering, Clemson University, Clemson, SC 29634, USA

²Department of Electrical and Computer Engineering, Missouri University of Science and Technology, Rolla, MO 65409, USA

³Research Center of Nondestructive Testing & Evaluation, Beijing University of Technology, Beijing 100124, China

⁴School of Communication and Information Engineering, Shanghai University, Shanghai 200072, China

⁵Department of Electrical Engineering, University of Nebraska-Lincoln, Lincoln, NE 68588-0511, USA

Correspondence should be addressed to Lei Yuan; yuan7@clemson.edu

Received 4 December 2016; Accepted 4 December 2016

Copyright © 2016 Lei Yuan et al. This is an open access article distributed under the Creative Commons Attribution License, which permits unrestricted use, distribution, and reproduction in any medium, provided the original work is properly cited.

Research and development in advanced sensors with embedded monitoring capability have experienced significant growth in recent years, fueled by their broad applications in real-time measurement of a wide variety of physical, chemical, and biological quantities. Compared with conventional sensors with bulky assemblies, recent progress in 3D manufacturing technologies (e.g., ultrafast laser micromachining and additive manufacturing) has opened up a new avenue in one-step fabrication of assembly-free micro devices in various materials as well as the development of compact, customized, and intricate smart structures/components. The merits of these advanced manufacturing techniques enable the integration of embeddable advanced sensors into smart structures and components for improved robustness, enriched functionality, enhanced intelligence, and unprecedented performance.

This special issue seeks to attract researchers to contribute their original research articles as well as review articles that will further improve the performance of advanced sensors. Particular focus is placed on smart parts (advanced sensors and smart structures/components) to address the monitoring needs within extreme environment conditions such as high temperature, high pressure, corrosive/erosive atmosphere, and large strain/stress. A well-chosen real practical application example, based on novel methods and/or known methods to new fields, will also be considered. Both experimental and theoretical/simulated results are welcome to this special issue.

The special issue consists of 12 papers whose brief summaries are listed below.

“Compressed Sensing, Pseudodictionary-Based, Super-resolution Reconstruction” by C. Li et al. focuses on using the classical OMP reconstruction algorithm to solve the sparse optimization problem and effectively increase image resolution. The proposed method provides an effective way to improve the application range and accuracy of aviation and aerospace photogrammetric images.

“WildSense: Monitoring Interactions among Wild Deer in Harsh Outdoor Environments Using a Delay-Tolerant WSN” by J. Ahn et al. developed, deployed, and evaluated a new system for monitoring the movement patterns and interaction behaviors of free-range deer in a rugged wilderness environment. The system combines the functionalities of both GPS and RF-radio sensors with low-cost and minimal-resource nodes. It is able to operate robustly for a period of up to several months for continual tracking and monitoring of the locations and interaction behaviors of wild deer in harsh environments.

“Location Fingerprint Extraction for Magnetic Field Magnitude Based Indoor Positioning” by W. Shao et al. analyzes the main interference sources of the magnetometer embedded on smartphone and presents feature distinguishability measurement technique to evaluate the performance of different feature extraction methods. Experiments revealed that selected fingerprints will improve position distinguishability.

“Measurement of Circumferential Liquid Film Based on LIF and Virtual Stereo Vision Sensor” by T. Xue et al. presents a measurement platform based on the laser-induced fluorescence (LIF) and virtual stereo vision sensor. The experimental results show that the method is valid and effective, which can give a more detailed characterization of the liquid film to reveal the flow structures and flow mechanism.

“Characteristics of Eddy Current Distribution in Carbon Fiber Reinforced Polymer” by S. Jiao et al. studies the characteristics of eddy current (EC) distribution in carbon fiber reinforced polymer (CFRP) laminates. The authors developed an electromagnetic field computation model of EC response to CFRP based on the finite element method. The simulation results are beneficial to optimizing sensor design and testing parameters, as well as damage detection and evaluation.

“Design and Fabrication of Air-Based 1-3 Piezoelectric Composite Transducer for Air-Coupled Ultrasonic Applications” by C. He et al. designed and fabricated air-based 1-3 piezoelectric composite transducers in order to solve the acoustic impedance matching problem. Simulation and experiments show that 3D printed air-based 1-3 piezoelectric composites structures are appropriate for fabricating the air-coupled transducers. They can both reduce the acoustic impedance and enhance the electromechanical conversion efficiency.

“New Leakage Current Particulate Matter Sensor for On-Board Diagnostics” by J. Wang et al. introduced the structure and principle of a new leakage current particulate matter (PM) sensor and performed further study on the PM sensor with combination of numerical simulation and bench test. The results of simulation and experiment reveal the possibility of PM concentration (mass) detection by the sensor.

“An IFPI Temperature Sensor Fabricated in an Unstriped Optical Fiber with Self-Strain-Compensation Function” by Y. Song et al. describes an intrinsic Fabry-Perot interferometry (IFPI) temperature sensor with self-strain-compensation function. Experiment shows the proposed sensor structure holds a constant temperature sensitivity when strained differently.

“Research on Fused Tapered Photonic Crystal Fiber Sensor Based on the Method of Intermittent Cooling” by G. Fu et al. proposed a fused tapered photonic crystal fiber interferometer based on the intermittent cooling method. The fringe contrast of the transmission spectra of this sensor is larger than ordinary fused tapered method. The sensor has high sensitivity to refractive index and low temperature cross-sensitivity.

“Research on Application of Wax Deposition Detection in the Nonmetallic Pipeline Based on Electrical Capacitance Tomography” by N. Li et al. developed an ECT (electrical capacitance tomography) sensor for wax deposition detection in nonmetallic pipelines. The experimental results indicate that the ECT system is valid and feasible for detecting the degree of wax deposition in the nonmetallic pipelines.

“Development of a Wireless Temperature Sensor Using Polymer-Derived Ceramics” by R. Zhao et al. developed a temperature sensor using an embedded system and a sensor head made of polymer-derived SiAlCN ceramics (PDC). The

developed temperature sensor has been experimentally tested to demonstrate the possibility of using such sensors for real world applications.

“Evaluation of the Degradation on a COTS Linear CCD Induced by Total Ionizing Dose Radiation Damage” by Z. Wang et al. presented the evaluation of the degradation on a COTS linear Charge Coupled Device (CCD) induced by total ionizing dose (TID) radiation damage. The dark current, dark signal nonuniformity (DSNU), photo response nonuniformity (PRNU), saturation output, full well capacity (FWC), quantum efficiency (QE), and responsivity versus the TID were analyzed. The behavior of the tested CCD had shown remarkable degradation after radiation. The degradation mechanisms of the CCD induced by TID damage were also discussed.

Acknowledgments

Introducing this special issue to this journal, we would like to thank all the researchers for their contributions and reviewers for their help in achieving a high technical quality of papers in this special issue. The Lead Guest Editor Dr. Lei Yuan would like to thank all the Guest Editors for their valuable contribution to this special issue. We hope all the readers can enjoy the papers in the special issue as we do.

*Lei Yuan
Yinan Zhang
Yan Lu
Xiaobei Zhang
Mengmeng Wang*

Research Article

Location Fingerprint Extraction for Magnetic Field Magnitude Based Indoor Positioning

Wenhua Shao,¹ Fang Zhao,¹ Cong Wang,¹ Haiyong Luo,²
Tunio Muhammad Zahid,¹ Qu Wang,² and Dongmeng Li²

¹*School of Software Engineering, Beijing University of Posts and Telecommunications, Beijing, China*

²*Institute of Computing Technology, Chinese Academy of Sciences, Beijing, China*

Correspondence should be addressed to Wenhua Shao; shaowenhua@ict.ac.cn

Received 28 May 2016; Accepted 30 October 2016

Academic Editor: Yan Lu

Copyright © 2016 Wenhua Shao et al. This is an open access article distributed under the Creative Commons Attribution License, which permits unrestricted use, distribution, and reproduction in any medium, provided the original work is properly cited.

Smartphone based indoor positioning has greatly helped people in finding their positions in complex and unfamiliar buildings. One popular positioning method is by utilizing indoor magnetic field, because this feature is stable and infrastructure-free. In this method, the magnetometer embedded on the smartphone measures indoor magnetic field and queries its position. However, the environments of the magnetometer are rather harsh. This harshness mainly consists of coarse-grained hard/soft-iron calibrations and sensor electronic noise. The two kinds of interferences decrease the position distinguishability of the magnetic field. Therefore, it is important to extract location features from magnetic fields to reduce these interferences. This paper analyzes the main interference sources of the magnetometer embedded on the smartphone. In addition, we present a feature distinguishability measurement technique to evaluate the performance of different feature extraction methods. Experiments revealed that selected fingerprints will improve position distinguishability.

1. Introduction

Location-based services (LBS) in smartphones have attracted tremendous attention in recent years, since convenient and high precision localization services improve people's daily life significantly. These services include navigating a driver to a destination in an unfamiliar area, searching a book inside a large library, or finding a friend at a complex airport.

However, traditional localization techniques, GPS, for example, are only available in outdoor scenarios. They become invalid when it comes to indoor areas, because walls and roofs dramatically attenuate signals from GPS satellites.

Therefore, many indoor localization techniques have been presented by researchers. These techniques include WiFi [1–4], echo [5, 6], and FM [7–9] based approaches. However, WiFi based localization methods are energy expensive for smartphones. Echo approaches are too sensitive to location change, which makes them improper for continuous positioning in a large area. FM methods often become invalid when radio frequency (RF) signals are attenuated by obstacles.

With the development of sensing systems mounted on smartphones, sensing based approaches to indoor localization became available. That is, location-related signals are sensed, and then the user's location is estimated based on these signals. Indoor magnetic field is one kind of location-related signals, which can be sensed by magnetometers embedded on smartphones.

Indoor magnetic field is a pervasive anomalies field induced by geomagnetic field. Because of its location-related, infrastructure-free, and energy efficient features, many researchers have focused on utilizing indoor geomagnetic field for indoor localization purposes. Some experts [10] leverage indoor magnetic anomalies as landmarks, since these anomalies generated by ferromagnetic objects, that is, pillars and doors, are relatively stable. Other researchers [11] construct an indoor magnetic magnitude model, using probability method to estimate user location. In order to improve localization feasibility, experts [10, 12] introduced particle filter framework, which makes it possible to fuse multipositioning methods, including WiFi, Bluetooth, and pedestrian dead reckoning (PDR).

The smartphone collects the indoor magnetic field signal by the magnetometer; however, this process is interfered in by hard/soft-iron effect, hand quivers, and electronic noise, which are not location-related. These interferences decrease the distinguishability of location fingerprints in magnetic field based localization systems.

The main purpose of this paper is to extract location-related only feature of indoor magnetic fields for indoor localization. Although indoor magnetic field contains location information, this information is interfered in by hard/soft-iron effect, hand quiver, and electronic noise. Therefore, rejecting interference signals and keeping location-related signals are beneficial for improving indoor localization performance.

There are two main challenges to magnetic field magnitude (MFM) based location feature extraction. The first one is to ascertain interference sources of magnetometers embedded on the smartphone. This paper first examines the model of magnetometer measurement and then derives the inverse model to estimate indoor magnetic field from magnetometer measurement. With this inverse model as well as related experiments, it is found that the fundamental interference sources of real MFM estimation are coarse-grained soft/hard-iron calibration and sensor electronic noise.

Secondly, there are various magnetic field fingerprint extraction methods; hence, it is necessary to select a high discernible one among them. However, a few researchers have studied this problem. Galván-Tejada et al. compared temporal, spectral, and energy features of indoor magnetic field [13]. But their work concentrates on room level classification. Although localization accuracy can reflect fingerprint performance in some degree, it is affected by the localization algorithm. Therefore, to measure fingerprint distinguishability, this paper presents a novel and lightweight distinguishability measurement method (DAME). This method provides an independent way to qualify fingerprint distinguishability, and it has low overhead compared to previous works.

In conclusion, our contributions are threefold:

- (i) We perform in-depth studies of indoor magnetic field attributes and magnetometer measurement. Then, we present the notion that coarse-grained soft/hard-iron calibration and sensor noise are the fundamental reasons of device heterogeneity and user diversity.
- (ii) We propose a novel fingerprint distinguishability measurement method, DAME, which is especially suitable for low discernibility MFM fingerprint.
- (iii) With DAME, we perform a study on various fingerprint extraction methods and find that Butterworth low pass filter (LPF) is a high discernible fingerprint extraction method of our experiments.

This paper conducts extensive experiments on commercially available smartphones to evaluate the research. Experiment result shows that coarse-grained soft/hard-iron calibration and sensor electronic noise were pervasive in various kinds of smartphones. Butterworth filter fingerprint is a high discernible fingerprint extraction method. Confusion matrixes and their localization errors are also computed to

show the localization accuracy improvement with the high discernible fingerprint.

This paper is organized as follows. Section 2 describes the related work. Section 3 reviews the background of indoor magnetic field formation as well as its advantages and challenges in indoor localization. Section 4 presents the main interferences sources of embedded magnetometer on the smartphone. Section 5 presents the DAME fingerprint distinguishability measurement method and the study for finding a high discernible fingerprint. Section 6 describes the experiments. Finally, Section 7 concludes the paper with a discussion.

2. Related Work

Localization technology is an enabling technology in pervasive computing area, which provides a foundation for the context-aware service. Many efforts have been devoted to this field, and there are already numerous commercially available positioning technologies. In recent years, various indoor MFM based localization methods have been presented; however, there are few researches related to MFM location feature extraction.

Chavez-Romero et al. presented a robotic wheelchair based indoor localization method using visual markers and particle filter [14]. Their system is mounted on a wheelchair, and the wheels can provide odometry data, which is not available for the pedestrian user holding a smartphone.

Li et al. addressed reliable and accurate indoor localization using inertial sensors commonly found on commodity smartphones [15]. They utilized indoor magnetic field based compass to provide orientation for their particle filter localization system.

Shu et al. described a fusion indoor localization system with pervasive magnetic field and opportunistic WiFi [16]. They noticed the phenomena where different devices and different smartphone attitudes cause magnetic field measurement offset. So, they remove the mean of MFM sequences to overcome this offset. Besides, their system uses these sequences to update particle weight at each step event.

Frassl et al. researched the magnetic maps of indoor environments [17]. They studied the magnetic field intensity and direction distribution features. Based on their analysis, they implemented a high precision indoor localization system using foot mounted inertial sensors as well as a magnetometer.

Angermann et al. conducted in-depth studies on the characterization of the indoor magnetic field [18]. They utilized a well calibrated sensor package mounted on a measuring device with code odometry to collect and evaluate indoor magnetic field. In their work, they presented the notion that the multiple measurements along a path showed strong modulation.

Le et al. studied magnetic field mapping and fusion method for indoor localization [11]. Their algorithm proves that local magnetic disturbances carry enough information to localize without the help from other sensors. They built a magnetometer measurement probability model to update

particle weight in their particle filter based positioning algorithm.

Xie et al. built MaLoc, a magnetic fingerprint based indoor localization system [12]. They presented the notion that magnetometer's sensitivity is different across different smartphones. Hence, they used magnetic magnitude difference to compare real-time sampling data with trained data.

Galván-Tejada et al. presented an extension and improvement of their previous indoor localization model [13]. The model tests many magnetic field signal features, including kurtosis, mean, and slope. However, their model is designed for room level classification.

Although there are various magnetic field feature extraction methods utilized by different indoor localization systems, they mainly focus on localizing users through original magnetic magnitude fingerprints. However, the original fingerprints are interfered in by coarse-grained soft/hard calibration and sensor electronic noise. Therefore, this paper gives an in-depth study on how to reduce magnetometer interferences and present the DAME algorithm to evaluate the performance of different MFM feature extraction methods.

3. Insight into Indoor Magnetic Field

Modern buildings generally adopt steel reinforced concrete in their structures. However, these ferromagnetic materials distort the magnetic field in various manners in different areas. Though this distortion is negative for orientation estimation of pedestrian dead reckoning (PDR), it can be used as indoor location feature.

Indoor magnetic field is distorted locally, because of pillars, escalators, and large iron furniture. These ferromagnetic objects change the spread of magnetic lines, so indoor MFM reveals different intensities across different locations. Figure 1 illustrates this distortion: the magnitude changes in different locations.

Indoor magnetic field's distortion patterns are static, because the geomagnetic field varies rather slowly. Moreover, the indoor magnetic anomalies are mainly formed by building ferromagnetic structure. As a result, provided that the structure remains unchanged, the magnetic anomalies will be invariant. For instance, Figure 1 demonstrates this stability. The MFM of one corridor was collected twice over 50 days. Although there is a calibration offset between the two signals, the anomalies of the two are similar. The calibration offset will be explained in Section 5.2.

Magnetic field has low discernibility. Geomagnetic magnitude at the earth's surface ranges from 25 to 65 μT [19]. Because indoor magnetic field is mainly formed by distortion of the geomagnetic field, this narrow range is also the approximate magnitude scope of indoor magnetic field. As a result, the number of similar distortion patterns will increase with the enlargement of the searching scope. Take the red line in Figure 1 as an example; there is only one location's magnitude, which is equal to 50 when the search scope is limited in the first one meter. But the location number increases to 3 when the search scope increases to ten meters.

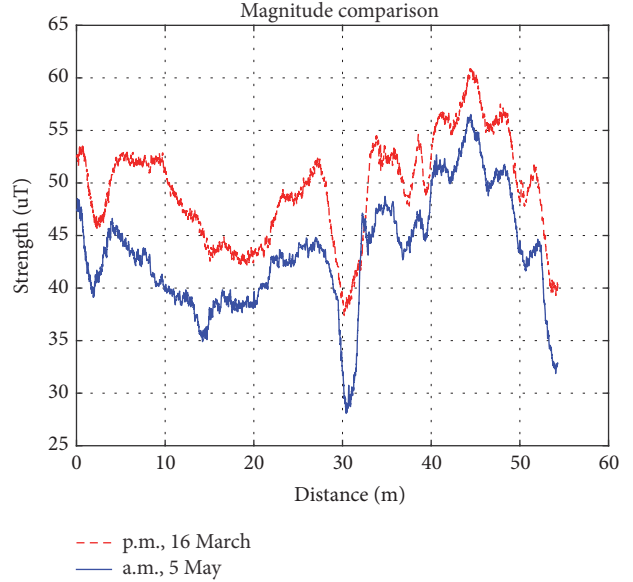


FIGURE 1: Stable and local disturbance of indoor magnetic field. This is the MFM of a 55-meter-long corridor collected in constant speed. The offset between the two signals will be explained in Section 5.2.

Hence, it can be deduced that the longer the search scope is, the more confusing locations there are.

As a brief summary, indoor magnetic field is locally distorted and location stable, which are the advantages for indoor localization, but the field's low discernibility brings about challenges to location feature comparison.

4. Indoor Magnetic Field Interferences

In this section, we discuss the process of magnetometer measuring the geomagnetic field and magnetometer noise. Furthermore, we analyze interference sources of magnetometer measurement.

4.1. Characteristics of Magnetometers on Smartphones. The complicated inner electromagnetic environment of smartphones and the diversity in user behavior make it difficult to precisely measure environment magnetic field.

The magnetometer measures indoor magnetic field's value of a position relative to the orientation of the phone. This value ${}^{\text{Phone}}B_{\text{measured}}$ is a triple with each element representing the magnitude of the magnetic field along the three dimensions of a phone's frame. Moreover, given that the expression of a vector V in frame F is ${}^F V$, then a magnetometer measurement can be represented as follows [20]:

$$V_{\text{add}} = V_{\text{hard}} + V_{\text{sensorOffset}}, \quad (1)$$

$$W_{\text{multiply}} = W_{\text{soft}} \cdot W_{\text{nonOrthog}} \cdot W_{\text{gain}}, \quad (2)$$

$${}^{\text{Phone}}B_{\text{measured}} = W_{\text{multiply}} \cdot {}^{\text{Phone}}R_{\text{Earth}} \cdot {}^{\text{Earth}}B_{\text{real}} + V_{\text{add}}. \quad (3)$$

The smartphone magnetometer is interfered with by additive interference and multiplicative interference when measuring geomagnetic field.

Additive interference V_{add} in magnetometer measurement consists of two parts: hard-iron effect and sensor offset, as (1) shows. In addition, hard-iron effect V_{hard} is the fact that permanently magnetized ferromagnetic components on Printed Circuit Boards (PCBs) add an offset field when the magnetometer is measuring geomagnetic field. Sensor offset $V_{\text{sensorOffset}}$ is the zero field offset in magnetometer's factory calibration.

Multiplicative interference W_{multiply} in magnetometer measurement consists of three parts: soft-iron effect, magnetometer nonorthogonality, and unequal gains, as (2) reveals. First, soft-iron effect is the fact that outer fields, for example, geomagnetic and speaker field, onto unmagnetized ferromagnetic components on the PCB, induce interfering magnetic field when the magnetometer is measuring geomagnetic field. Second, magnetometer nonorthogonality is the lack of perfect orthogonality between sensor axes and sensor relative to the phone's coordinate system. Finally, unequal gains are the different gains in magnetometer in all three axes.

Equation (3) demonstrates the overall process of smartphone magnetometer measuring geomagnetic field. Firstly, the real geomagnetic field is ${}^{\text{Earth}}B_{\text{real}}$, which is expressed in north, east, down (NED) frame. However, the magnetometer measurement is in phone frame, so the geomagnetic field in phone frame is ${}^{\text{Phone}}R \cdot {}^{\text{Earth}}B_{\text{real}}$, with ${}^{\text{Phone}}R$ representing transform matrix from earth frame to phone frame. Moreover, considering all possible phone frames, the universal set of geomagnetic fields in phone frames can be illustrated as the red sphere in Figure 2. Secondly, the magnetometer is interfered with by multiplicative interference, which makes the magnetic field gain different along different axes. As a result, the universal set becomes an ellipsoid. Finally, additive interference makes the universal set ellipsoid leave the original phone frame, as the blue sphere shows. In other words, one magnetometer measurement ${}^{\text{Phone}}B_{\text{measured}}$ is one vector from original to a point of the blue ellipsoid.

Equation (3) reveals that magnetometer measurement ${}^{\text{Phone}}B_{\text{measured}}$ is heavily interfered with, which cannot be used for localization. However, one practical way is to estimate ${}^{\text{Earth}}B_{\text{real}}$ from ${}^{\text{Phone}}B_{\text{measured}}$. From (3), the estimated ${}^{\text{Earth}}B_{\text{real}}$ can be easily derived:

$${}^{\text{Earth}}\tilde{B}_{\text{real}} = {}^{\text{Earth}}\tilde{R} \cdot \tilde{W}_{\text{multiply}}^{-1} \cdot ({}^{\text{Phone}}B_{\text{measured}} - \tilde{V}_{\text{add}}). \quad (4)$$

Furthermore, considering that ${}^{\text{Phone}}R$ is a unit frame transform matrix, the magnitude of ${}^{\text{Earth}}\tilde{B}_{\text{real}}$ can be drawn from (4):

$$\|{}^{\text{Earth}}\tilde{B}_{\text{real}}\| = \|\tilde{W}_{\text{multiply}}^{-1} \cdot ({}^{\text{Phone}}B_{\text{measured}} - \tilde{V}_{\text{add}})\|. \quad (5)$$

In (5), $\tilde{W}_{\text{multiply}}^{-1}$ and \tilde{V}_{add} are estimated multiplicative and additive interference parameter. Solving $\tilde{W}_{\text{multiply}}^{-1}$ and \tilde{V}_{add} is actually to compute the blue ellipsoid center and its ellipsoid parameters in Figure 2. To solve them, one general way for

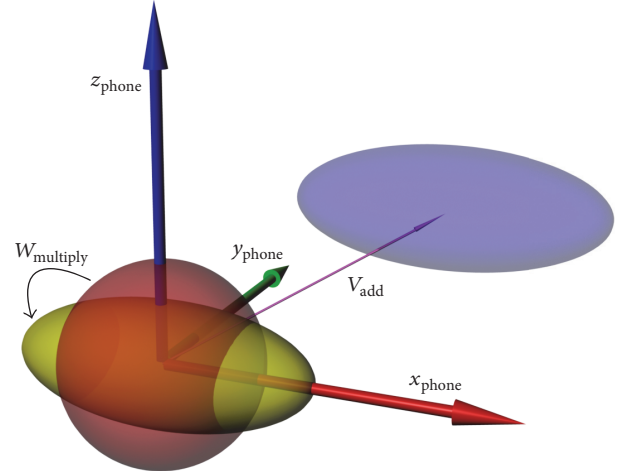


FIGURE 2: Soft- and hard-iron effect illustration.

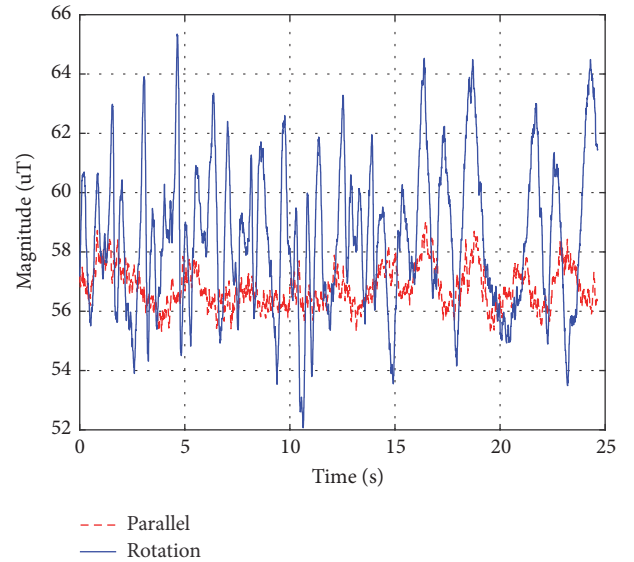


FIGURE 3: Parallel versus rotation data collection illustration.

commodity smartphones is to rotate the device in a figure of 8 in a small space. Consequently, the magnetometer collects omnidirectional data. These data are distributed on the blue ellipsoid in Figure 2. Hence, using Cholesky factorization [21], the ellipsoid center and ellipsoid parameter can be derived, that is, \tilde{V}_{add} and $\tilde{W}_{\text{multiply}}^{-1}$. As a result, $\|{}^{\text{Earth}}\tilde{B}_{\text{real}}\|$ is computed.

As (5) shows, the precision of $\|{}^{\text{Earth}}\tilde{B}_{\text{real}}\|$ estimation depends on the precision of estimated \tilde{V}_{add} and $\tilde{W}_{\text{multiply}}^{-1}$. Although the smartphone always runs background magnetometer calibration, it is a complicated problem. As a result, only coarse calibration parameter can be computed. Hence, the magnetic magnitude varies as the device rotates. Figure 3 clearly demonstrates these properties, where the magnetic signals were collected within a small cube with 15 cm edges: red dash line signal was collected with parallel movement. Blue full-line signal was collected with omnidirectional

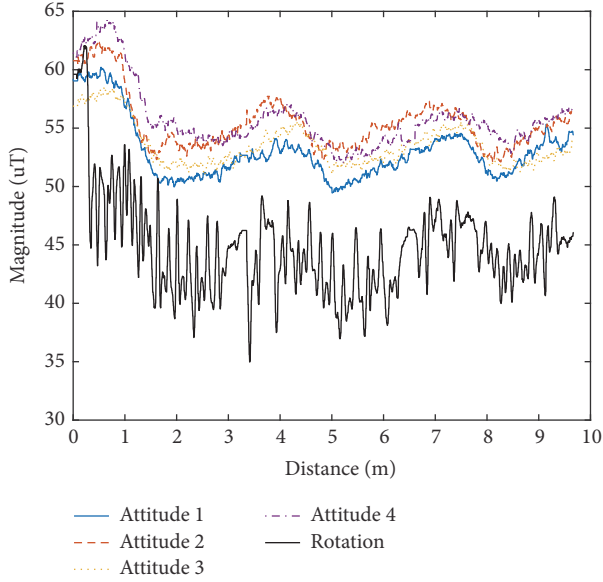


FIGURE 4: Magnetic magnitude in different attitudes.

rotational movement. In the experiment result, parallel signal fluctuation scope was $3.7 \mu\text{T}$, while rotational signal fluctuation scope was $13.3 \mu\text{T}$. In contrast, the fluctuation scope of a typical road is approximately $30 \mu\text{T}$, as Figure 1 depicted, comparable with that of omnidirectional rotation case. Therefore, random omnidirectional device rotation is interfering enough to pollute location feature, as Figure 4 shows: the magnetic signal is collected during walks along a straight corridor with 4 different attitudes and the last one was collected with rotating the device all the way. Obviously, although different attitude magnitude signals have different mean values, their alternating current (AC) component signals are similar. But, for rotation magnitude signals, they had become ambiguous.

Therefore, the coarse-grained additive and multiplicative parameters in the smartphone can be characterized as measured magnetic magnitude being sensitive to rotation movement. In other words, magnetic magnitude is only available when the device stays at a relatively stable situation.

4.2. Magnetometer Measurement. Smartphone magnetometer suffers from random fluctuation signals, including excitation current, feedback circuit and signal conditioning from the sensor inside [22], and currents within coils outside the sensor [23]. Consequently, these signals will make the magnetometer output signal combined with noise.

Figure 5 reveals histogram statistical result of the noisy MFM signal collected by a static smartphone. Obviously, the signal obeyed normal distribution, with mean which equaled $54.16 \mu\text{T}$ and standard deviation of $0.72 \mu\text{T}$. So, the indoor magnetic field measure equation (3) should be updated to (6), where Δ is Gaussian noise. Hence,

$$\begin{aligned} \text{Phone } B_{\text{measured}} &= W_{\text{multiply}} \cdot \text{Phone}_{\text{Earth}} R \cdot \text{Earth } B_{\text{real}} + V_{\text{add}} \\ &+ \Delta. \end{aligned} \quad (6)$$

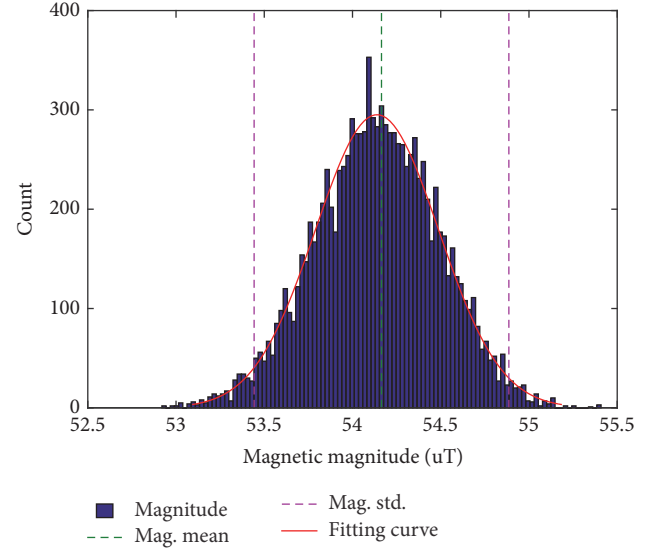


FIGURE 5: Static magnetic magnitude collection statistics. The phone was put up on a tree in a park, sampling magnetic data for 55 seconds.

Therefore, the estimated geomagnetic magnitude is updated to (7), where Δ' is Gaussian noise. Hence,

$$\begin{aligned} \|\text{Earth } \tilde{B}_{\text{real}}\| &= \|\tilde{W}_{\text{multiply}}^{-1} \cdot (\text{Phone } B_{\text{measured}} - \tilde{V}_{\text{add}}) + \Delta'\|. \end{aligned} \quad (7)$$

In conclusion, this section analyzes interference sources of the magnetometer, including hand movement and sensor noise, which are harmful to indoor localization.

5. Indoor Magnetic Fingerprint Extraction

This section presents several indoor MFM fingerprint extraction methods. In order to compare these methods, firstly, a fingerprint distinguishability evaluation model is presented. Secondly, a series of evaluations were conducted to find a high discernible extracted fingerprint.

5.1. Fingerprint Segment Distinguishability Evaluation Method. Indoor magnetic field is a location-related magnetic field induced by geomagnetic field that is steadily distorted by steel reinforced concrete building structures. Hence, it can be utilized as indoor location feature, that is, location fingerprint. A location fingerprint is a static map between location space and feature space whereby one can determine a location from observed features. In other words, an eligible fingerprint has two features: time stability and spatial distinguishability. The time stability of indoor MFM mainly depends on the stabilization of geomagnetic field and building structures discussed in the last section. As to the spatial distinguishability, experts have provided some insights into it [17, 18]; however, as far as we know, there is no study on quantifying distinguishability. In this section, the paper first

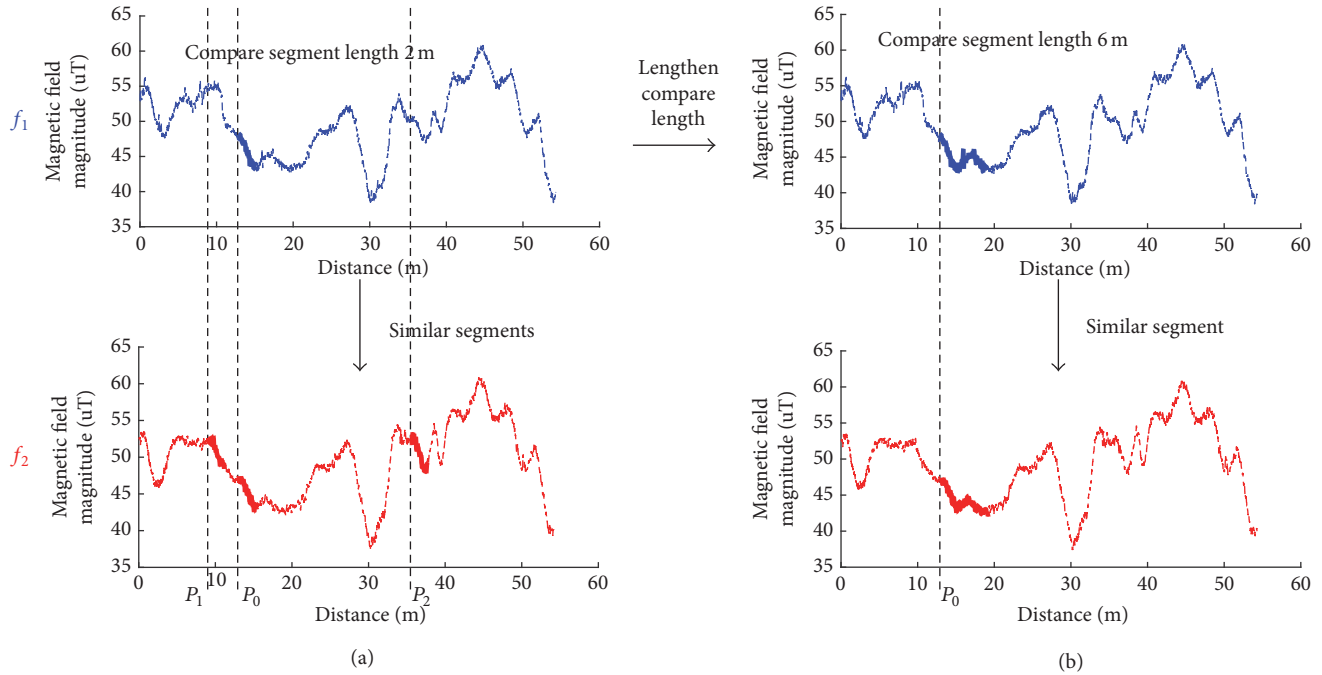


FIGURE 6: Fingerprints similarity with compare length 2 m (a) and compare length 6 m (b). The dash curve of f_1 is real-time fingerprint, and that of f_2 is magnetic localization model. The bold blue curves are fingerprint segments to be compared. The bold red curves are relative similar segments in the localization model.

introduces the feature of MFM distinguishability and then its calculation method.

Indoor magnetic field based positioning generally has two phases: model training phase and fingerprint localization phase. In the model training phase, trainers collect spatial fingerprint signal, then mark them with location information, and finally generate the localization model. In the fingerprint localization phase, users collect real-time fingerprint signal and then estimate users' locations by comparing the real-time fingerprint signals and the localization model. For example, given a localization model (represented as f_2 in Figure 6), suppose a user has collected a target segment (represented as f_1 in Figure 6). To localize the user is to find the most possible position of the target segment in the localization model. This process is usually implemented by comparing the similarity between the target segment and all candidate segments in the model with a sliding window technique. However, false positions (P_1 and P_2) sometimes are more similar than the true position P_0 due to the interferences analyzed in the last section. This paper defines the ability of a target fingerprint segment to be distinguished from the localization model as fingerprint segment distinguishability.

Fingerprint segment distinguishability is proportional to segment length while it is inversely proportional to model fingerprint length. Figure 6 clearly demonstrates these relations: (a) shows that, in the first 20 meters of the model fingerprint, there are only two candidate segments, but the number rises to 3 when model fingerprint extends to 55 meters. However, when target segment length increases to 4 meters, candidate segments number drops from 3 to 1.

The signal similarity between a target segment and a candidate segment can be measured with mean Euclidean distance between them. Moreover, the similarities between the target segment and all possible candidate segments in model fingerprint can be calculated through a sliding window. For instance, the similarities between the target segment and possible candidate segments in Figure 6 can be illustrated as Figure 7, in which the red stars are the ground truth location of target segment. In (a), the three highest peaks represent the three most similar candidate segment locations in fingerprint 2, and the same goes for (b).

In order to measure the distinguishability of MFM fingerprint segment against a model fingerprint, the segment distinguishability needs to be quantified. Although error distance is one common way to measure the performance of the localization algorithm, it is infeasible to assume that error distance represents distinguishability, because of MFM's low discernibility. Therefore, the paper proposes a distinguishability measurement method (DAME) based on the number of similar segments and the signal similarity of the Euclidean distance of AC signal component, which is summarized in Algorithm 1.

Segment distinguishability increases as target fingerprint compare length extends. Distinguishability range lies in $(0, 1]$. When target segment distinguishability equals 1, it will represent the notion that, with the corresponding compare length, the segment can be localized within the given fingerprint. Figure 8 reveals this relation of the fingerprints in Figure 6: when target segment length increases by 2.6 m, the segment distinguishability rises to the maximum, and hence

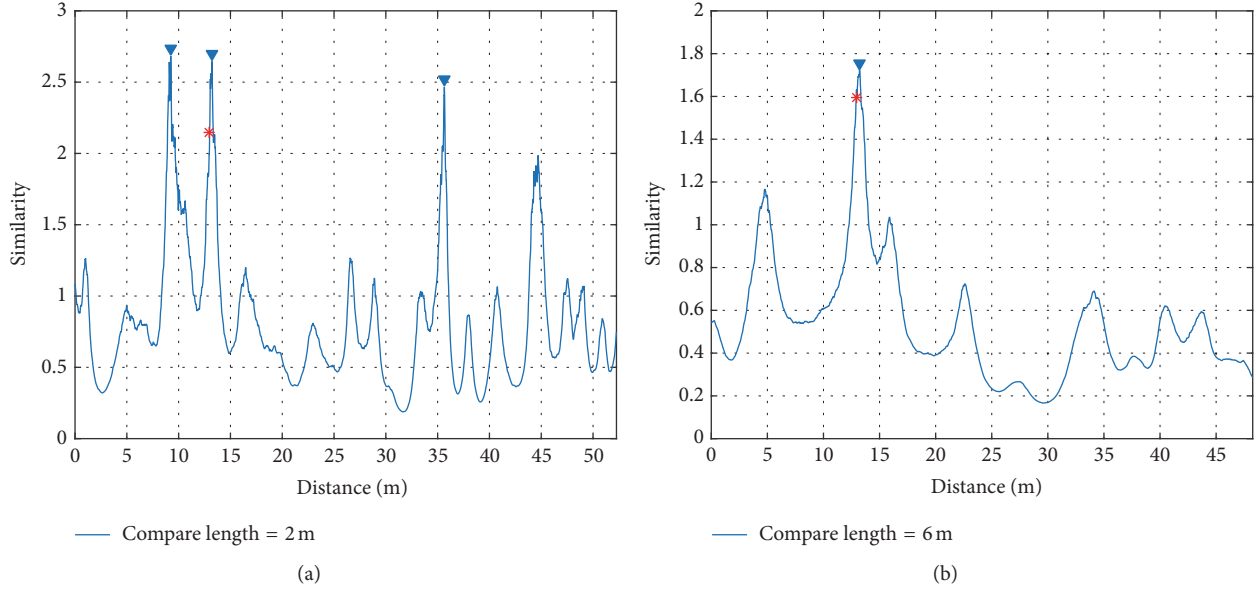


FIGURE 7: Fingerprint distinguishability with compare length 2 m (a) and compare length 6 m (b).

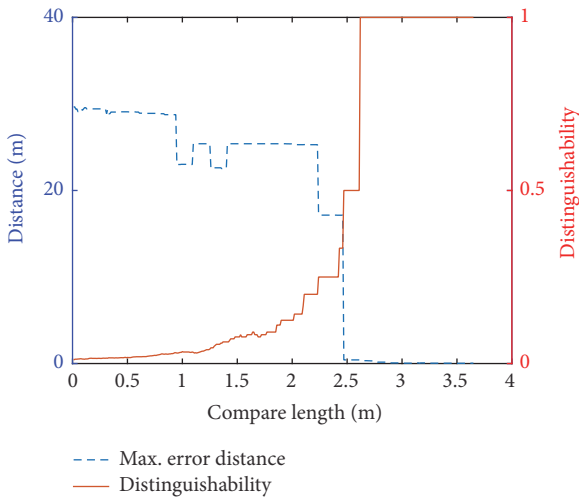


FIGURE 8: Fingerprint distinguishability and error distance under different compare lengths.

its location can be confirmed. Consequently, in order to locate a fingerprint segment from the given localization model, the compare length for this segment should be greater than the value whose distinguishability first equals 1.

5.2. Location-Related Fingerprint Extraction. Indoor magnetic field signal is location-related; however, it is difficult to precisely collect this signal by the magnetometer of the smartphone, because of coarse-grained calibration parameter and sensor electronic noise, as discussed in Section 4. Consequently, these interferences decrease magnetic magnitude distinguishability, causing localization accuracy to decay.

In order to improve localization performance, it is important to filter the signals collected by the magnetometer and

extract location-related only fingerprints from these signals. There are three main affecting factors in MFM collection: temporal influence and device attitude, body tremble, and sensor electronic noise. For temporal influence, users will inevitably approach ferromagnetic materials, including iron chairs and cars, with their smartphones in daily life. These materials will change the interior magnetic environment inside the devices. Although the calibration routine of the smartphone will automatically calibrate this change, this process is coarse-grained, which will cause calibrated signal shift up or down. This shift will remain stable until another calibration happens, as shown in Figure 1. The device attitude has similar effects with temporal influence, as shown in Figure 4. Therefore, it is necessary to remove the direct current (DC) component of the magnetic signal. However, the left AC component will still be interfered with by hand tremble and sensor electronic noise.

The body tremble factor is the slight random quiver when a user carrying a device moves around. Affected by coarse-grained hard/soft-iron effect, this tremble will add distorted magnetometer output. Finally, the sensor electronic noise factor is an additive noise to magnetometer output. Because these factors have little relation with locations, it is supposed that the removal of these signals components improves localization performance.

Several fingerprint extraction methods are studied to reject location-unrelated signal components: wavelet transform, Savitzky-Golay filter, moving average filter, wavelet denoising, and Butterworth filter. The wavelet transform method computes a series of wavelets on different scales with the given wavelet [24]. The wavelet transform of the signal in Figure 1 is represented as Figure 9. In other words, this method transforms time domain signal into frequency domain signal, and it is expected that this transform might reject location-unrelated signal components. In this transformation, different wavelet factor needs different spatial delay;

```

(1) Initialization
(2) Given two MFM fingerprints A and B
(3) Resample fingerprints with same space density
(4) Set AC target segment  $S_{t_{p_t}}$  in A beginning with  $p_t$ 
(5) Set confusion point no  $N_{\text{confusion}} = 0$ 
(6) Distinguishability Compute
(7) for each point  $p_i$  in B do
(8)   Select AC candidate segment  $S_{c_{p_i}}$  beginning with  $p_i$ 
(9)    $d_{c_{p_i}t_{p_t}} = \text{mean}(\|S_{c_{p_i}} - S_{t_{p_t}}\|_{\text{Euclidean}})$ 
(10)   $d_{c_{p_i}t_{p_t}}^{\text{inverse}} = 1/d_{c_{p_i}t_{p_t}}$ 
(11) end for
(12) Find all peaks in  $d^{\text{inverse}}$  set with min peak distance  $d_{\text{mp}}$ 
(13) Set thrash distance  $d_{\text{thrash}} = d_{c_{p_i}t_{p_t}}$ 
(14) for each peak  $d_{c_{p_i}t_{p_t}}^{\text{inverse}}$  do
(15)   if  $d_{c_{p_i}t_{p_t}}^{\text{inverse}} \geq d_{\text{thrash}}$  then
(16)      $N_{\text{confusion}} = N_{\text{confusion}} + 1$ 
(17)   end if
(18) end for
(19)  $D = 1/N_{\text{confusion}}$ 

```

ALGORITHM 1: DAME.

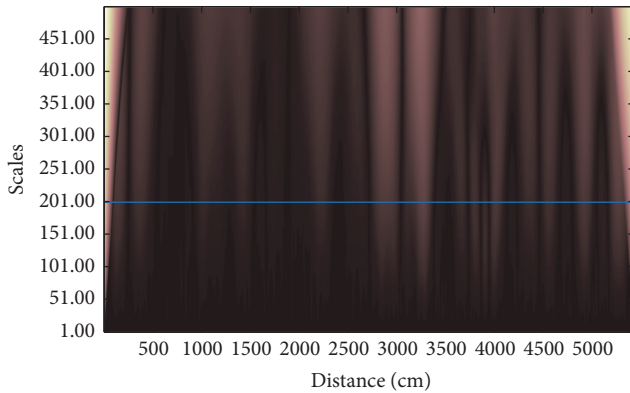


FIGURE 9: MFM wavelet transform.

therefore, 1 meter is chosen as max. tolerance delay, as the blue line shows. Consequently, the fingerprint is shown in Figure 10, and the vertical heads and tails are transition areas that should be discarded.

The Savitzky–Golay filter method fits successive subsets of adjacent data points with a low-degree polynomial by the method of linear least squares, which is also known as convolution [25]. This method is supposed to increase the signal-to-noise ratio without greatly distorting the signal. Consequently, the resulting fingerprint is shown in Figure 11.

The moving average filter method smooths data using a moving average filter, that is, denoising MFM signal by averaging adjacent measurements, with the sacrifice of some adjacent discernibility. The resulting fingerprint is revealed as Figure 12.

The wavelet denoising method performs denoising using given wavelets [26]. Typically, there are three steps in the

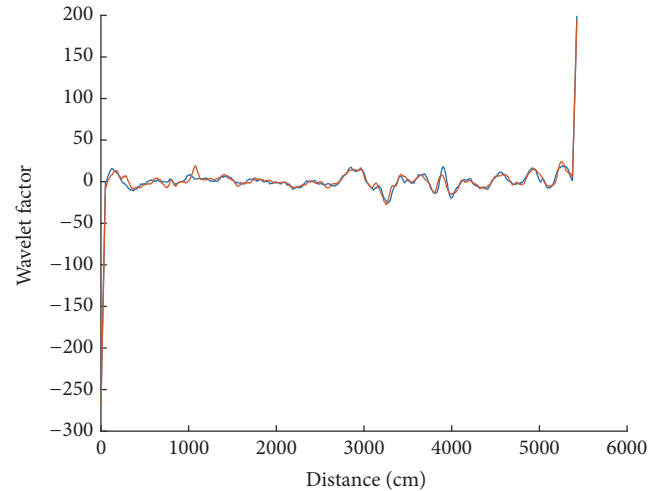


FIGURE 10: Haar wavelet transform fingerprint. The vertical heads and tails are caused by Haar wavelet.

procedure: original signal decomposition to get detail coefficients, detail coefficients modification based on threshold, and signal reconstruction based on modified detail coefficients. The consequent fingerprint is shown in Figure 13.

The Butterworth filter is a maximally flat magnitude filter that is designed to have as flat a frequency response as possible in the pass band [27]. Considering the indoor MFM mainly distorted by building structures which are much larger than user movement, low pass filter (LPF) is suitable for fingerprint extracting. The magnitude response of the LPF used in the system is depicted in Figure 14, with a pass band from 0 to 0.9 Hz. The resulting fingerprint is shown in Figure 15.

In order to compare the distinguishability of different fingerprint extraction methods, the experiment gathered

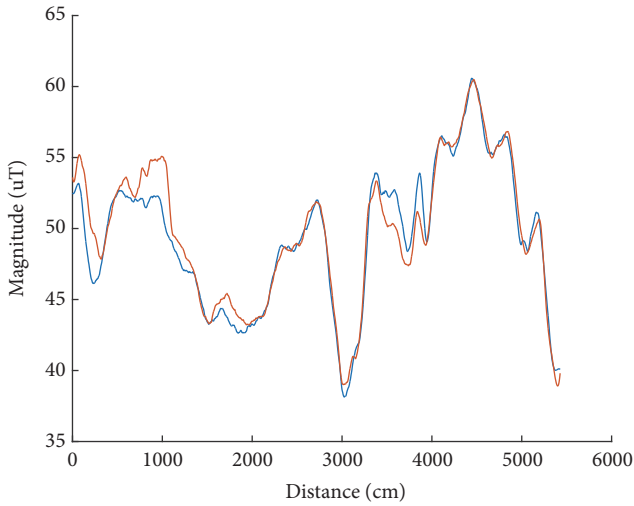


FIGURE 11: Savitzky-Golay filter fingerprint.

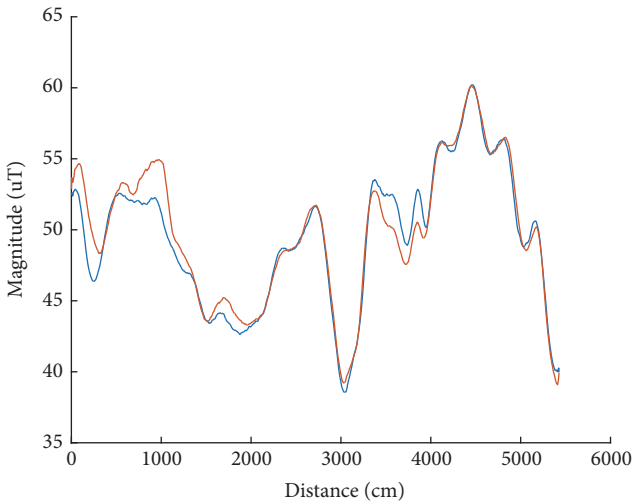


FIGURE 12: Moving average filter fingerprint.

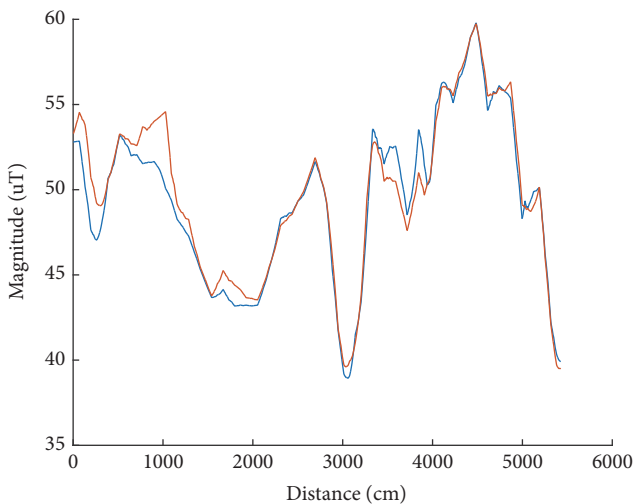


FIGURE 13: Wavelet denoising fingerprint.

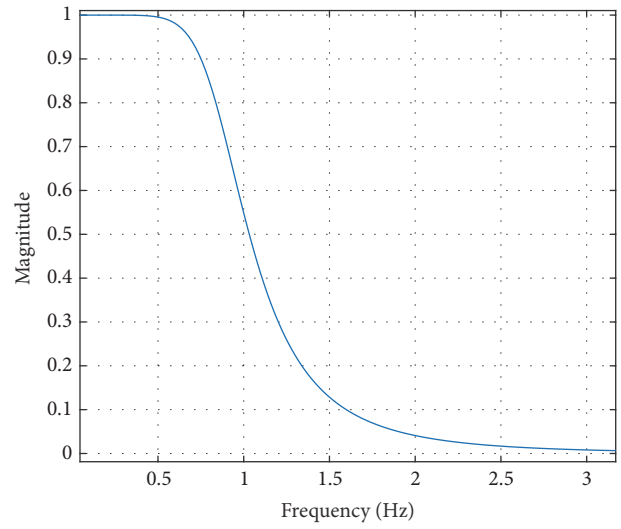


FIGURE 14: Magnitude response.

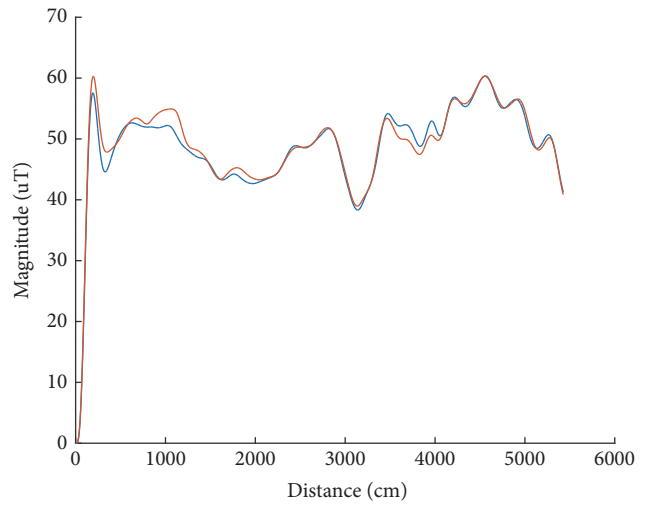


FIGURE 15: Butterworth filter fingerprint.

statistics of mean DAME distinguishability of each method under different compare lengths, as shown in Figure 16. Clearly, as far as the experiments reveal, except for wavelet transform method, other fingerprint extraction methods improved fingerprint distinguishability compared to that of original fingerprint, especially when the compare lengths of fingerprint segments are short. This improvement owes to the denoising of the original signal. In addition, Butterworth filter fingerprint has the highest distinguishability among all these extracted fingerprints, since it rejects noise based on the signal's frequency rather than simple average adjacent measurements.

In conclusion, this section proposes a fingerprint distinguishability measurement method, DAME; furthermore, with this method, Butterworth LPF is found to be a high discernible fingerprint extraction method for indoor magnetic field among the studies.

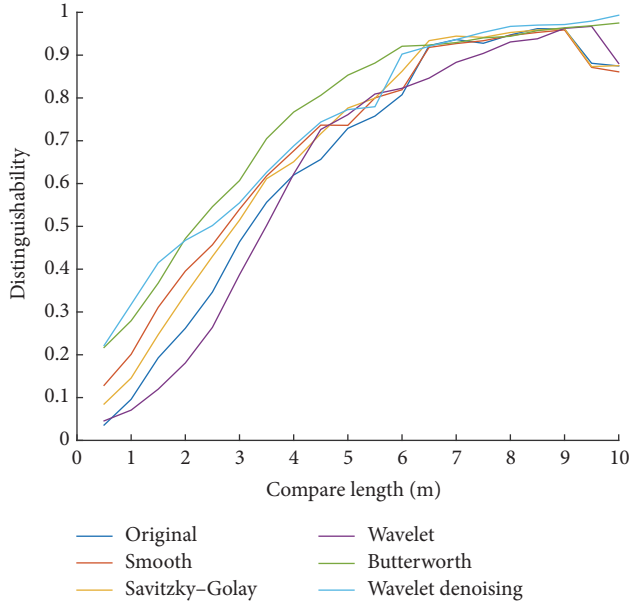


FIGURE 16: Mean fingerprint distinguishability under different compare lengths. Two thousand random segments calculate the result for each kind of fingerprint.

TABLE 1: Experiment smartphones.

Manufacturer	HTC	Samsung	Huawei
Phone series	One X	S4	Mate7
CPU	1.5 G, 4 cores	1.6 G, 4 cores	1.8 G, 4 cores
RAM	1 GB	2 GB	3 GB
Sensor vendor	Panasonic	Asahi Kasei	Asahi Kasei
Resolution	0.16667 μT	0.06 μT	0.0625 μT
Max. range	300 μT	2000 μT	2000 μT
Max. freq.	100 Hz	100 Hz	100 Hz
Real max. freq.	50 Hz	95 Hz	103 Hz

6. Experiments

This section first presents the experiment results of soft/hard-iron calibration on different smartphones. Then, the paper compares and evaluates the fingerprint extraction methods of indoor MFM from various aspects.

6.1. Implementation

6.1.1. Devices. The devices used in our experiments were three commercially available smartphones: HTC One X, Samsung S4, and Huawei Mate7, with their main CPU and sensor parameters specified in Table 1. The algorithm was implemented in Matlab 2016a, running on a PC with Intel i5 dual core CPU, 16 G RAM, and Win10 64-bit OS.

6.1.2. Testing Area. These experiments were conducted in a large building, with a testing area of about 1500 m². This is a typical office environment.

6.1.3. Fingerprint Collection. The road used in our experiment was about 50 meters long. Testers were required to walk at a natural pace along the road, with the phone held in their hand.

6.2. Interference Sources of Indoor Magnetic Field. This part evaluates magnetometer interference sources from two respects: magnetometer calibration error of hard/soft iron and magnetometer electronic noise.

6.2.1. Ubiquitous Hard/Soft-Iron Calibration Error on Smartphones. Testers selected a small free space (0.001 m³ approximately) inside the lab. Then, for the three test devices, testers successively picked up one of them conducting two movements for one minute: first, testers randomly parallel-moved the phone inside the small space keeping its attitude static. Then, testers randomly rotated the phone with omnidirectional movement. The space was so small that the magnetic field inside this space can be seen as a constant field. Consequently, the first parallel movement was a little affected by hard/soft-iron effect; in contrast, the second rotation movement collected MFM from multiple directions of the smartphone, which exhibited the anisotropy of the magnetometer, as Figure 17 reveals.

6.2.2. Relatively Stable Hard/Soft-Iron Calibration Offset on the Same Smartphone. Testers randomly selected three small spaces (0.001 m³ approximately for each) inside the lab. Then, testers conducted two movements as the last experiment did in each space with one device. Clearly, the magnetic fields of the three spaces were different. Figure 18 shows that despite the fact that collecting spaces were different, causing different magnitude mean value, the standard deviation differences between parallel movement and rotation movement are similar, which suggests relative stabilization of hard/soft-iron calibration for the same device.

6.2.3. Pervasive Magnetometer Noise on Smartphones. In order to measure magnetometer noise of different smartphones, testers successively put the three smartphones in the same place and then collected MFM for one minute. As Figure 19 reveals, all the three clusters of sample data fit normal distribution, which suggests a common Gaussian electronic noise. Furthermore, both the mean and the standard deviation of MFM of the three smartphones are different: firstly, the different means suggests different hard/soft-iron calibration error of different smartphones, while the different standard deviations reveal pervasive but different sensor noise level.

6.2.4. Relatively Stable Magnetometer Noise on the Same Smartphone. In order to examine magnetometer noise level of the same smartphone in different places, testers randomly selected three places in the lab and then put the phone in each place and kept the smartphone static sampling for one minute. As Figure 20 reveals, the three distributions have different mean magnitude, but their standard deviations were similar, which suggests relatively stable sensor noise on the same device.

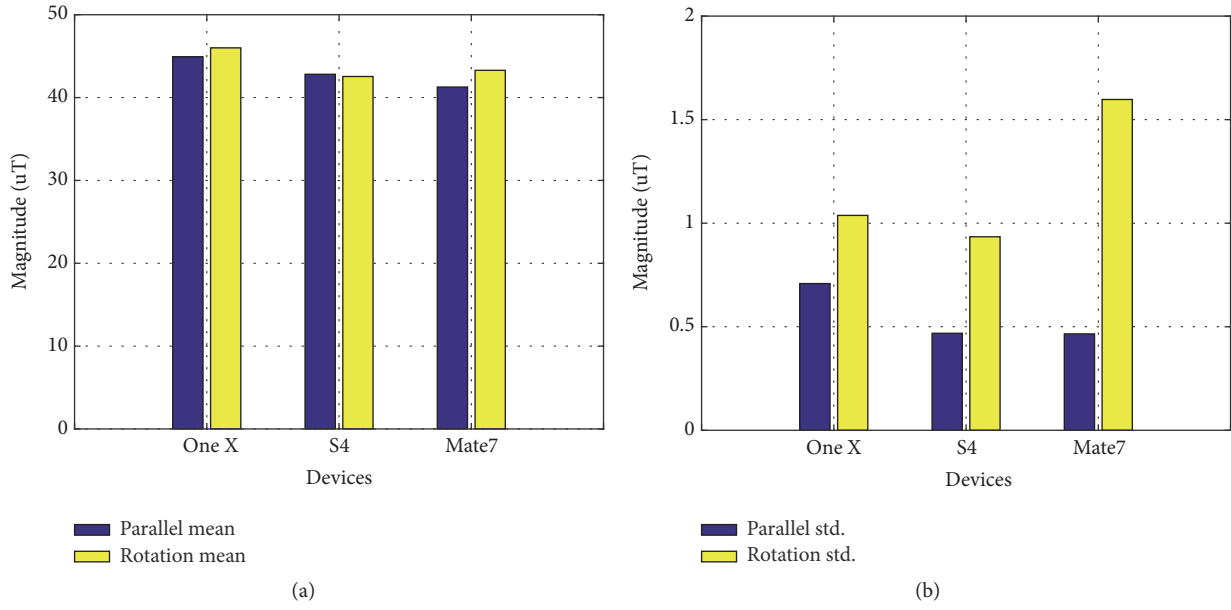


FIGURE 17: MFM statistics of different devices in the same place. Mean statistics (a), standard deviation statistics (b).

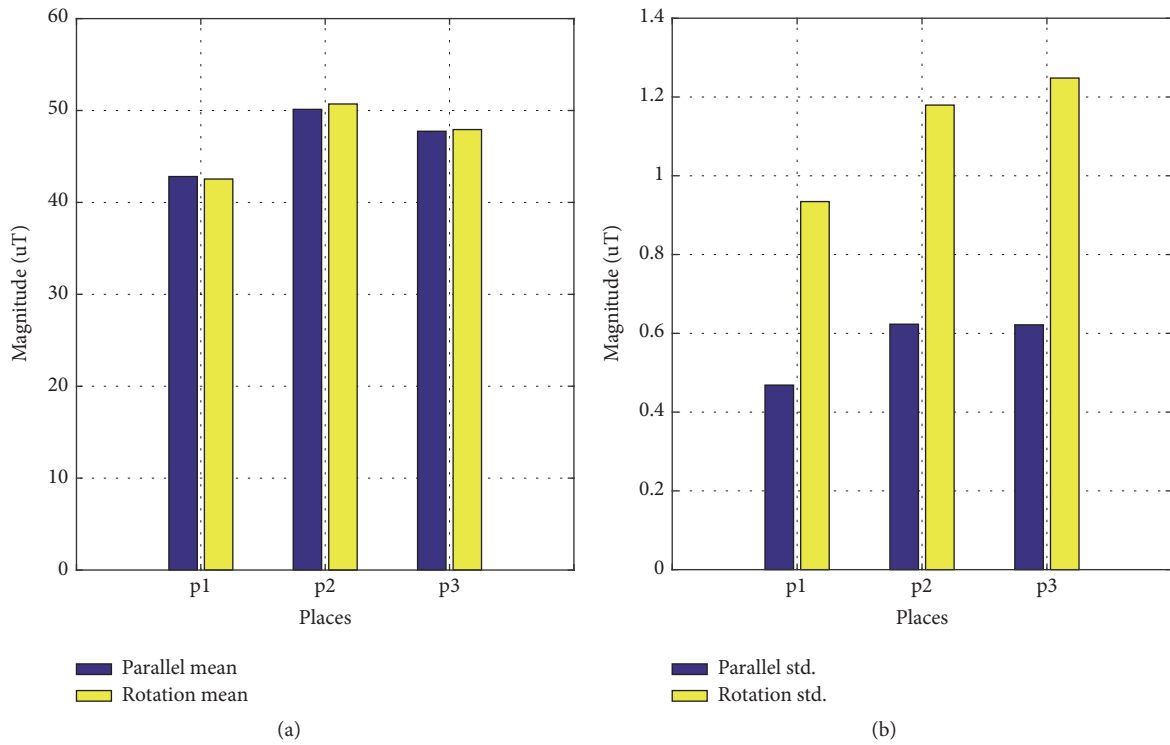


FIGURE 18: MFM statistics of different places by the same smartphone. Mean statistics (a), standard deviation statistics (b).

In conclusion, as far as the experiment is concerned, the soft/hard calibration offsets and magnetometer noise levels on different smartphones are different; however, these offsets and noise levels are relatively stable on the same device. These two factors are the main sources of magnetometer interferences.

6.3. Fingerprint Extraction Evaluation. In this part, testers first examine the distinguishability of MFM fingerprint extracted by different methods. Then, they evaluate the optimum fingerprint by confusion matrix.

To evaluate the distinguishability, testers calculate mean DAME distinguishability with different extraction methods

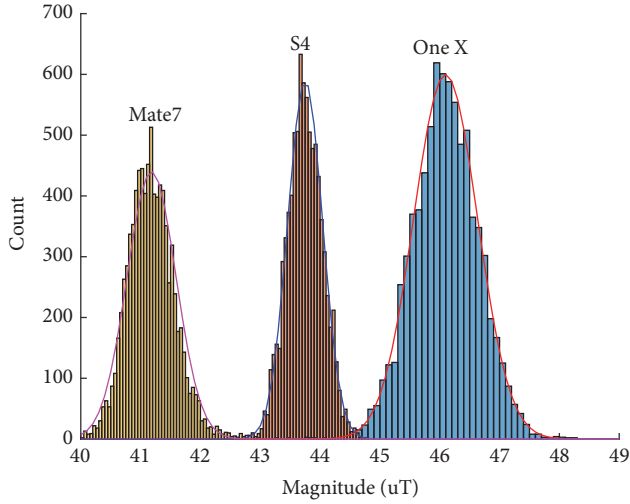


FIGURE 19: Static magnetometer measurement statistics of different smartphones in the same place.

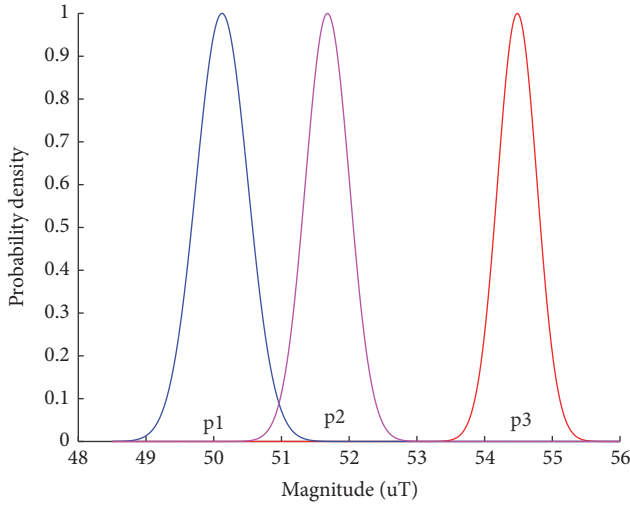


FIGURE 20: Static magnetometer measurement distribution of different places by the same smartphone.

between the two fingerprints shown in Figure 1. Moreover, distinguishability is affected by fingerprint compare length, so testers need to evaluate distinguishability under different compare lengths. Hence, the mean DAME distinguishability sequence calculation for each extracted fingerprint contains the following steps.

Step 1. Assign a compare length l_{compare} and fingerprint extraction method $m_{\text{extraction}}$.

Step 2. With $m_{\text{extraction}}$, extract two fingerprints $f_1^{\text{extracted}}$ and $f_2^{\text{extracted}}$ from the two original fingerprints in Figure 1.

Step 3. Randomly select a fingerprint segment s_1 with compare length l_{compare} from fingerprint $f_1^{\text{extracted}}$.

Step 4. Calculate the DAME distinguishability of this fingerprint segment s_1 against fingerprint $f_2^{\text{extracted}}$.

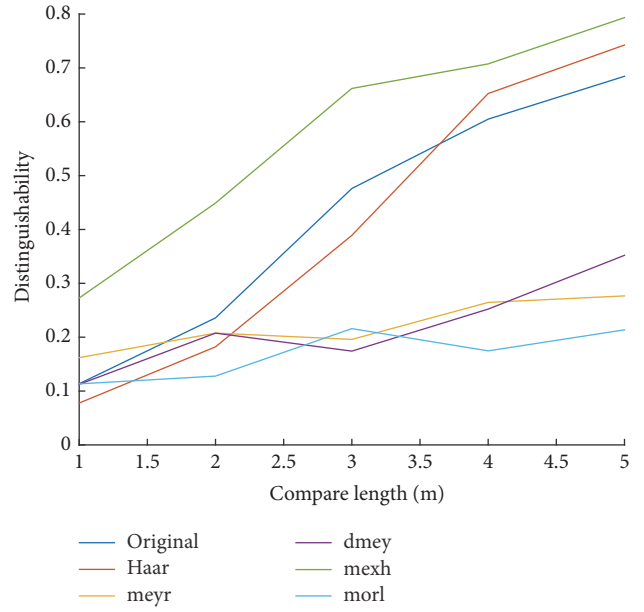


FIGURE 21: Wavelet fingerprint extraction by different analyzing wavelets.

Step 5. Repeat Steps 2–4 one hundred times to get 100 DAME distinguishability values and then calculate the mean DAME distinguishability.

Step 6. Assign a new compare length and repeat Steps 1–5 to get a DAME distinguishability sequence with different compare length.

For each experiment, the two original fingerprints were the reference group. Furthermore, to make the experiments precise, the fingerprint segments selected in Step 3 for different fingerprint extraction methods are the same.

6.3.1. Wavelet Fingerprints Extracted by Different Analyzing Wavelets. Testers used different analyzing wavelets in fingerprint extraction to get different fingerprints and computed their mean DAME distinguishability sequence. The statistic result is shown in Figure 21: morl wavelet performs the best, Haar wavelet has a little improvement, and the other 3 wavelets are even worse than the original fingerprint. This result shows that the performance of wavelet fingerprint extraction depends on wavelet selection.

6.3.2. Savitzky–Golay Fingerprints Extracted by Different Polynomial Orders. Testers changed the polynomial order in Savitzky–Golay filter fingerprint extraction to get different fingerprints and computed their mean DAME distinguishability sequence. Figure 22 reveals that low order filters have higher distinguishability.

6.3.3. Average Moving Fingerprints Extracted by Different Average Lengths. Testers changed the smooth length in average moving fingerprint extraction to get different fingerprints and computed their mean DAME distinguishability

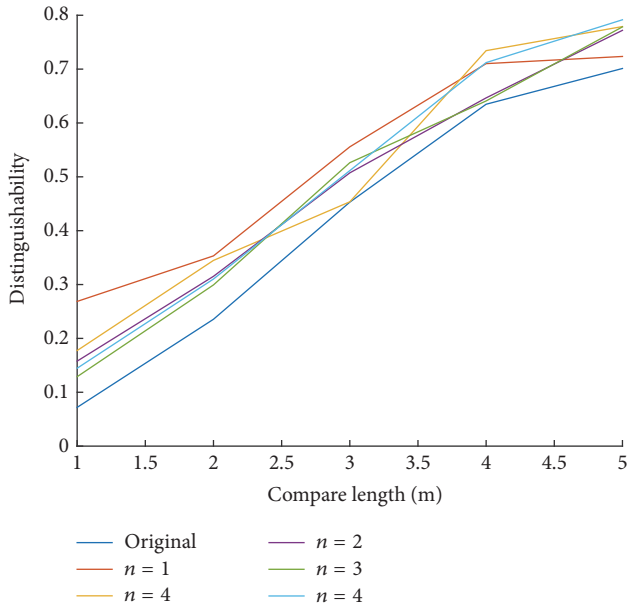


FIGURE 22: Savitzky-Golay fingerprint extraction by different polynomial orders.

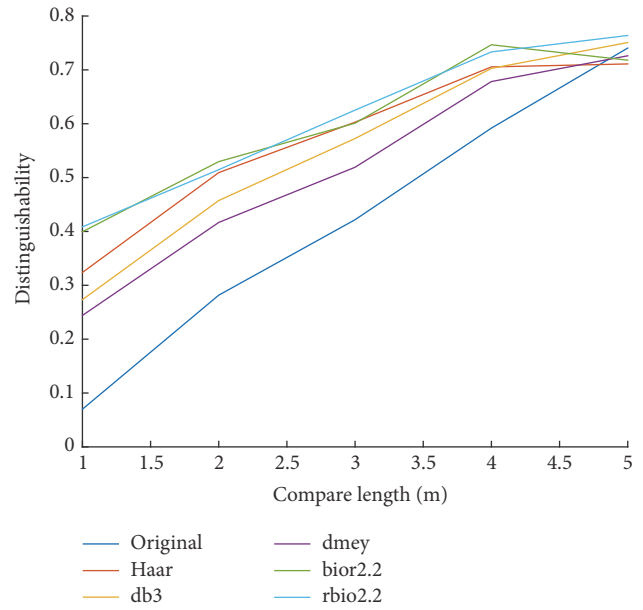


FIGURE 24: Wavelet denoising fingerprint extraction by different analyzing wavelets.

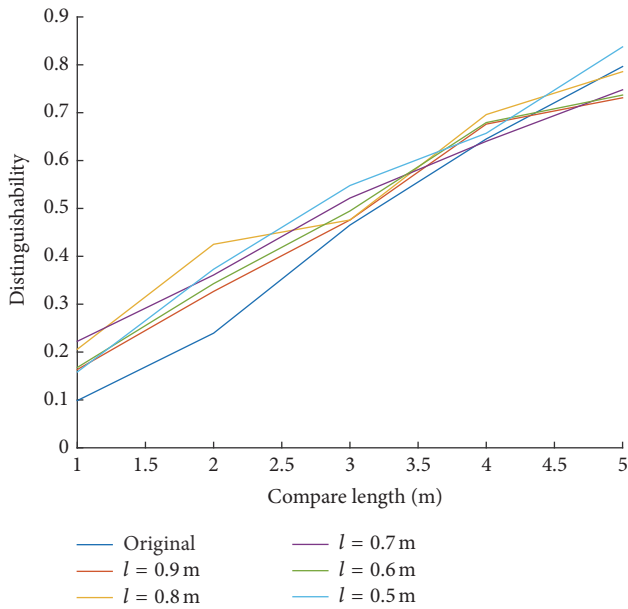


FIGURE 23: Average moving fingerprint extraction by different average lengths.

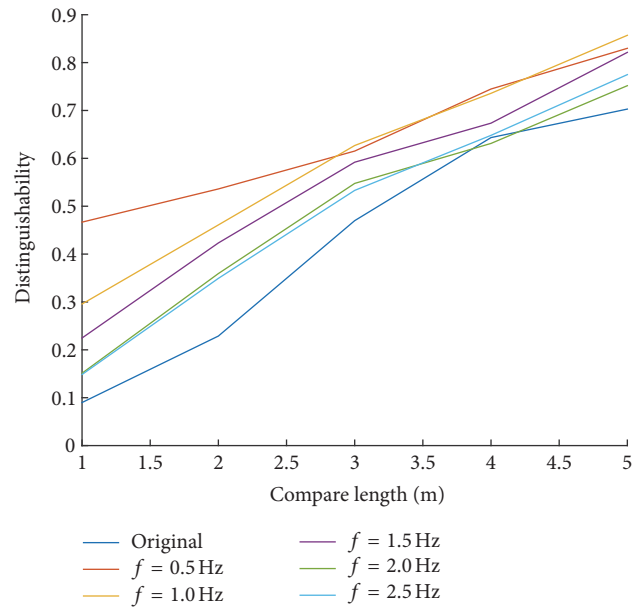


FIGURE 25: Butterworth LPF fingerprint extraction by different low pass bands.

sequence. Figure 23 reveals that moving average filter only improves distinguishability when compare lengths are short.

6.3.4. *Wavelet Denoising Fingerprints Extracted by Different Analyzing Wavelets.* Testers used different analyzing wavelets in fingerprint extraction to get different fingerprints and computed their mean DAME distinguishability sequence. The statistic result is shown in Figure 24: all analyzing wavelets have the ability to improve fingerprint distinguishability, especially rbio2.2.

6.3.5. *Butterworth LPF Fingerprints Extracted by Different Low Pass Frequencies.* In this experiment, testers changed the low pass frequency in fingerprint extraction to get different fingerprints and then computed their mean DAME distinguishability sequence. The statistic result is shown in Figure 25: low frequencies, for instance, 0.5 Hz and 1.0 Hz, improve distinguishability than higher frequencies.

6.3.6. *Diversity Fingerprint Extraction.* In this experiment, testers selected all the most discernible fingerprints in each

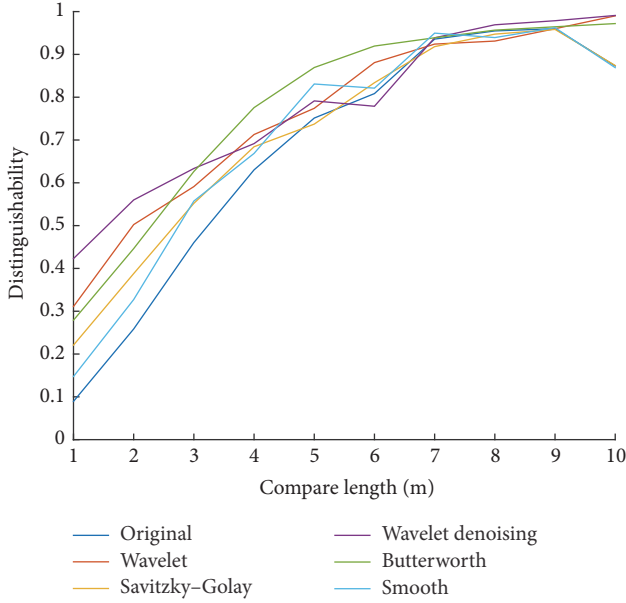


FIGURE 26: Diversity fingerprints comparison.

previous experiment and compared their distinguishability together. As Figure 26 shows, when compare length is less than 7 meters, Butterworth filter has overall the best distinguishability; however, when compare length is greater than 7 meters, there is no big difference between different fingerprint extraction methods.

6.3.7. Confusion Matrix of Butterworth LPF Fingerprint. In order to intuitively illustrate the improvements between original fingerprints and Butterworth LPF extracted fingerprints, testers leveraged confusion matrix. Each element of the matrix is the similarity between two locations of two fingerprints. The similarity is the mean Euclidean distance of the two fingerprint segments started from these locations. The segments are 5 m long. Testers calculated confusion matrices for the original signal pairs, the Butterworth fingerprint pairs, and the subtracted fingerprint pairs. The relations of the three fingerprint pairs are as follows:

$$\begin{aligned} f_1^{\text{subtracted}} &= f_1^{\text{original}} - f_1^{\text{Butterworth}}, \\ f_2^{\text{subtracted}} &= f_2^{\text{original}} - f_2^{\text{Butterworth}}. \end{aligned} \quad (8)$$

The three confusion matrices are shown in Figures 27, 28, and 29. Clearly, as Figure 27 shows, although the segments of the same location IDs are similar to each other (the highlight main diagonal), there are many confusing points in wrong locations (highlight points outside the main diagonal). Figure 28 reveals that the similarity between the segments of the same locations improved, while similarities between segments of different locations were decreased. In Figure 29, testers can see that there is no highlight main diagonal. This means that one segment in subtracted fingerprint 1 is similar to all segments in subtracted fingerprint 2. In other words, the subtracted fingerprints have no location information.

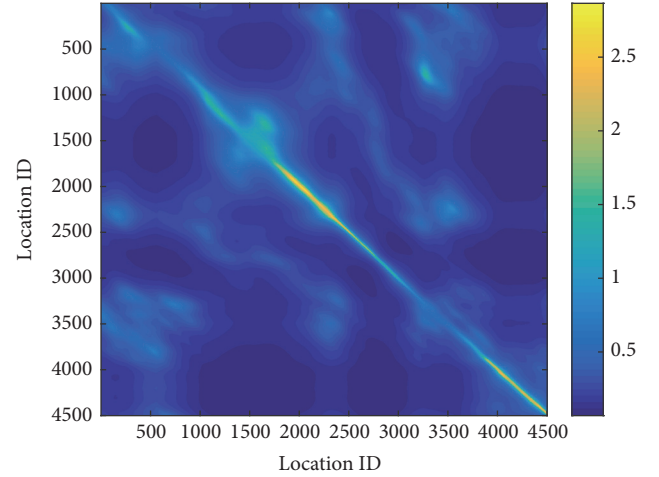


FIGURE 27: Confusion matrix of original MFM signal.

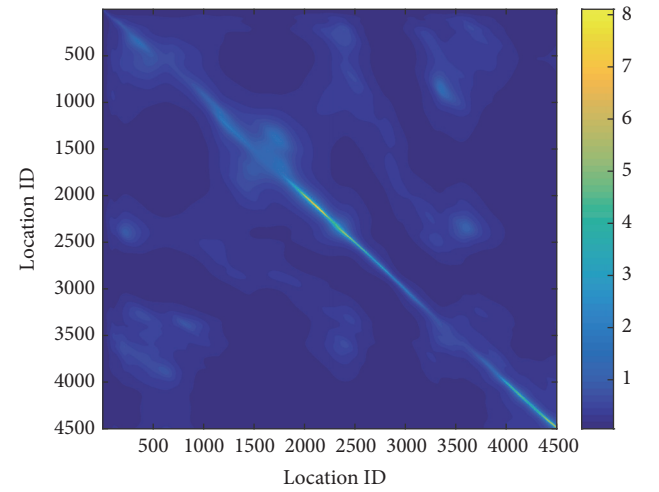


FIGURE 28: Confusion matrix of Butterworth fingerprint.

If testers use most similar points as localization result, then the third quartile of the localization errors for the original fingerprint is 0.78 m and for Butterworth fingerprint is 0.47 m, 40% improved.

Therefore, this experiment revealed that Butterworth fingerprint improved fingerprint distinguishability, and the subtracted signal is harmful for localization.

7. Conclusions

This paper firstly discusses the main interference sources for the data collection of a smartphone; that is, due to coarse-grained hard/soft-iron calibration, slight hand tremble brings about interference in magnetometer measurement. Sensor electronic noise is another source of magnetometer interference.

Then, we present DAME, a distinguishability evaluation model for MFM based fingerprint. With this model, the distinguishability of one fingerprint segment against another fingerprint can be represented. Moreover, given compare

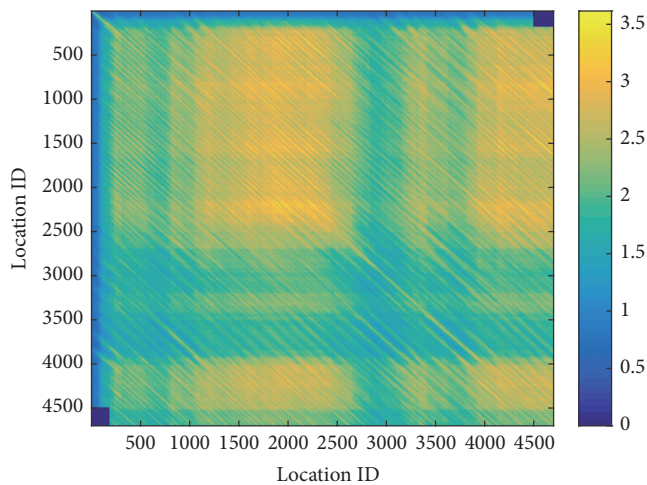


FIGURE 29: Confusion matrix of subtracted signal.

length, the distinguishability between two fingerprints can be quantified by mean DAME distinguishability.

Finally, utilizing the DAME distinguishability, we compare several extraction methods for MFM based fingerprint. Consequently, we find that Butterworth filter fingerprint is the most discernible one as far as our experiments are concerned.

Moreover, the experiments confirm the effectiveness of distinguishability measurement method, DAME, as well as the superiority of Butterworth filter fingerprint.

Competing Interests

The authors declare that there are no competing interests regarding the publication of this manuscript.

Acknowledgments

This work was supported in part by the National Natural Science Foundation of China (61374214), the Major Projects of the Ministry of Industry and Information Technology (2014ZX03006003-002), the Development Special Project of Shenzhen Emerging Industries of Strategic Importance ([2014]1787), the 863 Achievement Transformation Project of Tianjin (14RCHZGX00857), and the International S&T Cooperation Program of China (2015DFG12520).

References

- [1] C. Yang and H.-R. Shao, "WiFi-based indoor positioning," *IEEE Communications Magazine*, vol. 53, no. 3, pp. 150–157, 2015.
- [2] X. Xu, L. Xie, and L. Peng, "Design of indoor positioning system based on WiFi signal intensity characteristic," *Computer Engineering*, vol. 41, pp. 87–91, 2015.
- [3] Z. Tian, X. Fang, M. Zhou, and L. Li, "Smartphone-based indoor integrated WiFi/MEMS positioning algorithm in a multi-floor environment," *Micromachines*, vol. 6, no. 3, pp. 347–363, 2015.
- [4] F. Yu, M. Jiang, J. Liang et al., "An indoor localization of WiFi based on branch-bound algorithm," in *Proceedings of the International Conference on Information Science, Electronics and Electrical Engineering (ISEEE '14)*, vol. 1–3, pp. 1305–1307, Sapporo, Japan, April 2014.
- [5] Y.-C. Tung and K. G. Shin, "EchoTag: accurate infrastructure-free indoor location tagging with smartphones," in *Proceedings of the 21st Annual International Conference on Mobile Computing and Networking (MobiCom '15)*, pp. 525–536, Paris, France, September 2015.
- [6] K. Liu, X. Liu, and X. Li, "Guoguo: enabling fine-grained indoor localization via smartphone," in *Proceedings of the 11th Annual International Conference on Mobile Systems, Applications, and Services (MobiSys '13)*, pp. 235–248, Taipei, Taiwan, June 2013.
- [7] A. Popleteev and T. Engel, "Device-free indoor localization based on ambient FM radio signals," *International Journal of Ambient Computing and Intelligence*, vol. 6, no. 1, pp. 35–44, 2014.
- [8] V. Moghtadaiee and A. G. Dempstera, "Indoor location fingerprinting using FM radio signals," *IEEE Transactions on Broadcasting*, vol. 60, no. 2, pp. 336–346, 2014.
- [9] Y. Chen, D. Lymberopoulos, J. Liu, and B. Priyantha, "Indoor localization using FM signals," *IEEE Transactions on Mobile Computing*, vol. 12, no. 8, pp. 1502–1517, 2013.
- [10] K. P. Subbu, B. Gozick, and R. Dantu, "LocateMe: magnetic-fields-based indoor localization using smartphones," *ACM Transactions on Intelligent Systems and Technology*, vol. 4, no. 4, article 73, 2013.
- [11] E. Le Grand and S. Thrun, "3-Axis magnetic field mapping and fusion for indoor localization," in *Proceedings of the IEEE International Conference on Multisensor Fusion and Integration for Intelligent Systems (MFI '12)*, pp. 358–364, September 2012.
- [12] H. Xie, T. Gu, X. Tao, H. Ye, and J. Lv, "MaLoc: a practical magnetic fingerprinting approach to indoor localization using smartphones," in *Proceedings of the ACM International Joint Conference on Pervasive and Ubiquitous Computing (UbiComp '14)*, Seattle, Wash, USA, September 2014.
- [13] C. E. Galván-Tejada, J. Pablo García-Vázquez, and R. F. Brena, "Magnetic field feature extraction and selection for indoor location estimation," *Sensors*, vol. 14, no. 6, pp. 11001–11015, 2014.
- [14] R. Chavez-Romero, A. Cardenas, M. Maya, A. Sanchez, and D. Piovesan, "Camera space particle filter for the robust and precise indoor localization of a wheelchair," *Journal of Sensors*, vol. 2016, Article ID 8729895, 11 pages, 2016.
- [15] F. Li, C. Zhao, G. Ding, J. Gong, C. Liu, and F. Zhao, "A Reliable and accurate indoor localization method using phone inertial sensors," in *Proceedings of the 14th International Conference on Ubiquitous Computing (UbiComp '12)*, pp. 421–430, Pittsburgh, Pa, USA, September 2012.
- [16] Y. Shu, C. Bo, G. Shen, C. Zhao, L. Li, and F. Zhao, "Magicol: indoor localization using pervasive magnetic field and opportunistic WiFi sensing," *IEEE Journal on Selected Areas in Communications*, vol. 33, no. 7, pp. 1443–1457, 2015.
- [17] M. Frassl, M. Angermann, M. Lichtenstern, P. Robertson, B. J. Julian, and M. Doniec, "Magnetic maps of indoor environments for precise localization of legged and non-legged locomotion," in *Proceedings of the IEEE/RSJ International Conference on Intelligent Robots and Systems (IROS '13)*, pp. 913–920, Tokyo, Japan, 2013.
- [18] M. Angermann, M. Frassl, M. Doniec, B. J. Julian, and P. Robertson, "Characterization of the indoor magnetic field for applications in localization and mapping," in *Proceedings of the International Conference on Indoor Positioning and Indoor Navigation (IPIN '12)*, Sydney, Australia, November 2012.

- [19] A. Wahdan, J. Georgy, and A. Noureldin, "Three-dimensional magnetometer calibration with small space coverage for pedestrians," *IEEE Sensors Journal*, vol. 15, no. 1, pp. 598–609, 2015.
- [20] T. Ozyagcilar, *Calibrating an eCompass in the Presence of Hard- and Soft-Iron Interference*, Freescale Semiconductor, 2015.
- [21] J. M. G. Merayo, P. Brauer, F. Primdahl, J. R. Petersen, and O. V. Nielsen, "Scalar calibration of vector magnetometers," *Measurement Science and Technology*, vol. 11, no. 2, pp. 120–132, 2000.
- [22] M. Butta and I. Sasada, "Sources of noise in a magnetometer based on orthogonal fluxgate operated in fundamental mode," *IEEE Transactions on Magnetics*, vol. 48, no. 4, pp. 1508–1511, 2012.
- [23] T. Ozyagcilar, *Layout Recommendations for PCBs Using a Magnetometer Sensor*, Freescale Semiconductor, 2015.
- [24] B. Vidakovic and P. Müller, *An Introduction to Wavelets*, Springer, Berlin, Germany, 1999.
- [25] A. Savitzky and M. J. E. Golay, "Smoothing and differentiation of data by simplified least squares procedures," *Analytical Chemistry*, vol. 36, no. 8, pp. 1627–1639, 1964.
- [26] D. L. Donoho, "De-noising by soft-thresholding," *IEEE Transactions on Information Theory*, vol. 41, no. 3, pp. 613–627, 1995.
- [27] S. Butterworth, "On the theory of filter amplifiers," *Wireless Engineer*, vol. 7, pp. 536–541, 1930.

Research Article

An IFPI Temperature Sensor Fabricated in an Unstriped Optical Fiber with Self-Strain-Compensation Function

Yang Song,¹ Liwei Hua,¹ Jincheng Lei,¹ Qi Zhang,¹ Jie Liu,¹ Lingyun Ye,² and Hai Xiao¹

¹The Holcombe Department of Electrical and Computer Engineering, Center for Optical Materials Science and Engineering Technologies (COMSET), Clemson University, 105 Riggs Hall, Clemson, SC 29634, USA

²Zhejiang University, Yuquan Campus, Zheda Road 38th, Hangzhou, Zhejiang 310027, China

Correspondence should be addressed to Lingyun Ye; lyye@zju.edu.cn

Received 23 August 2016; Accepted 9 October 2016

Academic Editor: Banshi D. Gupta

Copyright © 2016 Yang Song et al. This is an open access article distributed under the Creative Commons Attribution License, which permits unrestricted use, distribution, and reproduction in any medium, provided the original work is properly cited.

This paper describes an intrinsic Fabry-Perot interferometer (IFPI) temperature sensor with self-strain-compensation function. The sensor was fabricated on a buffer-intact optical fiber using a femtosecond (fs) laser system. The use of fs laser allows the sensor to be fabricated in an optical fiber without the necessity of removing the polymer buffer coating, thus not compromising its mechanical property. The sensor is composed of two cascaded IFPIs in different cavity length of 100 μm and 500 μm , respectively. The shorter IFPI serves as the temperature sensor, while the second IFPI serves as a compensation sensor, which is used to decouple the strain from the raw signal collected by the shorter FPI. The reflection spectrum of sensor, containing both sensory information and compensation information, is collected in wavelength domain and demultiplexed in the Fourier domain of reflection spectrum. An algorithm was developed and successfully implemented to compensate the strain influence on the proposed temperature sensor. The results showed that the proposed sensor structure holds a constant temperature sensitivity of 11.33 $\text{pm}/^\circ\text{C}$ when strained differently.

1. Introduction

Optical fiber based sensors have been intensively studied for sensing various kinds of physical quantities, including temperature, strain, pressure, and bio/chemical quantities, like intracellular pH, chemical concentration, and so forth. A variety of optical fiber sensor structures, as well as sensing mechanisms, was investigated in the past two decades [1, 2]. A well-known example is Fabry-Perot (FP) interferometer, containing a pair of low-reflectivity mirrors to generate two reflection beams with differing phase delays. Thus, an interference pattern is formed in its reflection spectrum that can be used to accurately measure the phase delay between two mirrors for sensing applications. FPI sensors can be subcategorized into two types, extrinsic Fabry-Perot interferometer (EFPI) and IFPI. EFPI is able to facilitate direct wave-matter interaction, while IFPIs are supreme in its advantages in stability, all-in-fiber flexibility, and lower insertion loss. Uniquely, the features of IFPIs are highly desired for harsh environment sensing.

In the past years, several types of distributed sensor with cascaded FPIs have been demonstrated. The major tracking methods are to demodulate the multiplexed interferometers by fast Fourier transform (FFT). A quasi-distributed IFPI sensing system demultiplexed with FFT-based wavelength tracking method was presented at early years [2]. The wavelength tracking method was utilized to demodulate the temperature information applied to all IFPIs. Frequency components corresponding to each sensor are extracted from the transmission spectra and then transform back to the wavelength domain [3]. The experimental results of the multiplexed IFPI sensors showed the high reliability of wavelength tracking methods according to the high temperature sensitivity. Later, a reported type of sensor used cascaded extrinsic FP interferometer (EFPI) and IFPI as temperature and pressure sensing elements [1]. The sensing system could measure temperature and pressure unambiguously and similarly testified the wavelength tracking methods. But, on the other hand, those sensors which detected single varying quantity and gave

the analysis of sensitivity assumed no crosstalk from other changing parameters at the sensing area.

In this paper, a temperature sensor system with strain self-compensation is presented. Dual-parameters sensing design using cascaded IFPI structures resolved the deviation from temperature-strain crosstalk. To achieve the high quality of optical structure inside fiber, femtosecond laser micromachining was employed in fabricating IFPIs. This ultrafast laser delivers high-intensity energy to the core of single-mode fiber (SMF) and effectively changes the refractive index in inscribed region. During the fabrication, the intact polymer buffer coating of SMF is not striped off, which significantly enhances the mechanical prosperity of the sensor [4]. A pair of IFPIs with different cavity lengths including the main sensor and the compensation sensor composes this sensor system.

2. Demultiplex Principle

IFPI is sensitive to temperature due to the combination of the thermo-optic effect and thermal expansion of the fiber material. In addition, it is strain sensitive because of the variation of refractive index (RI) and the optical length changing simultaneously with physical length of the sensor changing under stretch. Strain-induced effect is defined by Young's modulus multiplexing the stress. Therefore, temperature and strain variation are independent variables to the IFPIs because temperature change will not significantly affect Young's modulus that could be ignored. Specifically, the laser ablated cavity mirrors reflect the guided light from laser source under the influence of temperature and strain [5, 6]. Figure 1 is the structural schematic of IFPI. The two reflected lights formed both sides of the IFPI and denoted and generated an inference pattern. The equation of FP interferometer can be modeled by the two-beam optical interference equation

$$I = I_1 + I_2 + 2\sqrt{I_1 I_2} \cos\left(\frac{2\pi \cdot \text{OPD}}{\lambda} + \varphi_0\right), \quad (1)$$

where I is the intensity of the interference signal; φ_0 is the initial phase of the interference (normally equals zero); and λ is the optical wavelength. The round-trip optical path difference (OPD) of the FP interferometer is given by

$$\text{OPD} = 2n_{\text{cavity}}L, \quad (2)$$

where n_{cavity} is the RI of the cavity medium and L is the physical cavity length of each IFPI. At the valleys of the interferogram in spectrum domain, the phase difference of the two light beams satisfies the condition of destructive interference:

$$\frac{4\pi n_{\text{cavity}}L}{\lambda_m} + \varphi_0 = (2m + 1)\pi, \quad (3)$$

where m is an integer and λ_m is the wavelength of the m th order interference valley [7]. The distance between two adjacent minima of the spectrum, defined as the free spectrum range (FSR), can then be expressed as [8]

$$\text{FSR} = \frac{\lambda^2}{2n_{\text{cavity}}L}. \quad (4)$$

In this sensor system, the compensation IFPI sensor has wavelength shift as a function strain as

$$\Delta\lambda_\varepsilon = (-P_{\text{eff}} + 1)\varepsilon \cdot \lambda_m, \quad (5)$$

where P_{eff} is the effective strain-optic coefficient, approximately 0.204 for fused silica material [8]. From (5), the strain sensitivity is dependent on the interrogated wavelength and the effective strain-optic coefficient [8].

The wavelength shift caused by temperature variation around main IFPI sensor can be expressed as the following equation:

$$\Delta\lambda_T = \left(\alpha_{\text{CTE}} + \frac{d_n}{d_T}\right) \cdot \lambda_m \cdot \Delta T, \quad (6)$$

where α_{CTE} and d_n/d_T are the thermal expansion coefficient and thermal-optic coefficient of the material, respectively. For fused silica material, the CTE is $0.55 \times 10^{-6}/^\circ\text{C}$ and the thermo-optic coefficient is approximately $7 \times 10^{-6}/^\circ\text{C}$ [9, 10]. Based on (5) and (6), the temperature-strain crosstalk of the main IFPI sensor is given by

$$\frac{\mu\varepsilon}{\Delta T} = \frac{\Delta\lambda_T/\Delta T}{\Delta\lambda_\varepsilon/\mu\varepsilon} = \frac{(\alpha_{\text{CTE}} + d_n/d_T) \cdot 10^6}{-P_{\text{eff}} + 1}. \quad (7)$$

The calculated result of the temperature-strain crosstalk for the main IFPI sensor is $9.57 \mu\varepsilon/^\circ\text{C}$ [1].

In general, the wavelength shift of the sensing system can be expressed as

$$\Delta\lambda_{\text{compensate}} = K_\varepsilon \times \mu\varepsilon, \quad (8)$$

$$\Delta\lambda_{\text{main}} = K_\varepsilon \times \mu\varepsilon + K_T \times \Delta T,$$

where K_ε is the coefficient of strain-induced effect and K_T is the coefficient of temperature-induced effect. The strain and temperature can be obtained by solving the following matrix:

$$\begin{bmatrix} \Delta T \\ \mu\varepsilon \end{bmatrix} = \frac{1}{A} \begin{pmatrix} K_\varepsilon & -K_\varepsilon \\ -K_T & 0 \end{pmatrix} \begin{bmatrix} \Delta\lambda_{\text{compensate}} \\ \Delta\lambda_{\text{main}} \end{bmatrix}, \quad (9)$$

where $A = -K_\varepsilon \cdot K_T$.

The interference signal of the sensing system is multiplexed. OPD of the two IFPIs can be resolved by performing the Fourier transform on the recorded interferogram. Broadband light source with a range from 1520 to 1620 with minimum detectable OPD change of $12 \mu\text{m}$ is used in this paper. As early reported, a wavelength tracking method based on FFT is used to improve the measurement accuracy and demodulate the multiplexed signals [2]. Demodulation of the IFPIs spectrum signal follows these steps. First, the two IFPI free spectrum ranges can be distinguished in frequency domain through FFT. Then band-pass filters are used to extract two separate frequency components and do the inverse FFT. The obtained individual wavelength domain spectrum is utilized to track the wavelength shift for each IFPI.

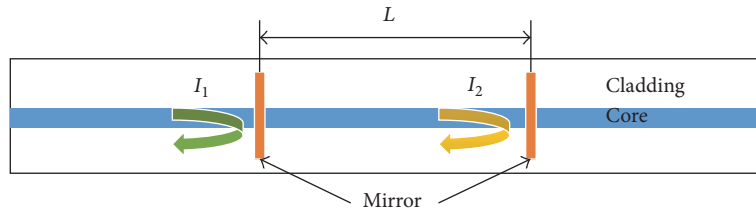


FIGURE 1: Structural schematic of IFPI.

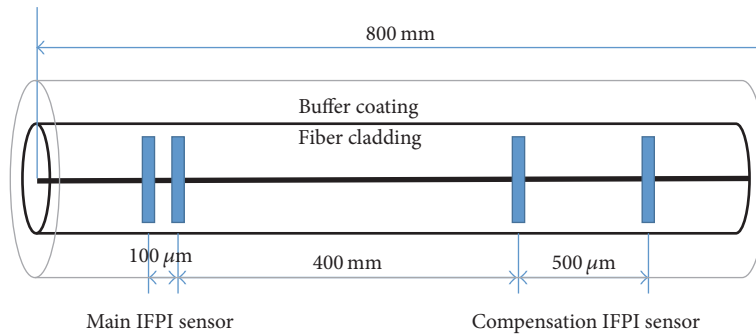


FIGURE 2: Cascaded IFPI sensor system structure.

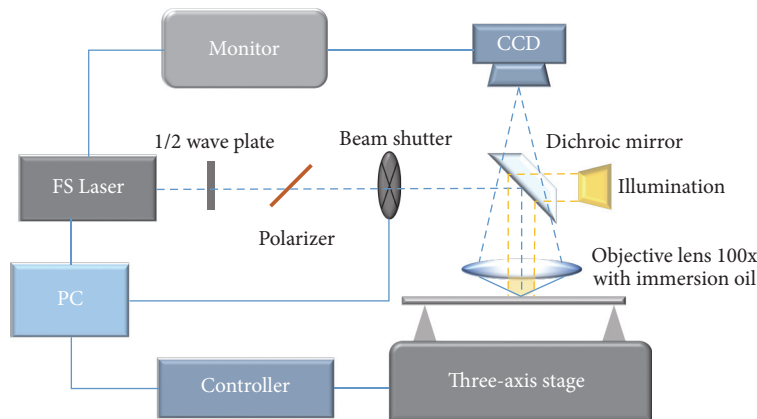


FIGURE 3: Schematic of the fs laser micromachining system.

3. Sensor Design and Fabrication

The sensor consists of two pairs of low reflectance cavity mirrors that form two cascaded IFPIs. Each reflector is created by laser micromachining in the core of a single-mode fiber (Corning SMF-28e). The cavity length of main IFPI sensor is $100\ \mu\text{m}$ and that of the so-called compensation one is $500\ \mu\text{m}$.

Figure 2 shows the sensor structure and dimensions. Four low reflectance mirrors are $15\ \mu\text{m}$ in width, $15\ \mu\text{m}$ in height, and $1\ \mu\text{m}$ in thickness. The distance between two IFPIs is $400\ \text{mm}$ to ensure that temperature changes merely around main IFPI sensor. The total mounted length of fiber is $800\ \text{mm}$. In practical application, the dimensions are flexible in design according to actual needs. As mentioned, the two IFPIs are both sensitive to temperature and strain.

In the case of the stripped-off fabrication, the bare fiber is lack of mechanical property and easy to break, not robust

in experiment or any other harsh environments [4]. Pliability is reduced due to the crippled integrity even with recoating process. Therefore, the engineering challenge in this sensor is to keep the acrylate buffer coating during fabrication with no damage in the coating. Improper laser power and focal delivery will result in melting the polymer coating and defocusing the laser beam.

To assist the fabrication of IFPIs in SMF, FS laser micromachining is used [11]. Figure 3 shows the system of Ti: sapphire fs laser (Coherent Inc.) with the central wavelength in $800\ \text{nm}$, pulse width in $200\ \text{fs}$, and repetition rate of the laser in $250\ \text{KHz}$, respectively. The maximum output power of the laser is $1\ \text{W}$. The actual power used for fabrication was controlled by adjusting the laser beam optics, including a half-wave plate, a polarizer, and one linear neutral density filter. A beam shutter (Thorlabs) was used for switching the laser from on and off. The actual pulse energy for fabrication in this experiment is $0.32\ \mu\text{J}$. The fs laser beam was

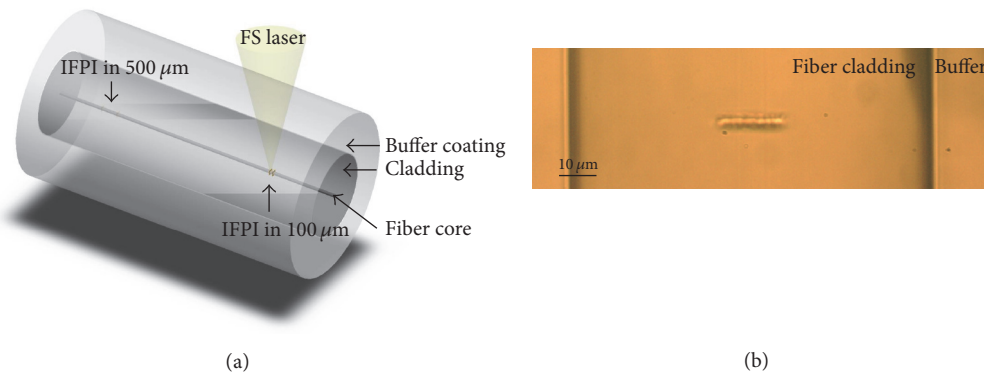


FIGURE 4: (a) Schematic of the fs laser fabrication. (b) Micrograph of the inscribed region.

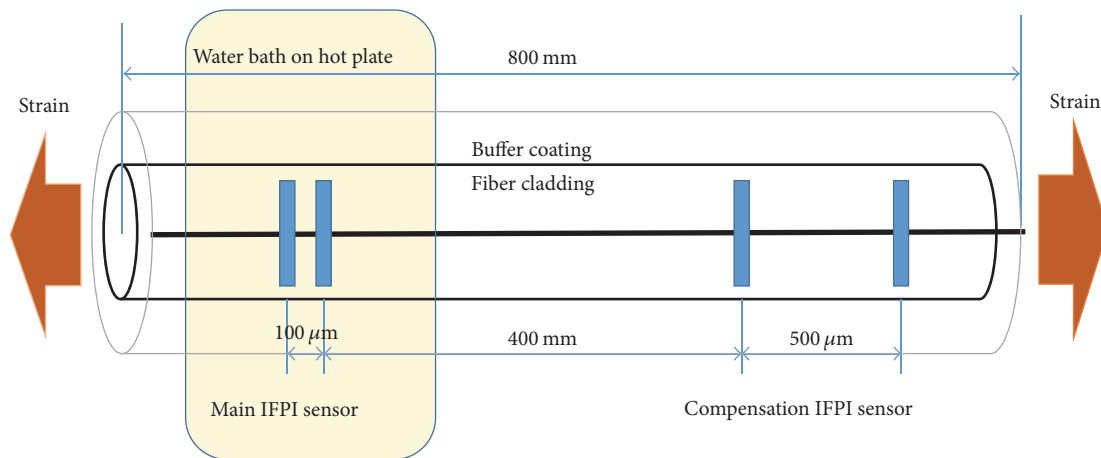


FIGURE 5: Schematic of the experiment setup.

focused into the fiber through an oil immersion objective lens (Olympus. UMPLanFX 100x) with a numerical aperture (NA) of 1.3 [7]. The whole cross-section of the fiber core is covered by a cuboid region of $15 \times 1 \times 15 \mu\text{m}$ inscribed in the center of the fiber from the bottom up. The scanning speed is $20 \mu\text{m/s}$. Figure 4 shows the schematic diagram of the fabrication with buffer intact and the micrograph of the inscribed region which forms a low reflectance mirror.

Refractive index matching oil (Type A, Cargille) with low viscosity and refractive index of 1.46 is used as transparent immersion medium. In oil immersion, the aspect ratio value of the laser spot is higher than that in water immersion significantly. This ratio value depends on the NA and the NA value can be obtained only with oil/water immersion objectives where the lateral spatial resolution can be less than 100 nm. The large NA due to the high refractive index of matching oil helps to improve the aspect ratio of the inscribed region. More importantly, it prevents the heat absorption and melting in the acrylate buffer coating more effectively.

4. Experimental Result

In experiment, the strain sensor system is mounted one side on a moto-driven one-axis stage (Newport) and the other side on a fixed post. The stage has axis resolution of 50 nm and it is controlled to move a certain length by its own software. Applied strain occurs when the stage move outwards until the fiber is tight. Figure 5 shows the experiment setup with strain and temperature environment. For the main IFPI sensor temperature test, a hotplate with thermal couple provides heating in water bath $30\text{--}90^\circ\text{C}$ as the acyclic buffer coating will not survive at high temperature due to the low melting points. The distance between two IFPIs is 400 mm and total length of fixed optical fiber is 800 mm, respectively. This cascaded sensor system is interrogated by a broadband light source. The wavelength range is from 1520 to 1620 nm. The light is routed by a 3 dB coupler and the interference spectrum is detected by an optical spectrum analyzer (AQ6319).

Figure 6 shows the recorded spectrum of multiplexed sensing signal in air and the demodulated result after FFT.

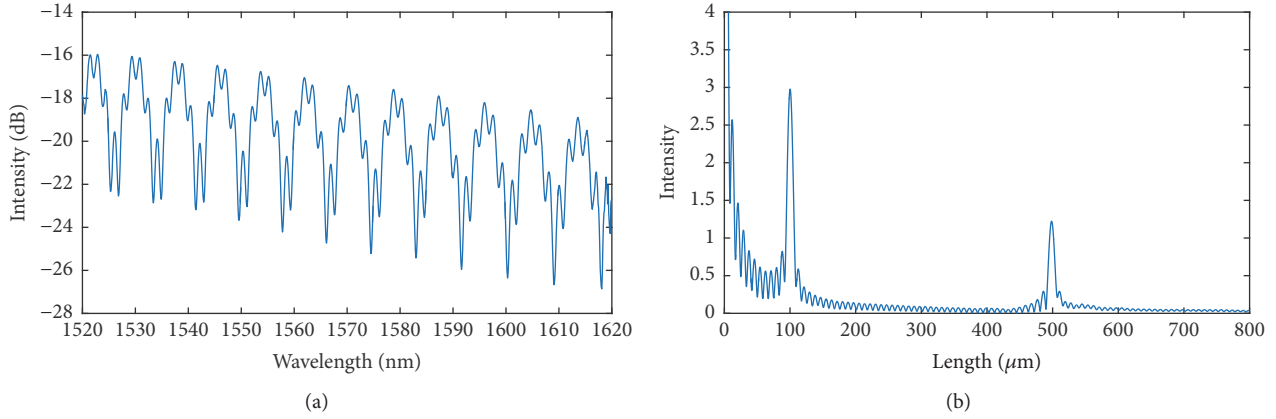


FIGURE 6: (a) Recorded spectrum of cascaded IFPI sensors. (b) FFT result of the multiplexed sensors.

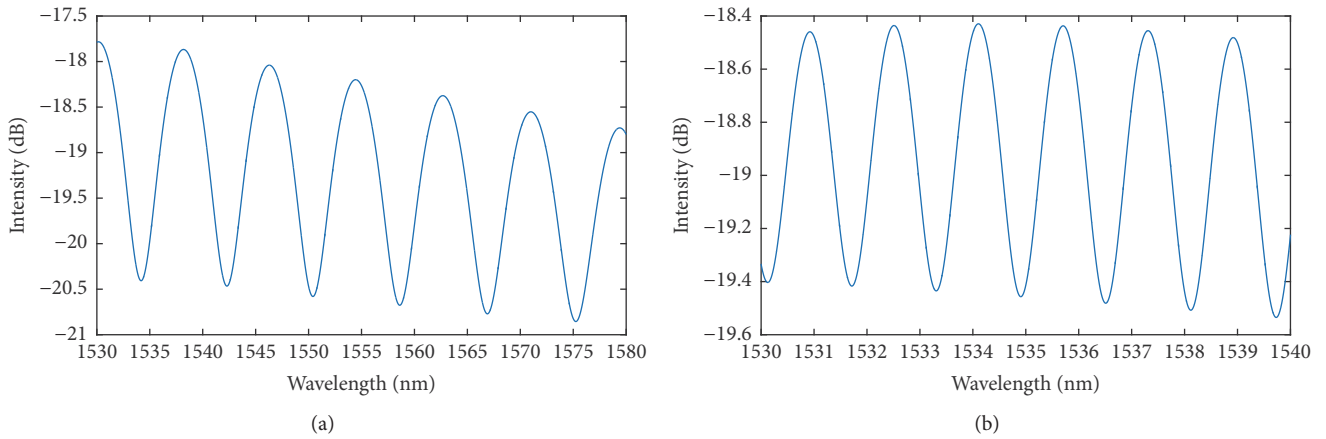


FIGURE 7: Reconstruction of wavelength signal of (a) main IFPI sensor in 100 μm and (b) compensation IFPI sensor in 500 μm .

The waveform domain signal has a high fringe visibility of 7 dB. Since the recorded signal is in wavelength axis and only the wave number axis spectrum is suitable for FFT, `linspace` function in MATLAB library is invoked to arrange the sampling points of wave number domain spectrum in equal interval. In Figure 6(b), two space frequency components with substantially different OPDs can be clearly identified. To select the individual frequency domain component, Hanning-windowed digital filters were used in FFT plotted result. Next, the filtered result is transferred back to the wavelength spectrum. Figures 7(a) and 7(b) are the reconstructed waveforms of two IFPIs, respectively. Once we have the individual interferogram of the two IFPIs, the tracking wavelength can be picked from a specific interference dip in the reconstructed spectrum. Further on, the waveform shift is obtained from this tracking method.

The first experiment is to calibrate the temperature response from main IFPI sensor. Water bath on hot plate (Corning) with thermal couple provides temperature change from 30 to 90°C with 10°C every step [12]. Fiber is loose in sensing area with no strain exerted. In theory, the compensation IFPI sensor will not give any wavelength shift.

Dynamic measurement result of the sensor system performs the specific function in temperature sensitive and

strain self-compensation. In dual varying parameters, main IFPI sensor gives wavelength spectrum shifts from combined impact of temperature and strain. The temperature effect is refined by linearly subtracting the strain information from main sensor signal. Figure 8(a) shows a dip in reconstructed spectrum shifting from the compensation IFPI sensor between 1534 nm and 1536 nm and Figure 8(b) is the strain-induced response. Initialized position of the strain text is set once the fiber is tight. According to the calculation of temperature-strain crosstalk in principle, strain from initialization to additional 600 $\mu\epsilon$ with 100 $\mu\epsilon$ per step is exerted. Simultaneously, temperature test on main IFPI sensor goes again. The number of sampling points in strain test matches the number in temperature test. In Figure 8(b), the compensation IFPI sensor spectrum shifts towards the longer wavelength under increasing strain linearly and the response slope is 1.17 pm/ $\mu\epsilon$.

For the main IFPI sensor, the waveform in Figure 9(a) shifts similarly to the longer wavelength range corresponding to dual parameters. Plotted result of linear relationships in Figure 9(b) shows the wavelength shift information from main IFPI sensor before and after the compensation. Strain-induced effect is dislodged from recorded spectrum by linearly subtracting the spectrum in Figure 8(b) from the main result. The calibration of temperature response in main IFPI

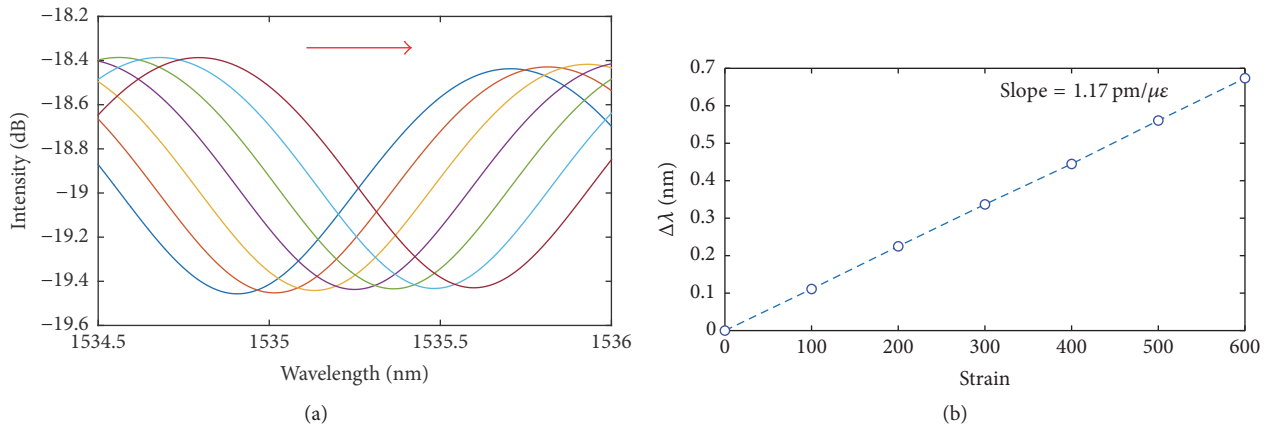


FIGURE 8: (a) Compensation IFPI sensor waveform shifts to the longer wavelength range. (b) Strain test result with slope in $1.17 \text{ pm}/\mu\epsilon$.

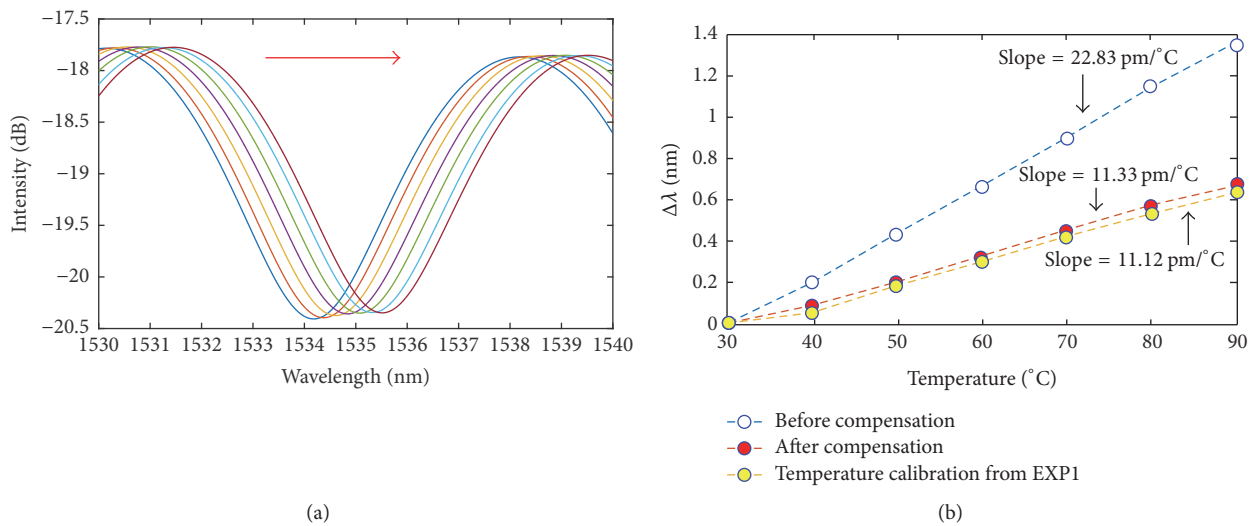


FIGURE 9: (a) Main IFPI sensor waveform shifts to the longer wavelength range. (b) Test result before compensation in blue line. After compensation, by linearly subtracting the strain information, the result of spectrum matches the temperature calibration from experiment 1.

trends linearly with slopes of $11.12 \text{ pm}/^{\circ}\text{C}$ provided from the first experiment. The compensated slope with sensitivity of $11.33 \text{ pm}/^{\circ}\text{C}$ is in full accord with the temperature calibration. The result shows that the temperature sensor system has analogous self-compensated sensing capability by interfering with strain.

5. Conclusions

In this paper, an IFPI-based temperature sensor system with strain self-compensation fabricated by FS laser has been demonstrated. Experimental results indicate that temperature information is completely refined based on the FFT-based wavelength tracking method. Reconstructed spectrum of the main IFPI sensor is analyzed on the basis of temperature-strain crosstalk calculation. The result shows that these cascaded IFPI sensors have high sensitivity of temperature in $11.33 \text{ pm}/^{\circ}\text{C}$ with interference from dynamic strain variation. The sensor system also has a linear response

of strain in $1.17 \text{ pm}/\mu\epsilon$, provided by the compensation IFPI sensor. There is no sensing performance difference under single or multiple parameters effect. These results indicate that the presented temperature sensor system is competent with theoretical analysis in terms of the sensitivity and measurement resolution. Specific fabrication method effectively improves the quality of inscribed region and keeps the intact buffer coating of fiber, which enhance the robustness of the sensor system.

Competing Interests

The authors declare that there is no conflict of interests regarding the publication of this paper.

References

- [1] Y. Zhang, J. Huang, X. Lan, L. Yuan, and H. Xiao, "Simultaneous measurement of temperature and pressure with cascaded

- extrinsic Fabry-Perot interferometer and intrinsic Fabry-Perot interferometer sensors,” *Optical Engineering*, vol. 53, no. 6, Article ID 067101, 2014.
- [2] W. Wang, D. Ding, N. Chen, F. Pang, and T. Wang, “Quasi-distributed IFPI sensing system demultiplexed with FFT-based wavelength tracking method,” *IEEE Sensors Journal*, vol. 12, no. 9, pp. 2875–2880, 2012.
- [3] K. Yüksel, M. Wuilpart, and P. Mégret, “Analysis and suppression of nonlinear frequency modulation in an optical frequency-domain reflectometer,” *Optics Express*, vol. 17, no. 7, pp. 5845–5851, 2009.
- [4] Z. Chen, G. Hefferman, L. Yuan, Y. Song, and T. Wei, “Ultraweak waveguide modification with intact buffer coating using femtosecond laser pulses,” *IEEE Photonics Technology Letters*, vol. 27, no. 16, pp. 1705–1708, 2015.
- [5] T. Wei, Y. Han, Y. Li, H.-L. Tsai, and H. Xiao, “Temperature-insensitive miniaturized fiber inline Fabry-Perot interferometer for highly sensitive refractive index measurement,” *Optics Express*, vol. 16, no. 8, pp. 5764–5769, 2008.
- [6] J. Huang, X. Lan, Y. Song, Y. Li, L. Hua, and H. Xiao, “Microwave interrogated sapphire fiber michelson interferometer for high temperature sensing,” *IEEE Photonics Technology Letters*, vol. 27, no. 13, pp. 1398–1401, 2015.
- [7] Y. Song, L. Yuan, L. Hua, and H. Xiao, “Ferrofluid-based optical fiber magnetic field sensor fabricated by femtosecond laser irradiation,” in *Integrated Optics: Devices, Materials, and Technologies XX*, 97501U, vol. 9750 of *Proceedings of SPIE*, 6 pages, March 2016.
- [8] L. Hua, Y. Song, J. Huang, X. Lan, Y. Li, and H. Xiao, “Microwave interrogated large core fused silica fiber Michelson interferometer for strain sensing,” *Applied Optics*, vol. 54, no. 24, pp. 7181–7187, 2015.
- [9] S. Takahashi and S. Shibata, “Thermal variation of attenuation for optical fibers,” *Journal of Non-Crystalline Solids*, vol. 30, no. 3, pp. 359–370, 1979.
- [10] D. P. Hand and P. S. Russell, “Photoinduced refractive-index changes in germanosilicate fibers,” *Optics Letters*, vol. 15, no. 2, pp. 102–104, 1990.
- [11] L. Yuan, J. Huang, X. Lan, H. Wang, L. Jiang, and H. Xiao, “All-in-fiber optofluidic sensor fabricated by femtosecond laser assisted chemical etching,” *Optics Letters*, vol. 39, no. 8, pp. 2358–2361, 2014.
- [12] E. Chmielewska, W. Urbańczyk, and W. J. Bock, “Measurement of pressure and temperature sensitivities of a Bragg grating imprinted in a highly birefringent side-hole fiber,” *Applied Optics*, vol. 42, no. 31, pp. 6284–6291, 2003.

Research Article

New Leakage Current Particulate Matter Sensor for On-Board Diagnostics

Jiawei Wang,¹ Dong Tang,¹ Songhua Wang,¹ Zehong Zhu,¹ Nan Li,¹ and Lie Chen²

¹Department of Automotive and Traffic Engineering, Jiangsu University, Zhenjiang 212013, China

²Jintan Jonssen Electric-Tech Corp, Changzhou 213200, China

Correspondence should be addressed to Dong Tang; dtang@mail.ujs.edu.cn

Received 22 May 2016; Accepted 2 August 2016

Academic Editor: Yan Lu

Copyright © 2016 Jiawei Wang et al. This is an open access article distributed under the Creative Commons Attribution License, which permits unrestricted use, distribution, and reproduction in any medium, provided the original work is properly cited.

Structure and principle of the new leakage current particulate matter (PM) sensor are introduced and further study is performed on the PM sensor with the combination of numerical simulation and bench test. High voltage electrode, conductive shell, and heaters are all built-in. Based on the principle of Venturi tube and maze structure design, this sensor can detect transient PM concentrations. Internal flow field of the sensor and distribution condition of PM inside the sensor are analyzed through gas-solid two-phase flow numerical simulation. The experiment was also carried out on the whole sensor system (including mechanical and electronic circuit part) and the output signals were analyzed. The results of simulation and experiment reveal the possibility of PM concentration (mass) detection by the sensor.

1. Introduction

Energy saving and environmental protection have always been the hot and difficult problems in the research field of internal combustion engine. Diesel engine is widely used in industry, agriculture, construction, transportation, and other domains because of its low fuel consumption, high thermal efficiency, reliability, and low CO₂ emission. But the high PM emission of diesel engine will have great influence on human health and environment [1, 2]. Diesel particulate filters (DPF) have been widely used in diesel vehicles to remove PM from exhaust gas and help meet stringent legislation [3–5]. On-board diagnostics (OBD) require monitoring of the DPF system for malfunction that may cause PM emission to exceed the regulated levels. In order to fulfill future OBD legislations, which include more stringent requirements on monitoring the functionality of those particulate filters, new sensors which can measure PM concentration directly and withstand harsh exhaust gas environment are necessary for OBD purposes [6]. The stringent emission limit of PM is illustrated in Table 1.

Several technologies of PM detection have been so far proposed such as insulator-based devices which generate

large change in electrical resistance or capacitance with the deposition of PM over the insulating layer [7, 8] and catalytic combustion method which converts the heat generated by the catalytic combustion of soot (C) and soluble organic fraction (SOF) into electrical signal separately [9]. Enterprises such as BOSCH and NTK are carrying out research on PM sensor [10, 11]. The sensors designed by BOSCH and NTK are based on insulator-based devices and measuring electrical capacitance and resistance over the insulating layer, respectively. But resolution of the two sensors is not too high which cannot meet the requirement of instantaneous concentration measurement of PM [12].

In this study, a real-time electronic device based on leakage current was proposed as a PM sensor [13]. Differing with other kinds of PM sensors, this kind of sensor has a conductive shell which is connected to ground and electrodes which are applied with a high voltage. When the exhaust gas flows through the gap between the high voltage electrode and conductive shell, PM inside the gas will be ionized and polarized into conductors, while it has no influence on other substances such as water vapor and carbon dioxide. Then leakage current will be produced between electrode and conductive shell. The PM concentration is obtained based

TABLE I: The emission limits of PM for automotive compression ignition engine.

	Euro-VI PM emissions limit	OBD-I threshold	OBD-II threshold
PM (mass)	4.5 mg/km (3.33 mg/m ³)	20 mg/km (14.8 mg/m ³)	9 mg/km (6.7 mg/m ³)
PN (count)	6×10^{11}	Requirements postponed for lack of adequate sensing technology	



FIGURE 1: Appearance of proposed leakage current PM sensor.

on the functional relationship between leakage current and PM concentration. When the PM concentration gets higher, the emission dielectric constant will also become bigger, which increases the leakage current. On the contrary, lower PM concentration decreases the leakage current. The control system in PM sensor can transform the leakage current signal into voltage signal to make signal processing convenient. After some interval of time, the heater will start to burn off the accumulated PM, which will influence output signals of the sensor [14, 15]. And gas-solid two-phase flow numerical simulation was carried out to analyze the flow of gas phase and particle phase inside the sensor [16–19]. Then bench test was performed on the whole sensor system (including mechanical and electronic circuit part) and output signals of the sensor were analyzed.

The results of simulation and experiment have guidance function for further design of the sensor and they reveal the possibility of PM detection by the leakage current PM sensor.

2. Sensor Introduction

The appearance of proposed leakage current PM sensor is shown in Figure 1. Subassembly of the sensor can be seen in Figure 2. Part 1 consists of the conductive shell, annular flow guide, and high voltage electrode. Parts 2, 3, and 4 are the heater, the insulated, and sealed section and the sensor-harness interconnect and environmental seals, respectively, while part 5 is electronic circuits and its housing.

2.1. Sensor Calibration. A PM sensor calibration system is adopted to calibrate the initial condition of the sensor: fuel is introduced into an inverse diffusion flame combustor which is connected with an exhaust pipe. Then the gas mixture is ignited and produces stable soot. After that, a compressor is started and introduces a stable quantity of air

which can be adjusted through a pressure-regulating valve and heated by a heater. The air enters the exhaust pipe to dilute the soot produced by combustion and the air input flow is read by a flowmeter. At the same time, a temperature sensor outputs the temperature of diluted particles. When the soot enters the sensor, a current signal is output and then amplified and converted by a circuit board; then a voltage signal is output. The signal value is acquired by an A/D converter and read by a computer. A transient smokemeter is started in the moment when the soot enters the sensor, and transient soot concentration is measured and output. The voltage values outputs by the PM sensor under different soot concentrations are recorded, a calibration curve representing the changes of the voltage values is drafted, and accurate particle concentration is obtained.

2.2. Measuring Methods. It can be seen from Figure 3 that the arrow direction represents the gas flow path. Because of the design based on Venturi tube principle, the pressure at the head of the sensor is low. So there is an adsorption forcing the gas flow inside the sensor. The conductive shell is connected to ground, and high voltage is applied to the high voltage electrode, which is about 800~1000 V. When exhaust gas flows through the gap between the high voltage electrode and conductive shell, PM will be ionized and polarized into conductors, while it has no influence on other substances such as water vapor and CO₂. Then leakage current will be produced between electrode and conductive shell. The PM concentration is obtained based on the functional relationship between leakage current and PM concentration.

2.3. High Voltage Generation and Signal Processing. The leakage current sensor investigated in this paper consists of mechanical part and electronic circuit. The mechanical part of the sensor mainly includes electrode and 1000 V power (the design of 1000 V power could meet the design requirement after experimental verification in the report of Emisense Company). One side of the electrode is connected to the positive of the 1000 V power and the other side to the operational amplifier of the electronic circuit. The design requirement of the control system in PM sensor is to transform the leakage current signal, which varies with the change of PM concentration, into voltage signal. The signal should be filtered, amplified, calibrated, amended, A/D converted, and so forth. And then it should be transformed into controller area network (CAN) telegram information through CAN controller integrated in the single chip microcomputer. Finally it is connected into the BUS by CAN transceiver [20].

Figure 4 indicates the electronic circuitry of leakage current PM sensor. The electronic circuit consists of signal amplification circuit, module of single chip microcomputer,

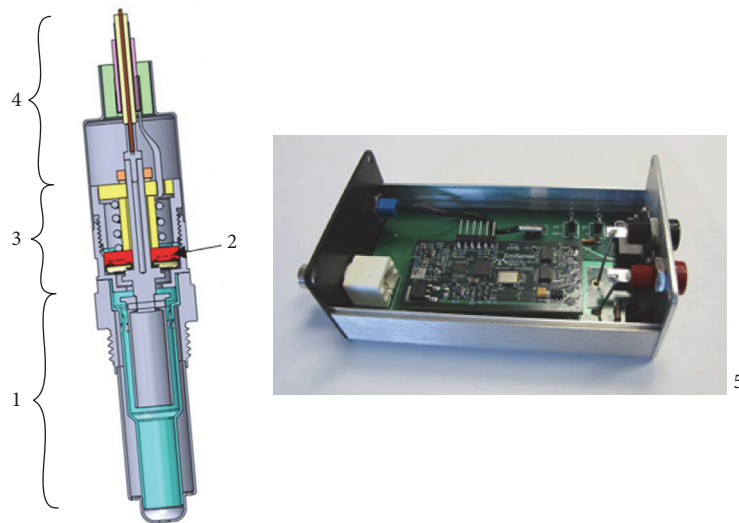


FIGURE 2: Subassembly of leakage current sensor.

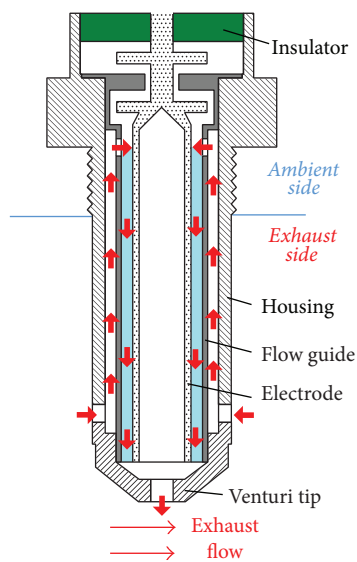


FIGURE 3: Flow drawing based on the principle of Venturi tube.

CAN transceiver, heating module, temperature measuring module, and power module.

2.4. Sensor Regeneration and Maze Design. Due to small size of sensor structure, the gap between high voltage electrode and conductive shell, heater, and lead wires cannot be set big enough. Therefore, PM is accumulated in all gaps some time later, and the leakage current will increase. The PM sensor cannot work normally when accumulated PM reaches a certain thickness. So a heater consists of exothermic ceramics, and positive and negative electrodes are integrated in the sealed space. The exothermic ceramics is closing to the side of exhaust flow space, and the negative electrode is connected to the ground. In the exothermic ceramics, positive and negative

electrodes are coated with insulating and high temperature resistance ceramic shielded layer. With PM accumulated, resistance between the metal shielded layer and conductive shell will decrease, which can be used as a judgment signal. When the resistance is lesser than the programmed value, the heater is started by the resistance controlling circuit and then the accumulated PM is burned off by electricity discharged by the high voltage electrode. In addition, though a heater is needed to burn off the accumulated PM, the excessive energy consumption can be ignored comparing to the total consumption.

To decrease the amount of PM flowing into the sealed space, maze structure is designed in front of the sealed space [21]. The maze design consists of two shoulders which can be seen in Figure 5. The mutually staggered two shoulders are designed between the shell and electrode. The first shoulder is set in the flow space of exhaust and integrated with the electrode, and the second one is set on baffle ring which connected firmly to the shell. The two shoulders formed several curves, which can reduce the amount of PM flowing into the sealed space and the effect of maze structure design can be seen in the numerical simulation part.

3. Numerical Simulation and Analysis

Since the inner structure of the PM sensor is complex, it is difficult to get the distribution condition of its inner flow field and PM. With the quick development of simulating calculation, it is available to use computational fluid dynamics (CFD) to simulate flow process inside the sensor and obtain various parameters of gas and PM which can be used to optimize structure of the PM sensor. The models of $k-\epsilon$ and DPM are adopted for the gas phase and disperse phase, respectively, while the SIMPLE model of gas-solid two phase flow is used for the numerical simulation. Three-dimension and mesh model of the PM sensor can be seen in Figure 6.

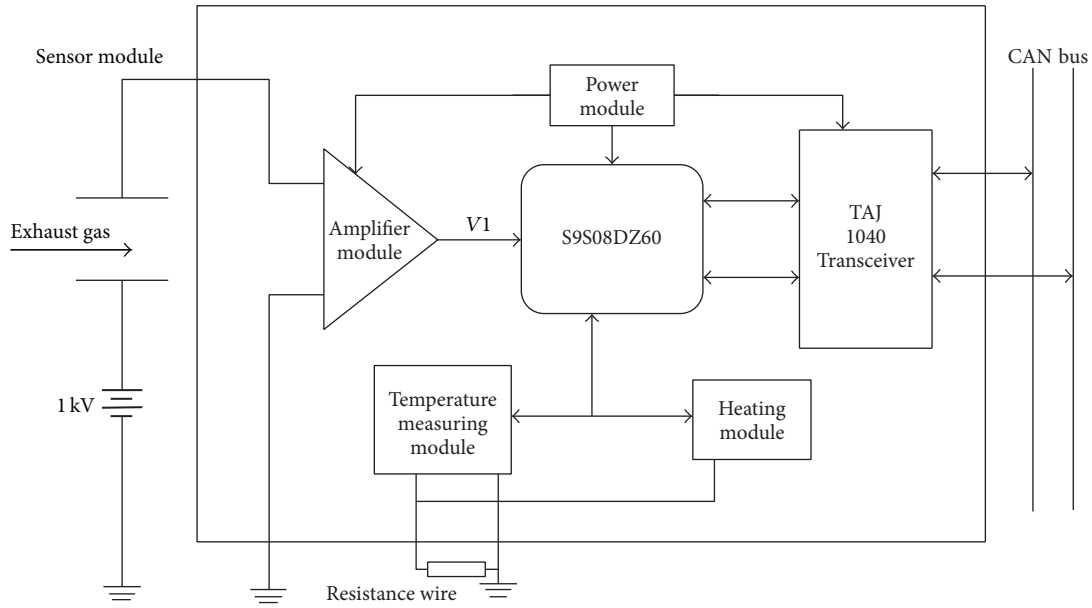


FIGURE 4: Electronic circuitry of leakage current PM sensor.



FIGURE 5: Maze design structure drawing.

3.1. Velocity Distribution. Figure 7 shows the velocity distribution of $z = 0$ section. It can be seen that flow rate of exhaust gas in the concentration testing area is steady, and there is an obvious velocity gradient distribution at the head of the sensor. Flow rate is gradually accelerated due to its small sectional area. On the other hand, the flow rate of exhaust gas in the space of maze design and central cavity is low.

Figure 9 shows the velocity vector distribution of part of the sensor. It is clearly showed that an eddy was produced at the central cavity due to sudden change of sectional area, which causes the collision of airflow and sensor interior face. However, it can be seen in Figure 8 that the pressure loss is small because of small disturbance intensity. But the eddy will cause suspension of PM in this place and increase its stagnation time. And rate of exhaust gas is steady in the subsequent flowing space without eddy formed. Figure 10 shows the velocity vector distribution of $x = -25$ annular section. The outermost, intermediate, and innermost torus is velocity vector distribution of the flow space of outboard protective element, concentration testing area, and central cavity, respectively. At the windward side of the outermost torus, velocity of airflow is low, while it is high at the leeward side. It is mainly because of the block of flow guide, which decreases the momentum of gas at the windward side and generates acceleration area at the side of annular flow guide. The flow rate of concentration testing area is steady, which

indicates that the flow space of outboard protective element can stabilize flow rate, and it makes contribution to the stabilization of PM flow rate in the concentration testing area.

3.2. Distribution Conditions of the PM. Figure 11 shows the distribution conditions of PM inside the sensor when exhaust flow rate is 72, 55, 37 meter per second, respectively. By comparison, there is an obvious reduction of PM inside the maze structure design when exhaust flow rate is 55 and 37 meter per second. It indicates that maze structure design can prevent PM effectively when flow rate is low. However, there is more PM distributed in maze structure design at high flow rate because exhaust gas of high flow rate has a strong carrying effect on PM. A little PM is distributed at windward side of outboard protective element for the low flow rate there and it is more obvious with low flow rate. But when flow rate is high, distribution of PM inside the sensor is relatively homogeneous.

According to the relevant research, all sizes of PM distributed evenly and unorderedly inside the sensor, but around the maze structure design, the amount of the PM tends to be less, and the size of the PM tends to be smaller. The maze structure reduces the PM concentration at the end space of the sensor and makes PM distribution of other parts homogeneous, which is advantageous to the accurateness of the sensor.

4. Experiment

Figure 12 shows the signal collection system, installation of sensors, test bench, and control circuits. Feasibility study of the sensor to measure PM concentration was performed. 186FA single-cylinder air cooled diesel engine was used in the first round bench test. An electric eddy current dynamometer and a smokemeter are used in the test, which are produced

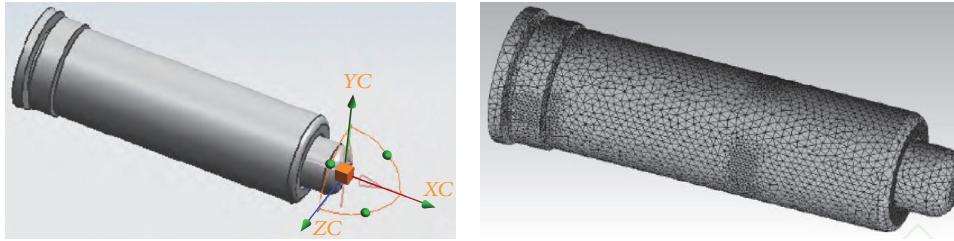


FIGURE 6: Three-dimension and mesh model of the PM sensor.

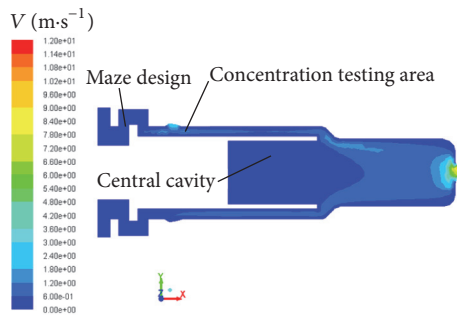
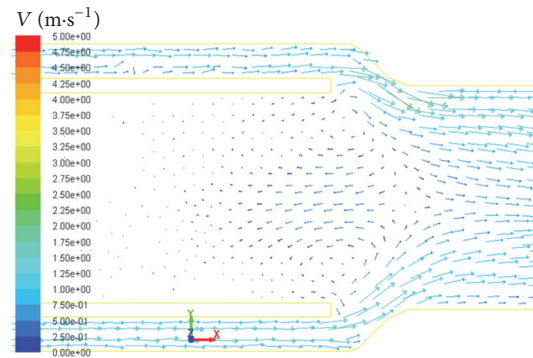
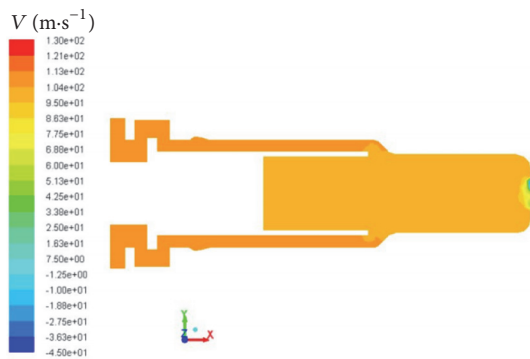
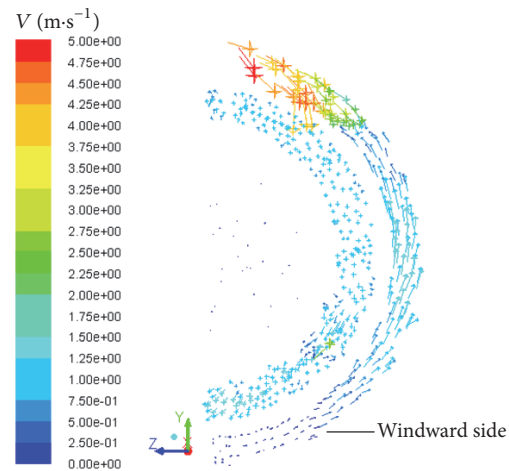
FIGURE 7: The velocity distribution of $z = 0$ section.

FIGURE 9: The local velocity vector distribution.

FIGURE 8: Static pressure distribution of $z = 0$ section.FIGURE 10: The velocity vector distribution of $x = 25$ ring section.

by Hangzhou Zhong Cheng Testing Technology Ltd. and Wenzhou Instrument Factory of China, respectively, and the data collection system is self-made.

4.1. Output Voltage at Different Testing Condition. The PM concentration is different under different testing conditions. And smoke intensity increases with the enhancement of load, as well as the PM concentration. Therefore, the load conditions of 10%, 50%, and 100% at rated speed can be selected in the bench test and then the average data are collected each time. When the engine load runs at full load, the working condition can be very tough because of the high velocity of the exhaust gas flow and high temperature. The stability of the sensor can be guaranteed if it still works well under full load. From the results in Table 2 and Figures 13 and 14, it can be seen that the output voltage increases with the increasing engine load (as well as the smoke intensity and

PM concentration). It reveals the feasibility of the sensor to measure PM concentration.

4.2. Influence of Exhaust Gas Temperature upon Sensor Output. For a leakage current PM sensor like this, changes in measured values have two possibilities: that the PM concentration has changed or that the PM concentration has not changed, but conditions have changed. In this paper, we study the influence of exhaust gas temperature upon sensor output. The schematic of artificial test bench can be seen in Figure 15. Concentration and temperature are controlled by the mass flow controller and heater separately. We measure the sensor output under different temperatures with the same

TABLE 2: Output signal in different loads.

Load	Average collected in the first time (V)	Average collected in the second time (V)	Average collected in the third time (V)
10%	0.78	0.72	0.83
50%	2.43	2.47	2.46
100%	4.13	4.14	4.16

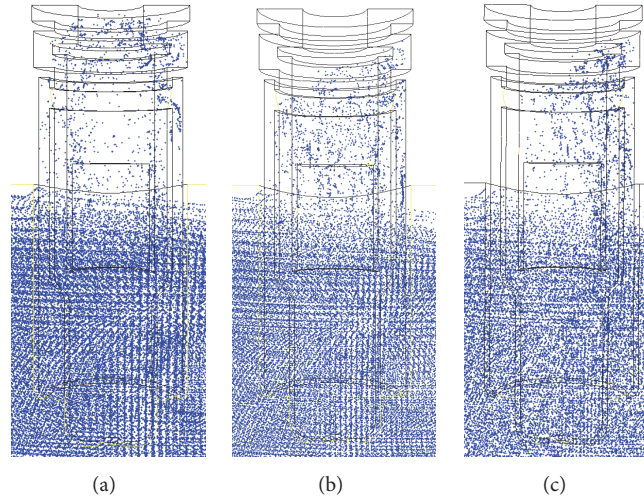


FIGURE 11: Particulate distribution inside the sensor.

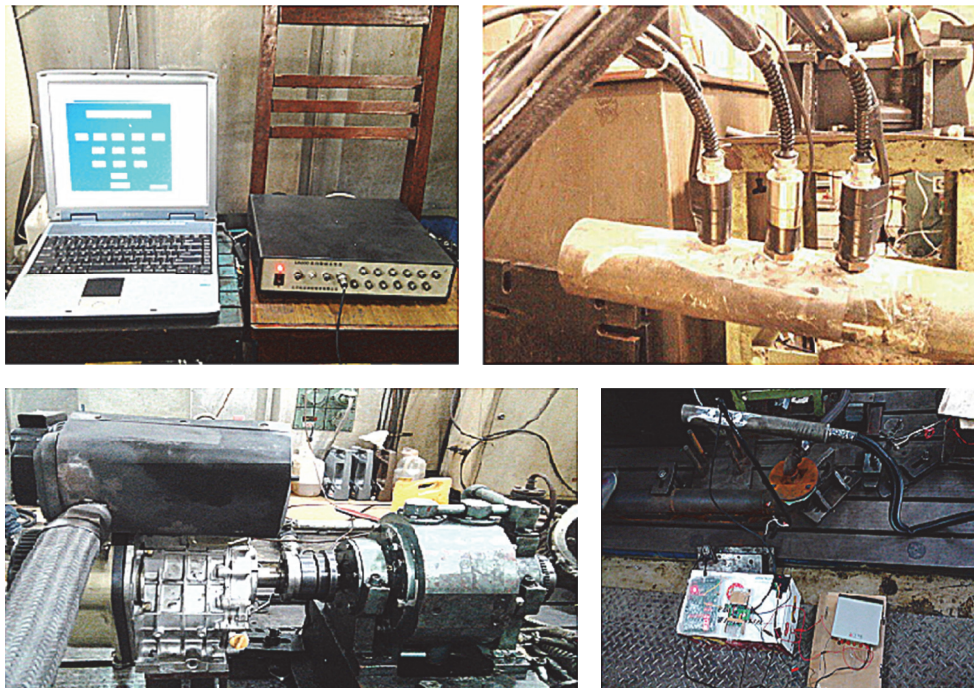


FIGURE 12: Different parts of bench test.

change of PM concentration. Normalized sensitivity was calculated under different temperatures, which can be seen in Figure 16, the change sensor output is strongly influenced by EGT, and sensitivity changes by 3 times over temperature

range from 240°C to 473°C. A ceramic heater can reduce the influence to the output signal during the heating procedure and burn off the carbon bridge caused by PM concentration. To ensure that the sensor is accurate enough to fulfill its task,

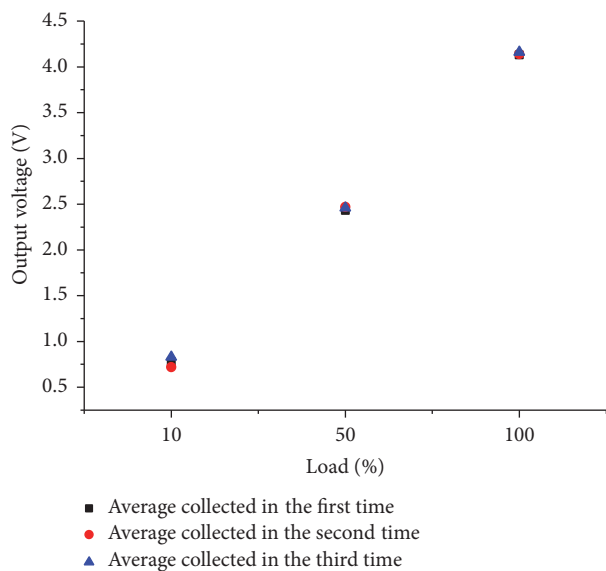


FIGURE 13: Output signal diagram in different loads.

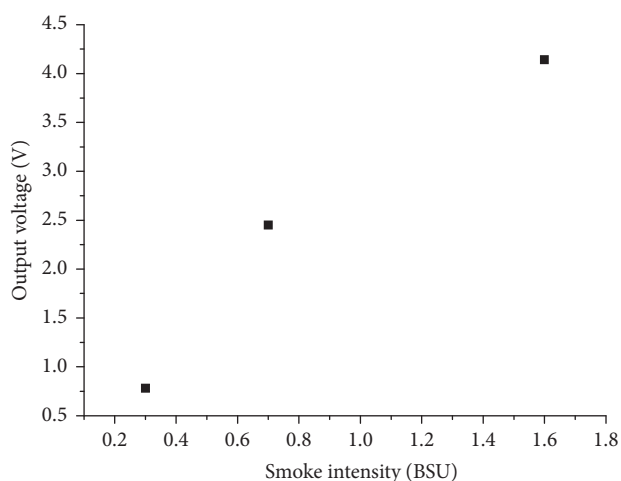


FIGURE 14: Output signal in different smoke intensity.

a controlled and interrupted heating processing should also be adopted. And a universal temperature correction should be applied to sensor output.

5. Conclusion

In this paper, the structure and principle of the PM sensor are introduced. The gas-solid two-phase flow numerical simulation is carried out, and simulation analysis was applied to the design of Venturi tube and maze structure design. Finally bench test was performed for a feasibility study of PM concentration detection and study of the influence of EGT upon sensor output.

The conclusions obtained can be seen as follows:

- (1) The design of Venturi tube in the sensor produces differential pressure and has a significant effect on stability of the internal air flow.

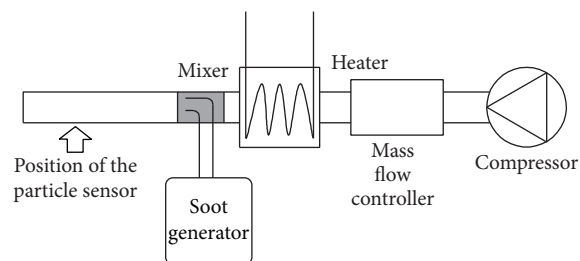


FIGURE 15: Schematic set-up of the artificial soot particle test bench.

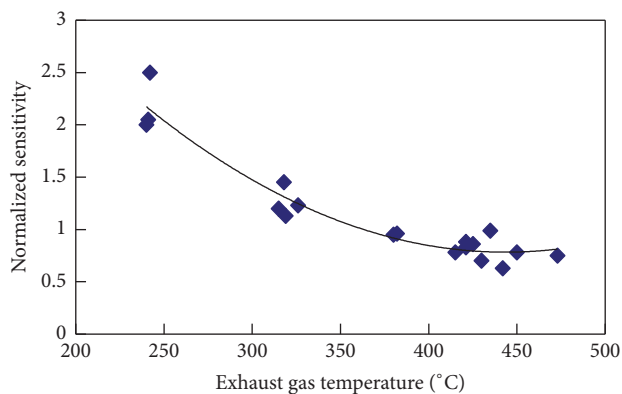


FIGURE 16: Sensitivity over different exhaust gas temperature.

- (2) The maze design can prevent the PM from entering into sealed space effectively at low flow rate.
- (3) The output signal increases with the increasing engine load, which confirms the feasibility of PM concentration detection of the leakage current PM sensor.
- (4) The sensor output is strongly influenced by EGT so universal temperature correction should be applied to sensor output.

But this is a fundamental study of the new PM sensor; a further study should be performed for commercial application. Thermal analysis based on finite element method needs to be taken. By establishing 3D model and carrying out numerical simulation, the transient and steady state of temperature fields of the sensor can be approached. The appropriate heating power of the sensor which can guarantee the quick and safe turning of the sensor into its response phase can be reached by studying the temperature fields and transient simulations under different heating power.

Additional Points

A new sensor for transient PM (discharged by diesel engine) concentration measurement was used.

Competing Interests

The authors declare that they have no financial and personal relationships with other people or organizations that can inappropriately influence their work; there is no professional

or other personal interests of any nature or kind in any product, service, and/or company that could be construed as influencing the position presented in, or the review of, the manuscript entitled.

Acknowledgments

This work was financially supported by the Priority Academic Program Development (PAPD) in China, the Project of International Cooperation (no. BZ2012025) in Jiangsu Province of China, the 2016 Priority Research Project (BE2016141) in Jiangsu Province of China, the 2016 Postgraduate Innovation Program in Jiangsu Province of China, and the Project of State Key Laboratory of Internal Combustion Engines (no. K2014-9) in Tianjin University of China.

References

- [1] H. S. Rosenkranz, "Mutagenic nitroarenes, diesel emissions, particulate-induced mutations and cancer: an essay on cancer-causation by a moving target," *Mutation Research—Genetic Toxicology*, vol. 367, no. 2, pp. 65–72, 1996.
- [2] J. G. M. Brandin, L. A. H. Andersson, and C. U. I. Odenbrand, "Catalytic reduction of nitrogen oxides on mordenite some aspect on the mechanism," *Catalysis Today*, vol. 4, no. 2, pp. 187–203, 1989.
- [3] L. Huang, S. V. Bohac, S. M. Chernyak, and S. A. Batterman, "Effects of fuels, engine load and exhaust after-treatment on diesel engine SVOC emissions and development of SVOC profiles for receptor modeling," *Atmospheric Environment*, vol. 102, pp. 228–238, 2015.
- [4] J. R. Serrano, H. Climent, P. Piqueras, and E. Angiolini, "Analysis of fluid-dynamic guidelines in diesel particulate filter sizing for fuel consumption reduction in post-turbo and pre-turbo placement," *Applied Energy*, vol. 132, pp. 507–523, 2014.
- [5] K. Oravisjärvi, M. Pietikäinen, J. Ruuskanen et al., "Diesel particle composition after exhaust after-treatment of an off-road diesel engine and modeling of deposition into the human lung," *Journal of Aerosol Science*, vol. 69, pp. 32–47, 2014.
- [6] Y. Shen, T. Takeuchi, S. Teranishi, and T. Hibino, "Alumina substrate-supported electrochemical device for potential application as a diesel particulate matter sensor," *Sensors and Actuators, B: Chemical*, vol. 145, no. 2, pp. 708–712, 2010.
- [7] T. Nakata, H. Akita, K. Saguchi, and K. Kunimatsu, CO gas sensor, JP Patent 2,001,041,925.
- [8] H. Scheer, H. J. Renz, S. Roesch, H. Koehnlein, B. Gaertner, and I. Gerner, "Sensor element for a particle sensor," DE Patent 102,006,032,741.
- [9] C.-B. Lim, H. Einaga, Y. Sadaoka, and Y. Teraoka, "Preliminary study on catalytic combustion-type sensor for the detection of diesel particulate matter," *Sensors and Actuators B: Chemical*, vol. 160, no. 1, pp. 463–470, 2011.
- [10] T. Ochs and H. Schittenhelm, *Particulate Matter Sensor for on Board Diagnostics (OBD) of Diesel Particulate Filters (DPF)*, SAE International, 2010.
- [11] A. Kondo, S. Yokoi, T. Sakurai et al., "New particulate matter sensor for on-board diagnostics," *Aachener Kolloquium Fahrzeug-und Motorentechnik*, vol. 19, pp. 405–415, 2010.
- [12] L. Cheng, X. J. Zhong, T. W. Xing et al., *A Particulate Matter Sensor and its Measuring Method*, 2012.
- [13] N. Li, D. Tang, and L. Cheng, "Research on new particulate matter sensor for diesel on-board diagnostics," *Instrument Technique and Sensor*, no. 6, pp. 1–3, 2013.
- [14] A. Kondo, T. Sakuma, T. Sakurai, and T. Egami, *New Particulate Matter Sensor for On-Board Diagnostics*, Aachener Kolloquium Fahrzeugund Motorentechnik, Aachen, Germany, 2010.
- [15] W. Manfred, R. Christian, and L. Thomas, *Particulate Filter Onboard Diagnostics by Means of a Particle Sensor*, FISITA, Munich, Germany, 2010.
- [16] K. W. Chu, B. Wang, A. B. Yu, and A. Vince, "CFD-DEM modelling of multiphase flow in dense medium cyclones," *Powder Technology*, vol. 193, no. 3, pp. 235–247, 2009.
- [17] D. Tang, Y. Z. Wu, N. Li, L. Cheng, Z. X. Liu, and Y. C. Xu, "Simulation of gas-solid two-phase flow of particulate matter sensor for diesel engine," *Chinese Internal Combustion Engine Engineering*, no. 3, pp. 147–151, 2015.
- [18] Y.-Y. Bu, X.-K. Kang, and S. Wu, "Simulation of the gas-solid turbulent flow of centrifugal radial-straight-blade wet fan," *Journal of Zhengzhou University (Engineering Science)*, vol. 32, no. 4, pp. 76–80, 2011.
- [19] X. Chen, W. Zhong, B. Sun, B. Jin, and X. Zhou, "Study on gas/solid flow in an obstructed pulmonary airway with transient flow based on CFD-DPM approach," *Powder Technology*, vol. 217, pp. 252–260, 2012.
- [20] Y. Nong, "Research and design on networked auto sensor based on CAN bus," *Transducer and Microsystem Technologies*, vol. 26, no. 8, p. 90, 2007.
- [21] L. Cheng, X. J. Zhong, T. W. Xing et al., "A High Precise Particulate Matter Sensor," China, CN202611820 U, 2012.

Research Article

Research on Fused Tapered Photonic Crystal Fiber Sensor Based on the Method of Intermittent Cooling

Guangwei Fu, Xinghu Fu, Peng Guo, Yushen Ji, and Weihong Bi

The Key Laboratory for Special Fiber and Fiber Sensor of Hebei Province, School of Information Science and Engineering, Yanshan University, Qinhuangdao 066004, China

Correspondence should be addressed to Guangwei Fu; earl@ysu.edu.cn and Weihong Bi; bwhong@ysu.edu.cn

Received 24 August 2016; Accepted 21 September 2016

Academic Editor: Lei Yuan

Copyright © 2016 Guangwei Fu et al. This is an open access article distributed under the Creative Commons Attribution License, which permits unrestricted use, distribution, and reproduction in any medium, provided the original work is properly cited.

Based on the intermittent cooling method, a fused tapered Photonic Crystal Fiber (PCF) interferometer is proposed. In the process of tapering, stop heating and wait for cooling at different taper length. Repeat heating and cooling, until taper goes to the expected length. Compared with the ordinary fused tapered method, the fringe contrast of the transmission spectra of this sensor is 15.06 dB. The transmission spectra in different concentrations of glycerol solution are obtained, and the temperature cross-sensitivity of the sensor is studied. The experimental results show that as the external refractive index increases, the transmission spectra of the sensor shift to longer wavelength. In the measuring glycerol solution, the refractive index sensitivity of the sensor can achieve 797.674 nm/RIU, and the temperature sensitivity is only 0.00125 nm/°C.

1. Introduction

Photonic Crystal Fiber (PCF) [1–3] is a new kind of optical fiber, with different structures and optical transmission characteristics from single-mode fiber. The cladding region is composed of microholes arraying paralleled to the axial direction of the fiber. Therefore, PCF has strong flexible structure design, which would open up a new area of the production and application of optical fiber device, such as no deadline single-mode transmission, large and effective field area, high nonlinearity, and high birefringence.

Taper technique of PCF can change the internal structure and optical properties of PCF, with important potential value to PCF device production and the exploration of application in the sensing field [4, 5]. Liu et al. [6] for the first time tapered the PCF and made research on optical soliton self-frequency shift. After that research about the theory, fabrication and application of tapered PCF became the focus of scholars studies. Leon-Saval et al. [7] proposed a “rapid low temperature” method to taper PCF and then to maximally control air holes collapse. Jasim et al. [8] took the measure of flame heating to stretch two compact taper areas, and the current sensitivity of Mach-Zehnder sensor could be up to 40.26 pm/A². And

there was a report [9] about an M-Z interferometer using SMF-PCF-SMF structure with conventional technique for refractive index measurement and the maximum refractive index sensitivity as of 198.77 nm/RIU. In addition, the optical properties [10–12], the optical waveguide coupling [13], and the generation of supercontinuum characteristics of tapered PCF [14, 15] are widely studied by many scholars.

Based on conventional tapering technique, an intermittent cooling fused tapered is adopted to make a kind of interferometer sensor with larger fringe contrast, and the refractive index sensing characteristics are analyzed; the refraction index sensitivity of the glycerin aqueous solution used in detection is up to 797.674 nm/RIU. Compared to conventional taper technology, its sensitivity has been greatly improved.

2. The Theoretical Analysis

Fused tapering technology is to put the fiber without coating into high temperature flame and then stretch the fused fiber on both sides at the same time. Finally, a special waveguide with tapered structure is formed in the heating area to

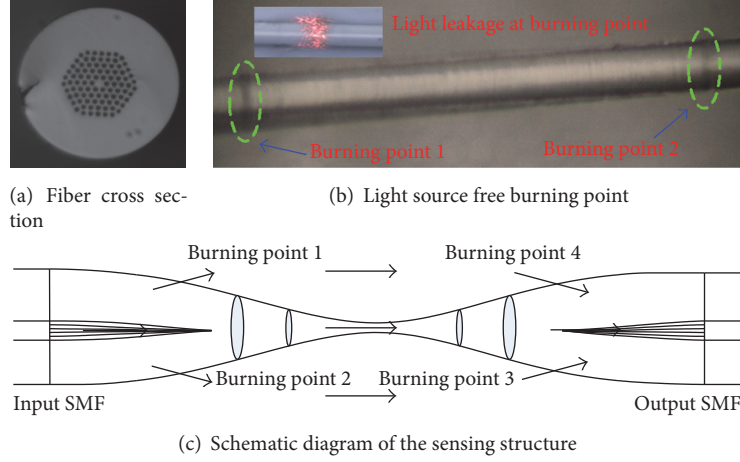


FIGURE 1: Fused tapered PCF sensor.

transmit light. As beam transmitting through the tapered area, there are two processes that are beam splitting and beam combining, respectively. And then the whole light path forms as a Mach-Zehnder interferometer. The technology of intermittent cooling is to suspend the tapering process at different tapering length and continue tapering after cooling. By means of this method, the ignition points are formed in tapered area. Because the change of refractive index in ignition point area causes the mode-mismatched phenomenon, part of light in the core will leak into cladding again. This light-leaking phenomenon leads to the cladding mode's effective refractive index being more susceptible to the outside refractive index. So it can improve the refractive index sensitivity.

Through the method of intermittent cooling, a section of PCF is stretched as tapered structure. The fused tapered PCF sensor is shown in Figure 1.

The PCF used in the experiment has the advantage of infinite single-mode transmission. And when PCF is connected with single-mode fiber by fiber fusion splicer, try not to make the PCF's air holes collapse by adjusting the fusion splicing parameters. So, as beam passing through the first ignition point, the light coupling into the PCF can still transmit in the PCF's fiber core. And only the fundamental mode is transmitted.

It is supposed that there exist four ignition points. When light transmits to tapered area, core mode transforms to cladding mode gradually with the diameter of tapered area decreasing regularly. Light energy transmitting as core mode reduces slowly and cladding mode is stimulated correspondingly. When light transmits through the first ignition point, part of light will leak into cladding, and the same situation will occur as light transmits to the next three ignition points. With the diameter of tapered area at the output end increase by degrees, the light energy transmitting as cladding mode reduces gently, and the fundamental mode enhances correspondingly. When light transmits to nontapered area, cladding mode couples into fiber core and interferes with

fundamental mode of fiber core. The interference intensity and central wavelength can be expressed as

$$I = I_1 + I_2 + 2\sqrt{I_1 I_2} \cos \varphi, \quad (1)$$

$$\lambda_m = \frac{\Delta n_{\text{eff}} L}{m}.$$

In (1), I is the total output light intensity; I_1 and I_2 are light intensities of the fundamental mode and cladding mode, respectively; φ is phase displacement; λ_m is the central wavelength of level m ; L is the interference length, which is the distance between two fused points; and Δn_{eff} is the difference between core's refractive index and cladding mode's effective refractive index.

When environmental refractive index changes, the cladding mode effective refractive index changes correspondingly, while the core refractive index remains constant. The wavelength shift caused by the change of outside refractive index is expressed as

$$\Delta \lambda_m = \frac{(\Delta n_{\text{eff}} + \Delta n) L}{m} - \frac{\Delta n_{\text{eff}} L}{m} = \frac{\Delta n L}{m}. \quad (2)$$

In (2), $\Delta \lambda_m$ is the central wavelength shift of level m ; Δn is the variation of refractive index difference caused by the change of environmental refractive index.

It can be seen from (2) that when interference length L is a constant, the interference fringe's wavelength shift changes linearly with the change of environmental refractive index. So the environmental refractive index could be measured by detecting the central wavelength shift of level m .

Because of the light leak at ignition points, the energy of cladding mode has been greatly enhanced, and the interference is more obvious. At the same time, the light carrying outside information enters into optical fiber, and the coupling degree between sensing area and outside environment is enhanced further. So, the sensitivity of sensor is improved.

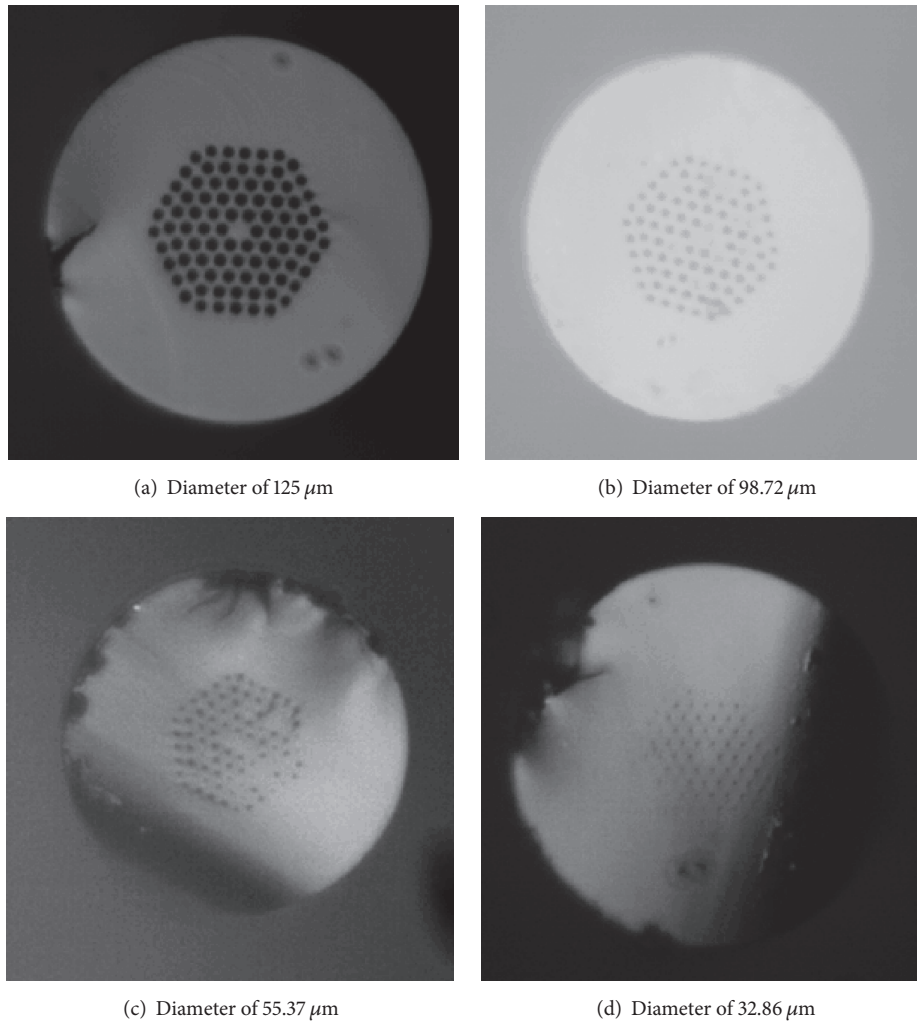


FIGURE 2: Cross sections of different diameters.

3. Experimental and Results

3.1. Sensor Production. The used PCF in the lab is SM-7 solid core PCF, the outer cladding layer diameter is $125\ \mu\text{m}$, the core diameter is $7.0\ \mu\text{m}$ with 5 layers of air hole and a hexagon structure arrangement, the air hole diameter is about $2.63\ \mu\text{m}$, and the hole spacing is about $4.22\ \mu\text{m}$.

The used splicing machine is FITELE S178 optical fiber fusion splicer, optical taper machine is SCS-4000 optical fused taper system, light source is ASE broadband light source ($1520\ \text{nm}$ – $1610\ \text{nm}$), and AQ6317B spectrometer is used to detect the sensor spectrum.

In the process of fabrication, first of all, it should adjust the parameter of fusion splicer and make a sensor with SMF-PCF-SMF structure, where length of PCF is $26\ \text{mm}$. Then the optical taper machine is used to fusedly taper the PCF, when the length is $1\ \text{mm}$, $3\ \text{mm}$, and $7\ \text{mm}$ in turn, break off heating and tapering, till it is cool and then start heating and tapering. In the overall taper process, fiber is fixed in the tensile platform, so that the fiber cannot move at all to ensure the heating zone does not change. When the taper

length reaches $12\ \text{mm}$, tapering process will be over. PCF taper region length is $12\ \text{mm}$; the taper additional loss is $12.56\ \text{dB}$. Different diameters of taper region result in different cross sections of fiber, as shown in Figure 2.

3.2. Glycerin Aqueous Solution Sensing Experiment. The configuration concentration of glycerin aqueous solution is 5% – 25% , and Abbe refractometer is used to measure the refractive index of solution; the refractive index changes in the range of 1.342 – 1.379 .

Put tapered PCF sensor into the sample pool, mix glycerin aqueous solution with different concentrations, until the tapered PCF sensor completely immersed into the solution, and then measure transmission spectra. Before measuring, PCF taper region must be cleaned with distilled water every time. ASE light source output power is $16\ \text{dBm}$. The experimental system is shown in Figure 3.

The experimental measurement results of transmission spectra corresponding with different concentrations of glycerol aqueous solution are shown in Figure 4.

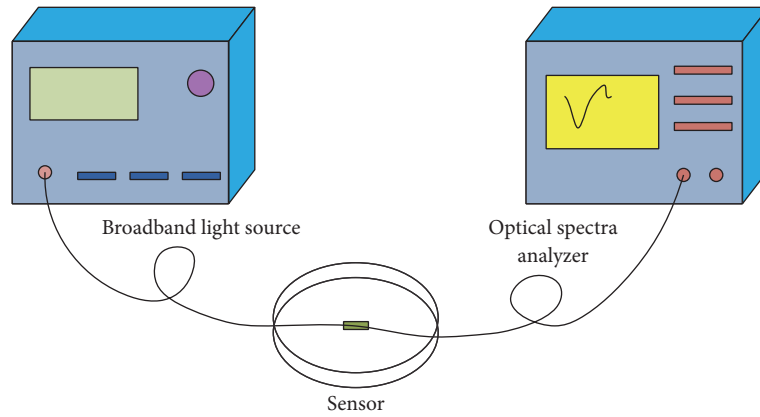


FIGURE 3: Schematic of the fused tapered PCF sensor system.

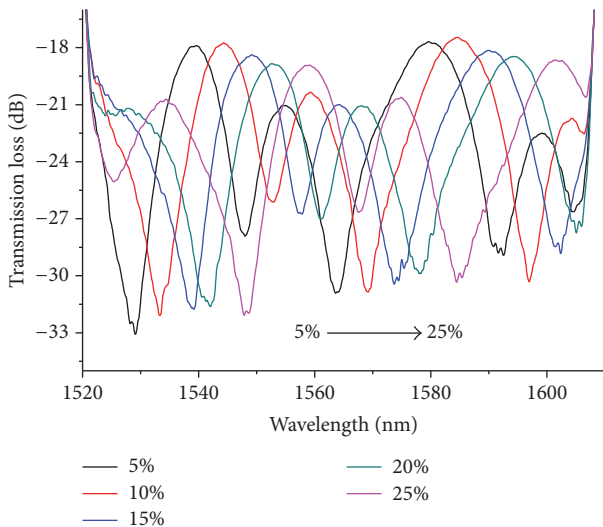


FIGURE 4: Transmission spectrum of the fused tapered PCF sensor.

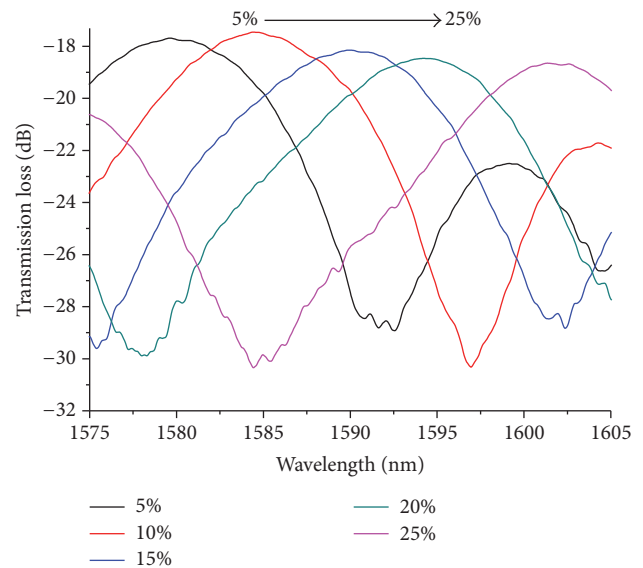


FIGURE 5: Transmission spectra of the tapered PCF sensor in different liquids at wavelength of 1590 nm.

In Figure 4, it can be seen that the transmission spectra have significant shifts to the long wave direction, with the increasing of concentration of glycerol solution. The peaks change within the vicinity of 1590 nm wavelength. The details of the spectrum are as shown in Figure 5.

As shown in Figure 5, it can be found that with the increasing of the concentration of the transmission, the spectrum is shifted to longer wavelength. As the solution concentration ranges from 5% to 25%, wavelength drifts over 20 nm. When repeating the experiment and making data fitting, the relationship between wavelength shift and the refractive index of solution can be obtained, as shown in Figure 6.

In Figure 6, with the increase of the refractive index of solution, the interference fringe center wavelength drifts to long wavelength direction a lot, and there is a good linear relationship; the sensitivity of the refractive index is 797.674 nm/RIU.

3.3. Temperature Sensing Experiment. Put the PCF sensor into the temperature controlled oven and connect both ends to ASE light source (1520~1610 nm) and the spectrometer, respectively. ASE light source output power is 16 dBm. Schematic diagram of the temperature sensing experimental system is as shown in Figure 7.

Heat the temperature controlled oven from 20°C to 70°C and measure it every 10°C. Detect the transmission spectrum with OSA when the temperature is stable. The same measurement is done in the opposite temperature changing as it declines from 70°C to 20°C. The result of the measurement is shown in Figure 8.

It can be seen from Figure 8 that the overall trend of the transmission spectra remains unchanged at different temperature. Study the wave crest at the region about 1597.90 nm and make the data linear fitting; a relationship between the

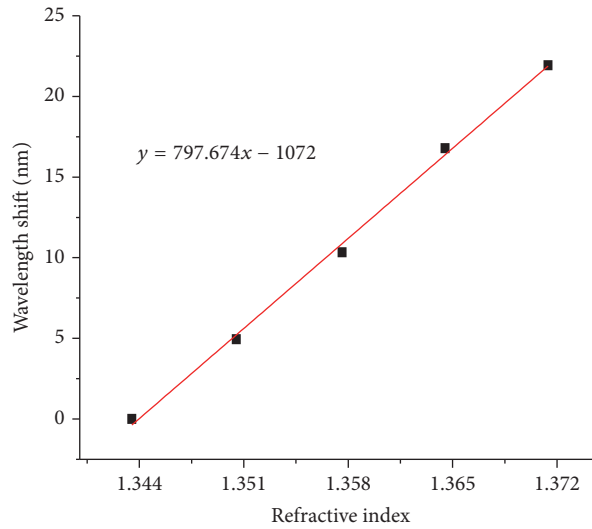


FIGURE 6: Relationship between wavelength shift and refractive index.

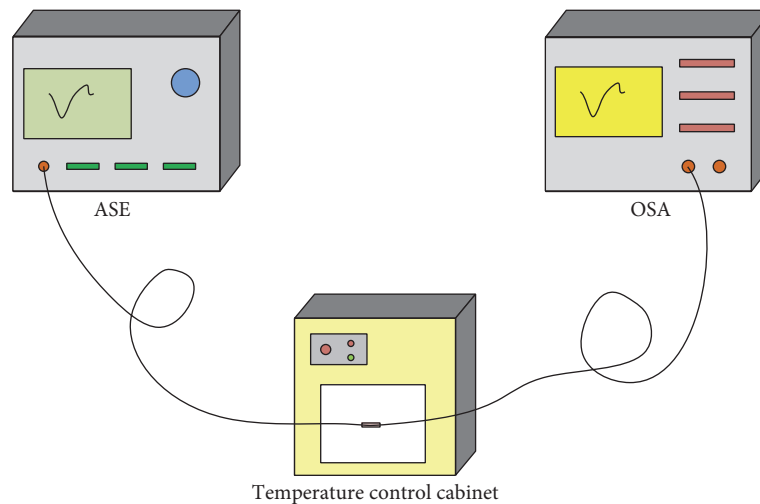


FIGURE 7: The temperature sensing system.

transmission spectrum wavelength shift of the tapered PCF and the outside temperature can be obtained, as shown in Figure 9.

It can be viewed that the transmission spectrum of the PCF sensor shifts gently towards long wavelength direction when the outside temperature is changed, according to Figure 9. The temperature sensitivity is merely $0.00125 \text{ nm}/^\circ\text{C}$ indicating that the intermittent cooling fused tapered PCF is not sensitive to temperature. Considering that temperature can induce the central wavelength shift of level m for transmission spectrum of interferometer, it can be known according to [16] that the relationship between interference central wavelength and temperature can be expressed as $\Delta\lambda'_m = (\alpha + P_t)\lambda_m\Delta T$, in which α is the coefficient of thermal expansion about the materials of interferometer; for pure SiO_2 , it is $5 \times 10^{-7}/^\circ\text{C}$. P_t is the variation of effective refractive index difference between two interference patterns caused by temperature change: $P_t = (1/\Delta n)\partial(\Delta n)/\partial T$, where ΔT

represents temperature change. Because both of the fiber core mode and the cladding mode in tapered PCF can transfer in undoped PCF, intervening with temperature on the influence of the fiber core and cladding mode is the same; thus $P_t = 0$. And the thermal expansion coefficient, $\alpha = 5 \times 10^{-7}/^\circ\text{C}$, owns a really small numerical value. Therefore, $\Delta\lambda'_m \approx 0$, which is identical to the experiment results obtained from Figures 8 and 9. To sum up, it can be concluded that the intermittent cooling fused tapered sensor interferometer is not sensitive to temperature.

4. Conclusion

This paper presents using an intermittent cooling fused taper method to produce an interferential Photonic Crystal Fiber (PCF) sensor. To fulfill PCF fused tapering in the process, intermittent cooling in the melting process is introduced. Compared with the ordinary fused taper, multiple times of

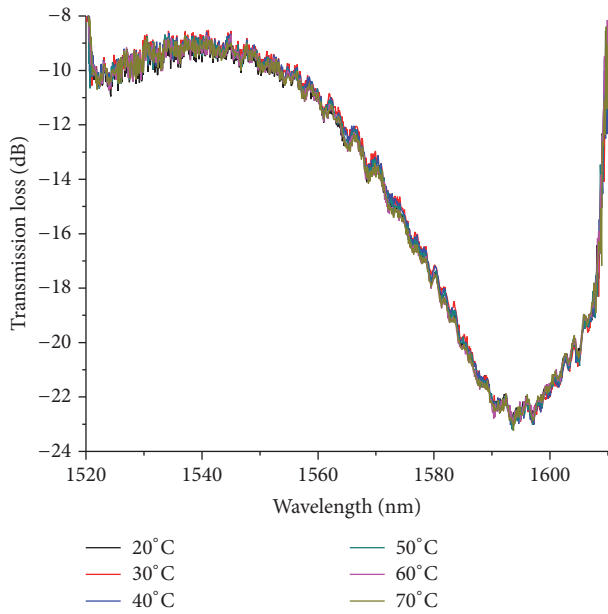


FIGURE 8: Transmission spectrum of the fused tapered PCF sensor with different temperature.

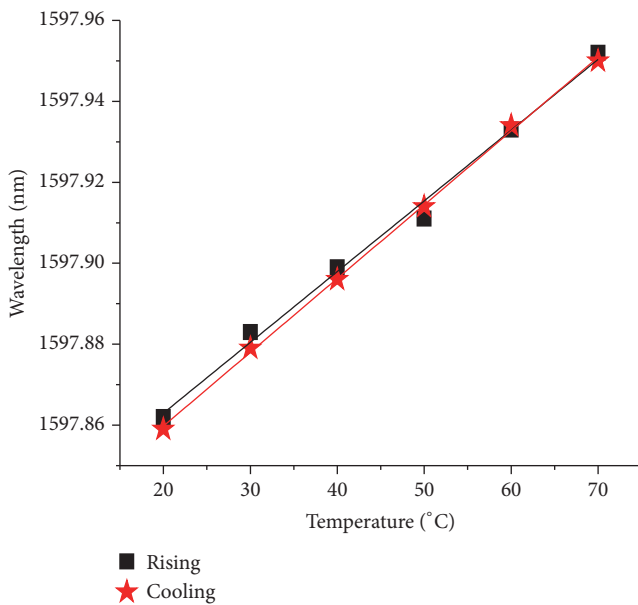


FIGURE 9: Relationship between wavelength shift and temperature.

manufacturing taper PCF sensor have larger fringe visibility. Further research is done to study the sensor response to external environment with different refractive index. The experimental results show that, when immersed the taper PCF sensor in the different concentration solution environment, along with the increasing external refractive index, the center wavelength significantly drifts to long wavelength direction. The refractive index sensitivity measured in aqueous glycerol solution is up to 797.674 nm/RIU. Compared with taper PCF produced by ordinary fused taper method, the sensitivity is

greatly improved. At the same time, the temperature sensitivity of the sensor is only 0.00125 nm/°C, which can be considered to be insensitive to temperature, and it can overcome the cross-sensitivity problem of the simultaneous measurement for refractive index and temperature.

Competing Interests

The authors declare that there is no conflict of interests regarding the publication of this paper.

Acknowledgments

This project is supported by the National Natural Science Foundation of China (nos. 61575170, 61475133, and 61675176), the Key Applied Basic Research Program of Hebei Province (nos. 16961701D and QN2016078), Hebei Provincial Natural Science Foundation (nos. F2015203270 and F2016203392), Qinhuangdao Science and Technology Support Program (no. 201601B050), College Youth Talent Project of Hebei Province (no. BJ2014057), and “XinRuiGongCheng” Talent Project of Yanshan University.

References

- [1] J. C. Knight, T. A. Birks, P. S. J. Russell, and D. M. Atkin, “All-silica single-mode optical fiber with photonic crystal cladding,” *Optics Letters*, vol. 21, no. 19, pp. 1547–1549, 1996.
- [2] T. A. Birks, J. C. Knight, and P. S. J. Russell, “Endlessly single-mode photonic crystal fiber,” *Optics Letters*, vol. 22, no. 13, pp. 961–963, 1997.
- [3] P. S. J. Russell, “Photonic-crystal fibers,” *Journal of Lightwave Technology*, vol. 24, no. 12, pp. 4729–4749, 2006.
- [4] E. C. Mägi, P. Steinvurzel, and B. J. Eggleton, “Tapered photonic crystal fibers,” *Optics Express*, vol. 12, no. 5, pp. 776–784, 2004.
- [5] H. C. Nguyen, B. T. Kuhlmeier, E. C. Magi et al., “Tapered photonic crystal fibres: properties, characterization, and applications,” in *Proceedings of the Micro-Technologies for the New Millennium International Society for Optics and Photonics Conference*, vol. 5840, pp. 29–43, Sevilla, Spain, May 2005.
- [6] X. Liu, C. Xu, W. H. Knox et al., “Soliton self-frequency shift in a short tapered air-silica microstructure fiber,” *Optics Letters*, vol. 26, no. 6, pp. 358–360, 2001.
- [7] S. G. Leon-Saval, T. A. Birks, W. J. Wadsworth, P. S. J. Russell, and M. W. Mason, “Supercontinuum generation in submicron fibre waveguides,” *Optics Express*, vol. 12, no. 13, pp. 2864–2869, 2004.
- [8] A. A. Jasim, S. W. Harun, M. Z. Muhammad, H. Arof, and H. Ahmad, “Current sensor based on inline microfiber Mach-Zehnder interferometer,” *Sensors and Actuators, A: Physical*, vol. 192, no. 7, pp. 9–12, 2013.
- [9] C.-P. Tang, M. Deng, T. Zhu, and Y.-J. Rao, “Photonic crystal fiber based M-Z interferometer for refractive index measurement,” *Journal of Optoelectronics Laser*, vol. 22, no. 9, pp. 1304–1308, 2011.
- [10] H. C. Nguyen, B. T. Kuhlmeier, M. J. Steel et al., “Leakage of the fundamental mode in photonic crystal fiber tapers,” *Optics Letters*, vol. 30, no. 10, pp. 1123–1125, 2005.
- [11] B. T. Kuhlmeier, H. C. Nguyen, M. J. Steel, and B. J. Eggleton, “Confinement loss in adiabatic photonic crystal fiber tapers,”

Journal of the Optical Society of America B: Optical Physics, vol. 23, no. 9, pp. 1965–1974, 2006.

- [12] X. Xi, Z. Chen, G. Sun, and J. Hou, “Mode-field expansion in photonic crystal fibers,” *Applied Optics*, vol. 50, no. 25, pp. E50–E54, 2011.
- [13] J. G. Liu, T.-H. Cheng, Y.-K. Yeo et al., “Light beam coupling between standard single mode fibers and highly nonlinear photonic crystal fibers based on the fused biconical tapering technique,” *Optics Express*, vol. 17, no. 5, pp. 3115–3123, 2009.
- [14] J. M. Dudley and S. Coen, “Coherence properties of supercontinuum spectra generated in photonic crystal and tapered optical fibers,” *Optics Letters*, vol. 27, no. 13, pp. 1180–1182, 2002.
- [15] G. Humbert, W. J. Wadsworth, S. G. Leon-Saval et al., “Supercontinuum generation system for optical coherence tomography based on tapered photonic crystal fibre,” *Optics Express*, vol. 14, no. 4, pp. 1596–1603, 2006.
- [16] U. Møller, S. T. Sørensen, C. Larsen et al., “Optimum PCF tapers for blue-enhanced supercontinuum sources,” *Optical Fiber Technology*, vol. 18, no. 5, pp. 304–314, 2012.

Research Article

Characteristics of Eddy Current Distribution in Carbon Fiber Reinforced Polymer

Shaoni Jiao, Jian Li, Fei Du, Lei Sun, and Zhiwei Zeng

School of Aerospace Engineering, Xiamen University, Xiamen, Fujian 361005, China

Correspondence should be addressed to Zhiwei Zeng; zeng@xmu.edu.cn

Received 26 May 2016; Revised 22 July 2016; Accepted 31 July 2016

Academic Editor: Yanan Zhang

Copyright © 2016 Shaoni Jiao et al. This is an open access article distributed under the Creative Commons Attribution License, which permits unrestricted use, distribution, and reproduction in any medium, provided the original work is properly cited.

The paper studies the characteristics of eddy current (EC) distribution in carbon fiber reinforced polymer (CFRP) laminates so as to guide the research and operation of eddy current testing of CFRP. To this end, an electromagnetic field computation model of EC response to CFRP based on the finite element method is developed. Quantitative analysis of EC distribution in plies of unidirectional CFRP reveals that EC changes slowly along the fiber direction due to the strong electrical anisotropy of the material. Variation of EC in plies of multidirectional CFRP is fast in both directions. The attenuation of EC in the normal direction in unidirectional CFRP is faster than that in isotropic material due to faster diffusion of EC. In multidirectional CFRP, EC increases near the interfaces of plies having different fiber orientations. The simulation results are beneficial to optimizing sensor design and testing parameters, as well as damage detection and evaluation.

1. Introduction

Carbon fiber reinforced polymer (CFRP) has found wide applications, such as load-carrying structures in aircrafts, because of its outstanding performance [1–3]. Unfortunately, defects and damage are inevitable during its production and service in harsh environment, which deteriorates the performance of CFRP structures [4, 5]. Therefore, nondestructive testing (NDT) is important for guaranteeing the quality and reliability of CFRP structures. Considering its electrically conducting property, CFRP structures can be examined by eddy current testing (ECT) technique [6–9]. Among various NDT methods [10–14], ECT is advantageous because of its easy operation, single-side detection, low requirement of surface preparation, and applicability in harsh environment, as well as other properties [15]. Hence ECT has taken an increasing interest in the detection and characterization of defects in CFRP recently [16–18].

Studying the characteristics of EC is beneficial to understanding field/flaw interaction, optimizing probe, and testing parameters, as well as guiding testing operations [19, 20]. As CFRP is electrically anisotropic [16], the distribution of EC in CFRP must be different from that in isotropic material. It has been found that EC in CFRP induced by the excitation

ac current in a circular coil flows in an elliptical shape [17, 18]. However, the phenomenon has not been quantitatively investigated. The paper studies the characteristics of EC distribution quantitatively and schematically. The research includes studying intraply distribution of EC and analyzing the attenuation of EC along the penetrating direction. In each case, characteristics of EC in both unidirectional CFRP and multidirectional CFRP are investigated.

The research is performed by numerical analysis. Section 2 presents briefly the simulation model and its validation. Section 3 studies the intraply distribution of EC. Section 4 investigates the attenuation of EC along the penetrating direction. Section 5 makes conclusive remarks.

2. Numerical Simulation

An air-core coil above a stratified CFRP laminate is modeled, as shown in Figure 1. Two Cartesian coordinate systems, namely, the global system and the local system, are used to describe the directions of fibers in the plies. The origin of the global system (x, y, z) is at the center of the material surface. The local system (l, t, n) is defined in each ply where l is parallel to the fiber direction, t is also intraply but

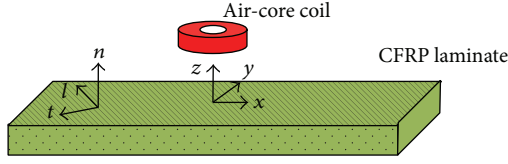


FIGURE 1: Geometrical model and coordinate systems.

perpendicular to l , and n is along the normal vector of ply. The angle between the l -axis and the x -axis is the ply angle, denoted as θ . The conductivity tensor of specific ply in global coordinate system can be formulated as [18]

$$\overline{\overline{\sigma}} = \begin{bmatrix} \sigma_l \cos^2(\theta) + \sigma_t \sin^2(\theta) & \frac{\sigma_l - \sigma_t}{2} \sin(2\theta) & 0 \\ \frac{\sigma_l - \sigma_t}{2} \sin(2\theta) & \sigma_l \sin^2(\theta) + \sigma_t \cos^2(\theta) & 0 \\ 0 & 0 & \sigma_n \end{bmatrix}, \quad (1)$$

where σ_l , σ_t , and σ_n are the conductivities along the l , t , and n directions, respectively. $\text{Diag}(10,000, 100, 100)$ S/m is a typical conductivity tensor of CFRP when $\theta = 0$ [21].

The FE model for calculating EC response to CFRP structure is based on the \mathbf{A}_r , $V - \mathbf{A}_r$ formulation whose governing equations are [22]

$$-\frac{1}{\mu_0} \nabla^2 \mathbf{A}_r + j\omega \overline{\overline{\sigma}} (\mathbf{A}_r + \nabla v) = -\nabla \times \mathbf{H}_s - j\omega \overline{\overline{\sigma}} \mathbf{A}_s \quad (\Omega_1), \quad (2)$$

$$\nabla \cdot (-j\omega \overline{\overline{\sigma}} \mathbf{A}_r - j\omega \overline{\overline{\sigma}} \nabla v) = \nabla \cdot j\omega \overline{\overline{\sigma}} \mathbf{A}_s \quad (\Omega_1), \quad (3)$$

$$-\frac{1}{\mu_0} \nabla^2 \mathbf{A}_r = 0 \quad (\Omega_2), \quad (4)$$

where \mathbf{A}_r and V stand for the reduced magnetic vector potential and the electric scalar potential, respectively. $v = V/(j\omega)$ is introduced in (2) and (3). The CFRP laminate region (Ω_1) and the air region (Ω_2) including the current source constitute the whole solution domain. In (2)–(4), \mathbf{A}_s and \mathbf{H}_s are the magnetic vector potential and the magnetic field intensity in free space produced by the excitation current, respectively, μ_0 is the permeability of free space, and ω is the angular frequency. The formulation has advantages of simple form and no requirement of meshing coil. For the details of the formulation and numerical implementation, please refer to [22]. After obtaining the solutions of the potentials, the coil impedance is calculated and the EC density \mathbf{J} is formulated as

$$\mathbf{J} = -j\omega \overline{\overline{\sigma}} (\mathbf{A} + \nabla v), \quad (5)$$

where \mathbf{A} is the sum of \mathbf{A}_s and \mathbf{A}_r .

The model is validated by comparing simulation result and analytical solution of the change of coil's impedance due to EC, denoted as ΔZ , in a unidirectional CFRP ($\theta = 0$). The coil has inner diameter of 8 mm, outer diameter of 12 mm, height of 1 mm, and lift-off of 1 mm, and the number of

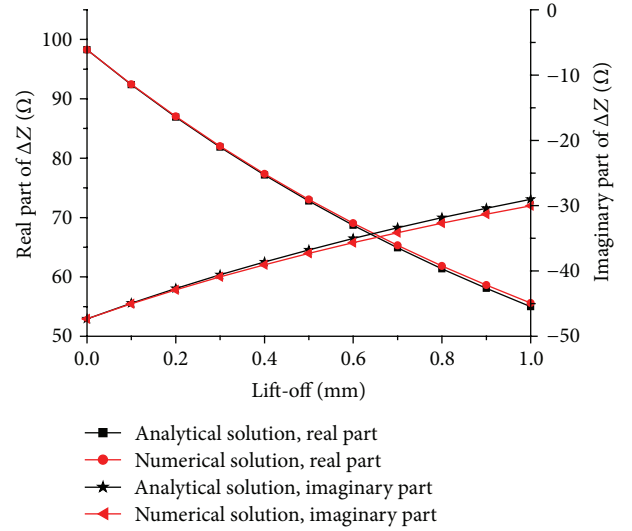


FIGURE 2: Change of coil impedance due to EC in CFRP as function of lift-off.

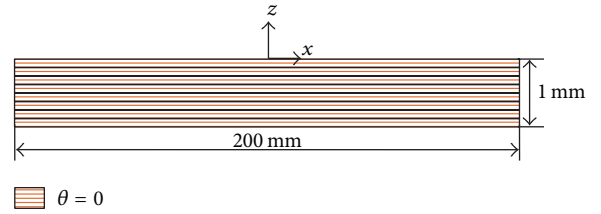


FIGURE 3: Geometrical model of anisotropic material.

turns is 50. The carrying sinusoidal current has frequency of 10 MHz and current density of 10^7 A/m². The coil and the excitation current are used throughout the paper. The test material is a plate of 200 mm × 200 mm area and 1 mm thickness. σ_l , σ_t , and σ_n are chosen to be 10,000 S/m, 100 S/m, and 100 S/m, respectively. The variation of ΔZ versus coil lift-off is shown in Figure 2. The numerical results agree well with the analytical solutions [23], which validates the effectiveness of the FE code.

3. Intraply Variation of EC

The distributions of EC in plies of unidirectional and multidirectional CFRP laminates are investigated in this section. All the CFRP laminates concerned here have eight plies and each ply is 0.125 mm thick.

3.1. Intraply Variation of EC in Unidirectional CFRP. To study the effect of electrical anisotropy on the distribution of EC, EC densities with three cases of conductivities are computed. The conductivities ($\sigma_l, \sigma_t, \sigma_n$) are (10,000, 10,000, 10,000) S/m, (10,000, 1,000, 1,000) S/m, and (10,000, 100, 100) S/m, respectively. The geometrical model of anisotropic material is shown in Figure 3. In these cases, the local coordinate system is position independent and is identical to the global coordinate system. Figure 4 shows the

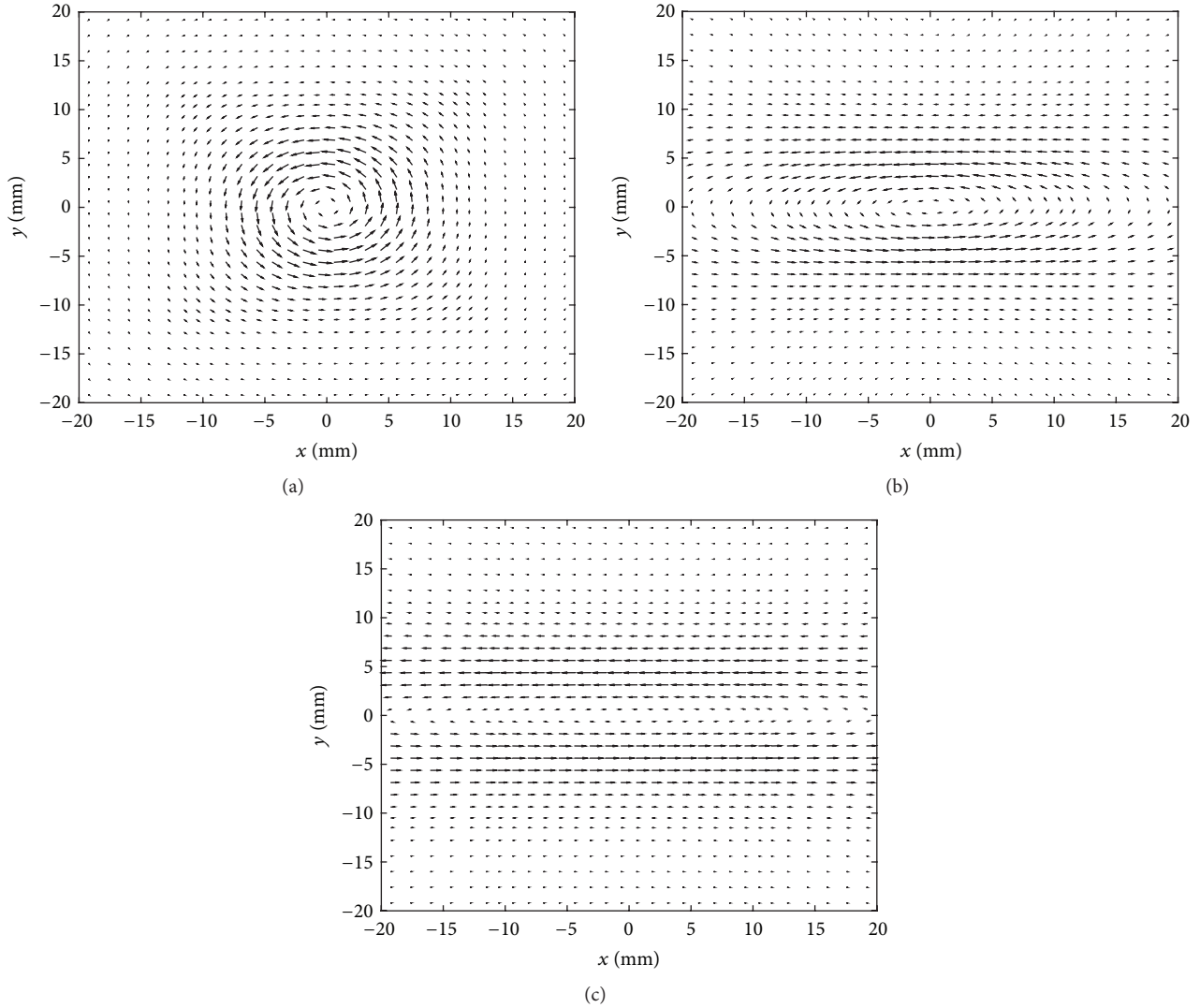


FIGURE 4: Distribution of EC (real part) in the top plies of the isotropic material and the unidirectional laminates with $\sigma_t = 10,000$ S/m and (a) $\sigma_t = \sigma_n = 10,000$ S/m, (b) $\sigma_t = \sigma_n = 1,000$ S/m, and (c) $\sigma_t = \sigma_n = 100$ S/m.

real parts of EC densities in the x - y plane of the top ply. We can easily see that EC flows in a circular shape in the isotropic material, whereas EC in each of the anisotropic laminates is mainly along the direction of maximum conductivity.

The EC density reaches maximum at the points of $x = 0$, $y = \pm 5$ mm regardless of the degree of anisotropy, as can be seen in Figure 4. Figures 5(a) and 5(b) show the EC densities along the y direction with $x = 0$ and along the x direction with $y = 5$ mm, respectively. It is indicated that the effect of electrical anisotropy on the rate of change of EC along the fiber direction is more significant than that along the direction perpendicular to the fibers. The variations of EC along the fiber direction in the anisotropic materials are much slower than that in the isotropic material. This phenomenon results in strong edge effect when the coil is near a side perpendicular to the fiber orientation and weak edge effect when the coil is close to a side parallel to the fiber orientation. Therefore, when doing scanning testing, moving probe in the

direction transverse to fibers will have small and consistent influence of edge effect. In addition, from Figure 5 it is seen that, under the same excitation, more degree of anisotropy of material results in weaker EC response. This phenomenon indicates that the excitation current needs to be enlarged to induce strong enough EC when testing anisotropic material.

3.2. Intraply Variation of EC in Multidirectional CFRP.

This subsection studies the intraply distribution of EC in multidirectional CFRP laminate. Four pieces of multidirectional CFRP laminates are used. The structures have laminate stacking sequences of $[0_4/90_4]$, $[0_2/90_2/0_2/90_2]$, $[0_2/-45_2/90_2/45_2]$, and $[0/90/0/90/0/90/0/90]$. The subscript denotes the number of plies stacked successively with the same θ . All the fibers in the top plies of the materials are oriented with $\theta = 0$. Figure 6 illustrates the laminate structure of the material of $[0_2/-45_2/90_2/45_2]$. In the rest of the paper,

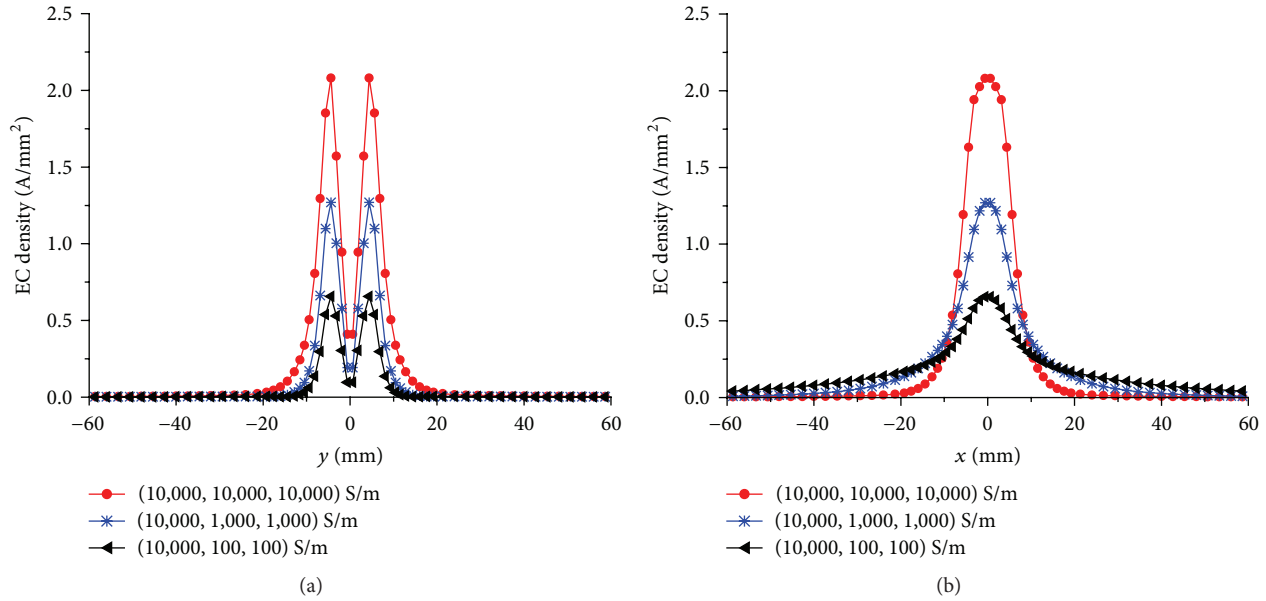


FIGURE 5: EC densities in the top plies of the isotropic material and the unidirectional laminates (a) along the y direction with $x = 0$ and (b) along the x direction with $y = 5$ mm.

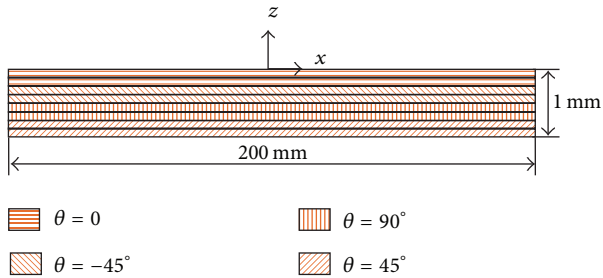


FIGURE 6: Geometrical model of the multidirectional CFRP laminate of $[0_2/-45_2/90_2/45_2]$.

σ_l , σ_t , and σ_n of CFRP laminates are 10,000 S/m, 100 S/m, and 100 S/m, respectively.

Figures 7(a)–7(d) show the distributions of EC in the 1st carbon ply ($\theta = 0$), the 3rd ply ($\theta = -45^\circ$), the 5th ply ($\theta = 90^\circ$), and the 7th ply ($\theta = 45^\circ$) of the laminate of $[0_2/-45_2/90_2/45_2]$, respectively. As is shown, EC flows mainly in the fiber orientation. Unlike the slow change of EC density along the fiber orientation in unidirectional CFRP, EC density in each ply of the multidirectional CFRP changes fast along fiber orientation. This is because EC in a fiber in a specific ply of multidirectional CFRP can change direction when it reaches the connecting point of the fiber and another fiber of different direction in an abutting ply.

Figures 8(a) and 8(b) show the EC densities along the y direction with $x = 0$ and along the x direction with $y = 5$ mm, respectively, in the top plies of the multidirectional laminates. The EC densities have similar rates of change along the y direction, whereas the variations of EC along the x direction in the multidirectional laminates are much faster than that in the unidirectional laminate. The more interfaces

the multidirectional laminate has, the faster variation of EC along the x direction is. As the distribution of EC in multidirectional laminate is compact in all directions, the influence of edge effect associated with multidirectional laminate is similar to that associated with isotropic material. Meanwhile the maximum values of EC density in the multidirectional laminates are larger than that in the unidirectional laminate, which can be explained by the extra EC paths as mentioned above and the reflection of EC on the interfaces of adjacent plies having fibers in different orientations in multidirectional laminates.

4. Attenuation of EC in the Normal Direction

In order to study the attenuation of EC in the normal direction, the thicknesses of the test materials are increased to 10 mm such that EC has become very small before reaching the bottom. Correspondingly each ply is of 1.25 mm.

4.1. Skin Effect in Unidirectional CFRP. The FE model remains the same as the one used in Section 3.1 except that the thicknesses of the materials and of each ply are increased and the conductivities are changed. The conductivities (σ_l , σ_t , σ_n) of the three materials are (100, 100, 100) S/m, (10,000, 10,000, 10,000) S/m, and (10,000, 100, 100) S/m, respectively. Figure 9 shows the amplitudes of EC densities as functions of depth with $x = 0$ and $y = 5$ mm in the materials having various conductivity tensors. For each material, the EC densities are normalized by the value at the material surface. Obviously, the attenuation of EC in the anisotropic material is much faster than those in the isotropic materials; namely, the skin depth of EC in the anisotropic material is smaller than those in the isotropic materials, which is important for choosing testing parameters.

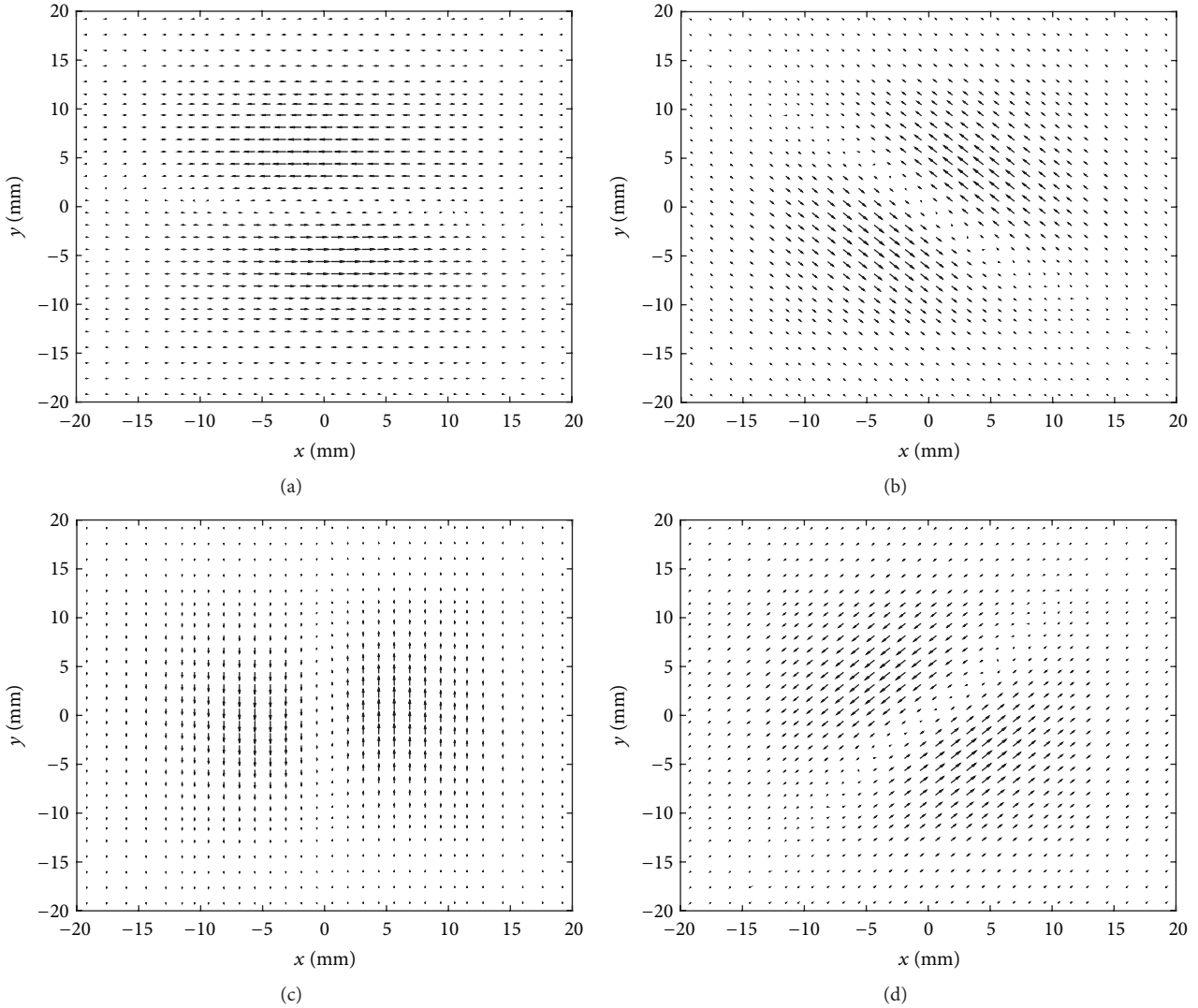


FIGURE 7: Distribution of EC (real part) in the multidirectional laminate of $[0_2/-45_2/90_2/45_2]$ in (a) the 1st ply ($\theta = 0^\circ$), (b) the 3rd ply ($\theta = -45^\circ$), (c) the 5th ply ($\theta = 90^\circ$), and (d) the 7th ply ($\theta = 45^\circ$).

To understand Figure 9, the diffusion and cancellation of EC are studied. Suppose an infinitely long single straight wire carrying ac current is placed parallel to the surface of a conductor, as shown in Figure 10(a). The spread of EC in a plane parallel to the surface becomes wider with increasing depth of the plane, as illustrated in Figure 10(b), which is referred to as diffusion of EC. At certain depth, define spread width of EC as the distance of the two points at which the values of EC are $1/\sqrt{2}$ of the peak value. Let L_1 and L_2 be the spread widths of EC in the surface and at depth of 2 mm, respectively. Their relative difference is

$$\Delta L = \frac{L_2 - L_1}{L_1}. \quad (6)$$

Larger ΔL means faster diffusion of EC. If another infinitely long straight wire is placed parallel to the previous wire with the same lift-off and the currents in the two wires are in opposite directions, then the ECs induced by the wires will

have 180° phase difference. Hence, their superposition results in the reduction of EC magnitude, which is referred to as cancellation of EC. Obviously faster diffusion of EC makes cancellation of EC more serious.

Simulation results show that the values of ΔL are 7.42%, 15.93%, and 26.28% for the samples having conductivities of (100, 100, 100) S/m, (10,000, 10,000, 10,000) S/m, and (10,000, 100, 100) S/m, respectively. We can conclude that faster diffusion of EC in the anisotropic material makes cancellation of EC more serious, which makes attenuation of EC along the depth direction faster than those in the isotropic materials.

4.2. Skin Effect in Multidirectional CFRP. The multidirectional CFRP laminates used in Section 3.2 are utilized here for studying skin effect, with the thickness of each ply increased by 10 times. In a multidirectional laminate, the (x, y) coordinates at which EC densities reach maximum of different

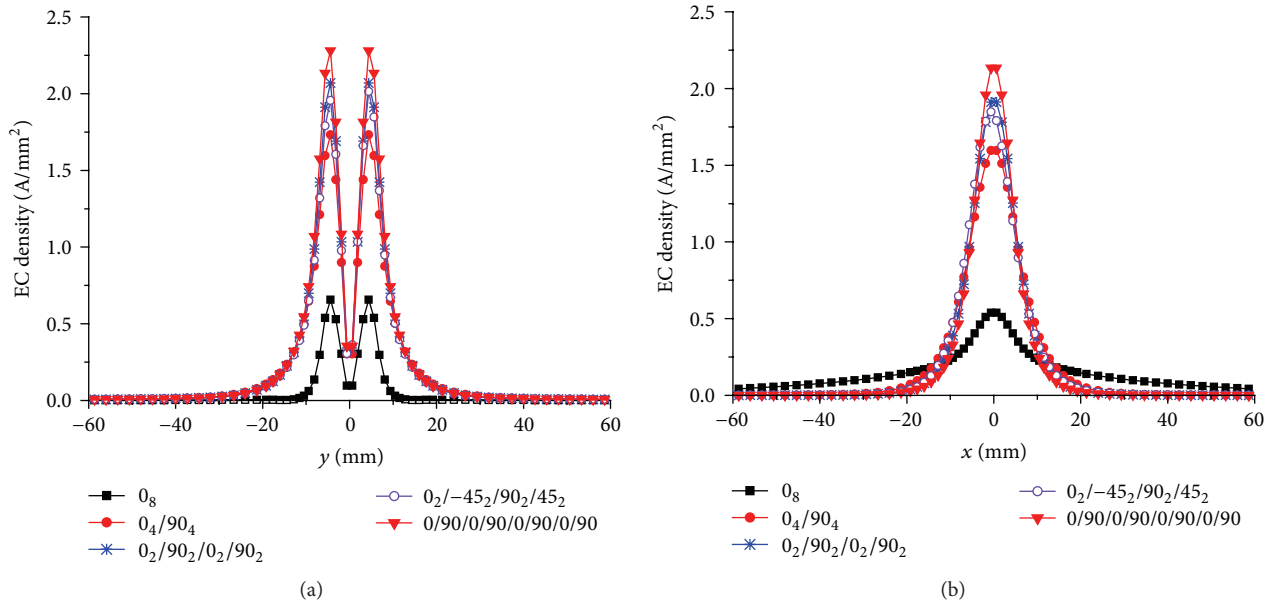


FIGURE 8: EC densities in the top plies ($\theta = 0$) of the multidirectional laminates: (a) along the y direction with $x = 0$ and (b) along the x direction with $y = 5$ mm.

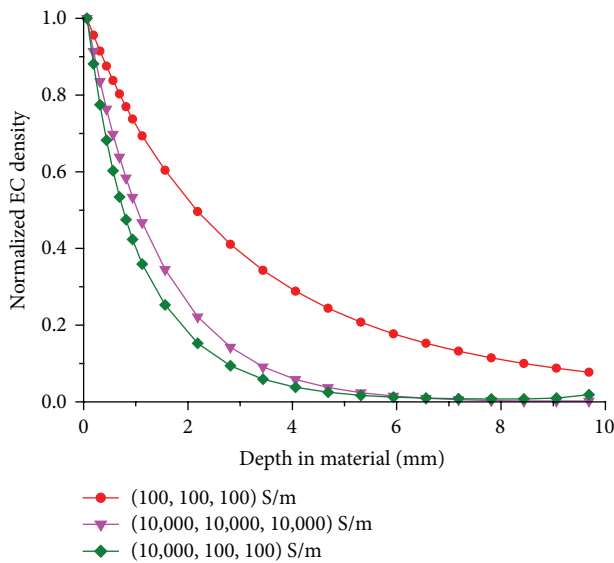


FIGURE 9: Attenuation of EC along the penetrating direction in isotropic and anisotropic materials.

plies may be different. For instance, the (x, y) coordinates of maximum EC densities of the ply with $\theta = 0$ and the ply with $\theta = 90^\circ$ are $x = 0, y = \pm 5$ mm and $x = \pm 5$ mm, $y = 0$, respectively. For each multidirectional laminate, we pick up the maximum EC densities in every layer of the FE mesh in the laminate and normalize them by the value in the top layer. Figure 11 shows the normalized EC densities as functions of depth of the four multidirectional laminates. The normalized EC density function of the unidirectional laminate is also shown for comparison. The points of calculating EC densities are inside the plies. The attenuation of EC in the $[0_4/90_4]$

laminate is quite similar to that in the unidirectional laminate except that EC dramatically increases near the interface of the two adjacent plies having different fiber orientations, that is, the interface between the 4th and the 5th plies. The enhancement of EC near interface, for example, the interface between the 2nd and the 3rd plies, can also be easily seen in the attenuation curves of EC of the $[0_2/90_2/0_2/90_2]$ and $[0_2/-45_2/90_2/45_2]$ laminates. In the $[0/90/0/90/0/90/0/90]$ laminate, there is only one peak in the attenuation curve of EC, because there are so many interfaces in the material and the increase of EC associated with an interface is largely affected by those associated with nearby interfaces.

It is concluded that the variation of EC in multidirectional laminate is different from that in unidirectional laminate due to extra EC paths and reflection of EC on interfaces and is affected by the stacking sequence of laminates. As the function of EC density versus depth is no longer monotonic, it is hard to define skin depth of EC in multidirectional CFRP.

5. Conclusions

Study of the characteristics of EC distribution is critical for designing probe and selecting testing parameters as well as damage detection and evaluation. The paper conducts quantitative analysis of EC distribution in unidirectional and multidirectional CFRP laminates.

Firstly, we study the intraply distribution of EC. In unidirectional CFRP, EC varies slowly along the fiber direction and changes fast in the orthogonal direction, which results in different levels of edge effect on different sides of the material. In multidirectional CFRP, the distribution of EC is compact in all directions. Therefore, the edge effect in this case is akin to that associated with isotropic material.

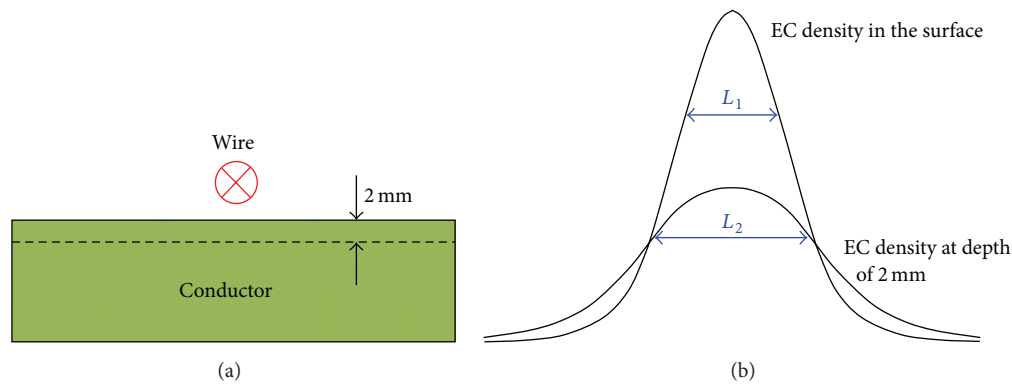


FIGURE 10: Illustration of diffusion of EC. (a) An infinitely long single straight wire carrying ac current placed above a conductor. (b) Distributions of EC in the conductor surface and at depth of 2 mm.

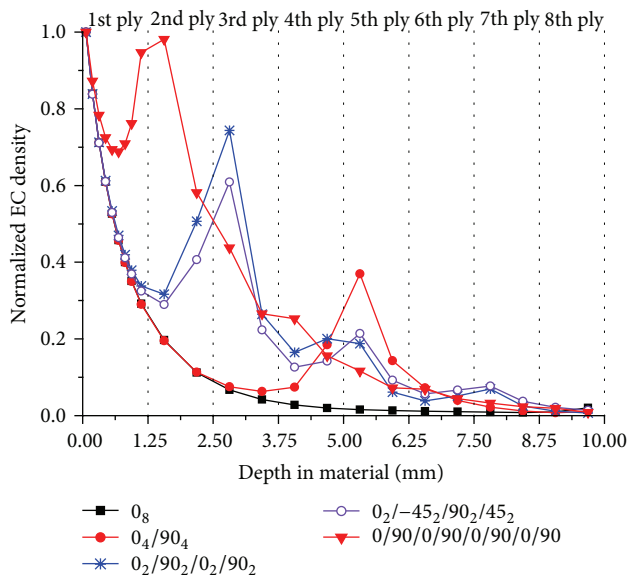


FIGURE 11: Attenuation of EC in the multidirectional CFRP laminates.

Then the attenuation of EC in the depth direction is analyzed. In unidirectional CFRP, EC attenuates faster than in isotropic material due to faster diffusion. In multidirectional CFRP, EC attenuates at similar speed as in the unidirectional CFRP except that it is enhanced near the interface of adjacent plies having different fiber orientations.

The characteristics of EC distribution in CFRP presented in the paper are obtained with working frequency of 10 MHz. When the frequency is 1 MHz, the characteristics of EC distribution are similar to those at 10 MHz.

Competing Interests

The authors declare that they have no competing interests.

Acknowledgments

This work is supported by the National Science Foundation of China under Grant 51277154 and the Research Fund for the Doctoral Program of Higher Education under Grant 20120121110026.

References

- [1] H. A. Maples, S. Wakefield, P. Robinson, and A. Bismarck, "High performance carbon fibre reinforced epoxy composites with controllable stiffness," *Composites Science and Technology*, vol. 105, pp. 134–143, 2014.
- [2] T. Bergmann, S. Heimbs, and M. Maier, "Mechanical properties and energy absorption capability of woven fabric composites under $\pm 45^\circ$ off-axis tension," *Composite Structures*, vol. 125, pp. 362–373, 2015.
- [3] A. Todoroki, K. Yamada, Y. Mizutani, Y. Suzuki, and R. Matsuzaki, "Impact damage detection of a carbon-fibre-reinforced-polymer plate employing self-sensing time-domain reflectometry," *Composite Structures*, vol. 130, pp. 174–179, 2015.
- [4] H. K. Bui, G. Wasselynck, D. Trichet, B. Ramdane, G. Berthiau, and J. Fouladgar, "3-D modeling of thermo inductive non destructive testing method applied to multilayer composite," *IEEE Transactions on Magnetics*, vol. 49, no. 5, pp. 1949–1952, 2013.
- [5] S. Zenia, L. B. Ayed, M. Nouari, and A. Delamézière, "Numerical prediction of the chip formation process and induced damage during the machining of carbon/epoxy composites," *International Journal of Mechanical Sciences*, vol. 90, pp. 89–101, 2015.
- [6] S. Gäbler, H. Heuer, G. Heinrich, and R. Kupke, "Quantitatively analyzing dielectric properties of resins and mapping permittivity variations in CFRP with high-frequency eddy current device technology," *AIP Conference Proceedings*, vol. 1650, pp. 336–344, 2015.
- [7] J. Wu, D. Zhou, and J. Wang, "Surface crack detection for carbon fiber reinforced plastic materials using pulsed eddy current based on rectangular differential probe," *Journal of Sensors*, vol. 2014, Article ID 727269, 8 pages, 2014.
- [8] X. Xu, M. Liu, Z. Zhang, and Y. Jia, "A novel high sensitivity sensor for remote field eddy current non-destructive testing

- based on orthogonal magnetic field,” *Sensors*, vol. 14, no. 12, pp. 24098–24115, 2014.
- [9] J. Cheng, H. Ji, J. Qiu, T. Takagi, T. Uchimoto, and N. Hu, “Role of interlaminar interface on bulk conductivity and electrical anisotropy of CFRP laminates measured by eddy current method,” *NDT & E International*, vol. 68, pp. 1–12, 2014.
- [10] B. Akuthota, D. Hughes, R. Zoughi, J. Myers, and A. Nanni, “Near-field microwave detection of disbond in carbon fiber reinforced polymer composites used for strengthening cement-based structures and disbond repair verification,” *Journal of Materials in Civil Engineering*, vol. 16, no. 6, pp. 540–546, 2004.
- [11] S.-J. Yoon, D. Chen, S.-W. Han, N.-S. Choi, and K. Arakawa, “AE analysis of delamination crack propagation in carbon fiber-reinforced polymer materials,” *Journal of Mechanical Science and Technology*, vol. 29, no. 1, pp. 17–21, 2015.
- [12] F. Sket, A. Enfedaque, C. Alton, C. González, J. M. Molina-Aldareguia, and J. Llorca, “Automatic quantification of matrix cracking and fiber rotation by X-ray computed tomography in shear-deformed carbon fiber-reinforced laminates,” *Composites Science and Technology*, vol. 90, pp. 129–138, 2014.
- [13] L. Ma and M. Soleimani, “Hidden defect identification in carbon fibre reinforced polymer plates using magnetic induction tomography,” *Measurement Science and Technology*, vol. 25, no. 5, Article ID 055404, 2014.
- [14] Y. He, G. Tian, M. Pan, and D. Chen, “Impact evaluation in carbon fiber reinforced plastic (CFRP) laminates using eddy current pulsed thermography,” *Composite Structures*, vol. 109, no. 1, pp. 1–7, 2014.
- [15] Z. Liu, W. Li, F. Xue, J. Xia, B. Bu, and Z. Yi, “Electromagnetic tomography rail defect inspection,” *IEEE Xplore: IEEE Transactions on Magnetics*, vol. 51, no. 10, Article ID 6201907, 1907.
- [16] W. Yin, P. J. Withers, U. Sharma, and A. J. Peyton, “Noncontact characterization of carbon-fiber-reinforced plastics using multifrequency eddy current sensors,” *IEEE Transactions on Instrumentation and Measurement*, vol. 58, no. 3, pp. 738–743, 2009.
- [17] H. Menana and M. Féliachi, “An integro-differential model for 3-D eddy current computation in carbon fiber reinforced polymer composites,” *IEEE Transactions on Magnetics*, vol. 47, no. 4, pp. 756–763, 2011.
- [18] J. Cheng, H. Ji, J. Qiu, T. Takagi, T. Uchimoto, and N. Hu, “Novel electromagnetic modeling approach of carbon fiber-reinforced polymer laminate for calculation of eddy currents and eddy current testing signals,” *Journal of Composite Materials*, vol. 49, no. 5, pp. 617–631, 2015.
- [19] S. Bensaid, D. Trichet, and J. Fouladgar, “Optimal design of a rotating eddy-current probe—application to characterization of anisotropic conductive materials,” *IEEE Transactions on Magnetics*, vol. 51, no. 3, Article ID 6200504, 2015.
- [20] H. Menana and M. Féliachi, “Electromagnetic characterization of the CFRPs anisotropic conductivity: modeling and measurements,” *EPJ Applied Physics*, vol. 53, no. 2, Article ID 21101, 2011.
- [21] R. Grimberg, A. Savin, R. Steigmann, and A. Bruma, “Eddy current examination of carbon fibres in carbon-epoxy composites and Kevlar,” *International Journal of Materials and Product Technology*, vol. 27, no. 3-4, pp. 221–228, 2006.
- [22] L. Sun, *Finite element analysis of eddy current testing of carbon fiber reinforced polymers [M.S. thesis]*, Xiamen University, 2014.
- [23] S. K. Burke, “Eddy-current induction in a uniaxially anisotropic plate,” *Journal of Applied Physics*, vol. 68, no. 7, pp. 3080–3090, 1990.

Research Article

WildSense: Monitoring Interactions among Wild Deer in Harsh Outdoor Environments Using a Delay-Tolerant WSN

Junho Ahn,¹ Akshay Mysore,¹ Kati Zybko,² Caroline Krumm,² Sravan Thokala,¹ Xinyu Xing,³ Ming Lian,¹ Richard Han,¹ Shivakant Mishra,¹ and Thompson Hobbs²

¹*Department of Computer Science, University of Colorado, Boulder, CO 80309, USA*

²*Natural Resource Ecology Laboratory, Department of Ecology, Colorado State University, Fort Collins, CO, USA*

³*Georgia Institute of Technology, Department of Computer Science, Atlanta, GA, USA*

Correspondence should be addressed to Junho Ahn; junho.ahn@colorado.edu

Received 26 May 2016; Accepted 13 July 2016

Academic Editor: Xiaobei Zhang

Copyright © 2016 Junho Ahn et al. This is an open access article distributed under the Creative Commons Attribution License, which permits unrestricted use, distribution, and reproduction in any medium, provided the original work is properly cited.

Biologists and ecologists often monitor the spread of disease among deer in the wild by using tracking systems that record their movement patterns, locations, and interaction behavior. The existing commercial systems for monitoring wild deer utilize collars with GPS sensors, deployed on captured and rereleased deer. The GPS sensors record location data every few hours, enabling researchers to approximate the interaction behavior of tracked deer with their GPS locations. However, the coarse granularity of periodically recorded GPS location data provides only limited precision for determining deer interaction behavior. We have designed a novel system to monitor wild deer interaction behavior more precisely in harsh wilderness environments. Our system combines the functionalities of both GPS and RF-radio sensors with low-cost and minimal-resource nodes. We designed and built our system to be able to operate robustly for a period of up to several months for continual tracking and monitoring of the locations and interaction behaviors of wild deer in harsh environments. We successfully deployed six deer collars on six wild deer that were captured and rereleased in the Soapstone Prairie Natural Area of northern Colorado over a one-month period. In this paper, we describe how we designed and built this system and evaluate its successful operation in a wilderness area.

1. Introduction

The development of systems for remote tracking of animals represents the single most influential advance in instrumentation for observing ecological processes in populations and communities of vertebrates. Until this development, it was impossible to consistently observe animals in their natural habitats except under the most idiosyncratic conditions. Despite its wide use, current technology for these systems suffers from three fundamental limitations. First, existing low-cost and low-performance wireless sensors are highly sensitive and can easily malfunction in harsh outdoor environments (e.g., high humidity, strong winds, heavy dust or mud, and drastic temperature changes). Second, costs of implementing telemetry constrain sample sizes, leading to undesirable limitations on statistical power. It follows that there is a need for instruments that allow spatially accurate

observations at costs that are one-tenth of the costs of current telemetry systems. Third, current instrumentation is “location centric” only—it allows the investigator to know the position of the individual animal relative to some geographic position at some specified time but cannot inform questions about its frequent interactions with other individuals. It follows that there is a need for remote tracking technology that can better record accurate interactions among animals.

This paper describes the design, implementation, and evaluation of WildSense, a software and hardware system that allows scientists to collect location and contact information of free-range deer in a low cost and robust manner in a harsh wilderness environment, as shown in Figure 1. WildSense is comprised of collar nodes and a delay-tolerant network for relaying contact information between radio-based collar nodes. The collar node shown is worn by each animal being monitored and consists of a MICAz mote (equipped with a



FIGURE 1: Collar deployment for wild deer.

low-power short range IEEE 802.15.4 2.4 GHz radio, TinyOS, and a GPS receiver) and also a VHF transmitter. WildSense employs a special type of networking protocol called a delay-tolerant network (DTN) to route information between nodes. Such a network is robust to disconnection between nodes in the network, allowing nodes to exchange each other's information when in close proximity, while storing information for future exchanges when nodes are out of range. As a result, DTNs are ideally suited for exchanging information among mobile wildlife that may only intermittently be in contact.

WildSense is designed for sustained low-cost deployment in rugged wilderness areas. It is designed to last more than 45 days without requiring any battery recharging, so that it is sufficiently weather/terrain independent. It is also designed to tolerate failures that may occur in real world deployments. For example, the DTN protocol has the property that it improves the fault tolerance of the communication network. Location and interaction information is automatically replicated and propagated in the network, so that the loss of any one collar node will still allow a subset of that animal's contact information to be retrieved from other nodes in the network. WildSense is also designed to be a low-cost system, where each collar costs less than \$450 in total. This paper presents detailed results from a successful deployment of WildSense on six free-range mule deer, for a period of one month, in the Soapstone Prairie Natural Area near Livermore, Colorado.

This paper makes the following key research contributions to enable improved tracking of wild animals in rugged, harsh outdoor environments. First, our understanding is that the results of this paper provide some of the most detailed validation to date of DTN protocols in practice, particularly how their fault tolerance properties enable effective operation in harsh real world environments. We show that wild deer coming in contact with one another enables the forwarding and spread of contact information via a DTN protocol, thereby providing robustness to failures; that is, when a collar node was lost, its contact information was preserved in the

information exchanged with other DTN nodes on each contact. This robustness property of DTN protocols, successfully highlighted by the WildSense deployment's results, improves the ability of scientists to recover an increased amount of data from their field experiments. Second, WildSense shows the feasibility of sampling free-range animal interactions in a manner that is both fine grained and low powered. In comparison, the current approach using GPS collars is faced with a tradeoff: if finer grained location sampling is desired, then longevity is hampered due to the power-hungry GPS unit operating for an increased time; conversely, if longevity is desired, then the sampling granularity is forced to be more coarse grained. WildSense provides the ability to collect the frequency of contacts down to the minute granularity, while also providing long-duration observations.

The remainder of this paper is organized as follows. Section 2 provides an overview of related work. Section 3 describes the details of the software and hardware design of WildSense. Section 4 describes the details of the WildSense deployment in Soapstone Prairie Natural Area for a period of about 30 days, as well as the data collection process involved in this deployment. Section 5 provides a detailed evaluation of the data we collected from the deployment of our system on the free-range deer in a wilderness environment. We finish with a discussion and summarize our findings in the conclusion.

2. Related Work

Existing ecological research [1–3] that tracked white-tailed deer utilized GPS-based systems to measure their movements and interaction behavior among them (same group and different group). The movement research [1] has shown that deer walk within a home range of 10 kilometers. Mean daily travel distance [2] was 778 meters with a range between 506 and 1500 meters during the excursion duration. Our system

also utilized the GPS sensor to monitor their movements and we compared the results collected in our system and the existing research results to analyze our system's feasibility. Additionally, although the existing interaction research measured deer behavior in both the same group and different group, it was limited to measuring the deer' locations on an hourly basis to conserve its battery power. The research [3] has found that white-tailed deer interact with others frequently in the same group and very infrequently in a different group by analyzing location data collected hourly. Our WildSense system provides the most precise ability to collect the frequency of contacts down to a granularity of less than one minute of interaction duration with a delay-tolerant WSN.

Though there is extensive literature exploring the topic of delay- and disruption-tolerant networks (DTNs), as summarized in a number of surveys [4–7], the vast majority of these papers are based exclusively on simulation. While simulations can provide helpful insights, they can also be limited by potentially unrealistic assumptions that do not hold true in real world deployments, like unrealistic mobility models, idealized wireless channel models, energy models that are too optimistic, and overly simplistic failure models, to name just a few. For example, Spray and Wait [8] simulate a routing scheme that uses a flooding algorithm for intermittently connected networks where a few packets are sprayed into the network and an acknowledgment is sent when the sprayed packet is received at the sink. This piece of information is then used to improve the performance of the network. Li et al. [9] used trace-based simulation to evaluate a socially selfish algorithm where the node forwards its data only to other nodes with which it has strong ties. Pásztor et al. [10] propose context aware data forwarding so that nodes in the network can calculate an efficient path of transfer to the base station. Code is built for motes, but the protocol is evaluated via a simulator and is not deployed in the field. Routing approaches strongly related to DTN routing include message ferrying [11], also called data muling, and routing in vehicular ad hoc networks (VANETS) [12]. These works are primarily simulations based.

Our focus has been on practically deploying a DTN system in the field, so our contributions concern how to operate a DTN successfully in a harsh real world environment. As a result, our literature review below focuses primarily on the small number of practical deployments of DTN systems that have been reported, where the small number testifies we believe to the inherent difficulty and imposing challenges of successfully deploying DTN systems in the wild. The results of this paper provide we believe some of the most detailed validation to date that DTN protocols can operate effectively in demanding in situ conditions.

In terms of real world DTN deployments, perhaps the most similar to ours is Zebranet [13–16]. In this project, wild zebras were collared in Kenya and their activity was monitored for 10 days. They used GPS for recording location information and VHF communication for flooding the data in their network. Solar energy was used to power the hardware in the collars and a rechargeable battery stored the energy for future use. The Zebranet collar was set to sample

GPS every 8 minutes due to power/longevity constraints. Rather than relying on power-hungry GPS to infer contact information, we instead employ low-power radios with a short range (about 30 m) to record contact information. This low-power approach enables both fine-grained sampling of contacts (at the rate of at least once per minute) and long term observation (up to 45 days). GPS sampling at a much lower rate of once per hour was retained to provide timing data and approximate location references to the proximity contacts, which was suitable for the domain scientists. Our design also differed from Zebranet by eliminating solar recharging, which could miss contacts due to insufficient recharging under overcast skies. Indeed, ten of our thirty deployment days were either completely overcast/snowing or partly cloudy. As we show later, our system was able to capture all contacts at the granularity of at least once per minute over a span of thirty days, including a key contact that would have been missed by coarser sampling.

A store and forward DTN-like implementation has been briefly reported [17] wherein cattle act as data ferries to information sinks situated near common watering holes. This was tested only with captive animals and not with wildlife. We employed a similar preliminary phase of testing WildSense on managed cattle in paddocks. While this kind of phased testing is useful, these tests could not fully emulate the actual wildlife deployment. For example, we found that the cattle testing failed to predict a failure mode encountered in the actual deployment, namely, losing a collar node. Carnivore [18] is a disruption-tolerant system deployed on mountain lions, in which nodes forward data to the node which has most recently accessed a sink. One collar of three was recovered, with no contacts reported.

DTN-like data forwarding has also been applied in other scenarios such as transportation and agriculture. Daknet [19] extends internet connectivity to public information kiosks in rural India and Cambodia, in which buses plying on transport routes are fitted with mobile access points to ferry the information from rural areas to cities with better internet connectivity. The Wizzy Digital Courier service employs a similar approach to connect to schools in remote villages in South Africa [20]. An energy harvesting data mule [21] system has also been implemented in which a person cycles around soil moisture sensor nodes to collect data and relay them to an internet gateway, where the data mule is powered by dynamos fixed on the cycle. Some studies have logged location information among buses [22], or Bluetooth-based contact information among mobile devices like PDAs and motes [23, 24], in order to develop trace-based simulations for evaluating DTN protocols but do not deploy any DTN forwarding in practice.

Wireless sensor networks (WSNs) have also been applied to track animals in a variety of other scenarios, though these do not employ multihop DTN-like forwarding or ferrying of data among the animals. Rather, these systems typically report directly from a sensing node to a collection point, such as a base station. A WSN was deployed to monitor cattle in a 21-hectare paddock [25, 26]. The cattle were fitted with collars containing GPS and proximity loggers and the information was relayed to a base station using the

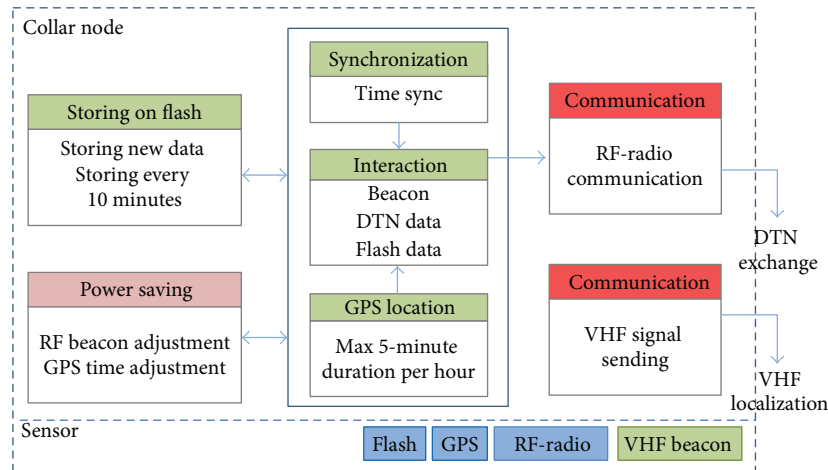


FIGURE 2: System architecture.

reliable and always connected communication network of collars. The velocity and eating habits of cattle were studied [27]. A related electronic shepherd [28] project employed a wireless sensor/actuator network to monitor cattle and control them via mild electric shocks from fighting with each other. Elsewhere, a badger monitoring network was implemented by deploying RFID collars on badgers and fixed RFID sensing stations that transferred the data via 3G cellular connections [29]. CraneTracker [30] deployed nodes that used cellular communication on whooping cranes to determine their migration pattern and wireless sensor nodes in areas of smaller range, for example, nesting sites. These cellular approaches were not suitable for our deployment, which involved remote terrain that lacked cellular connectivity. wildCense [31] also sought to deploy sensor nodes on deer (in India) but ultimately did not report on any deployments in the field.

3. System Design

In this section, we discuss the key aspects of our software and hardware system design. The software must be able to collect and relay contact information with the goal of 45 days of continuous operation, and the hardware must be sufficiently weather proof to endure exposure to the elements in an outdoor area, as well as durable enough for collar deployment on free-range deer.

3.1. Software Design. Our software was designed to track the movement of deer in the wild and especially monitor their interaction, so that scientists can determine contact rates and estimate the rate of disease propagation in wild deer populations, for example, chronic wasting disease. Standard collar nodes used by ecologists track and record the deer's locations based on periodic GPS sampling at the rate of once every few hours to conserve battery power, resulting in a granularity that is too coarse to capture detailed deer interaction behavior. Our software system is designed to

capture contact rates at a much finer granularity while operating robustly for extended continuous periods of time.

The deer collar nodes were constructed based on MICAz motes [32], which were desirable for their low cost, low power, light weight, small form factor, RF network and ranging capabilities, software support, and extensibility. We added a GPS module and operated with TinyOS v1.2.3. The size of our software's source code that operated on this hardware was 65.6 KB out of 128 kilobytes of ROM, utilizing 3905 bytes RAM out of 4012 bytes. Figure 2 shows our system's software architecture.

The collar node collects GPS-based locations and interaction behavior data via low-power RF-radio signals. Collars can be programmed with a timed falloff mechanism. In order to locate a collar that has fallen off and thereby retrieve the collar node and its data, a VHF radio was also installed in each collar node, allowing the collar to be located from its VHF beacon within a maximum 8 km range. Note that the VHF beacon is strictly used for collecting the collars after they have fallen off. VHF cannot be used for recording contact information that involves exchanging data packets as it uses analog signals.

We describe below each component of our system's software design and how it operates with the collar.

3.1.1. Location. We integrated GPS sensor modules into our deer collar system design for both coarse-grained localization and time synchronization purposes, with the latter motivation explained in more detail below. We tested the GPS sensor in various different types of terrain, such as hills, valleys, streams, forests, and open plains, and found that a safe duration for keeping the GPS sensor on in order for it to acquire a location lock typically took 5 minutes. We also found the safest approach was to reinitialize the GPS sensor periodically, because otherwise it would cease to localize properly. We found if we reinitialized and activated the GPS sensor to run for periods of only up to 5 minutes every hour, we could successfully collect localization data on the

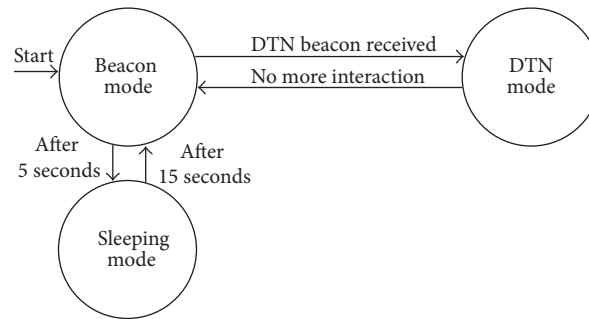


FIGURE 3: State diagram of collar node's software.

deer collar nodes for the duration of the experiment while conserving power via duty cycling.

3.1.2. Interaction. We were able to achieve subminute granularity in terms of capturing contact rates by using MICAz RF-radio communication. The transmit power of the IEEE 802.15.4 radio was set to 0 dBm, which gave us a range of approximately 30 m. This was viewed as acceptable by the wildlife biologists to estimate proximity-based contacts for the purposes of this experiment. The radios would beacon by default every 20 seconds, duty cycling to save power by staying up 5 seconds and sleeping 15 seconds. The radios were synchronized to awaken at the same time using GPS time. If a collar node hears another collar node, it drops out of beaconing mode and into DTN mode explained below. These different software states are outlined in Figure 3.

With RF-radio communication, we sought to measure two aspects of deer behavior interaction with our software: the occurrence of a contact interaction event and the duration of such an event. First, when two deer come into close range, each node drops into DTN mode and begins exchanging DTN table data with the other node every 6 seconds. The DTN table is cached in RAM for fast access and due to the small size of the RAM stores only the 8 most recent interaction data segments at one time. New interaction data continually overwrite older data segments, based on the interaction time. The interaction data stored on each collar node includes paired collar node information such as the two interacting node's IDs, locations, local times, GPS times, and additional table data. Records of the most recent contacts thus propagate further throughout the DTN hop by hop each time there is an encounter between two deer.

Second, we log the above-described interaction information on the node's flash, so that we can later assess interaction time duration for the paired nodes.

3.1.3. Synchronization. We needed mechanisms to synchronize the duty cycles of our GPS and low-power radio, as well as time-stamp our interaction data. We utilized two forms of time synchronization, one based on GPS to synchronize our radios for contact information and another based on ETA [33] to measure time differences and thus time-stamp the data by day. First, in order to synchronize the beacon signals

and activate the RF-radio sensors at the same time, we based our algorithm on GPS to the second granularity. We found, however, that based on GPS seconds, there could be up to a 3-second time delay in the sensor nodes receiving the GPS location data. For this reason, we set the radio beacon signals activation time to extend up to 5 seconds during collar node interaction periods and sent two beacon signals at the 2nd and 4th seconds in each 5-second activation period, rather than one beacon. Using the two beacon signals allowed us to ensure that, within the 20-second activation and sleeping period, we could hear at least one of the RF-radio sensor beacons among interacting collar nodes.

In order to time-stamp the data over the duration of the experiment, which spanned days and weeks of elapsed time, we used a time differencing algorithm based on local time synchronization similar to ETA for wireless sensor networking. We did not use GPS time for time-stamping because the GPS time includes only hours, minutes, and seconds and does not include any date information (year, month, and day). For purposes of our experiment, we needed to track date information to determine where and when the interaction among the deer collar nodes occurred. The ETA algorithm synchronizes node times in milliseconds. It uses local node time to calculate the time difference between a current and past event and then sends this information in packets of 4 bytes each to a neighbor node. We implemented our ETA-style local time synchronization at the application layer.

Pseudocodes 1 and 2 outline the pseudocodes for GPS localization, interaction and packet exchange between nodes, and synchronization of duty cycles of GPS and low-power radio.

3.1.4. Storage on Flash. We wished to permanently store the interaction data and durably log other parameters of the experiment and used flash memory for these purposes. Whenever data is stored on the flash, it is stored in 64-byte chunks. The total storage space of the flash is 512 kilobytes, which can hold 8000 units of such data. Once the flash space is full, the oldest data is continually overwritten by the newest data, using circular buffering. Our software stores both the deer collar node GPS location and the interaction data on flash. Each collar node records GPS location sensor data

```

void Timer.fired() // repeatedly call every one second
{
    // RF communication for 5 seconds every 20 seconds
    If (there is the fired time within 5 seconds over a 20 second span)
        Turn on the RF power
        Send its own Beacon signal twice via RF
    Else
        If (No response via RF)
            Turn off the RF power
    // GPS Localization for the maximum 5 minutes every one hour
    If (there is the fired time within 5 minutes over one hour span)
        Turn on the GPS power and Localize the current mote
    Else
        Turn off the GPS power
}

```

PSEUDOCODE 1: Pseudocode for the timer to send beacon via RF and localize the mote using GPS.

```

void RF_signal.receive(data) // When the mote received data via RF,
{
    Set the DTN mode using the continuous RF communication without the sleeping mode
    If (The received data is a beacon packet)
        Update the DTN table with the received data
        Send each row data in the DTN table in order
    Else // DTN data
        Update the DTN table with the received data
        Store the latest received data in the DTN table to EEPROM in a 10 minute period
}

```

PSEUDOCODE 2: Pseudocode for the RF-receiving part when a mote receives a beacon or DTN data via RF.

directly on the flash every hour. For DTN data, as we noted, data is exchanged and stored every 6 seconds when a contact event is detected. However, if two deer are in continuous contact, as we saw in this deployment, then this could fill the flash quickly with redundant data, when what we really want is duration of contact information. To economize on memory for long-duration contacts, we compare the latest exchanged DTN information, and if it is identical to the previous exchange, we do not store the latest exchange.

While implementing the flash storage functionality, we discovered a complication that caused a crashing problem. Whenever we activated the GPS sensor and data was attempting to store on the flash, both the GPS sensor and the flash crashed. At this point, the flash would no longer store any more data. To solve this problem, we implemented a flag in the source code to check whether the GPS sensor was activating or not, and if it was, we suspended the flash storing functionality until the GPS sensor was finished activating and localizing. Once we had done this, there were no further problems with our flash storage functionality.

3.1.5. Power Saving. In order to save power, both the GPS and the radio are duty cycled, with the GPS at a 1/12 duty cycle and the radio at a 1/4 duty cycle. In addition, we implemented an optimization that shut off our GPS sensors before the full 5

minutes elapsed if they were able to acquire 5 satellites sooner. This could be determined by polling the GPS sensor.

We measured the power consumption of our deer collar nodes when operating in each of four different modes: GPS + RF-radio, only GPS, only RF-radio, and sleeping. For each mode, we measured the amperage and then calculated the power consumption in each of the four modes, based on a voltage of 3.3. For each mode of operation, respectively, we found that our collar node consumed the following amount of battery power: 306.9 mW in GPS + RF-radio mode; 300.3 mW in only GPS mode; 75.9 mW in only RF-radio mode; 0.30 mW in sleeping mode.

We also investigated the length of time our collar node operated on battery power, with and without all of our power saving approaches. We found that with our algorithms we could extend our sensor node battery operating time up to three times longer than without power savings. For example, in a test with four 1.6 V/7500 mah C-cell batteries, the sensor node operated only 12 days without power savings, but with our power saving techniques it operated for a total of 33 days. However, this approach had insufficient longevity; so ultimately we settled on a design incorporating two paralleled D-cell 3.6 V batteries with 19,000 mah per each, with a 3.3 V regulator, and tests showed that it exceeded our 45-day lifetime goal. We explain the need for the regulator in

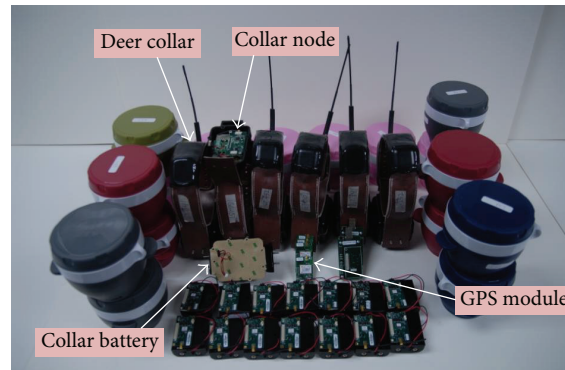


FIGURE 4: Hardware setup.

Section 3.2. We constructed our deer collar nodes based on these findings.

Second, we recovered the deer collar nodes that had detached from the deer's necks and fallen on the ground. We implemented a dump program to download all of the flash data to a computer and installed this program on the recovered collar nodes. The dump program sent the collar node's flash data every one second through a serial port on the computer.

3.1.6. VHF Beacon. In each deployed deer collar node, we also installed a VHF beacon board that emitted low level, minimal battery power usage signals. These signals are used for locating the collars after they have been dropped off the deer. The VHF beacon board emits two signals every second, but while the collar remained on the deer's neck only one signal could be detected, likely due to its movement and the deer's body and fur absorbing the signal. However, once the collars detached and fell to the ground, both signals emitted by the VHF beacon could be detected within an 8 km range. To retrieve the detached deer collars that had fallen to the ground and collect our data, we used a VHF receiver and antenna to search for the emitting VHF signals and locate the collar nodes.

3.2. Hardware Design. For our experiment, we assembled and deployed 6 nodes on deer collars in the outdoor prairie wilderness area. Figure 4 shows the hardware equipment used in our experiment. The equipment consisted of 20 MICAz motes, six GPS modules, six GPS antennas, six regulators, six VHF beacon boards, and six VHF antennas. We designed six weather-proof deer collar nodes, that each included a MICAz mote, a GPS module and antenna, a regulator, and a VHF board and antenna. In the section below, we describe the features of the equipment we used in our design of the deer collar nodes.

The MICAz mote we chose to use for our deer experiment is a 2.4 GHz wireless sensor module (mote) used for low-power applications. It is based on an ATmega128L microcontroller with 512 K bytes of serial flash and a Chipcon CC2420 RF transceiver. To construct the GPS module, we connected

an MTS420 environmental sensor board to the MICAz mote via a 51-pin connector. The MTS420 sensor board [34] is equipped with a GPS chip, with position accuracy of 10 meters and acquisition time (warm) of 33 seconds. The mote and sensor board were powered by two 3.6 V Saft LSH D cells via a Texas instruments TPS 61201 boost converter (the regulator) [35] which provided an output of a constant voltage of 3.3. The converter has an operating input voltage range from 0.3 V to 5 V, with a maximum 300 mA output, and draws a quiescent current of less than 55 μ A.

We ended up using parallelized 3.6 voltage batteries with the regulator to provide stable power to our sensor board. Initially, we experimented with using a regulator with two 1.6 V batteries connected in series but found that the voltage would decrease below 2.7 V, at a level where the motes are not guaranteed to collect data reliably. By operating two 3.6 V D-cell batteries in parallel combined with the regulator, we were able to provide a consistent voltage of 3.3 V to the sensor node for the duration of the experiment.

The collar nodes were built with the help of ATS (Advanced Telemetry Systems) company [36], which designed the VHF beacon board and the drop-off mechanism. Figure 5 shows the collar node installed with the sensors in a secure and robust assemblage. The VHF beacon board, batteries, and regulator were connected with each other and set in acrylic in the outer shell of the collar to prevent disconnection of wires due to the movement of the hardware within the case. The MICAz mote and the sensor board were secured with screws so that they can be easily removed in case they needed to be reprogrammed and connected to the regulator output. Finally, the shell was sealed with a double sided sealing tape to prevent moisture from seeping in and was screwed in to lock it in place.

We affixed a GPS antenna and VHF beacon antenna at the top of the deer collar and connected these to the collar sensor node as shown in Figure 6. We also installed a mechanism for the collar that was programmed to automatically detach and disconnect the collar construction, so that the collar could fall off the deer's neck, and the collar could later be retrieved. This mechanism was programmed to be released on a specific date by ATS company.

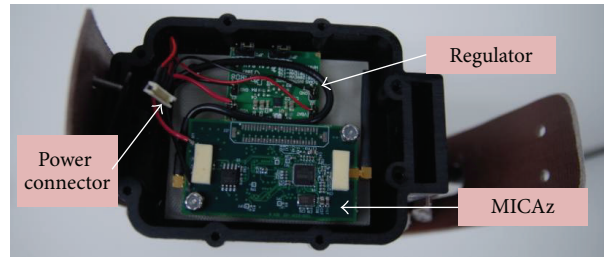


FIGURE 5: Collar node.

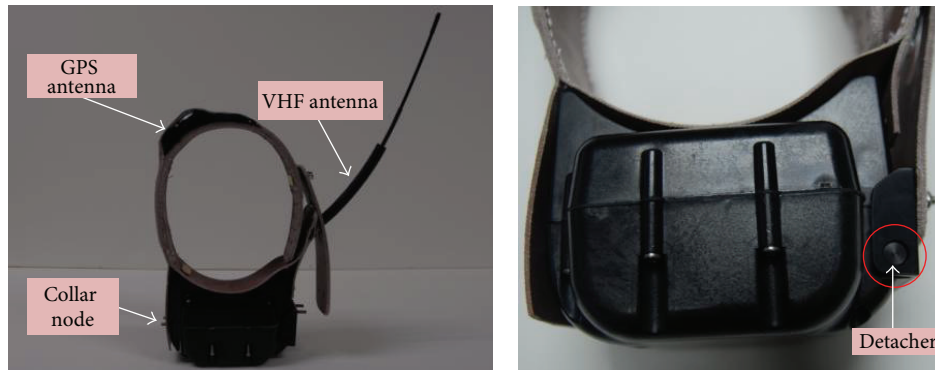


FIGURE 6: Deer collar.

4. Deployment and Data Collection

In February 2013, we deployed WildSense over six different deer [37–39] in the Soapstone Prairie Natural Area (a 75.8-square-kilometer area) [40] near Livermore, Colorado. The collars were programmed to detach from the deer after approximately three weeks, so that we could retrieve them to collect the sensor data for this research. We describe this deployment process and explain how the collars were retrieved from the outdoor area after the completion of the experiment.

4.1. Collar Node Deployment. Our deployment of collar nodes on wild deer consisted of the following steps: getting permission from appropriate authorities, base camp setup, aerial searching for free-range deer, capture of deer, medical examination and installation of collars on deer, and, finally, the release of deer back into the wilderness. Figure 7 shows an overview of our deer collar deployment process in the wilderness area.

We needed to obtain three different permissions for our wildlife experiment. First, we had to obtain IRB (Institutional Review Board) permission [41] from the federal government to conduct our deer collar deployment experiment. Second, we had to apply to the National Park Service to obtain permission to capture and release deer in this area. Third, because this research was conducted under the auspices of a research institution, each individual involved in the experiment also had to obtain permission to work in the wilderness area on the research team. All individuals involved in this experiment had to be trained on safety precautions

by the research team leaders and sign releases, in order to participate in this wildlife experiment. Once all permissions were obtained, we could access the wilderness area to deploy our collars on the deer.

Our research team consisted of ecologists, biologists, a ranger to manage the park, and engineers. The team brought in two helicopters, two fueling trucks for the helicopters, a truck with the medical trailer attached, and six additional trucks to carry the researchers back and forth to the base camp. A small search airplane was also contracted to continually fly over a wide area surrounding the base camp, in search of deer that could then be captured by researchers in the helicopters. Whenever team members caught a free-range deer, the deer were transported by one of the helicopters to the base camp to be medically examined before we installed the collar. We measured the deer's health status, installed the collars on the neck of the deer, and then released the deer back into the wild in the area surrounding the base camp. Figure 8(a) shows the base camp setup we used for deploying our collars on the captured deer. The two helicopter fueling trucks were positioned at a safe distance away from the medical trailer and center of the base camp, to ensure the safety of the research personnel and the deer.

The small search airplane was utilized to locate free-range deer in the large area surrounding the base camp. Once a deer was spotted, the researcher in the plane notified the team at base camp of the deer's location. Then the helicopters were deployed to that location to capture and retrieve the deer. Up to two helicopters were used to capture the deer. The helicopters were manned by two people: a pilot and one of the researchers on the team. Figure 8(b) illustrates how

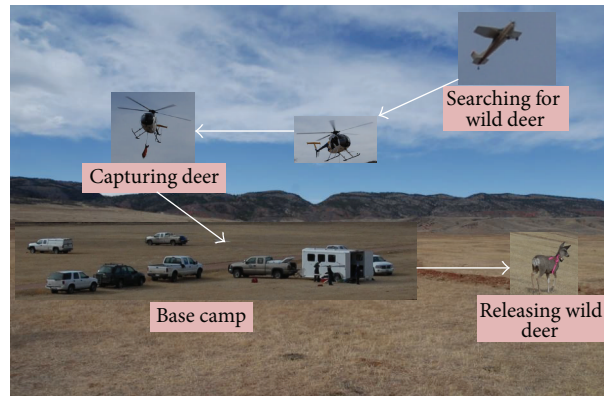


FIGURE 7: Overview of collar deployment.

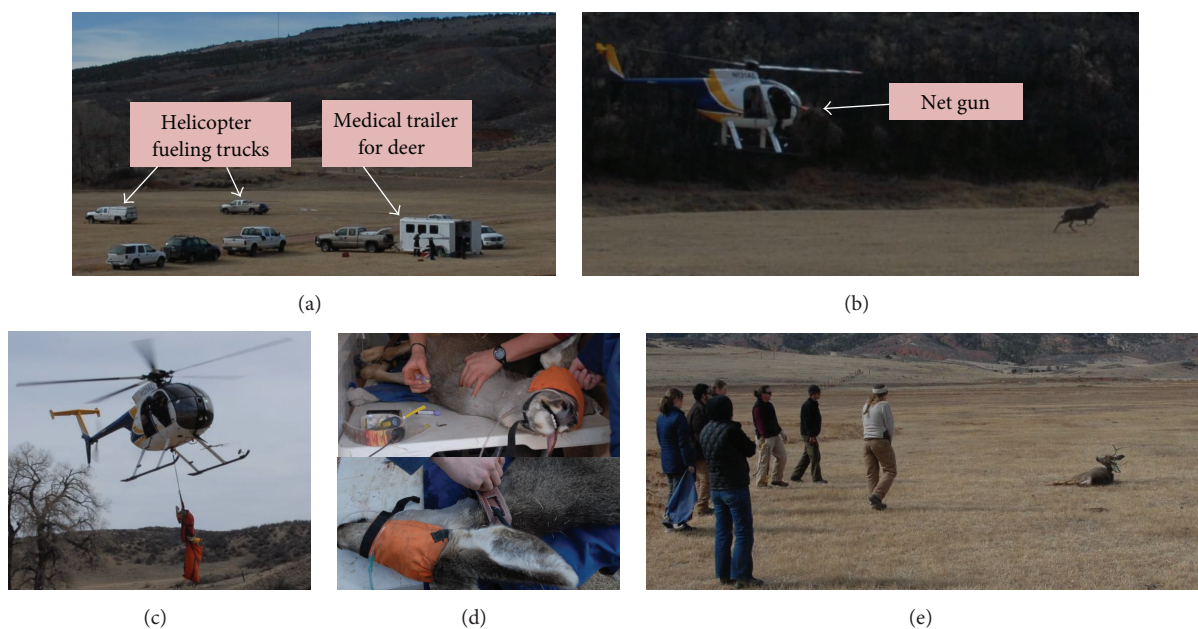


FIGURE 8: Steps of collar deployment.

the helicopter research personnel captured the deer using a net gun. As the helicopter approaches a deer, the research personnel were usually able to capture the deer by shooting a net that would entangle the feet of the running deer. At that point, the helicopter would immediately land on the ground, so that the researcher could jump off the helicopter and run to the deer to give it a sleeping drug injection. The researcher then bound the deer's legs and blindfolded the deer. The deer was then placed into a large carrying bag that was attached to and suspended from the helicopter, so it could be transported back to the base camp. Figure 8(c) shows one of the helicopters carrying two captured deer at one time back to base camp.

The captured deer is then delivered to the medical trailer at the base camp in order to allow research personnel to check the health of the deer and collect biological information, before we installed the deer collar. The helicopter dropped off the captured deer at the base camp and four team members

carried it into the medical trailer. The deer was given water to prevent dehydration and was provided with oxygen to stabilize it while it was in a drugged state. Figure 8(d) shows the deer being carried into the medical trailer. Biologists did a general checkup and performed tests, such as checking its gender, temperature, and ear passages, and drew blood for further analysis. They also collected a bit of fur and a stool sample for further analysis and did an ultrasound of the female deer to make sure they were not pregnant. They also recorded the unique VHF frequency of the deer collar that was to be used for this particular deer. The collected health status measurements are used to monitor any changes in the deer's health when it is recaptured, at which time new health measurements can be taken and compared to the previous data.

After all the health measurements were taken and the collar was installed, we released the deer back into the wild, at the edge of the base camp area. We untied the rope, still

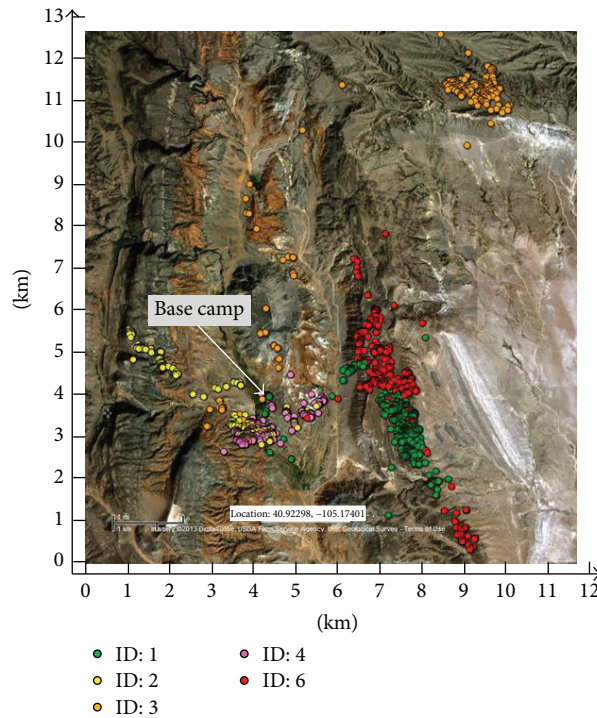


FIGURE 9: GPS tracking of five collected collars on map.

binding the legs, and removed the blindfold from its eyes. Team members stood in a line between the deer and the base camp area, in order to prevent the deer from venturing back to the base camp. We waited until the deer was completely alert, stood up, and ran off into the wild. Figure 8(e) shows the research team releasing the deer back into the wilderness area.

4.2. Collar Collection. We had programmed the collars to automatically detach from the deer's necks after three weeks and began collecting them soon after that, though some of the deer continued carrying the detached collar (draped over their necks) up to a week after that. Team members using a truck with a VHF antenna first located the general area of the dropped-off collar and then walked through the area with a handheld VHF antenna to locate the actual collar. By using this method, we successfully located five of the six collars; one collar's signal was never detected, possibly dropped off in a deep valley or river where we could not detect the signal. We retrieved two of the collars by the beginning of the fourth week, two more collars by the middle of this week, and the fifth collar at the end of the fourth week.

5. Evaluation

We have analyzed all GPS location and RF-radio interaction data retrieved from the five recovered collars. Our evaluation focused on analyzing deer movement over time as well as interactions among them. It shows that our system is able to collect detailed information about not only the locations of various deer at different times, but also time, location,

and duration of interactions among them. We show that this information can be used to study fine-grained interactions among deer within a social group. Furthermore, our evaluation demonstrates the fault tolerance property of our system, wherein we were able to collect location and movement information of a lost deer as well. Finally, we demonstrate the DTN functionality of our system. We show a detailed view of how location and interaction data was transferred from one deer to another using our DTN protocol over the course of 30 days.

5.1. Experimental Results for Collar Nodes

5.1.1. Deer Location and Movement. For clarification, we have assigned IDs from 1 to 6 to the six deer we used in our experiment. Figure 9 shows the locations of five deer whose collars we were able to collect over one-month period. All locations are mapped over the prairie region in which they lived and traveled during the experiment period. Collar nodes collected GPS location data every hour and stored them on flash. Our analysis shows that the deer generally stayed within a four-square-kilometer region and frequently traveled the same or similar paths. We confirmed our findings with the ecologists from our team, who study deer movement behavior. Earlier research [37, 38] in ecology has shown that the roaming range of deer is typically within two to four square kilometers. This provides us with high confidence about the correctness of the location and sequential movement data we have collected.

We have investigated their movements using the GPS tracking information collected from the five collars placed on the white-tailed deer. Four of the deer stayed within a

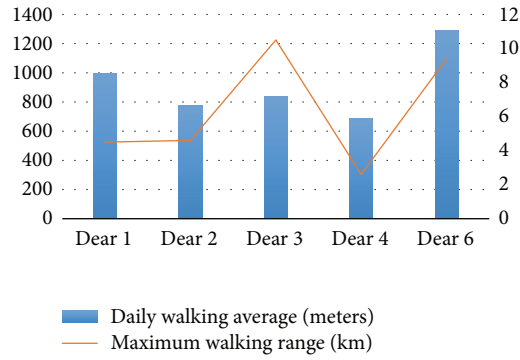


FIGURE 10: Daily walking average and maximum walking range of five collared deer.

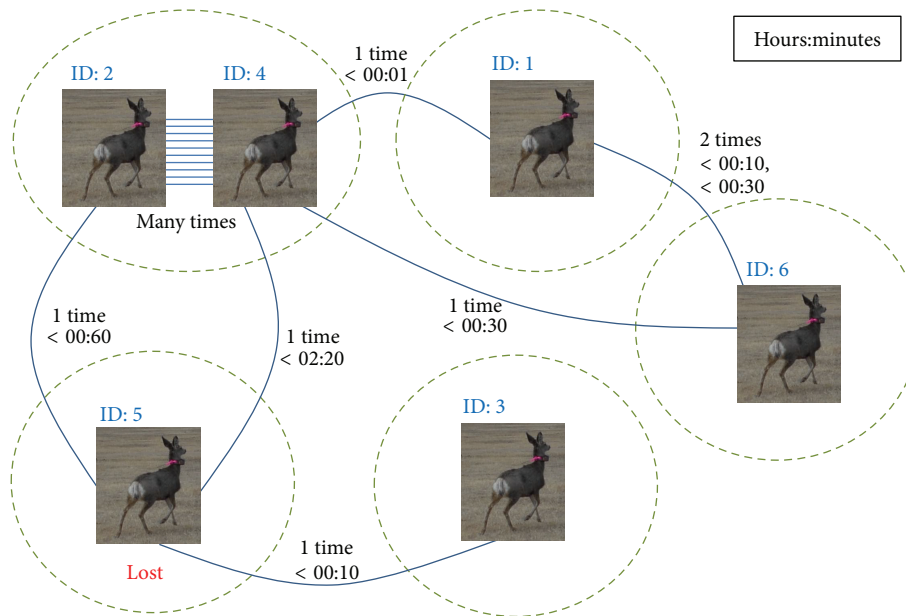


FIGURE 11: Interaction between deer and among deer groups within one month.

10-kilometer range as referred in [1] during the experiment period as shown in Figure 10. The five deer traveled the following distances: 4.5 km, 4.6 km, 10.5 km, 2.6 km, and 9.4 km. Only deer number 3 walked over 10 kilometers because it was trying to find its original living location where it was seen by the helicopter as shown in Figure 9. When considering this, all of the deer stayed in a 10-kilometer range. We have also analyzed their daily walking distance on average as shown in Figure 10. Our research showed they walked a short distance (993 m, 776 m, 840 m, 684 m, and 1290 m) per day on average during the winter season compared with a range between 506 and 1500 meters found in existing research [2]. Therefore, we concluded that our system operates sufficiently to obtain valid results to track the movements of white-tailed deer.

5.1.2. *Deer Interactions.* Figure 11 shows a diagram of the interactions among the six deer using the interaction data we recorded using the RF-radio-based communication. The deer collars that were within range of the low-power radios, about

30 m, shared data with each other by sending two beacon signals every 5 seconds within 20-second intervals. Once two deer located each other, they shared their interaction data every 6 seconds. Thus, our system was designed for neighboring deer to share their DTN information at a granularity of less than one minute of interaction duration. Interactions and interaction time durations between two deer in the same group and among deer from different groups are shown in this figure.

As we can clearly see from this figure, deer 2 and deer 4 were a social group as they interacted quite extensively during the experiment period. The identification of the social group (deer 2 and 4) is confirmed by the team that captured deer for our experiments (as described in Section 4). The team confirmed that two of the deer captured were from the same herd and the other four were from different herds. Our interaction analysis as shown in Figure 11 confirms that the two deer from the same herd interacted regularly and frequently with each other. The other four deer, captured from different herds, interacted only once or twice with each other.

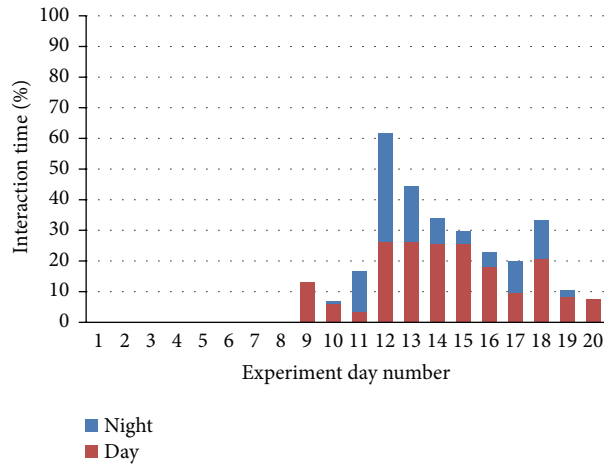


FIGURE 12: Interaction between the two deer from the same herd.

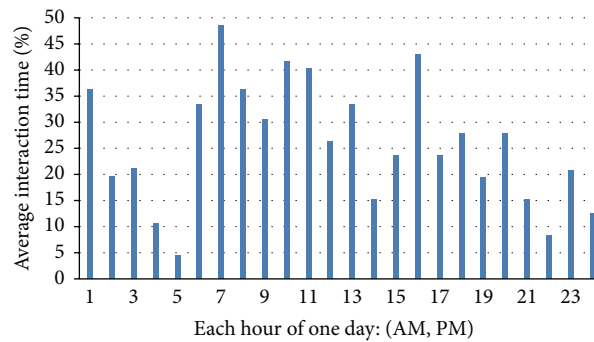


FIGURE 13: Average interaction time for each hour per day.

The deer interaction time duration for the deer from different herds ranged from one minute to 2 hours and 20 minutes.

In particular, we note that our fine-grained sampling was able to capture the brief interaction between deer 1 and 4, which occurred only once and lasted for less than one minute. Such an interaction would have been missed by all of the other wildlife tracking and monitoring systems that we reviewed in related work.

5.1.3. Social Group. Delving more deeply to understand the behavior of a single social group, we analyzed the full 20 days of interactions between deer 2 and 4 who were captured at the same time from the same herd. Figure 12 shows the interaction times of the two deer. After the two captured deer were collared and then released back into the wild, they could not find each other for eight days. Although they were released within five minutes of each other, they were likely disoriented after being sedated for collaring and examination, and so they ran off in different directions. After day 8, they located each other. The interaction data, shown in Figure 12, reveals that once they located each other, they interacted with each other on average 25% of the time per day for the remaining 12 days. During this period, we have found a 6-percent packet loss by analyzing their interaction data communicated between the motes 2 and 4. From this data,

we can assume that they normally prefer to travel together in the same group but also sometimes maintain their own range while traveling and foraging for food. This figure also shows that the duration of their interaction in a 24-hour day and night period ranged from 8% to 60%, depending on the day. We classified the interactions as occurring in either the day or night-time within a 24-hour period, by using sunrise and sunset times: approximately 6 AM and 6 PM, respectively. We found that they interacted more frequently during the daytime than they did at night: 63.6% of their interactions occurred during the day and only 36.4% occurred during night.

We also analyzed the average proportion of time the two deer spent interacting with each other each hour of a 24-hour period, as shown in Figure 13. We found that on average they spent the most time interacting with each other between 6 AM and 1 PM. We estimated sunrise to be approximately 6 AM, and thus our findings show that the two deer started interacting more frequently right about sunrise, perhaps waking up and starting to forage for food or water. The other noticeable hour period of increased frequency of interaction occurred around 4 PM, which would likely be when they would be grazing and trying to get enough to eat or drink before dark.

We also measured the average proportion of time the two deer spent interacting continuously over the 12-day

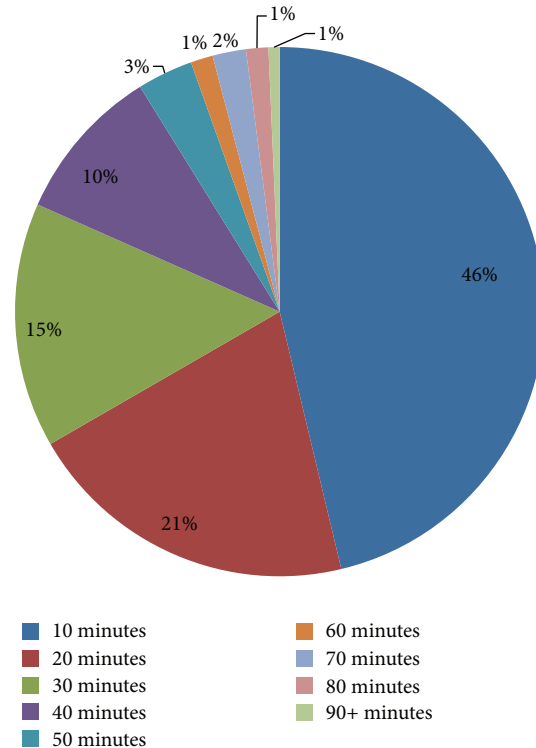


FIGURE 14: Duration of continuous interactions in the same group during the experiment days.

period. Figure 14 shows the average proportion of continuous interaction time between these two deer. Almost half of their total interaction time, 46%, lasted for up to 10 minutes. The majority of the other half (46%) of their interaction time lasted between 10 and 40 minutes: 21% between 10 and 20 minutes, 15% between 20 and 30 minutes, and 10% between 30 and 40 minutes. The remaining 8% of their continuous interaction time lasted from more than 40 minutes to more than 90 minutes. These observations demonstrate the feasibility of sampling free-range animal interactions in a manner that is both fine grained and low powered.

5.1.4. DTN. We have evaluated the functionality of our DTN implementation to measure and record the interactions among the six deer in our experiment. Whenever two deer came within range of each other, our DTN algorithm directly shared the two deer IDs as well as any other interaction data in the RAM table from other deer encounters. Figure 15 illustrates an example of the interaction data that was collected, stored, and shared among the five deer who originated from different deer herds. The circled number near each deer picture indicates the order in which each of the deer interacted with one another and the order in which deer interaction information was shared.

First, deer 3 and 5 interacted with each other and shared their DTN data. Next, deer 1 and 6 interacted with each other and shared their information. Third, deer 4 and 6 interacted and shared their DTN data with each other. This interaction also resulted in deer 4 getting all previous interaction data collected by deer 6, namely, deer 1's contact information.

Fourth, deer 4 and 5 interacted and shared their data with each other. Thus, by this fourth encounter, node 4 had collected and recorded all the DTN interaction data from the 5 "different-herd" deer's previous encounters: from deer 1, 3, 5, and 6. All of deer 4's collected interaction data was equally shared with deer 2, because these two deer originated from the same herd and were in frequent contact with each other throughout the duration of this experiment.

5.1.5. Fault Tolerance. First, we observe that our system exhibited one type of fault tolerance in terms of how it recorded RF-based proximity contacts. Recall that deer 1 and 4 interacted only once for less than one minute. Upon closer inspection, we found that deer 1 did not collect this interaction data. However, deer 4's low-power radio did successfully collect this interaction data. Such an asymmetric interaction could occur for a variety of reasons: the brevity of the interaction such that there was not enough time to exchange both beacons and/or DTN tables; the asymmetry of wireless channels; and the mobility of the animals. Regardless, our system is able to capture the interaction as long as one of the radios is able to hear the other radio.

More importantly, our system was able to recover some location and interaction information from deer 5 even though we were never able to retrieve its collar. Based on our DTN algorithm for sharing interaction data, we were able to recover enough information from other nodes to be able to calculate the possible area in which deer 5 might have been lost. Deer 3 and 4 had recorded interaction data with node 5 in the beginning and the middle of the experiment

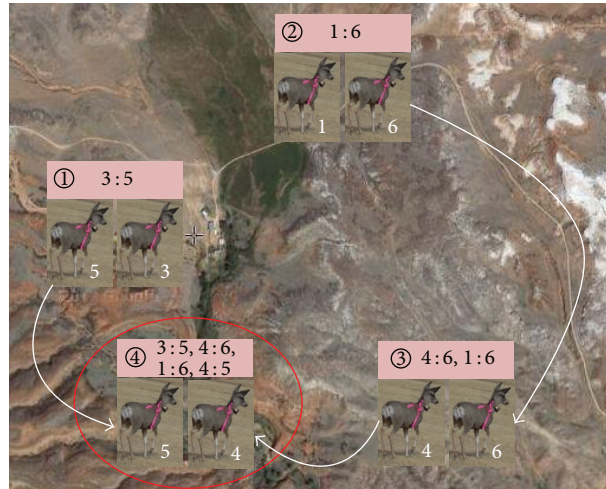


FIGURE 15: Sharing of DTN data among deer originating from different herds.

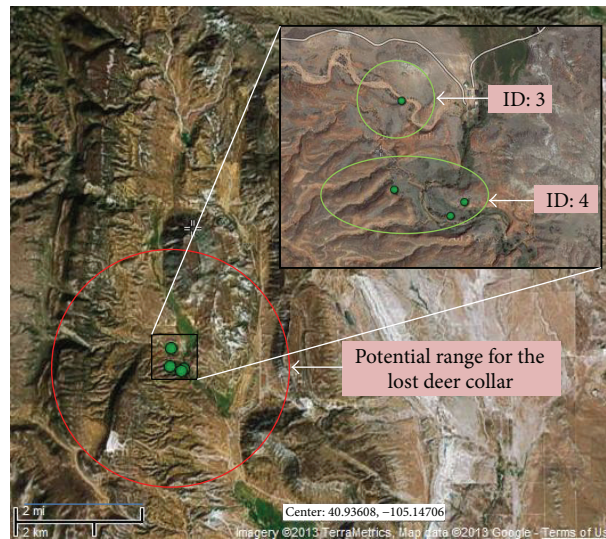


FIGURE 16: Area range of lost deer collar node's possible location.

period. After that time, no further data from deer 5 was collected or recorded. Figure 16 shows four GPS location measurements of deer 5 recorded by deer 3 and 4 at different times. From these measurements, and knowing that deer usually travel within four-square-kilometer region, we can predict the lost collar's potential location area range and map out this area by starting at these GPS coordinates and drawing a 2-kilometer radius circle around these points. The area itself was too rugged to explore to verify this prediction, but this demonstrates the utility of the DTN in recovering otherwise lost data.

A key result from this research experiment was that the DTN algorithm successfully implemented fault tolerance in the wild. Namely, the DTN's sharing of data among nodes that are close enough in proximity to communicate with each other enabled us to collect data from a lost collar that would

otherwise have been unavailable. Our system was able to collect deer 5's interactions through the data shared with deer 2, 3, and 4 (again, see Figure 11).

5.2. Hardware Robustness. As mentioned, we deployed six collars and retrieved five of them. All five retrieved collars functioned and operated flawlessly throughout the 30-day experiment period. Although the area in which we deployed our system experienced considerable snow and wind with temperatures ranging from below zero degree Fahrenheit to about 60 degrees Fahrenheit during the experiment period, all five collars and hardware cases remained intact and protected the MICAz nodes and GPS receivers as well as batteries. No leakage or structural design problems were

encountered. This demonstrates that our hardware was sufficiently robust.

5.3. False Positives and False Negatives. We have analyzed the location and interaction data we collected to detect if there are any false positives or false negatives. For location data, for each deer, we carefully observed each GPS location recorded and constructed a movement path based on the time when those locations were recorded. Since our GPS sampling rate was once every hour, we checked if the distance between any two consecutive locations is reasonable; that is, a deer can generally cover that distance in one hour. For interaction data, we cross-checked each recorded interaction with the location data of the corresponding deer at about the same time when the interaction was recorded. Using this methodology, we did not find any false positives or false negatives in the location data and neither did we find false positives in the interaction data. We could not calculate false negatives in the interaction data, as we do not have any ground truth of all interactions that happened during the experiment. While location data can provide some information about potential interactions, there is no way to verify that those interactions actually happened.

6. Discussion

One feature of WildSense's DTN network that was not exploited in the aforementioned deployment was the ability to extract information in a more timely manner from the DTN even before collars drop from the deer. This would provide scientists with ongoing information as the experiment was progressing, providing closer to real time insights rather than waiting until the end for the collars to drop off. Having ongoing information may be useful to monitor the health and status of deployed collar nodes, so that, for example, new collar nodes could be strategically deployed during the experiment based on intermediate feedback, or the experiment could be modified in middeployment. We could devise a "capture" node that, if deployed close enough to a collar node, would communicate with that collar node and download its DTN table and logged state information to the extent possible. Such a capture node could be mobile, for example, an airborne drone, or could be statically deployed in strategic locations using domain knowledge, for example, a watering hole frequented by the deer. Though we have built software for such a capture node, we have not fully matured this functionality within our DTN system.

The challenges in deploying this DTN system in the wild and retrieving useful data from the deployment were considerable and incurred substantial expense in terms of manpower, time, and funding. As a result, even though we desired to conduct further experiments to improve the amount of data harvested from WildSense, such as by adjusting parameters of the DTN protocol and system or by increasing the duration of the experiment, it was beyond our resources to conduct further deployments in this time frame. We plan to make our software and hardware designs available as open source so such future deployments may benefit from

our work and we are also considering options to transfer the WildSense technology to a commercial company.

7. Conclusions

In this research, we have described in detail how we developed, deployed, and evaluated a new system for monitoring the movement patterns and interaction behaviors of free-range deer in a rugged, wilderness environment. Our system differs from present-day GPS-only collar systems used for monitoring wildlife by incorporating a low-cost low-power RF-radio mote with each collar, thereby enabling sampling that is both fine grained and long lived. We successfully deployed our WildSense system for 30 days in the Soapstone Prairie Natural Area near Livermore, Colorado, on six wild deer. WildSense recorded proximity-based contacts among deer by using the low-power mote-based radios and implemented a delay-tolerant networking (DTN) protocol to exchange contact information among deer collars. Our system was able to report detailed findings regarding deer behavior and social groupings. Further, WildSense demonstrated the fault tolerance property of DTN protocols; namely, through the propagation of contact information among other collar nodes, we were able to retrieve substantial information from a lost collar node.

Competing Interests

The authors declare no competing interests.

Acknowledgments

This work was supported by a grant from the National Science Foundation, IDBR 0754832.

References

- [1] T. W. Grovenburg, J. A. Jenks, R. W. Klaver, C. C. Swanson, C. N. Jacques, and D. Todey, "Seasonal movements and home ranges of white-tailed deer in north-central South Dakota," *Canadian Journal of Zoology*, vol. 87, no. 10, pp. 876–885, 2009.
- [2] G. R. Karns, R. A. Lancia, C. S. DePerno, and M. C. Conner, "Investigation of adult male white-tailed deer excursions outside their home range," *Academic Journal*, vol. 10, pp. 1–39, 2011.
- [3] E. M. Schaubert, C. K. Nielsen, L. J. Kjær, C. W. Anderson, and D. J. Storm, "Social affiliation and contact patterns among white-tailed deer in disparate landscapes: implications for disease transmission," *Journal of Mammalogy*, vol. 96, no. 1, pp. 16–28, 2015.
- [4] Z. Zhang, "Routing in intermittently connected mobile ad hoc networks and delay tolerant networks: overview and challenges," *IEEE Communications Surveys and Tutorials*, vol. 8, no. 1, pp. 24–37, 2006.
- [5] K. Fall and S. Farrell, "DTN: an architectural retrospective," *IEEE Journal on Selected Areas in Communications*, vol. 26, no. 5, pp. 828–836, 2008.
- [6] R. D'Souza and J. Jose, "Routing approaches in delay tolerant networks: a survey," *International Journal of Computer Applications*, vol. 1, pp. 8–14, 2010.

- [7] M. Liu, Y. Yang, and Z. Qin, "A survey of routing protocols and simulations in delay-tolerant networks," in *Wireless Algorithms, Systems, and Applications*, Y. Cheng, D. Y. Eun, Z. Qin, M. Song, and K. Xing, Eds., vol. 6843 of *Lecture Notes in Computer Science*, pp. 243–253, Springer, New York, NY, USA, 2011.
- [8] T. Spyropoulos, K. Psounis, and C. S. Raghavendra, "Spray and wait: an efficient routing scheme for intermittently connected mobile networks," in *Proceedings of the ACM SIGCOMM Workshop on Delay-Tolerant Networking (WDTN '05)*, pp. 252–259, ACM, Philadelphia, Pa, USA, 2005.
- [9] Q. Li, S. Zhu, and G. Cao, "Routing in socially selfish delay tolerant networks," in *Proceedings of the IEEE INFOCOM 2010*, pp. 1–9, IEEE, San Diego, Calif, USA, March 2010.
- [10] B. Pásztor, M. Musolesi, and C. Mascolo, "Opportunistic mobile sensor data collection with SCAR," in *Proceedings of the IEEE International Conference on Mobile Adhoc and Sensor Systems (MASS '07)*, 12, 1 pages, Pisa, Italy, October 2007.
- [11] W. Zhao, M. Ammar, and E. Zegura, "A message ferrying approach for data delivery in sparse mobile ad hoc networks," in *Proceedings of the 5th ACM International Symposium on Mobile Ad Hoc Networking and Computing (MoBiHoc '04)*, pp. 187–198, ACM, Tokyo, Japan, May 2004.
- [12] K. C. Lee, U. Lee, and M. Gerla, "Survey of routing protocols in vehicular ad hoc networks," in *Advances in Vehicular Ad-Hoc Networks: Developments and Challenges*, pp. 149–170, IGI Global, 2010.
- [13] P. Zhang, C. M. Sadler, S. A. Lyon, and M. Martonosi, "Hardware design experiences in ZebraNet," in *Proceedings of the 2nd International Conference on Embedded Networked Sensor Systems (SenSys '04)*, pp. 227–238, ACM, Baltimore, Md, USA, November 2004.
- [14] T. Liu, C. M. Sadler, P. Zhang, and M. Martonosi, "Implementing software on resource-constrained mobile sensors: experiences with Impala and ZebraNet," in *Proceedings of the 2nd International Conference on Mobile Systems, Applications and Services (MobiSys '04)*, pp. 256–269, ACM, Boston, Mass, USA, June 2004.
- [15] P. Juang, H. Oki, Y. Wang, M. Martonosi, L. S. Peh, and D. Rubenstein, "Energy-efficient computing for wildlife tracking: design tradeoffs and early experiences with ZebraNet," *ACM SIGOPS Operating Systems Review*, vol. 36, no. 5, pp. 96–107, 2002.
- [16] Y. Wang, P. Zhang, T. Liu, C. Sadler, and M. Martonosi, "CRAWDAD data set princeton/zebranet (v. 2007-02-14)," 2007, <http://crawdad.cs.dartmouth.edu/princeton/zebranet>.
- [17] T. Wark, W. Hu, P. Sikka et al., "A model-based routing protocol for a mobile, delay tolerant network," in *Proceedings of the 5th International Conference on Embedded Networked Sensor Systems (SenSys '07)*, pp. 421–422, ACM, Sydney, Australia, November 2007.
- [18] M. Rutishauser, V. V. Petkov, J. Boice et al., "CARNIVORE: a disruption-tolerant system for studying wildlife," in *Proceedings of the 19th International Conference on Computer Communications and Networks (ICCCN '10)*, pp. 1–8, IEEE, Zurich, Switzerland, August 2010.
- [19] A. Pentland, R. Fletcher, and A. Hasson, "DakNet: rethinking connectivity in developing nations," *Computer*, vol. 37, no. 1, pp. 78–83, 2004.
- [20] Wizzy Project, http://www.oocities.org/township_transport/courier.html.
- [21] T. V. Prabhakar, S. Nambi, A. U. n et al., "A novel DTN based energy neutral transfer scheme for energy harvested WSN Gateways," *ACM SIGMETRICS Performance Evaluation Review*, vol. 38, no. 3, pp. 71–75, 2011.
- [22] X. Zhang, J. Kurose, B. N. Levine, D. Towsley, and H. Zhang, "Study of a bus-based disruption-tolerant network: mobility modeling and impact on routing," in *Proceedings of the 13th Annual ACM International Conference on Mobile Computing and Networking (MobiCom '07)*, pp. 195–206, New York, NY, USA, 2007.
- [23] J. Su, A. Goel, and E. de Lara, "An empirical evaluation of the student-net delay tolerant network," in *Proceedings of the Annual International Conference on Mobile and Ubiquitous Systems*, pp. 1–10, 2006.
- [24] P. Hui, A. Chaintreau, J. Scott, R. Gass, J. Crowcroft, and C. Diot, "Pocket switched networks and human mobility in conference environments," in *Proceedings of the ACM SIGCOMM Workshop on Delay-Tolerant Networking (WDTN '05)*, pp. 244–251, ACM, Philadelphia, Pa, USA, August 2005.
- [25] R. N. Handcock, D. L. Swain, G. J. Bishop-Hurley et al., "Monitoring animal behaviour and environmental interactions using wireless sensor networks, GPS collars and satellite remote sensing," *Sensors*, vol. 9, no. 5, pp. 3586–3603, 2009.
- [26] P. Sikka, P. Corke, and L. Overs, "Wireless sensor devices for animal tracking and control," in *Proceedings of the 29th Annual IEEE International Conference on Local Computer Networks*, pp. 446–454, IEEE, Tampa, Fla, USA, November 2004.
- [27] Y. Guo, P. Corke, G. Poulton, T. Wark, G. Bishop-Hurley, and D. Swain, "Animal behaviour understanding using wireless sensor networks," in *Proceedings of the 31st Annual IEEE Conference on Local Computer Networks (LCN '06)*, pp. 607–614, Tampa, Fla, USA, November 2006.
- [28] B. Thorstensen, T. Syversen, T. A. Bjørnvold, and T. Walseth, "Electronic shepherd—a low-cost, low-bandwidth, wireless network system," in *Proceedings of the 2nd International Conference on Mobile Systems, Applications, and Services (MobiSys '04)*, pp. 245–255, ACM, Boston, Mass, USA, June 2004.
- [29] V. Dyo, S. A. Ellwood, D. W. MacDonald et al., "Evolution and sustainability of a wildlife monitoring sensor network," in *Proceedings of the 8th ACM International Conference on Embedded Networked Sensor Systems (SenSys '10)*, pp. 127–140, ACM, Zurich, Switzerland, November 2010.
- [30] D. Anthony, W. P. Bennett, M. C. Vuran et al., "Sensing through the continent: towards monitoring migratory birds using cellular sensor networks," in *Proceedings of the ACM/IEEE 11th International Conference on Information Processing in Sensor Networks (IPSN '12)*, pp. 329–340, Beijing, China, April 2012.
- [31] V. R. Jain, R. Bagree, A. Kumar, and P. Ranjan, "wildCENSE: GPS based animal tracking system," in *Proceedings of the International Conference on Intelligent Sensors, Sensor Networks and Information Processing (ISSNIP '08)*, pp. 617–622, Sydney, Australia, December 2008.
- [32] Crossbow MICAz datasheet, <http://www.openautomation.net/uploads/productos/micazdatasheet.pdf>.
- [33] B. Kusy, P. Dutta, P. Levis, M. Maroti, A. Ledeczi, and D. Culler, "Elapsed time on arrival: a simple and versatile primitive for canonical time synchronisation services," *International Journal of Ad Hoc and Ubiquitous Computing*, vol. 1, pp. 239–251, 2006.
- [34] Crossbow MTS420 Sensor Board, <http://tinyos.stanford.edu/tinyos-wiki/index.php/MTS420>.
- [35] Texas instruments TPS61201 Low input voltage synchronous boost converter with 1.3-a switches, 2007, <http://www.ti.com/product/TPS61201>.

- [36] Advanced Telemetry Systems, <https://atstrack.com/>.
- [37] R. A. Garrott, G. C. White, R. M. Bartmann, L. H. Carpenter, and A. W. Alldredge, "Movements of female mule deer in northwest Colorado," *Journal of Wildlife Management*, vol. 51, no. 3, pp. 634–643, 1987.
- [38] P. Beier and D. R. McCullough, "Factors influencing white-tailed deer activity patterns and habitat use," *Wildlife Monographs*, vol. 109, pp. 3–51, 1990.
- [39] K. E. Lagory, "Habitat, group size, and the behaviour of white-tailed deer," *Behaviour*, vol. 98, no. 1, pp. 168–179, 1986.
- [40] Soapstone Prairie Natural Area, 2007, <http://m.fcgov.com/naturalareas/pdf/soapstone-management-plan.pdf>.
- [41] T. Hobbs, "IDBR: WildSense: instrumenting wildlife to gather contact rate information using delay tolerant wireless sensor networks," IACUC Protocol 11-2503A, 2011.

Research Article

Measurement of Circumferential Liquid Film Based on LIF and Virtual Stereo Vision Sensor

Ting Xue, Xiaokang Lin, and Liuxiangzi Yang

College of Electrical Engineering and Automation, Tianjin University, Tianjin 300072, China

Correspondence should be addressed to Ting Xue; xueting@tju.edu.cn

Received 27 May 2016; Revised 25 July 2016; Accepted 26 July 2016

Academic Editor: Lei Yuan

Copyright © 2016 Ting Xue et al. This is an open access article distributed under the Creative Commons Attribution License, which permits unrestricted use, distribution, and reproduction in any medium, provided the original work is properly cited.

Gas-liquid annular flow is widely used in many industrial applications such as petroleum, chemical, and nuclear engineering. The feature parameters of liquid film in the annular flow are of great significance to understand the flow characteristics and measure the flow precisely. For the annular flow, the circumferential features of liquid film are more important than the axial features to acquire abundant flow structures and reveal the flow mechanism. In the paper, a measurement platform based on the laser-induced fluorescence (LIF) and virtual stereo vision sensor is presented. The virtual stereo vision sensor comprises a high-speed camera and two optical reflection sets, which can acquire the liquid film from two views simultaneously and reconstruct the features of liquid film. Image processing techniques are proceeded with to extract the feature parameters of liquid film; then the circumferential flow characteristic can be reconstructed by views transformation and fusion. The flow characteristic based on the thickness distribution is analysed. The experimental results show that the method is valid and effective, which can give a more detailed and accurate description for the liquid film in annular flows.

1. Introduction

The annular flow is one of the important flow patterns in gas-liquid two-phase flow. The flow pattern is characterized by the presence of a thin liquid film flowing along the wall of the tube and surrounding a fast-moving gas core. The core may bring the entrainment of liquid droplets at the high gas velocity, and the flow rate of the gas and liquid phase can vary a lot in the annular flow. Due to the low power consumption, high coefficient of mass transfer, and heat flux density, gas-liquid annular flow is widely used in many industrial applications such as petroleum, chemical, and nuclear engineering and wet natural gas transportation. Due to high quality of the exchange efficiency, the flow pattern is widely used in various industrial productions. The feature parameters of liquid film in the annular flow are of great significance to understand the flow mechanism precisely [1].

The characteristic parameters of annular flow include the thickness of the liquid film, wave velocity, wave height, and shear force, and the liquid film thickness is the basic and most important parameter to be measured accurately [2]. There are many methods that have been developed to investigate

the liquid film in gas-liquid annular flow. Among the various detection sensors, the measurement methods are generally divided into the contact techniques and the noncontact techniques. Han et al. [3] used a parallel wire probe to collect the film thickness time-trace measurements in a small vertical pipe. The method based on the conductance measurement of the liquid film thickness is simple and reliable, but it only can achieve a single local point measurement and may interfere with the flow field. Then many sensors are developed to achieve the multiple points measurement [4–7]. Based on the circumferential array of conductance probes, Andreussi et al. [8] measured the thickness distribution around the pipe wall of a liquid layer flowing in near horizontal pipes. Belt et al. [9] developed a nonintrusive conductivity-based technique to measure the film thickness at 32 positions around the circumference and 10 positions in the axial direction. Mouza et al. [10] measured the time-averaged and instantaneous local film thickness in flowing liquid based on the absorption of light passing through a layer of dyed liquid and the sensitive light detection sensor. Recently, Han et al. [11] measured the averaged annular liquid film thickness by laser confocal displacement meter (LCDM). Based on the digital image

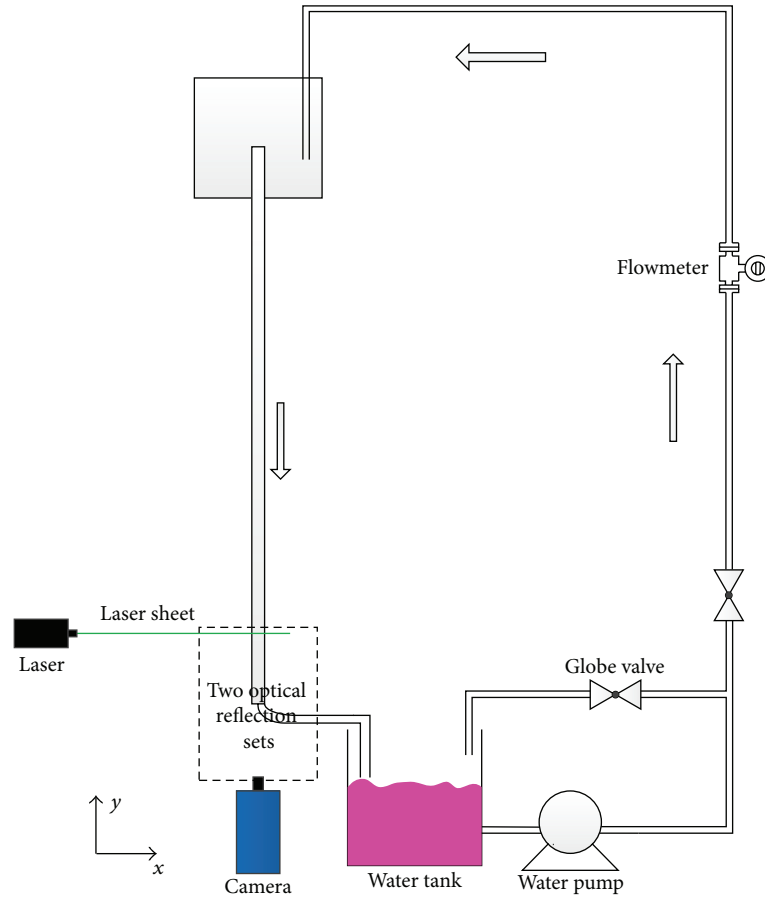


FIGURE 1: Experimental flow loop.

processing and planar laser-induced fluorescence (PLIF) technique, the target images taken by the high-speed camera can be quite a contrast to the background. Alekseenko et al. [12] studied the wavy structure of liquid film in downward annular gas-liquid flow with LIF technique, and the liquid film thickness measurements are resolved in the longitudinal based on the brightness model. Based on the PLIF technique, Kokomoor and Schubring [13] developed a nonintrusive optical technique to provide the film thickness distribution by data reduction algorithms. Zadrazil and Markides [14] studied experimentally the hydrodynamics of downwards gas-liquid annular flows and falling films in a pipe based on the PLIF and Particle Image Velocimetry (PIV). For the annular flow, the cross-sectional images of the liquid film are more important than the longitudinal images to reveal the unsymmetrical flow characteristic of interfacial wave and flow mechanism, especially under high pressure, but the circumferential measurement is also more difficult to achieve. Generally, the two cameras can be employed to observe the liquid film of the cross section in the two different views and reconstruct the circumferential images.

The paper aims to reconstruct the circumferential liquid film of vertical air-water annular flow and extract the characteristic parameter of the liquid film thickness based on the laser-induced fluorescence (LIF) and virtual stereo

vision sensor. The virtual stereo vision sensor comprises a high-speed camera and two optical reflection sets, which can acquire the liquid film from two views simultaneously and reconstruct the multiple features of liquid film. A series of image processing techniques are also proceeded with, and the circumferential flow characteristics are reconstructed by views transformation and fusion to analyse the flow characteristic based on the thickness distribution.

The paper is organized as follows: Section 2 introduces the experimental flow loop and develops a virtual stereo vision sensor to achieve the cross-sectional views of liquid film. Section 3 describes the image processing and the feature parameter measurement of the liquid film. In Section 4, we present validation of the liquid film measurement result and the analysis, which is followed by a final conclusion in Section 5.

2. Experimental Facility

2.1. Flow Loop. Figure 1 shows a schematic view of the test section to measure the annular liquid film on the cross section of the test pipe. The test and connection pipe was fabricated from Plexiglass and installed vertically. Water was pumped into the upper tank through a pump and then fell downwards into a 25 mm diameter and 5 mm thickness test pipe to

form annular flow. The flow rate of water was controlled by the globe valves and measured by the electromagnetic flow meter with $\pm 0.5\%$ measurement uncertainty. The virtual stereo vision sensor was fixed at the lower end of the pipe and perpendicular to the x - y plane to measure the fully developed falling films. In the experiment, a high-speed camera of Weinberger MiniVis E2 series coupled with a 35 mm lens of Nikkor was used. To achieve the instantaneous liquid film on the whole cross section, the high-speed camera is set at a resolution of 960×720 pixels at the frame rate of 500 Hz.

Due to the monochrome, directivity, high intensity, and high measurement resolution and accuracy, the laser is widely used for many optical diagnoses. In the paper, the planar laser-induced fluorescence technique (LIF) is employed to provide time-resolved images of the liquid film in vertical annular air-water flows. Rhodamine B was dissolved in the flow field as the fluorescent agent based on their specific molecular structure. The laser (NanoLine, Canada) with the wavelength of 532 nm projects a laser sheet to irradiate the cross section of the test pipe and stimulate the Rhodamine B fluorescence. Then the high speed camera captured the fluorescence signal of liquid film and processed by a series image processing.

2.2. Virtual Stereo Vision Sensor. The measurement scheme of liquid film based on the virtual stereo vision sensor is shown in Figure 2. The optical centre of camera overlaps the central axis of the pipe, and the laser sheet is perpendicular to the optical axis of the camera. A virtual stereo vision sensor is composed of a high-speed camera and two optical reflection sets, and the two optical reflection sets are between the camera and the pipe. Xue et al. [15] developed a virtual binocular stereo vision system to reconstruct the three-dimensional morphological parameters and track the bubbles in the bubbly flow. In the paper, it is optimized to view nearly half of cross-sectional liquid film rather than the same point on the two views according to the mathematical model and lots of stimulations.

The virtual binocular stereo vision sensor is employed to capture the two-dimensional images of the liquid film in the left and right image plane of the camera at the same time. The camera is reflected by the reflection mirror group, which can be mirrored to two virtual cameras C_{2L} and C_{2R} . The two virtual cameras are symmetrical with each other, and there is an optimized angle between the virtual and the real cameras based on the effective FOV (Field of View) and spatial resolution. Therefore, the high-speed camera can view the circumferential liquid film from the two directions. When the images are captured by a single high-speed camera containing the two parts of cross-sectional liquid film, they can be processed by a series of digital image processing and reconstructed as a complete cross-sectional liquid film image.

In the virtual stereo vision sensor, there are two important angle parameters, which are the angle α of the centre mirror and the vertical distance from the optical centre and the angle γ between the centre mirror and the same side refraction mirror group. The angle α is optimized by 45° and γ is 20° eventually. Taking the left optical path as an example, the

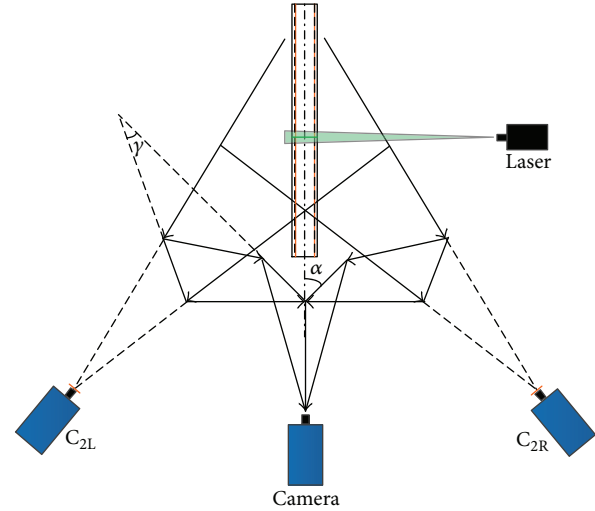


FIGURE 2: Schematic illustration of the virtual stereo vision.

measured object is reflected by the centre mirror and the left reflection mirror, and the angle of the virtual image of the measured object in the vertical direction is 40° , the same as the right side of the optical reflection set.

3. Image Processing

A series of image processing and reconstruction procedures should be developed to extract the feature parameters of liquid film based on the virtual stereo vision sensor.

3.1. Circumferential Images Processing Based on Virtual Stereo Vision Sensor. A typical instantaneous original image of liquid film captured by the virtual stereo vision sensor is shown in Figure 3(a). Simultaneously, the background image is captured in the absence of water cycle, and the image gray is proceeded with for the original and background image, respectively, and followed by the image subtraction, which can remove the noise due to the ambient light and the defects of the flow pipe effectively. Figure 3(b) shows the anticoloured image after median filter, which uses a 3×3 template to remove the single-pixel noise and maintain the edge of liquid film. We can see that there are two ring sectors in the left part of Figure 3(b). The bigger sector represents the left cross-sectional film, while the smaller one is the right cross-sectional film, which overlaps the refraction distortion of left cross-sectional film and the pipe wall and is discarded for the characteristics extraction.

According to the analysis of the virtual stereo vision sensor in Section 2.2, the circumferential liquid film of the pipe was viewed from a certain angle, and it is necessary to proceed with the 40° projection transformation to simplify the subsequent fusion and reconstruction. The binarized image after projection transformation can be seen in Figure 3(c). Due to the effect of pipe refraction, the liquid film is not the standard semicircle and a calibration should be performed to form an instantaneous cross section image of liquid film. In order to reconstruct the cross-sectional liquid

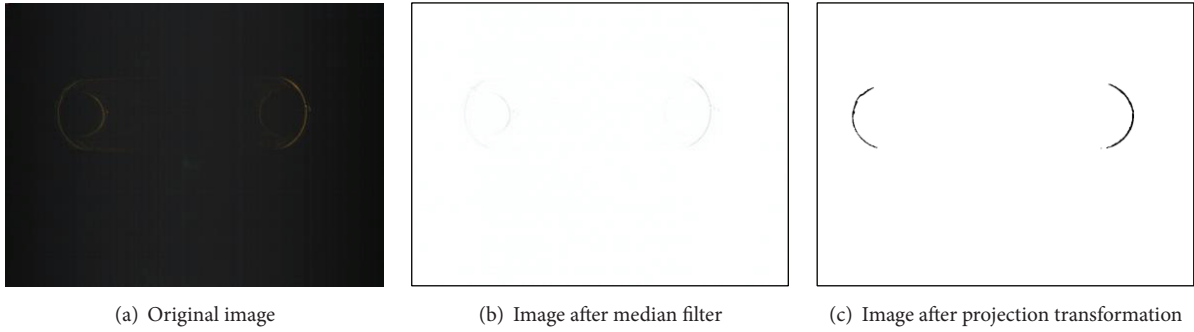


FIGURE 3: Circumferential image processing, (b) and (c) are anticoloured.

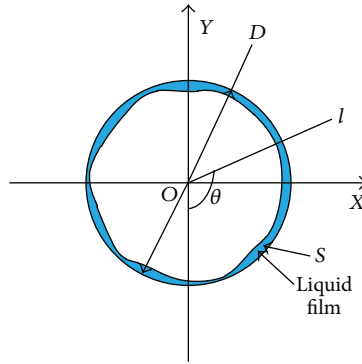


FIGURE 4: Liquid film thickness extraction.

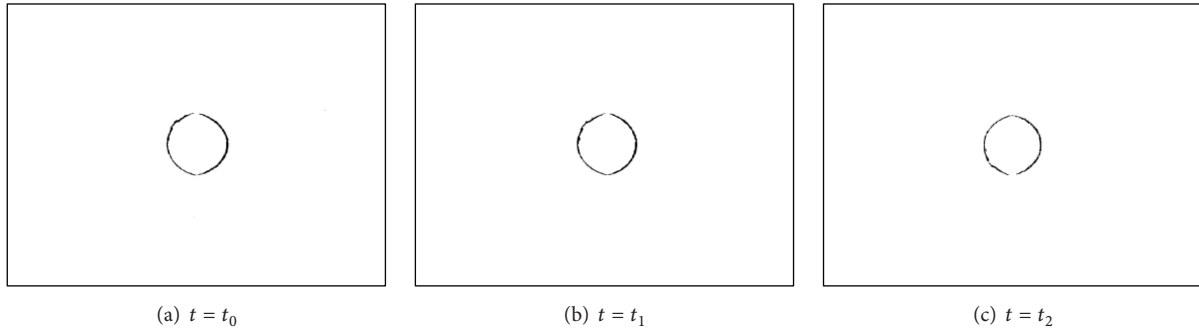


FIGURE 5: Reconstructed image sequence, (a)–(c) are anticoloured.

film, the centre position of the calibration target should be recorded, which is a guide to reconstruct the two sectors of the liquid film and obtain a whole annular cross section, as shown in Figure 5.

3.2. Characteristic Parameter Extraction. The characteristic parameters of the liquid film can be extracted based on the above reconstructed images. Figure 4 shows the extraction scheme of the liquid film thickness. The centre of the annular liquid film is denoted as the origin of the coordinate system O , the angle between the line l and the negative Y -axis is defined as θ , and D is the inner diameter of the pipe, that is, the average outer circle diameter in the reconstructed images. With the change of θ , the equation of the line l is transformed.

The liquid film thickness at the l direction can be extracted based on a resolution of 0.154 mm/pixel. Therefore, the circumferential distribution of the film thickness can be extracted. The circumferential average thickness of liquid film can be given as follows:

$$\delta = k \left(\frac{D}{2} - \sqrt{\left(\frac{D}{2}\right)^2 - \frac{S}{\pi}} \right), \quad (1)$$

where δ is measured thickness in millimetres, k is calibration parameter, relating the pixel coordinate in image plane and the real distance, and S is the area of the circumferential liquid film in the reconstructed image with the unit of pixel.

4. Results and Analysis

All the experiments were performed with the 25 mm inner diameter downward pipe, which is described in Section 2. Cross-sectional views of the liquid film are captured at 500 Hz, and the image exposure time is about 2 ms. According to a series of image processing and feature parameters extraction, the high-quality instantaneous images of the liquid film can be reconstructed and are available for analysis.

Figure 5 shows three samples of the reconstructed liquid film images at different time. The average film thickness of the image sequence is 0.55 mm, 0.53 mm, and 0.427 mm, respectively. The selected image sequence shows that the annular flow is stable, and the liquid film has a little fluctuation and similar circumferential distribution.

5. Conclusions

In the paper, an optical technique based on the laser-induced fluorescence (LIF) and virtual stereo vision sensor is presented to measure the circumferential liquid film in annular flow. The laser-induced fluorescence was applied to separate the intensity of the liquid film in and out of the experimental cross section. A virtual stereo vision sensor is developed to capture the fluorescence image of the whole cross-sectional liquid film. Particularly a series of image processing is developed to extract the feature parameters of liquid film and reconstruct the annular liquid film images. The quantitative thickness features of liquid film are analysed, and the experimental results show that the method is valid and effective, which can give a more detailed characterization of the liquid film to reveal the flow structures and flow mechanism.

Competing Interests

The authors declare that they have no competing interests.

Acknowledgments

The authors gratefully acknowledge the support by the National Natural Science Foundation of China (60902084, 61372143).

References

- [1] M. J. Da Silva, T. Sühnel, E. Schleicher, R. Vaibar, D. Lucas, and U. Hampel, "Planar array sensor for high-speed component distribution imaging in fluid flow applications," *Sensors*, vol. 7, no. 10, pp. 2430–2445, 2007.
- [2] M. Damsohn and H.-M. Prasser, "High-speed liquid film sensor for two-phase flows with high spatial resolution based on electrical conductance," *Flow Measurement and Instrumentation*, vol. 20, no. 1, pp. 1–14, 2009.
- [3] H. W. Han, Z. F. Zhu, and K. Gabriel, "A study on the effect of gas flow rate on the wave characteristics in two-phase gas-liquid annular flow," *Nuclear Engineering and Design*, vol. 236, no. 24, pp. 2580–2588, 2006.
- [4] S. Thiele, M. J. Da Silva, and U. Hampel, "Capacitance planar array sensor for fast multiphase flow imaging," *IEEE Sensors Journal*, vol. 9, no. 5, pp. 533–540, 2009.
- [5] M. Demori, V. Ferrari, D. Strazza, and P. Poesio, "A capacitive sensor system for the analysis of two-phase flows of oil and conductive water," *Sensors and Actuators A: Physical*, vol. 163, no. 1, pp. 172–179, 2010.
- [6] X. Hu and W. Yang, "Planar capacitive sensors—designs and applications," *Sensor Review*, vol. 30, no. 1, pp. 24–39, 2010.
- [7] D. Schubring, T. A. Shedd, and E. T. Hurlburt, "Studying disturbance waves in vertical annular flow with high-speed video," *International Journal of Multiphase Flow*, vol. 36, no. 5, pp. 385–396, 2010.
- [8] P. Andreussi, E. Pitton, P. Ciandri et al., "Measurement of liquid film distribution in near-horizontal pipes with an array of wire probes," *Flow Measurement and Instrumentation*, vol. 47, pp. 71–82, 2016.
- [9] R. J. Belt, J. M. C. Van't Westende, H. M. Prasser, and L. M. Portela, "Time and spatially resolved measurements of interfacial waves in vertical annular flow," *International Journal of Multiphase Flow*, vol. 36, no. 7, pp. 570–587, 2010.
- [10] A. A. Mouza, N. A. Vlachos, S. V. Paras, and A. J. Karabelas, "Measurement of liquid film thickness using a laser light absorption method," *Experiments in Fluids*, vol. 28, no. 4, pp. 355–359, 2000.
- [11] Y. Han, H. Kanno, Y.-J. Ahn, and N. Shikazono, "Measurement of liquid film thickness in micro tube annular flow," *International Journal of Multiphase Flow*, vol. 73, pp. 264–274, 2015.
- [12] S. V. Alekseenko, A. V. Cherdantsev, O. M. Heinz, S. M. Kharlamov, and D. M. Markovich, "Analysis of spatial and temporal evolution of disturbance waves and ripples in annular gas-liquid flow," *International Journal of Multiphase Flow*, vol. 67, pp. 122–134, 2014.
- [13] W. Kokomoor and D. Schubring, "Improved visualization algorithms for vertical annular flow," *Journal of Visualization*, vol. 17, no. 1, pp. 77–86, 2014.
- [14] I. Zadrazil and C. N. Markides, "An experimental characterization of liquid films in downwards co-current gas-liquid annular flow by particle image and tracking velocimetry," *International Journal of Multiphase Flow*, vol. 67, pp. 42–53, 2014.
- [15] T. Xue, L. Qu, Z. Cao, and T. Zhang, "Three-dimensional feature parameters measurement of bubbles in gas-liquid two-phase flow based on virtual stereo vision," *Flow Measurement and Instrumentation*, vol. 27, no. 10, pp. 29–36, 2012.

Research Article

Research on Application of Wax Deposition Detection in the Nonmetallic Pipeline Based on Electrical Capacitance Tomography

Nan Li,^{1,2} Kui Liu,² Xiangdong Yang,³ and Mingchen Cao²

¹School of Automation, Northwestern Polytechnical University, Xi'an 710071, China

²Beijing Engineering Research Center of Precision Measurement Technology and Instruments, Beijing University of Technology, Beijing 100124, China

³Quality Department, BAIC MOTOR, Beijing 101300, China

Correspondence should be addressed to Nan Li; nan.li@hotmail.co.uk

Received 22 April 2016; Revised 17 June 2016; Accepted 3 July 2016

Academic Editor: Lei Yuan

Copyright © 2016 Nan Li et al. This is an open access article distributed under the Creative Commons Attribution License, which permits unrestricted use, distribution, and reproduction in any medium, provided the original work is properly cited.

Wax deposition detection in nonmetallic pipelines is an important requirement in the oil industry. In this paper, an ECT (electrical capacitance tomography) sensor is developed for wax deposition detection in nonmetallic pipelines. Four wax models with different concentrations were established for detection. These models were analyzed through simulations and practical experiments simultaneously and data were compared. A linear back projection algorithm is applied to reconstruct the image with both simulated and experimental data. A comparison of binary images with different concentration of stratified flow was demonstrated; this illustrates that the difference in concentration between the experimental results and profile distribution is less than 1.2%. The experimental results indicate that the ECT system is valid and feasible for detecting the degree of wax deposition in the nonmetallic pipelines.

1. Introduction

Heat and pressure are widely used in oil and gas pipeline transmission to reduce the viscosity of crude oil and the deposition of wax. However, due to difference in radial temperature, radiation loss occurs rapidly. The wax is gradually separated out and deposited on the pipe wall, which can lead to condensate tube accidents [1]. The situation is more serious in China, as the crude oil produced in China has several distinguishing characteristics, such as high waxy distillate and low temperature viscosity. Therefore, it is important and necessary to develop a technique that can detect the deposition degree of wax inside the pipe. With consideration to the operating environment of the pipeline, as well as the cost of detection, for practical application, nondestructive-based techniques are highly recommended. Many nondestructive techniques have achieved some degree of success in the pipeline detection field, for instance, the eddy current testing method [2, 3], ultrasonic-based technique [4–10],

radiological image method [11], and magnetic flux leakage detection method [12–14]. However, most of these techniques are applied to detect pipeline defects, and it is difficult to detect the sediment (i.e., paraffin wax) of the pipeline by using the above technologies, due to various reasons.

The detection of wax deposition in the pipeline is essentially a multiphase detection, which is composed of the wax layer, oil layer, and gas. ECT (electrical capacitance tomography) is a visual procession from measurement capacitance to object distribution. The method is a noninvasive and nondestructive technique. An ECT sensor is a typical “soft” field sensor, which means that the Electromagnetic (EM) field propagates across the entire probed volume, as shown in Figure 1. The measurement at the volume surface depends on the values of the measured quantity everywhere in the volume.

The related research began in the 1980s at the University of Manchester and, from hardware, image construction algorithms to sensor design has made considerable progress

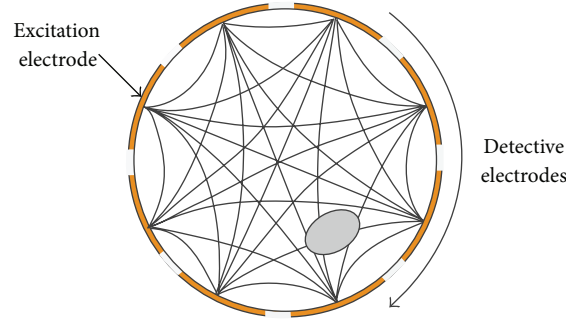


FIGURE 1: Schematic diagram of the “soft” field.

[15–21]. Johansen et al. developed a dual sensor system consisting of an 8-electrode ECT sensor and γ -ray sensor. The new system was applied to reconstruct the image of oil-gas-water three-phase flow [22]. Dyakowski et al., based on this sensor structure, presented an image reconstruction algorithm, which can be used to evaluate the concentration of a measured cross-section [23]. Schmitz and Mewes applied the ECT to the chemical industry, and the system was used to detect the transient multiphase flow in bubble columns [24]. In 2010, Yang introduced an application that used an ECT sensor to analyze the drying, pellets, and coating process of pharmaceutical fluidized beds [25]. Ismail et al. applied the ECT to the oil and gas separation process in the oil industry to determine the concentration and flow rate of each stage [26]. Al Hosani et al. suggested to use a narrowband pass filter to enhance the resolution of the produced images; the experimental results indicated that the method can improve the resolution of reconstruction images [27].

Sensor optimization is an important part of the ECT system. Xie et al. presented a uniformity of sensitivity distribution as an evaluation criterion to determine the performance of the ECT sensor [28]. Peng et al. analyzed the influence of electrode length on sensitivity distribution of the ECT sensor. The results showed that the electrode length of the ECT sensor should be at least equal to the width of the sensor electrode [29]. In 2012, Peng et al. discussed the influence of the number of the ECT sensor electrodes on the quality of image reconstruction and recommended that the number of electrodes be 12 [30]. Ren et al. presented a new algorithm to reconstruct the three-dimensional inclusion shapes; the method is valid and effective [31].

The purpose of the present paper is to develop an ECT system for wax deposition detection of a nonmetallic pipeline. The optimal sensor structure is determined based on our previous research [32]. An ECT system is demonstrated in the experimental part, and the feasibility of the system is verified based on a comparison of the reconstructed images according to simulation and experimental results.

2. Methodology

2.1. Wax Models. In the long-range transportation process, the temperature of the crude oil decreases and wax deposition

occurs due to the thermal radiation. The permittivity of wax is 1.9~2.5. The wax is deposited on the inner wall of the pipeline, and the structure could be simplified as a stratified flow pattern in a laboratory environment. A series of wax deposition models is built and the cross-sections are shown in Figure 2. Note that the last model of Figure 2 is a special model, namely, heteromorphous flow. In order to further clarify the different structures of the wax, u is defined as concentration. Note that (1) is valid for 2D problems:

$$u = \frac{A_{\text{wax}}}{A_0} \times 100\%, \quad (1)$$

where A_{wax} is the area of wax and A_0 refers to the area of sensing area, that is, the cross-section of the pipeline.

2.2. Setup of Measurement System. The ECT sensor electrodes consist of copper, and earthed shielding plates are placed around the sensor electrodes. The measurement system and the sensor structure are shown in Figure 3.

The shielding wire and BNC joints are used to prevent interference. In this study, the pipe consists of PVC material. The end guarding plate consists of copper, and the earthed shielding plate consists of aluminum. According to our previous research [32], the parameters of the ECT sensor are determined as listed in Table 1: N is the number of electrodes; W refers to the central angle of the electrodes; and r_1 , r_2 , and r_3 are the radii of the pipe's interior and exterior and the radius of the earthed shielding plate, respectively. L_{plate} represents the length of the sensor electrodes. The width of the end guarding plate is L_{end} , and the distance between the end guarding plate and sensor electrode is defined as L_{gap} .

3. Results and Discussion

The practical stratified models are shown in Figure 4, and the concentrations u of the deposited wax are 11%, 18.5%, 52.2%, and 62.5%, respectively. In order to calibrate the measurement results, two more situations should be considered, namely, those for an empty pipe and a pipe full of wax. Moreover, simulation and practical experiments are processed and analyzed simultaneously, presented, respectively, as C_{sim} and C_m . The results are listed in Table 2. The simulation model is 3D model; FEM (finite element method) is used to analyze the

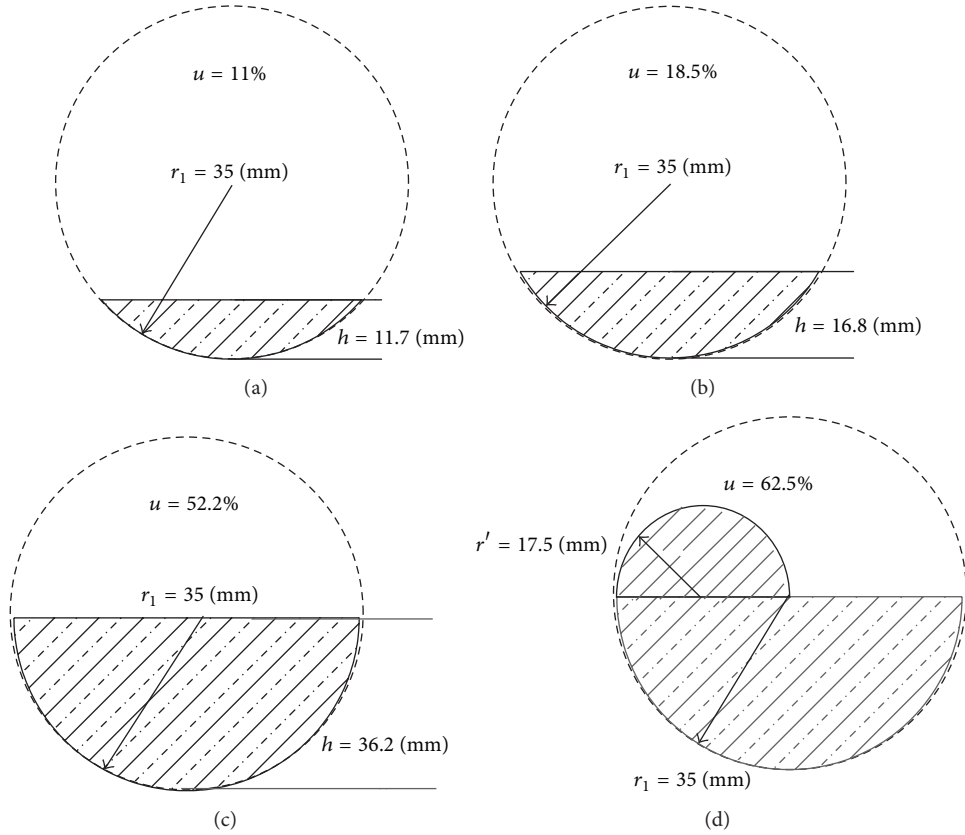


FIGURE 2: Different thicknesses of wax deposition models. (a) Concentration is 11%. (b) Concentration is 18.5%. (c) Concentration is 52.2%. (d) Concentration is 62.5% (note: the last one is special stratified flow–heteromorphous flow).

TABLE 1: Parameters of the sensor.

	Sensor electrodes			Pipeline		Earthed shielding plate	End guarding plate	
Materials	Copper			PVC		Aluminum	Copper	
Parameters	N	W	L_{plate}	r_1	r_2	r_3	L_{end}	L_{gap}
	6	15°	105 mm	35 mm	40 mm	50 mm	20 mm	10 mm

sensitivity distribution. The conditions of simulation models are the same as practical models. However, because the electrostatic module is applied, the frequency of excitation is not considered during simulation.

In order to illustrate the comparison results more intuitively, the normalized capacitances are calculated according to (2), and the results are shown in Figure 5. Consider

$$\text{nor}C = \frac{(C_m - C_l)}{(C_h - C_l)}, \quad (2)$$

where $\text{nor}C$ is the normalized value and C_l and C_h are measured capacitance filled with low dielectric constant and high permittivity materials, respectively. For example, in this study C_l is the capacitance when the pipe is empty, and C_h is the capacitance when the pipe is full of wax.

According to Figure 5, the following can be derived. The same tendencies for the measurement results from the simulation and experiments are observed. For regular stratified flow patterns, the difference of the two curves decreases with the increase of concentration u , as shown in Figures 5(a)–5(c). The reason for this comes from two aspects: (i) the sensitivity distribution of the ECT sensor which was nonuniform; the sensitivity close to the sensor electrodes was much higher than that in the center of the sensing area; (ii) the inaccurate forward modeling or the noise in measurements. Note that the difference of the two curves increases in Figure 5(d) compared with Figure 5(c), the reason for which is that a heteromorphous model affects the measurement results.

In order to examine the effects of the design factors, it was necessary to perform the image reconstructions. Large numbers of algorithms have been developed to derive

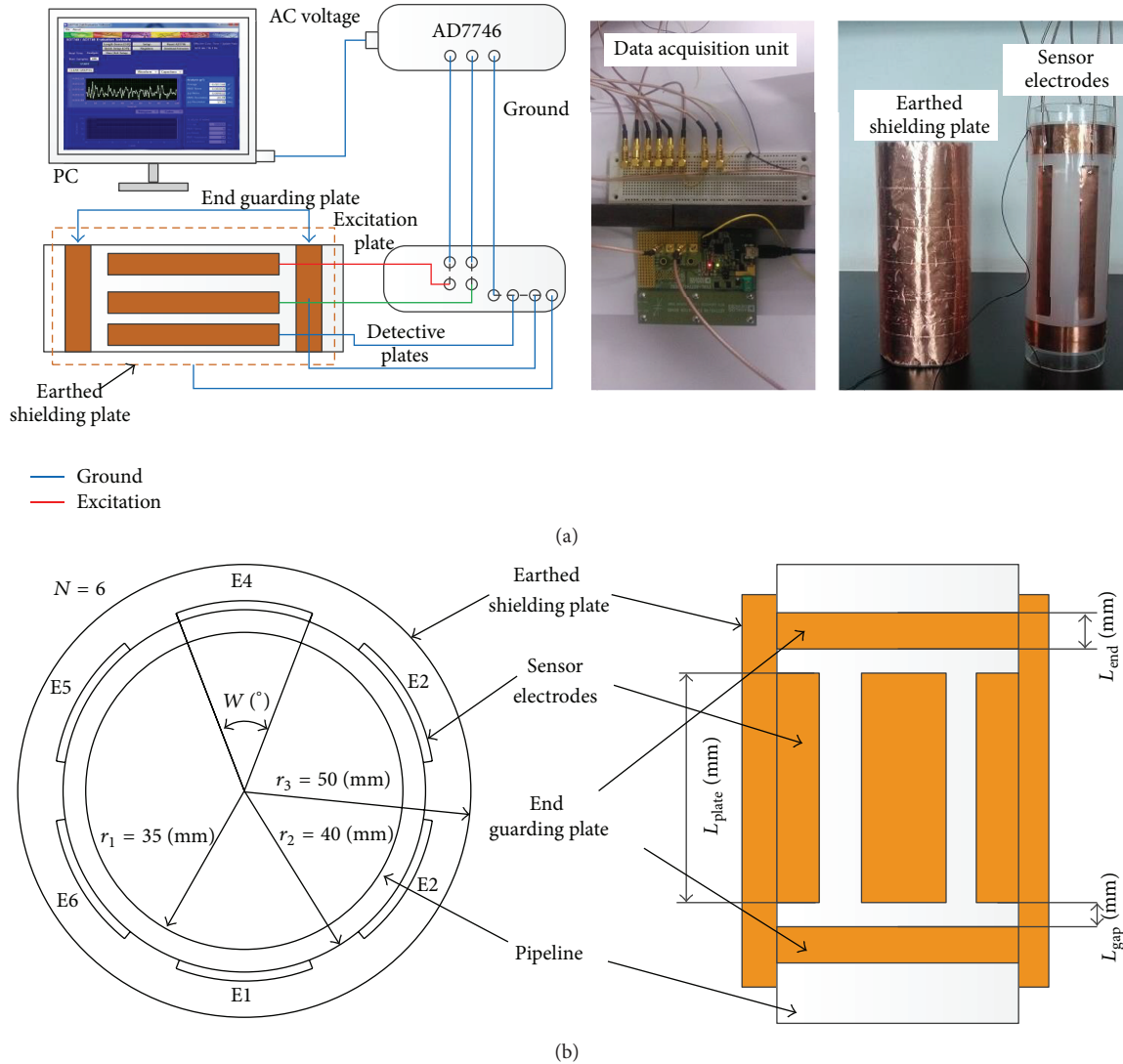


FIGURE 3: ECT system and sensor structure. (a) Diagram of measurement system and practical ECT sensor. (b) Parameters of the ECT sensor.

reconstructed images over the past several decades, such as linear back projection (LBP), Landweber iteration, and the sparsity-inspired image reconstruction method. In [19], Yang and Peng have analyzed the characterizations of five image reconstruction algorithms and three criteria were used to evaluate the performance of reconstructed images:

- (1) relative image error,
- (2) relative capacitance residual,
- (3) correlation coefficient between the test object and the reconstruction.

Consider

$$\text{Image error} = \left\| \frac{\hat{g} - g}{g} \right\|,$$

$$\text{Capacitance residual} = \frac{\|\lambda - S \cdot \hat{g}\|}{\|\lambda\|},$$

Correlation coefficient

$$= \frac{\sum_{i=1}^N (\hat{g}_i - \bar{\hat{g}})(g_i - \bar{g})}{\sqrt{\sum_{i=1}^N (\hat{g}_i - \bar{\hat{g}})^2 \sum_{i=1}^N (g_i - \bar{g})^2}}, \quad (3)$$

where g is the true permittivity distribution of the test object, \hat{g} is the reconstructed permittivity distribution, and \bar{g} and $\bar{\hat{g}}$ are the mean values of g and \hat{g} , respectively. λ is the normalized capacitance vector, S represents the normalized sensitivity matrix, and N refers to the number of pixels. According to [19], the image error and correlation coefficient of LBP are better than SVD and Tikhonov and worse than Iterative Tikhonov method. The capacitance residual of LBP is similar to Iterative Tikhonov and Projected Landweber, but worse than SVD and Tikhonov methods. Due to the fact

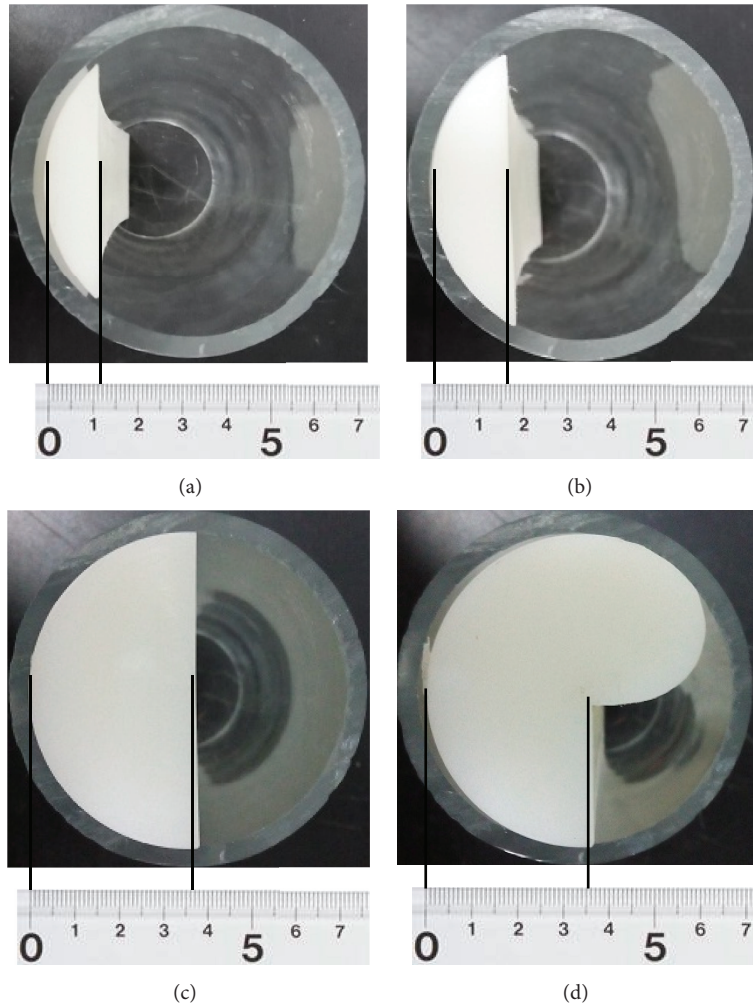


FIGURE 4: Practical models of stratified flow wax. (a) Concentration is 11%. (b) Concentration is 18.5%. (c) Concentration is 52.2%. (d) Concentration is 62.5%.

TABLE 2: Comparison of simulation results with experimental results.

Flow patterns		Empty [fF]		Full wax [fF]		Stratified flow (a) [fF]		Stratified flow (b) [fF]		Stratified flow (c) [fF]		Stratified flow (d) [fF]	
u		0%		100%		11%		18.5%		52.2%		62.5%	
C_{ij}		C_{sim}	C_m	C_{sim}	C_m	C_{sim}	C_m	C_{sim}	C_m	C_{sim}	C_m	C_{sim}	C_m
1	2	300.9	288.3	419.8	382.3	380.0	335.6	427.6	350.5	448.9	383.0	444.8	385.3
1	3	45.9	47.7	100.9	100.7	56.0	53.2	58.7	56.8	72.1	71.2	70.2	71.4
1	4	30.8	30.5	70.3	69.3	37.2	35.8	39.0	37.1	42.7	42.7	45.8	50.4
1	5	45.3	44.7	99.7	85.3	55.1	44.7	58.4	47.6	71.4	60.8	96.4	90.5
1	6	298.0	264.1	416.5	351.4	376.0	317.7	430.4	335.0	445.3	358.0	432.0	346.6
2	3	304.4	307.5	424.4	405.8	300.6	301.1	300.3	297.0	343.7	331.1	340.3	338.3
2	4	45.2	48.7	99.4	100.8	43.1	47.6	44.7	48.1	56.8	59.2	57.0	66.1
2	5	30.9	29.1	70.7	68.7	29.0	29.1	31.0	32.4	45.8	44.2	62.9	72.4
2	6	45.1	46.6	99.3	99.1	48.3	60.2	68.0	77.3	116.0	110.5	111.9	104.3
3	4	298.1	297.0	416.4	397.5	296.8	294.5	295.6	295.6	280.2	285.3	281.3	274.8
3	5	45.3	44.3	99.5	96.6	43.9	43.2	42.5	43.5	38.3	38.4	47.9	62.4
3	6	30.7	30.4	70.2	67.7	29.0	30.7	31.1	33.0	45.8	47.0	47.1	45.7
4	5	300.4	295.9	419.6	390.3	299.6	296.7	298.7	284.9	288.1	285.9	291.7	334.8
4	6	45.2	41.5	99.5	90.4	43.6	41.0	45.2	42.7	57.9	54.4	69.9	72.1
5	6	298.6	171.5	417.2	268.7	296.9	168.4	298.7	173.2	340.3	209.1	397.1	273.4

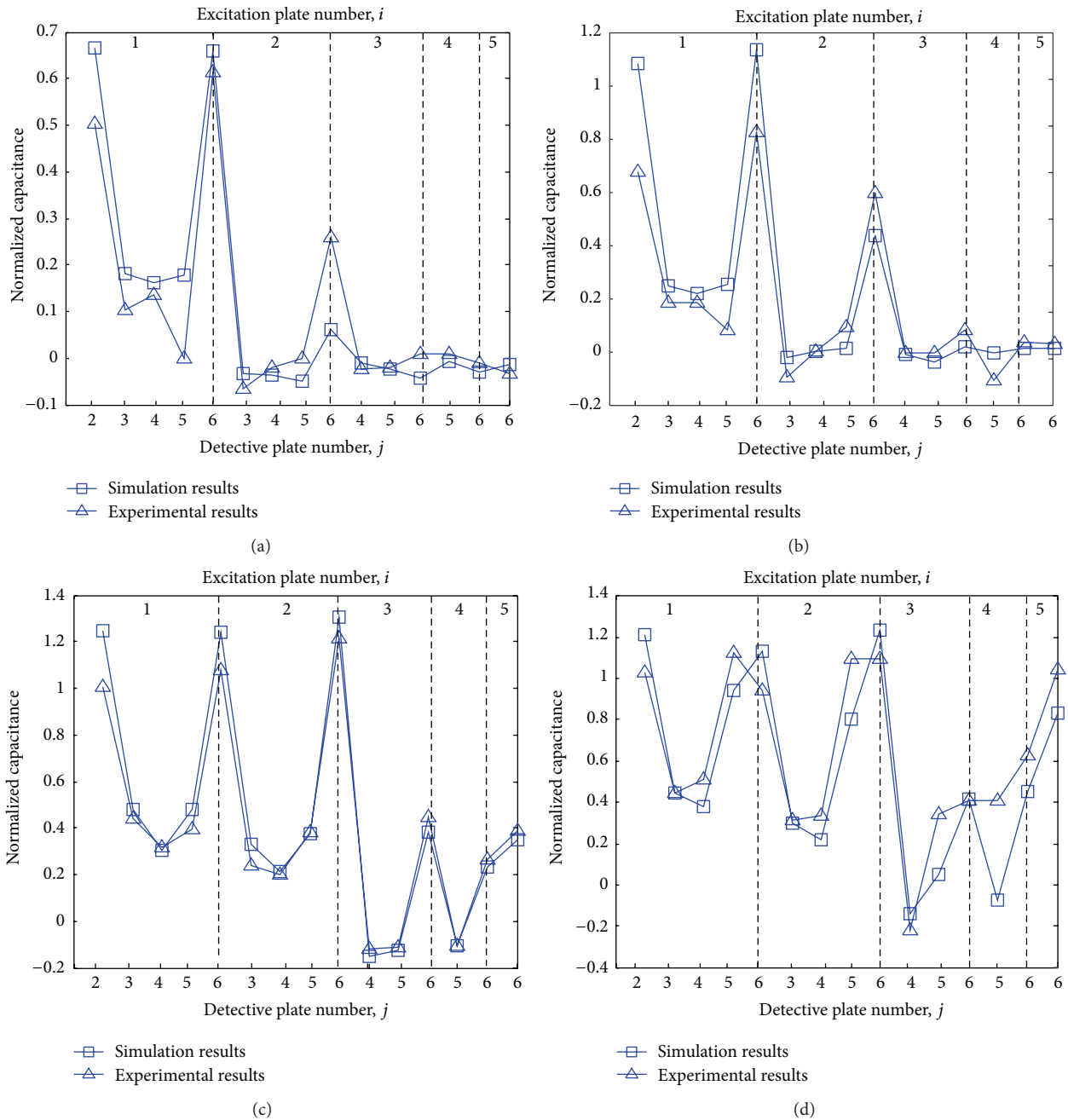


FIGURE 5: Normalized capacitance trend analysis. (a) Concentration is 11%. (b) Concentration is 18.5%. (c) Concentration is 52.2%. (d) Concentration is 62.5%.

that noniterative algorithms are typically used in practical applications and that the time consumption is less than in iterative algorithms, in order to simplify the comparison, the LBP algorithm is used to reconstruct the image [32]. Moreover, the LBP method is more suitable than iterative algorithms for dealing with stratified flow patterns. The reconstructed images are shown in Figure 6. Note that the images are based on the normalized data of the simulation and experiment data, separately. Figure 6(a) is a series of reconstructed images based on the simulation results, and

Figure 6(b) is a series of reconstructed images based on the experimental results.

The imaging results of the experiments are consistent with the reconstructed images of the simulations, which signifies that the designed ECT system is valid and feasible. For different concentrations of the wax, the reconstructed images are varied. Especially for the heteromorphous flow pattern, the shape of the semicircular convex is difficult to identify. The boundary of the heteromorphous flow pattern is difficult to determine, and the stratified flow resembles an

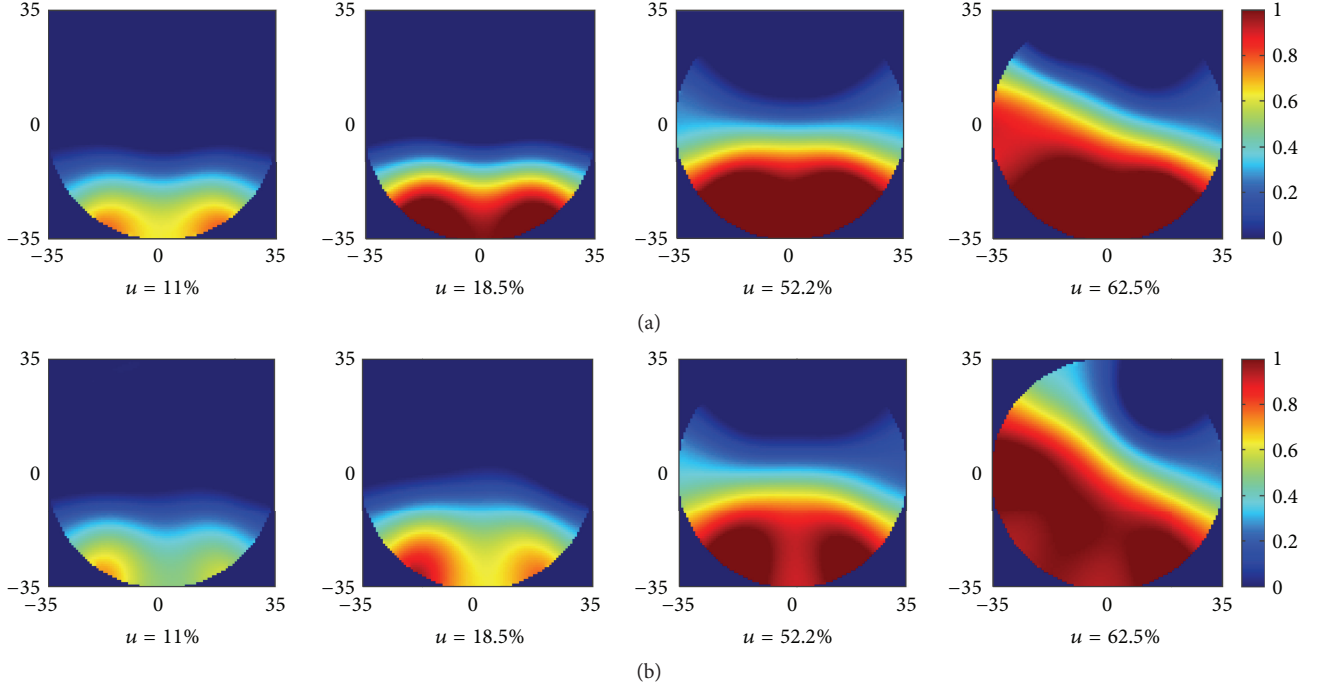


FIGURE 6: Different concentrations of stratified flow image results. (a) Simulation results. (b) Experimental results.

inclined plane. According to [19, 21], this issue could be solved in terms of two aspects, namely, algorithm improvement and ECT sensor optimization. In order to evaluate the validation of using reconstructed images to identify the concentration of the wax, threshold processing was completed, and binary images of different concentrations of stratified flow are presented and compared with the standard models. The threshold processing is based on adaptive threshold filtering method which was presented by Xie et al. [33] as shown in Figure 7.

In Figure 7, β_m is the initial concentration, which can be determined via a nonthreshold imaging results and experience. In this study, we define $\beta_m = N(G_s(e_k)_{\max})/N(G_s(e_k))$, where N is the number of pixels, G_s represents standard binary image, $N(G_s(e_k)_{\max})$ refers to the number of pixels whose value is 1 in standard binary image, and $N(G_s(e_k))$ represents the total number of pixels in standard binary image. The concentration increment $\Delta\beta = |\beta_t - \beta_m|$ and the initial value is set to 0, where $\beta_t = N(G_{\text{new}}(e_k)_{\max})/N(G_{\text{new}}(e_k))$; $N(G_{\text{new}}(e_k)_{\max})$ represents number of pixels whose value is 1 in processed image and $N(G_{\text{new}}(e_k))$ represents the total number of pixels in processed image. T_r refers to threshold, and ΔT is the threshold increment whose initial value is set to 0. Taking the flow chart as an example, each iteration step increment is 0.0005; steps can be corrected according to the actual operation. Threshold is determined by the following equation:

$$T_r = G_{\min} + \Delta T (G_{\max} - G_{\min}). \quad (4)$$

TABLE 3: Contrast between standard images and reconstructed images.

	Model 1	Model 2	Model 3	Model 4
Concentration of standard images	11%	18.5%	52.5%	62.5%
Concentration of reconstructed images	12.2%	19.2%	52.97%	62.9%
Correlation coefficient	93.79%	92.78%	98.01%	87.04%

The threshold value takes the minimum pixel value as a reference; the increment is the product of pixel value difference and threshold increment. In this paper, the threshold values are 0.705, 0.78, 0.38, and 0.395, respectively, for the four reconstructed images.

The binary images of different concentrations of stratified flows are shown in Figure 8, and the concentrations and correlation coefficients are listed in Table 3. The difference of concentrations between the standard models and reconstructed images is less than 1.2%, which indicates the validation of the ECT system. However, the definition of concentration is the ratio of wax deposition to the total sensing cross-section. It may be improper to evaluate the quality of reconstructed image. Therefore, the correlation coefficients of different models are listed in Table 3.

As we can see from Table 3, when concentration is 52.5% (model 3), the correlation coefficient is the best (98.01%).

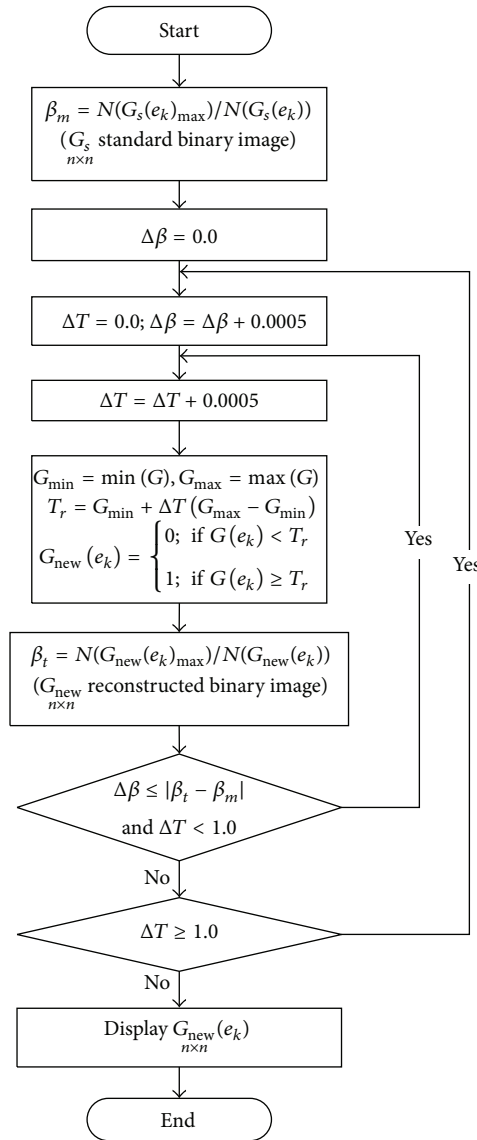


FIGURE 7: Flowchart of the linear back projection threshold processing method.

When the concentration is 11% and 18.5% (model 1 and model 2), the correlation coefficients are similar to each other and the quality of images is acceptable. However, when the concentration is 62.5% (model 4), the correlation coefficient is the worst (87.04%). The main reason is the limitation of the LBP algorithm which is not good at imaging of heteromorphous flow, especially for edge imaging.

4. Conclusions

For wax deposition detection in nonmetallic pipelines, the use of an ECT sensor was demonstrated. LBP algorithm was applied to reconstruct images. Four models were tested, and the reconstructed images showed that the sensor is feasible. However, due to the limitations of the algorithm, it was

difficult to identify the special stratified model. The boundary of the heteromorphous flow pattern was recognized as an incline in the reconstructed images. For the concentrations of 11%, 18.5%, 52.5%, and 62.5%, the differences between the profile and reconstructed image were 1.2%, 0.7%, 0.47%, and 0.4%, respectively. The correlation coefficients between standard images and reconstructed images were 93.79%, 92.78%, 98.01%, and 87.04%, separately. This proves that the system designed in this paper can be applied to wax deposition detection of nonmetallic pipelines.

Competing Interests

The authors declare that there is no conflict of interests regarding the publication of this paper.

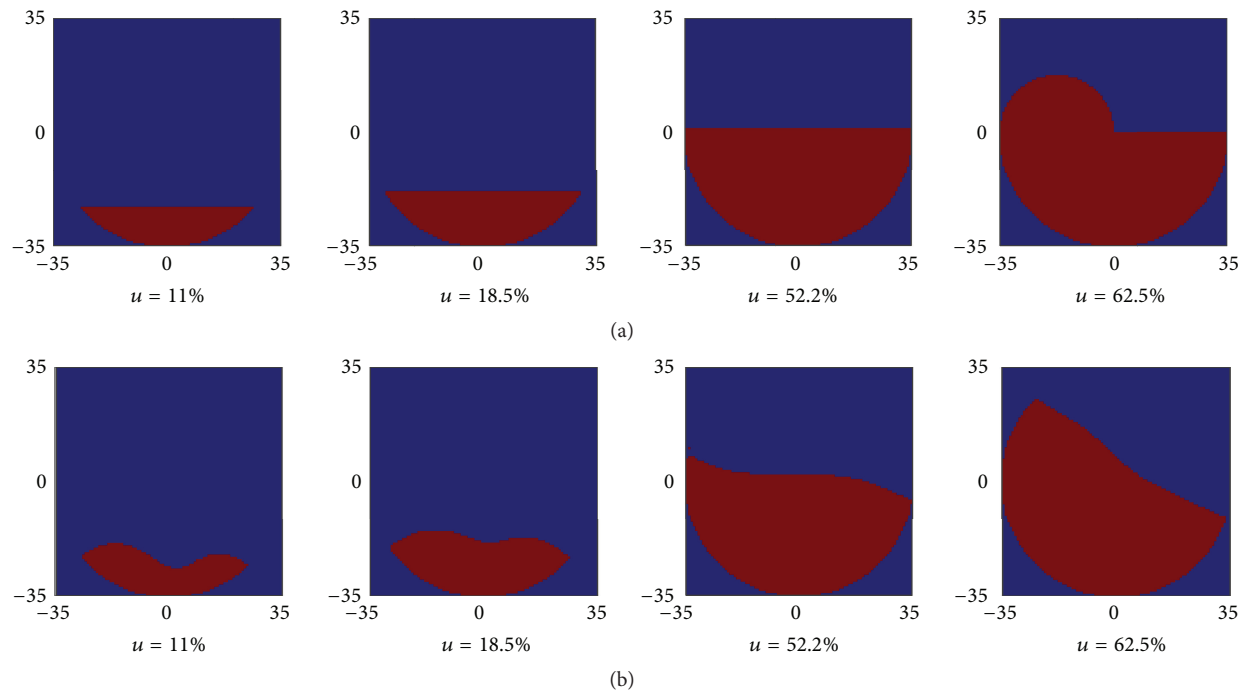


FIGURE 8: Binary images of different concentrations of stratified flow. (a) Profile distribution. (b) Threshold processing image based on experimental data.

Acknowledgments

This work is financially supported by the National Natural Science Foundation of China (Grants nos. 51475013, 51505013, and 51405381).

References

- [1] E. D. Burger, T. K. Perkins, and J. H. Striegler, "Studies of wax deposition in the trans Alaska pipeline," *Journal of Petroleum Technology*, vol. 33, no. 6, pp. 1075–1086, 1981.
- [2] B. Bouttier, Y. Gourbeyre, M. Hassine, J. C. Potier, and P. Bréant, "Evaluation of an intrusive technology to diagnose buried pipelines," *Water Science and Technology: Water Supply*, vol. 14, no. 5, pp. 931–937, 2014.
- [3] C. S. Angani, D. G. Park, C. G. Kim, P. Leela, P. Kollu, and Y. M. Cheong, "The pulsed eddy current differential probe to detect a thickness variation in an insulated stainless steel," *Journal of Nondestructive Evaluation*, vol. 29, no. 4, pp. 248–252, 2010.
- [4] G. P. P. Gunarathne and R. W. Keatch, "Novel techniques for monitoring and enhancing dissolution of mineral deposits in petroleum pipelines," *Ultrasonics*, vol. 34, no. 2–5, pp. 411–419, 1996.
- [5] J.-W. Cheng, S.-K. Yang, and S.-M. Chiu, "The use of guided waves for detecting discontinuities in fluid-filled pipes," *Materials Evaluation*, vol. 65, no. 11, pp. 1129–1134, 2007.
- [6] S. Shire, J. Quarini, and R. S. Ayala, "Ultrasonic detection of slurry ice flows," *Proceedings of the Institution of Mechanical Engineers, Part E: Journal of Process Mechanical Engineering*, vol. 219, no. 3, pp. 217–225, 2005.
- [7] Z. Wu, S. Ma, Y. Chen, and Y. Wang, "Detection and identification of dents in pipelines using guided waves," *Materials Evaluation*, vol. 74, no. 1, pp. 79–89, 2016.
- [8] G. T. Yim and T. G. Leighton, "Real-time on-line ultrasonic monitoring for bubbles in ceramic 'slip' in pottery pipelines," *Ultrasonics*, vol. 50, no. 1, pp. 60–67, 2010.
- [9] Y. Lu, C. He, G. Song, B. Wu, C.-H. Chung, and Y.-C. Lee, "Fabrication of broadband poly(vinylidene difluoride-trifluoroethylene) line-focus ultrasonic transducers for surface acoustic wave measurements of anisotropy of a (1 0 0) silicon wafer," *Ultrasonics*, vol. 54, no. 1, pp. 296–304, 2014.
- [10] L. Yan, H. Cunfu, S. Guorong, W. Bin, C.-H. Chung, and Y.-C. Lee, "Elastic properties inversion of an isotropic plate by hybrid particle swarm-based-simulated annealing optimization technique from leaky lamb wave measurements using acoustic microscopy," *Journal of Nondestructive Evaluation*, vol. 33, no. 4, pp. 651–662, 2014.
- [11] D. Xiao, G. Zhang, Y. Liu et al., "3D detection and extraction of bladder tumors via MR virtual cystoscopy," *International Journal of Computer Assisted Radiology and Surgery*, vol. 11, no. 1, pp. 89–97, 2016.
- [12] M. Ricci, A. Ficola, M. L. Fravolini et al., "Magnetic imaging and machine vision NDT for the on-line inspection of stainless steel strips," *Measurement Science and Technology*, vol. 24, no. 2, Article ID 025401, 2013.
- [13] Y. Shi, C. Zhang, R. Li, M. Cai, and G. Jia, "Theory and application of magnetic flux leakage pipeline detection," *Sensors*, vol. 15, no. 12, pp. 31036–31055, 2015.
- [14] R. Wagner, O. Goncalves, A. Demma, and M. Lowe, "Guided wave testing performance studies: comparison with ultrasonic and magnetic flux leakage pigs," *Insight*, vol. 55, no. 4, pp. 187–196, 2013.
- [15] S. M. Huang, A. B. Plaskowski, C. G. Xie, and M. S. Beck, "Tomographic imaging of two-component flow using capacitance sensors," *Journal of Physics E: Scientific Instruments*, vol. 22, no. 3, pp. 173–177, 1989.

- [16] C. G. Xie, A. L. Stott, S. M. Huang, A. Plaskowski, and M. S. Beck, "Mass-flow measurement of solids using electrodynamic and capacitance transducers," *Journal of Physics E: Scientific Instruments*, vol. 22, no. 9, pp. 712–719, 1989.
- [17] H. Wang, W. Yin, W. Q. Yang, and M. S. Beck, "Optimum design of segmented capacitance sensing array for multi-phase interface measurement," *Measurement Science and Technology*, vol. 7, no. 1, pp. 79–86, 1996.
- [18] W. Q. Yang, "Modelling of capacitance tomography sensors," *IEE Proceedings—Science, Measurement and Technology*, vol. 144, no. 5, pp. 203–208, 1997.
- [19] W. Q. Yang and L. Peng, "Image reconstruction algorithms for electrical capacitance tomography," *Measurement Science and Technology*, vol. 14, no. 1, pp. R1–R13, 2003.
- [20] Y. Li and W. Q. Yang, "Virtual electrical capacitance tomography sensor," *Journal of Physics: Conference Series*, vol. 15, no. 1, pp. 183–188, 2005.
- [21] W. Q. Yang, "Design of electrical capacitance tomography sensors," *Measurement Science and Technology*, vol. 21, no. 4, Article ID 042001, 2010.
- [22] G. A. Johansen, T. Frøystein, B. T. Hjertaker, and Ø. Olsen, "A dual sensor flow imaging tomographic system," *Measurement Science and Technology*, vol. 7, no. 3, pp. 297–307, 1996.
- [23] T. Dyakowski, G. A. Johansen, B. T. Hjertaker, D. Sankowski, V. Mosorov, and J. Włodarczyk, "A dual modality tomography system for imaging gas/solids flows," *Particle & Particle Systems Characterization*, vol. 23, no. 3-4, pp. 260–265, 2006.
- [24] D. Schmitz and D. Mewes, "Tomographic imaging of transient multiphase flow in bubble columns," *Chemical Engineering Journal*, vol. 77, no. 1-2, pp. 99–104, 2000.
- [25] W. Yang, "Imaging pharmaceutical fluidised beds by electrical capacitance tomography," in *Proceedings of the IEEE International Conference on Imaging Systems and Techniques (IST '10)*, pp. 52–56, Thessaloniki, Greece, July 2010.
- [26] I. Ismail, J. C. Gamio, S. F. A. Bukhari, and W. Q. Yang, "Tomography for multi-phase flow measurement in the oil industry," *Flow Measurement and Instrumentation*, vol. 16, no. 2-3, pp. 145–155, 2005.
- [27] E. Al Hosani, M. Zhang, and M. Soleimani, "A limited region electrical capacitance tomography for detection of deposits in pipelines," *IEEE Sensors Journal*, vol. 15, no. 11, pp. 6089–6099, 2015.
- [28] C. G. Xie, A. L. Stott, A. Plaskowski, and M. S. Beck, "Design of capacitance electrodes for concentration measurement of two-phase flow," *Measurement Science and Technology*, vol. 1, no. 1, pp. 65–78, 1990.
- [29] L. Peng, C. Mou, D. Yao, B. Zhang, and D. Xiao, "Determination of the optimal axial length of the electrode in an electrical capacitance tomography sensor," *Flow Measurement and Instrumentation*, vol. 16, no. 2-3, pp. 169–175, 2005.
- [30] L. Peng, J. Ye, G. Lu, and W. Yang, "Evaluation of effect of number of electrodes in ECT sensors on image quality," *IEEE Sensors Journal*, vol. 12, no. 5, pp. 1554–1565, 2012.
- [31] S. Ren, Y. Xu, C. Tan, and F. Dong, "Reconstructing the geometric configuration of three dimensional interface using electrical capacitance tomography," *International Journal for Numerical Methods in Engineering*, vol. 96, no. 10, pp. 628–644, 2013.
- [32] N. Li, X. Yang, Y. Gong, and P. Wang, "Enhancing electrical capacitance tomographic sensor design using fuzzy theory based quantifiers," *Measurement Science and Technology*, vol. 25, no. 12, Article ID 125401, 2014.
- [33] C. G. Xie, A. Plaskowski, and M. S. Beck, "8-electrode capacitance system for two-component flow identification. part 1: tomographic flow imaging," *IEE Proceedings A: Physical Science, Measurement and Instrumentation, Management and Education. Reviews*, vol. 1, pp. 173–183, 1992.

Research Article

Compressed Sensing, Pseudodictionary-Based, Superresolution Reconstruction

Chun-mei Li,^{1,2} Ka-zhong Deng,¹ Jiu-yun Sun,¹ and Hui Wang¹

¹School of Environment Science and Spatial Informatics, China University of Mining and Technology, Xuzhou, Jiangsu 221116, China

²School of Geodesy and Geomatics of Jiangsu Normal University, Xuzhou, Jiangsu 221116, China

Correspondence should be addressed to Ka-zhong Deng; kzdeng@cumt.edu.cn

Received 5 April 2016; Revised 28 June 2016; Accepted 10 July 2016

Academic Editor: Yinan Zhang

Copyright © 2016 Chun-mei Li et al. This is an open access article distributed under the Creative Commons Attribution License, which permits unrestricted use, distribution, and reproduction in any medium, provided the original work is properly cited.

The spatial resolution of digital images is the critical factor that affects photogrammetry precision. Single-frame, superresolution, image reconstruction is a typical underdetermined, inverse problem. To solve this type of problem, a compressive, sensing, pseudodictionary-based, superresolution reconstruction method is proposed in this study. The proposed method achieves pseudodictionary learning with an available low-resolution image and uses the K -SVD algorithm, which is based on the sparse characteristics of the digital image. Then, the sparse representation coefficient of the low-resolution image is obtained by solving the norm of l_0 minimization problem, and the sparse coefficient and high-resolution pseudodictionary are used to reconstruct image tiles with high resolution. Finally, single-frame-image superresolution reconstruction is achieved. The proposed method is applied to photogrammetric images, and the experimental results indicate that the proposed method effectively increase image resolution, increase image information content, and achieve superresolution reconstruction. The reconstructed results are better than those obtained from traditional interpolation methods in aspect of visual effects and quantitative indicators.

1. Introduction

High-quality images are required for high-precision measurements, and their spatial resolution is the key indicator in the assessment of digital image quality; an image with a higher spatial resolution contains more information content. The level of image detail has a decisive role in absolute photogrammetry precision and the range of applications for which a given image can be used. However, limited by flight condition and cost as well as optical diffraction, certain difficulties exist in directly acquiring high-resolution images. To satisfy the demand of image resolution using single-frame-photogrammetry of local geospatial data, superresolution image reconstruction was investigated in this study.

There are two types of single-frame-image, superresolution reconstruction methods: interpolation and learning. Traditional interpolation methods achieve high resolutions using an interpolation kernel function and include methods such as the nearest neighbor, bilinear interpolation, bicubic interpolation, and spline function methods. Scholars later

proposed edge-oriented interpolation methods. For example, Jensen and Anastassiou [1] improved visual effects by template-fitting after image edge detection; Carey et al. [2] proposed a wavelet-based interpolation method; and Chang et al. [3] used a wavelet transform to describe edge points, infer extreme point coefficients at finer scales, and reconstruct high-resolution images. Li and Orchard [4] also proposed an edge-guide interpolation algorithm based on the least squares method, where the edge feature of an interpolated image was maintained based on the edge-guide feature of the adaptive covariance. Zhou et al. [5] proposed a multisurface fitting-based interpolation algorithm that could increase the edge clarity of an interpolated image; that algorithm had good robustness against noise. The interpolation method is simple and applicable to many situations; however, it lacks prior information, can only enhance image visual effects, and typically has difficulty in recovering high-frequency information that is lost in low-resolution images, producing blurred reconstructed images.

Learning-based superresolution reconstruction is achieved by establishing corresponding relationships between high- and low-resolution images using prior information. The example-based superresolution method proposed by Freeman et al. [6] obtained prior information between high- and low-resolution images via Markov random field learning; this type of method achieved excellent reconstruction results in human-facial [7] and word-processing applications. The sparse-representation-based SR algorithm proposed by Yang et al. [8] used the sparse characteristics of natural images and linear programming to solve for the sparse representation of the low-resolution images and then combined the obtained representation coefficient with a high-resolution dictionary to create high-resolution image tiles. Dong et al. [9] proposed an image interpolation algorithm based on a nonlocal autoregression model under the framework of sparse representation. This method used similar image blocks that were common in natural images to construct a nonlocal autoregression model; it then used self-similarity in the image structure as additional information to reconstruct high-resolution images.

The premise of the learning method is to obtain prior knowledge of the high-resolution images. Studies typically start with existing images, produce corresponding low-resolution images via blurring and downsampling, and then use a reconstruction algorithm to approximate the original images. The reconstructed images typically do not exhibit substantial improvements in image quality or resolution. Although the amount of information in the interpolated, superresolution, image reconstruction did not increase, the resolution can be increased markedly. Due to the limitations of traditional reconstruction methods, this study uses the local, geometrically consistent, spatial relationship between the interpolated and original images; organically combines the interpolation and learning methods; and proposes a compressed sensing, pseudodictionary-based, superresolution reconstruction method.

2. Method and Model

The proposed method treats an existing image as a low-resolution image, uses bicubic interpolation images as guides, and creates a joint dictionary for image training based on the sparse characteristics of digital images by requiring that the high- and low-resolution images have the same sparse representation in the corresponding high- and low-resolution dictionary. Then, the related rule between the high- and low-resolution images is applied to the bicubic interpolation image, and the optimization problem is solved using compressed sensing theory. The proposed method can effectively retrieve more detailed high-frequency information while producing a superresolution image.

2.1. Training Sample Extraction and Pseudodictionary Learning. The goal of the superresolution reconstruction of a single-frame image is to restore a given low-resolution image to a high-resolution image of the same scenery. To resolve this ill-posed problem, the requirement of a consistent

observation model for high- and low-resolution images must be satisfied [10]. Based on the digital imaging mechanism, the low-resolution image can be obtained by sampling the high-resolution image, and the observation model can be expressed as follows:

$$y_l^i = Bsy_h^i + v = Ly_h^i + v, \quad (1)$$

where B and s describe the blurring and downsampling operations on the image, respectively; v is the Gaussian noise; y_h^i and y_l^i are the high- and low-resolution images, respectively; and the approximation image \hat{y}_h^i of the original high-resolution image can be reconstructed by processing y_l^i . To avoid complexity induced by the differences in the high- and low-resolutions of the images, the low-resolution image is upsampled to the same dimension as the high-resolution image via interpolation, thus obtaining high- and low-resolution image sample sets $\{y_{dl}^i\}$ and $\{y_h^i\}$, respectively.

The preprocessing of the samples is first performed after the construction of the training samples. Because the images' structural characteristics are primarily represented in the high-frequency range, the image interpolation value $e_h^i = y_h^i - y_{dl}^i$ is used as the high-frequency information of the high-resolution image. The preprocessing of the low-resolution image is performed by a convolution integral of degree K on the geometric structure components; the characteristic vector components are combined to form the characteristic vector of the low-resolution image. Finally, the characteristic vectors of the high- and low-resolution images at the same position are formed into a training sample data pair $P = \{p_l^k, p_h^k\}$.

The compressed sensing, pseudodictionary-based, superresolution reconstruction problem requires the simultaneous use of an over-defined dictionary pair A_h and A_l of the high- and low-resolution image tiles. Because the pair belongs to a heterogeneous data type, the following equation must be solved for the training data to have the same sparse representation in both dictionaries [11]:

$$\min_{A_l, A_h, s} \sum_i (\|y_l - A_l s_i\|_2^2 + \lambda_0 \|y_h - A_h s_i\|_2^2 + \lambda \|s_i\|_0), \quad (2)$$

where A_h and A_l are the high- and low-resolution image tile dictionaries, respectively; s_i is the sparse coefficient that simultaneously satisfies y_h in dictionary A_h and y_l in dictionary A_l ; and λ_0 and λ are the regularization parameters of the second and third terms, respectively. The joint dictionary receives the correlation between the high- and low-resolution training samples in full consideration, and learning is required to use prior knowledge of the high-resolution image to effectively guide the superresolution reconstruction of other low-resolution images. This study uses the K -SVD method [12] to solve an over-defined dictionary.

2.2. Mathematical Model of Compressed Sensing. The other key element in superresolution reconstruction is to reconstruct the low-resolution dictionary's sparse representation with respect to the low-resolution image tiles. Compressed sensing is a new theory in the field of signal processing.

N dimensional signal $X \in R^n$ can be expressed by the superposition of a set of orthonormal basis as follows [13, 14]:

$$X = \Psi S. \quad (3)$$

If S has only k nonzero elements or k elements that are far greater than other points, then the signal X is called k sparse signal, where $k \leq N$, and Ψ is the sparse domain of X . The sampling process of compressed sensing is achieved using a sensing matrix Φ that is not correlated to the basis [13]:

$$Y = \Phi X = \Phi \Psi S = AS, \quad (4)$$

where $Y = (Y_1, Y_2, \dots, Y_M)^T$ is an M -dimensional sample matrix, $M \ll N$, and $A = [A_1, A_2, \dots, A_M]$ is the sensing matrix, which is also called the sparse dictionary.

Signal reconstruction is the core of compressed sensing. For a k sparse signal X , the sparse coefficient S can be reversely derived with a high probability from the M -dimensional observation value Y and the k -sparsity constraint condition when the sensing matrix satisfies the isometric condition. The original signal X can then be restored with a high probability based on the reversibility of the orthogonal transformation. Thus the signal reconstruction problem can be considered as a search for the sparsest solution to the underdetermined equation set $Y = AS$.

2.3. Flow of the Proposed Superresolution Reconstruction Algorithm. This study uses the bicubic interpolation image of an existing image as the high-resolution image Z_h . Then, Z_h is processed by the same blurring and downsampling as in the training stage, to obtain the corresponding low-resolution Z_l . Based on the detailed characteristics of the bicubic interpolation that remain unchanged in spatial location, the pseudodictionary obtained in the training stage is directly applied to the higher level bicubic interpolation image. The superresolution reconstruction problem can be described as the problem of solving for the optimum approximation \hat{z}_c of the superresolution image z_c with the given Z_l . After completing the high- and low-resolution pseudodictionaries, the superresolution reconstruction process can be summarized as follows:

(1) Use the interpolation operator to perform a bicubic interpolation of Z_l , producing Z_{dl} , which has the same resolution as Z_c .

(2) Use the same method as that used in image training to decompose the image into tiles, producing $P = \{p_{zl}^k, p_{zh}^k\}$.

(3) Use the image tile sparsity as prior information. Because the natural information is compressible, the superresolution construction of the compressed sensing can be solved using l_0 norm optimization. The mathematical model of this process is shown as follows:

$$\begin{aligned} \min \quad & \|q\|_0 \\ \text{s.t.} \quad & p_{zl}^k = A_l q^k. \end{aligned} \quad (5)$$

However, this is NP-Hard problem, and the l_0 norm and l_1 norm have equivalency under certain conditions [15, 16].

Thus, the above equation can be converted into the convex optimization problem under a minimum l_1 norm:

$$\begin{aligned} \min \quad & \|q\|_1 \\ \text{s.t.} \quad & p_{zl}^k = A_l q^k. \end{aligned} \quad (6)$$

This study estimates the sparse representation coefficient q^k of the low-resolution characteristic block p_{zl}^k with respect of the pseudodictionary A_l via the optimal orthogonal matching pursuit (OMP) algorithm for the l_0 norm.

(4) Based on the same sparse representation in the high- and low-resolution images in their respective sparse pseudodictionaries, their superresolution image tiles are reconstructed by $\hat{p}_{zh}^k = A_h q^k$, and the superresolution image $\hat{z}_c = \{\hat{p}_{zh}^k\}_{k=1}^K$ is then created.

2.4. Quality Evaluation Method of Reconstruction Results. This study evaluates the superresolution reconstruction results from both subjective and objective perspectives. Image information entropy (InEn) and average contrast (AC) are used as the objective quality evaluation index (NR-IQA) [17] for the superresolution reconstruction results of a no-reference image:

$$\begin{aligned} \text{InEn} &= - \sum_{i=0}^{255} p(i) \log_2 p(i), \\ \text{AC} &= \frac{1}{\sqrt{2}} \sqrt{\text{AC}_x^2 + \text{AC}_y^2}, \end{aligned} \quad (7)$$

where $p(i)$ represents the distribution probability of the i th gray/color scale; AC_x and AC_y are the image average contrasts in the x - and y -directions, respectively; and AC_x can be calculated by the following equation:

$$\begin{aligned} \text{AC}_x &= \frac{1}{(M-1)(N-1)} \\ &\cdot \sum_{y=0}^{N-2} \sum_{x=0}^{M-2} |\text{Gray}(x, y) - \text{Gray}(x+1, y)|, \end{aligned} \quad (8)$$

where $\text{Gray}(x, y)$ is the gray-scale of pixel (x, y) and M and N are the number of pixels in the x - and y -directions, respectively. The calculation method for AC_y is the same as that for AC_x .

When $p(i) = 0$, let $\log_2^{p(i)} = 0$, where $\text{InEn} \in [0, 8]$. The information entropy and the average contrast of the color image can be obtained from the three-channel information entropy normalization. The information entropy is a measure of the information richness contained in the image; a higher information entropy indicates richer information contained in the image, and a higher average contrast indicates a clearer image.

3. Experiment and Analysis

3.1. Data Source. The foremost task in achieving superresolution reconstruction is to construct a high-resolution training

sample. In this study, 96 randomly selected natural images are used as training samples. To verify the effectiveness of the superresolution reconstruction model and algorithm and analyze the results of the superresolution reconstruction of photogrammetric images using the proposed method, the 1:5000 photogrammetric image of Xuzhou city (resolution = 5 cm), Hammer Aerial Photographic data (resolution = 375 cm), and a close-up image (resolution = 6 mm) collected by a Canon EOS 5D nonmetric digital camera are used in the superresolution reconstruction experiment in this study. The results are compared to those produced by the bicubic interpolation method. Because all experimental data are colored, the conversion from RGB to YUV space is performed first in a MATLAB environment; the superresolution reconstruction of Y component uses proposed method, while the other two channels use bicubic interpolation method and finally reconvert the colored image to RGB space. To increase the speed of the experiment, a test image with a size of 512×512 pixels is used for this superresolution experiment.

3.2. Parameter Setting. The training image is used as a high-resolution image, and the corresponding low-resolution image is obtained by downsampling, where the downsampling factor S is 3, and a one-dimension filter of $[1, 3.4, 3, 1]/12$ is used to blur the training image in the horizontal and vertical directions, respectively. The image is then magnified using the bicubic interpolation method, and the training sample set is composed of 50,000 image tile pairs that were extracted during the experiment. The extraction of low-resolution image characteristics is achieved using first- and second-order gradient operators:

$$\begin{aligned} f_{h1} &= [-1, 0, 1], \\ f_{v1} &= [-1, 0, 1]^T, \\ f_{h2} &= [1, 0, -2, 0, 1], \\ f_{v2} &= [1, 0, -2, 0, 1]^T. \end{aligned} \quad (9)$$

The size of a low-resolution image tile is 3×3 pixels, and the overlap is 1 pixel. The number of iterations of the pseudodictionary-pair learning process using the K -SVD algorithm is 30, and the dictionary size is 1024. In the testing stage, the bicubic interpolation method is used to magnify the image three times, creating the high-resolution test image Z_h . Then, the proposed method is used to achieve a reconstruction that has a superresolution that is three times larger. The iteration termination value of the OMP reconstruction algorithm is $\varepsilon = 0.05$.

3.3. Results and Analysis

Experiment 1 (impact of ground-feature type on reconstruction accuracy). To analyze the impact of different ground-feature types on the image reconstruction results, the Xuzhou 1:5000 aerial photogrammetric image is used as source data for capturing images of four typical ground features (a building, vegetation, bare soil, and a body of water) used as

TABLE 1: Quantitative index values of the reconstruction result.

Ground-feature type algorithm	Index	Bicubic interpolation method	Proposed method	Δ
Building	InEn	7.7930	7.8214	0.0284
	AC	2.3480	2.8494	0.5014
Vegetation	InEn	7.1726	7.2068	0.0342
	AC	4.3220	5.5267	1.2047
Bare soil	InEn	6.7129	6.7554	0.0425
	AC	3.1622	4.0588	0.8966
Water	InEn	6.9424	6.9929	0.0505
	AC	1.7332	2.2258	0.4926

test data in this study. The reconstruction results are shown in Figure 1. For comparison, the original image is simply magnified using the nearest neighbor interpolation method.

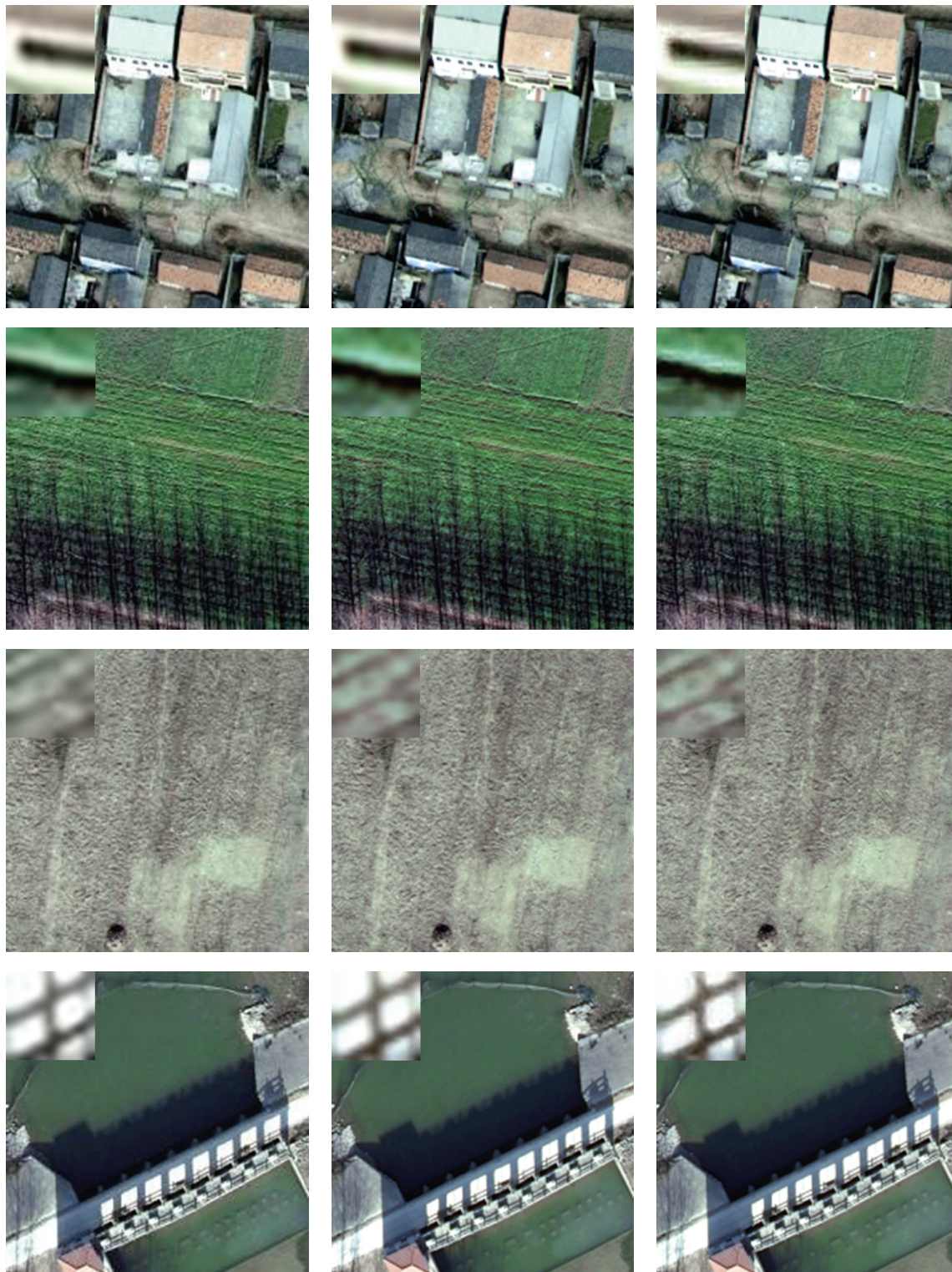
To evaluate the quality of a color image, the human objective effect is strong. As shown in the resulting images, the image produced by the traditional bicubic interpolation method is blurred, and the reconstructed image lacks clear details at edges and exhibits an irregular structural region with serious losses of texture. The reconstructed image produced by the compressed sensing method is clearer; the locally magnified image that is 10 times larger shows more detailed textures and an improved edge effect.

The quantitative index values of the reconstructed images produced by the bicubic interpolation method and the proposed method are shown in Table 1. Compared to the bicubic interpolation method, the compressed sensing method exhibits certain improvements in both the information entropy and average contrast. The information entropy of the four typical features (i.e., building, vegetation, bare soil, and water body) increases by 0.0284, 0.0342, 0.0425, and 0.0505, respectively; the image contrast also increases by 0.5014, 1.2047, 0.8966, and 0.4926, respectively. The information entropy of the image reconstructed by the proposed method increases by 0.0347, and the average image contrast increases by 0.7128.

To describe the degree of enhancement of various ground-feature image reconstruction indices, the increased values are drawn into related curves based on ground-feature types, producing Figure 2.

With regard to image information entropy, the entropy gradually increases from building to vegetation, bare soil, and water body. The increase in entropy is most marked for the water body. In terms of image contrast, the increase in vegetation is the most prevalent, while that of the water body is least prevalent.

Experiment 2 (impact of image resolution on reconstruction accuracy). Image spatial resolution is an important index when evaluating image quality; it directly reflects the level of detail of the information of the imaged object. A higher spatial resolution indicates that the image has more detailed information, including edges. The purpose of superresolution reconstruction is to increase the spatial resolution of an image



(a) Original LR image

(b) Bicubic interpolation method

(c) Proposed method

FIGURE 1: Superresolution reconstruction results of various ground-feature types in a photogrammetric image.

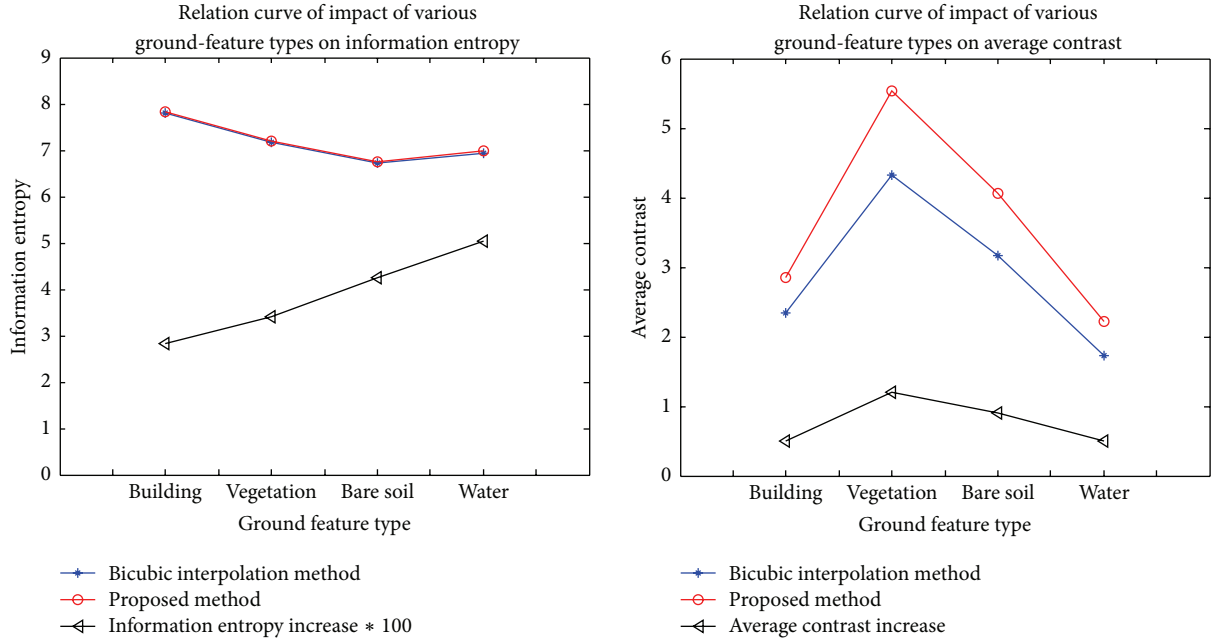


FIGURE 2: Relation curves based on the impact of various ground-feature types on reconstruction results.

and restore more image information. To examine the impact of the original image resolution on the superresolution reconstruction results, the reconstruction of a 375 mm resolution Hammer photogrammetric image, a 50 mm resolution photogrammetric image of Xuzhou city, and a 6 mm resolution close-up image captured by a nonmetric digital camera are compared; the reconstruction results are shown in Figure 3.

Considering the visual effect, the images reconstructed by the proposed method show more detailed high-frequency information, and their geometric textures are more prevalent. The corresponding quantitative indices are listed in Table 2. To mitigate the influence of different ground-feature types on the reconstruction results, the averages of building, vegetation, bare soil, and water body in the reconstructed image of Xuzhou city were determined. As shown in Table 2, for images with resolutions of 375, 50, and 6 mm, the information entropy of the reconstructed images produced by the proposed method increased by 0.0417, 0.0389, and 0.0232, respectively, compared to those produced by the bicubic interpolation method; additionally, the image contrast increased by 1.131, 0.7739, and 0.5659, respectively.

To describe the impact of image resolution on the reconstruction accuracy in more detail, the reconstruction results in Table 2 are used to create quantitative indices of improvement curves with regard to image resolution, as shown in Figure 4. Because the original image's resolution continues to decrease, the improvement in the accuracy of the reconstructed image shows a continuously increasing trend.

4. Discussion

Currently, many studies of the superresolution reconstruction of single-frame images using the sparse representation

TABLE 2: Comparison of quantitative indices of reconstruction results.

Image resolution algorithm	Index	Bicubic interpolation method	Proposed method	Δ
6 mm	InEn	6.2986	6.3218	0.0232
	AC	2.2326	2.7985	0.5659
50 mm	InEn	7.4953	7.5247	0.0294
	AC	2.4916	3.2048	0.7132
375 mm	InEn	6.9261	6.9678	0.0417
	AC	2.9165	4.0475	1.131

and dictionary-learning methods have been published in the literature [8, 18, 19]. These studies generally use methods such as the adaptive sparse domain and adaptive regularization parameters [20] to improve reconstruction accuracy using the improved dictionary-learning method [21, 22], and they typically produce good reconstruction results. However, these studies used existing images as high-resolution images, and the superresolution reconstruction process is merely a signal restoration of the downsampled images; the image resolution did not receive essential improvement. For this reason, this study used compressed sensing as a theoretical construct along with the similarity of the high- and low-resolution image characteristics to train high- and low-resolution image dictionaries using the K -SVD method. Using a bicubic interpolation image as prior information, the proposed method performed a superresolution reconstruction of the existing images, which resulted in an image with a resolution triple that of the original image. The experimental results of this study indicated that the image

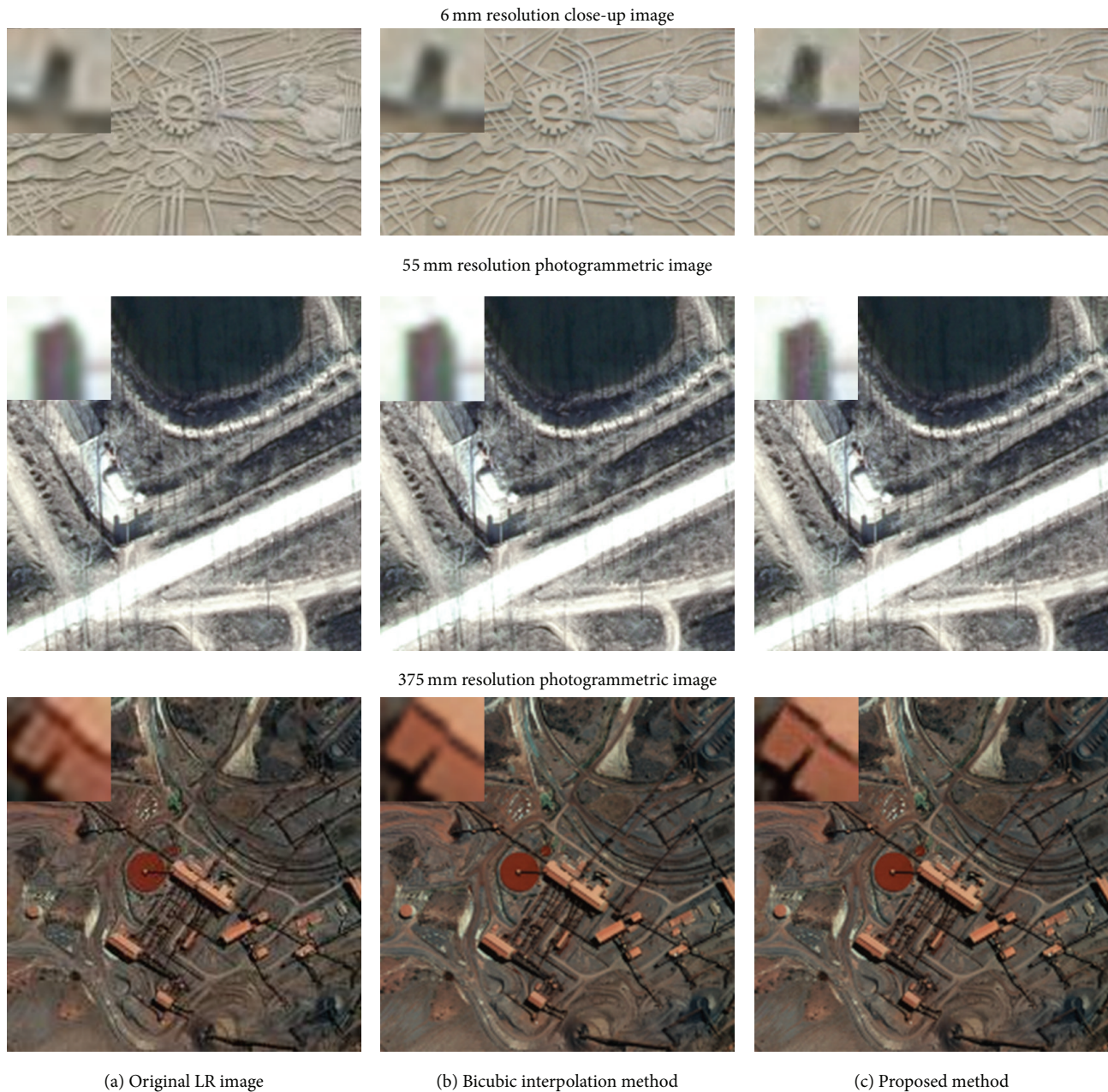


FIGURE 3: Superresolution reconstruction results of photogrammetric images of different resolutions.

obtained by the proposed reconstruction method increased both in visual effect and quantitative index compared to the image reconstructed using the bicubic interpolation method.

The superresolution reconstruction of single-frame images has been successfully applied in the reconstruction of remote-sensing images [23], medical imaging, “Resource Satellite III” images [24], Moon Rover images [25], and SAR images [26]. High-resolution imagery is necessary for high-precision photogrammetry and can increase the absolute measurement precision of photogrammetry. Thus, this study of the superresolution reconstruction of a single-frame photogrammetric image is important. This study introduces the

superresolution reconstruction concept into the photogrammetry field, producing superresolution reconstructions of single-frame photogrammetric image experiments from the MATLAB platform and superresolution images that exhibit improved visual effect and accuracy compared to those produced by the bicubic interpolation method.

The current studies in the field all concentrate on improving the sparse domain and dictionary-learning methods to improve algorithm accuracy. However, the impact of different ground-feature types and the image resolution of the photogrammetric images on the reconstruction accuracy is marked; this study conducted detailed studies of these

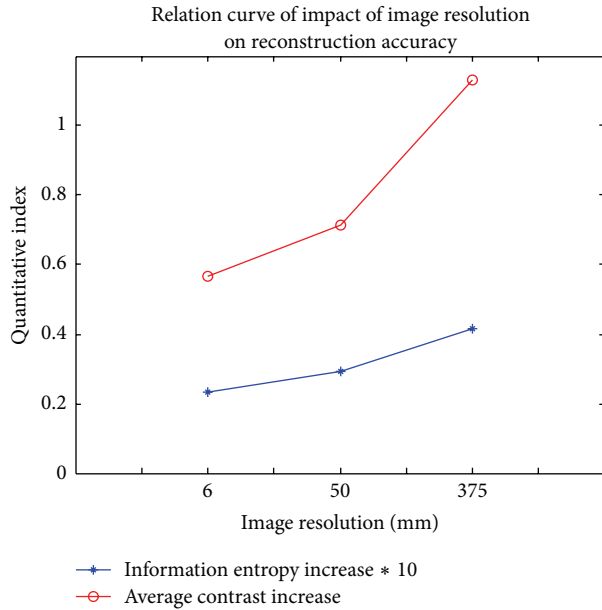


FIGURE 4: Effect of image resolution on the quantitative indices of reconstructed images.

phenomena. The texture structure and gray-scale variation of different types of ground features are reflected differently on photogrammetric images, which inevitably induce differences in reconstruction accuracy. Thus, to achieve superresolution reconstruction, this study used a 5 cm resolution image of Xuzhou city as an experimental object to create a superresolution reconstruction of four typical ground features in the photogrammetric image. This study then conducted an accuracy comparison with the traditional bicubic interpolation method based on the quantitative index analysis. The experimental results of this study indicate that the building image has the most improved reconstruction result due to the clarity and richness of the image. Additionally, the four resulting images all exhibit certain degrees of improvement, and the improvement in the image information entropy exhibits an increasing trend from building, vegetation, and bare soil to water body. In general, lower original image entropy produces more marked improvements. Conversely, the increase in image contrast is marked because vegetation exhibits the richest color information and the most frequent variation in gray-scale. The texture of the water-body image is the most monotone, and thus, its increase in contrast is the lowest. Additionally, the increment in image contrast of different ground features maintains a consistent relationship with the self-contrast of the images of these features.

Image spatial resolution is an important index for judging the amount of detailed information in an image. The direct purpose of superresolution reconstruction is to increase image resolution; however, the reconstruction process is built on the basis of existing images, and thus, the resolution of the existing image will inevitably influence the reconstruction accuracy. Thus, this study performed a superresolution reconstruction experiment on three images of different resolutions. The results of this study indicate that as the original

image resolution decreases, the reconstructed images exhibit increases in the quantitative indices. Thus, the proposed superresolution reconstruction method is particularly suitable for low-resolution images.

5. Conclusions

Blurry images produced during image reconstruction are common when using the traditional interpolation method. Additionally, the learning method requires prior information of the resulting high-resolution image to perform superresolution reconstruction; reconstructed images with superresolutions are thus not produced. This study uses compressed sensing as a theoretical framework; organically combines the interpolation method with the learning method, guided by bicubic interpolation images; and produces a superresolution reconstruction of an existing image at three times the scale. This study uses the classical OMP reconstruction algorithm to solve the sparse optimization problem and effectively increases image resolution. Compared to traditional bicubic interpolation method, the reconstruction based on the proposed method increases the image information content and clarity. The proposed method provides an effective way to improve the application range and accuracy of aviation and aerospace photogrammetric images. In the future, the sparse optimization method will be improved further to produce even better reconstruction results.

Competing Interests

The authors declare that they have no competing interests.

Acknowledgments

The authors wish to acknowledge funding from the National Fund Committee of China, which supports a Project no. 41171343 through National Natural Science Foundation for Research on precise mark location and precision estimation of digital photogrammetry image.

References

- [1] K. Jensen and D. Anastassiou, "Subpixel edge localization and the interpolation of still images," *IEEE Transactions on Image Processing*, vol. 4, no. 3, pp. 285–295, 1995.
- [2] W. K. Carey, D. B. Chuang, and S. S. Hemami, "Regularity-preserving image interpolation," *IEEE Transactions on Image Processing*, vol. 8, no. 9, pp. 1293–1297, 1999.
- [3] S. G. Chang, Z. Cvetković, and M. Vetterli, "Locally adaptive wavelet-based image interpolation," *IEEE Transactions on Image Processing*, vol. 15, no. 6, pp. 1471–1485, 2006.
- [4] X. Li and M. T. Orchard, "New edge-directed interpolation," *IEEE Transactions on Image Processing*, vol. 10, no. 10, pp. 1521–1527, 2001.
- [5] F. Zhou, W. Yang, and Q. Liao, "Interpolation-based image super-resolution using multisurface fitting," *IEEE Transactions on Image Processing*, vol. 21, no. 7, pp. 3312–3318, 2012.

- [6] W. T. Freeman, T. R. Jones, and E. C. Pasztor, "Example-based super-resolution," *IEEE Computer Graphics and Applications*, vol. 22, no. 2, pp. 56–65, 2002.
- [7] C. Liu, H.-Y. Shum, and W. T. Freeman, "Face hallucination: theory and practice," *International Journal of Computer Vision*, vol. 75, no. 1, pp. 115–134, 2007.
- [8] J. C. Yang, J. Wright, T. S. Huang, and Y. Ma, "Image super-resolution via sparse representation," *IEEE Transactions on Image Processing*, vol. 19, no. 11, pp. 2861–2873, 2010.
- [9] W. S. Dong, L. Zhang, R. Lukac, and G. Shi, "Sparse representation based image interpolation with nonlocal autoregressive modeling," *IEEE Transactions on Image Processing*, vol. 22, no. 4, pp. 1382–1394, 2013.
- [10] J. Yang, J. Wright, T. S. Huang, and Y. Ma, "Image super-resolution via sparse representation," *IEEE Transactions on Image Processing*, vol. 19, no. 11, pp. 2861–2873, 2010.
- [11] K. Su, Q. Tian, Q. Xue, N. Sebe, and J. Ma, "Neighborhood issue in single-frame image super-resolution," in *Proceedings of the IEEE International Conference on Multimedia and Expo (ICME '05)*, pp. 1122–1125, IEEE, Amsterdam, Netherlands, July 2005.
- [12] M. Aharon, M. Elad, and A. Bruckstein, "K-SVD: an algorithm for designing overcomplete dictionaries for sparse representation," *IEEE Transactions on Signal Processing*, vol. 54, no. 11, pp. 4311–4322, 2006.
- [13] E. J. Candes, J. Romberg, and T. Tao, "Robust uncertainty principles: exact signal reconstruction from highly incomplete frequency information," *IEEE Transactions on Information Theory*, vol. 52, no. 2, pp. 489–509, 2006.
- [14] M. Lustig, D. Donoho, J. Santos et al., "Compressed sensing MRI," *IEEE Signal Processing Magazine*, vol. 3, pp. 72–82, 2008.
- [15] D. L. Donoho and Y. Tsaic, "Extensions of compressed sensing," *Signal Processing*, vol. 86, no. 3, pp. 533–548, 2006.
- [16] D. L. Donoho, "For most large underdetermined systems of linear equations the minimal l_1 -norm solution is also the sparsest solution," *Communications on Pure and Applied Mathematics*, vol. 59, no. 6, pp. 797–829, 2006.
- [17] X. Zhengxiang, W. Zhifang, X. Xingliang et al., "Color image quality assessment based on noise model of human vision perception and color image quality optimization," *Journal of Image and Graphics*, vol. 15, no. 10, pp. 1454–1464, 2010.
- [18] J. Pu and J.-P. Zhang, "Super-resolution through dictionary learning and sparse representation," *Pattern Recognition and Artificial Intelligence*, vol. 23, no. 3, pp. 335–340, 2010.
- [19] J. Yang, J. Wright, T. Huang, and Y. Ma, "Image super-resolution as sparse representation of raw image patches," in *Proceedings of the 26th IEEE Conference on Computer Vision and Pattern Recognition (CVPR '08)*, pp. 1–8, IEEE Press, Anchorage, Alaska, USA, June 2008.
- [20] W. Dong, L. Zhang, G. Shi, and X. Wu, "Image deblurring and super-resolution by adaptive sparse domain selection and adaptive regularization," *IEEE Transactions on Image Processing*, vol. 20, no. 7, pp. 1838–1857, 2011.
- [21] Z. Jiancheng and Z. Wenting, "A new algorithm of image super-resolution reconstruction based on MOD dictionary-learning," *Journal of Graphics*, vol. 36, no. 3, pp. 402–406, 2015.
- [22] J. Shi and X.-H. Wang, "Image super-resolution reconstruction based on improved K-SVD dictionary-learning," *Acta Electronica Sinica*, vol. 41, no. 5, pp. 997–1000, 2013.
- [23] J. Zhong, N. Jiang, B. Hu, and Q. Hu, "A super-resolution model and algorithm of remote sensing image based on sparse representation," *Acta Geodaetica et Cartographica Sinica*, vol. 43, no. 3, pp. 276–283, 2014.
- [24] Y. Jia, Z. Lü, and M. Zhou, "Super resolution reconstruction of ZY-3 satellite images," *Journal of Applied Sciences-Electronics and Information Engineering*, vol. 33, no. 3, pp. 309–316, 2015.
- [25] S. Wei, Z. Shen, S. Zhang, and S. Liu, "Moon rover image super-resolution reconstruction algorithm," *Geomatics and Information Science of Wuhan University*, vol. 38, no. 4, pp. 436–439, 2013.
- [26] X.-L. Wang, C.-Q. Ran, and Z. M. Wang, "Super-resolution processing of SAR images by basis pursuit method based on compacted dictionary," *Acta Electronica Sinica*, vol. 34, no. 6, pp. 180–183, 2006.

Research Article

Evaluation of the Degradation on a COTS Linear CCD Induced by Total Ionizing Dose Radiation Damage

Zujun Wang, Baoping He, Wuying Ma, Zhibin Yao, Shaoyan Huang, Minbo Liu, and Jiangkun Sheng

State Key Laboratory of Intense Pulsed Irradiation Simulation and Effect, Northwest Institute of Nuclear Technology, P.O. Box 69-10, Xi'an 710024, China

Correspondence should be addressed to Zujun Wang; wzj029@qq.com

Received 16 April 2016; Revised 22 June 2016; Accepted 27 June 2016

Academic Editor: Mengmeng Wang

Copyright © 2016 Zujun Wang et al. This is an open access article distributed under the Creative Commons Attribution License, which permits unrestricted use, distribution, and reproduction in any medium, provided the original work is properly cited.

The evaluation of the degradation on a COTS linear Charge Coupled Device (CCD) induced by total ionizing dose (TID) radiation damage was presented. The radiation experiments were carried out at a ^{60}Co γ -ray source. The parameters of DALSA's linear CCD were measured at the CCD test systems as the EMVA1288 standard before and after the radiation. The dark current, dark signal nonuniformity (DSNU), photo response nonuniformity (PRNU), saturation output, full-well capacity (FWC), quantum efficiency (QE), and responsivity versus the TID were analyzed. The behavior of the tested CCD had shown a remarkable degradation after radiation. The degradation mechanisms of the CCD induced by TID damage were also discussed.

1. Introduction

Charge Coupled Device (CCD) has been extensively used in imaging, signal processing, and serial memories, especially for particle detection and space applications [1, 2]. The CCDs operated in space environments are very vulnerable to space radiation damage. In general, two types of CCD radiation damage are referred to as ionizing and displacement damage [3]. ^{60}Co γ -ray radiation mainly causes ionizing damage. Ionizing damage can cause the oxide traps and interface traps increase in the CCDs. This damage may induce the obvious degradations of CCD parameters such as the increase of dark current, dark signal nonuniformity (DSNU), and photo response nonuniformity (PRNU) and the decrease of saturation output, full-well capacity (FWC), quantum efficiency (QE), responsivity. The increase of dark current caused by radiation induces the decrease of the effective signal and the imaging quality. When the dark currents (dark signals) are full of the potential wells, the CCD will be functional failure. The increase of the DSNU and the PRNU caused by radiation induces the increase of the inhomogeneities of pixel output, which decreases the imaging uniformity. The decrease of saturation output and FWC caused by radiation induces the decrease of imaging quality such as the dynamic range

(DR) and the signal-to-noise ratio (SNR). The decrease of the QE and responsivity caused by radiation induces the decrease of the photon-sensitivity of a CCD. These parameters are well known as the radiation sensitive parameters of a CCD. The degradations of these parameters can severely affect the performance of a CCD.

Simone et al. have presented the dark current density and threshold shift of hardening CCDs versus the accumulated dose and annealing time [4]. Hopkinson has investigated the methods which can restrain the increase of dark current in the CCDs induced by total ionizing dose (TID) [5]. Wang et al. have studied the degradation of the saturation output signal voltage of the array CCDs caused by the TID radiation damage [6]. However, fewer papers laid emphasis on the TID-induced degradations of QE, responsivity, PRNU, and FWC in the CCDs. DALSA's linear CCDs have been widely used for space applications in recent years. Few papers focus on the radiation effects on this type of CCD. The evaluation of the degradations on DALSA's linear CCDs induced by total ionizing dose (TID) damage is important to the satellite designers.

The research reported herein examines the experiments of TID radiation effects on DALSA's linear CCDs. The degradations of the parameters induced by TID damage were evaluated. The dark current, DSNU, PRNU, saturation output,

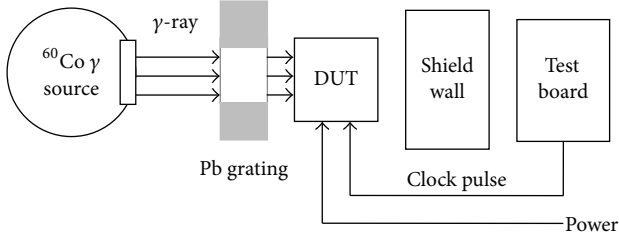


FIGURE 1: Experimental setup for a CCD TID radiation test.

and FWC as a function of TID at 30.0 rad(Si)/s were presented. The QE and responsivity as a function of wavelength before and after 20 krad(Si) radiation were also presented. The degradation mechanisms of the CCD induced by TID damage were analyzed in detail.

2. Experimental Details

The radiation experiments were carried out at a ^{60}Co γ -ray source. The CCD was unbiased with all pins grounded during ^{60}Co γ radiation and tested at 30.0 rad(Si)/s. The CCD was measured at the TID of 5, 10, 15, and 20 krad(Si). The CCD parameters were tested within 30 min after each radiation step. The output video signals were tested with illumination and dark conditions. The parameters were measured before and after radiation at the CCD test equipment. Experimental setup for a CCD TID radiation test is shown in Figure 1.

The sample used in the experiment is DALSA's IL-P3-B linear CCD. The linear CCD includes 2048 pixels and exhibits high resolution. The pixel size is $14 \times 14 \mu\text{m}^2$. The IL-P3-B linear CCD has a data rate of 40 MHz. Block diagram of DALSA's IL-P3-B linear CCD is shown in Figure 2 [7].

3. Results and Discussion

3.1. Increase of Dark Current. The dark current is the current measured in the absence of incident photons, which is expressed in $e/\text{s}/\text{pixel}$ or nA/cm^2 . The dark current in a CCD is the

current which is not generated by photoelectric effects. As the European Machine Vision Association 1288 (EMVA1288) standard, the dark current is given as [8]

$$\mu_d = \mu_{d0} + \mu_I t_{\text{exp}}, \quad (1)$$

where μ_I is the dark current, μ_{d0} is the average number of electrons without light for exposure time zero, and μ_d is the average number of electrons without light.

Both TID and displacement radiation induce the increase of dark current. It is known that the increase of dark current in a CCD is mainly caused by TID radiation damage, so we will focus on the TID radiation-induced increase of dark current.

There are several dark current sources such as thermal generation, surface generation, tunneling, and impact ionization. The main sources of the increase of dark current are thermal generation at the space charge region (SCR) and thermal generation caused by surface states at the Si and SiO_2 interface induced by TID radiation.

Ionizing radiation creates new interface states between the gate oxide and bulk silicon. Since the energy level of the newly formed states lies within band-gap, their presence typically causes the dark current generation increase [9]. The dark current versus the TID is shown in Figure 3. When the TID is lower than 10 krad(Si), the dark current increases slightly. However, when the TID is higher than 10 krad(Si), the dark current increases remarkably. The reason is that the ionizing radiation damage is worse with the accumulation of TID. Ionizing radiation causes the interface state increase which induces the increase of dark current generation rate.

Ionizing damage causes an increase in the density of oxide traps and interface traps of CCDs. The generation of the traps will increase the electron-hole pair generation, which increases the dark current [6]. The creation of traps will increase the width of SCR by changing the potential of the Si/ SiO_2 interface, which will induce the increase of dark current. As Shockley-Read-Hall theory, the generation rate, G , is expressed as [5]

$$G = \frac{\sigma_n \sigma_p v_{\text{th}} D_t (n_i^2 - pn)}{\sigma_n [n + n_i \exp \{(E_t - E_i)/kT\}] + \sigma_p [p + n_i \exp \{-(E_t - E_i)/kT\}]}, \quad (2)$$

where σ_n and σ_p represent the captured cross sections of electrons and holes, v_{th} is the thermal velocity, and D_t represents the trap concentration.

For the depleted surface $n \ll n_i$ and $p \ll n_i$,

$$G = \frac{\sigma_n \sigma_p v_{\text{th}} D_t (n_i^2 - pn)}{\sigma_n [n + n_i \exp \{(E_t - E_i)/kT\}] + \sigma_p [p + n_i \exp \{-(E_t - E_i)/kT\}]}. \quad (3)$$

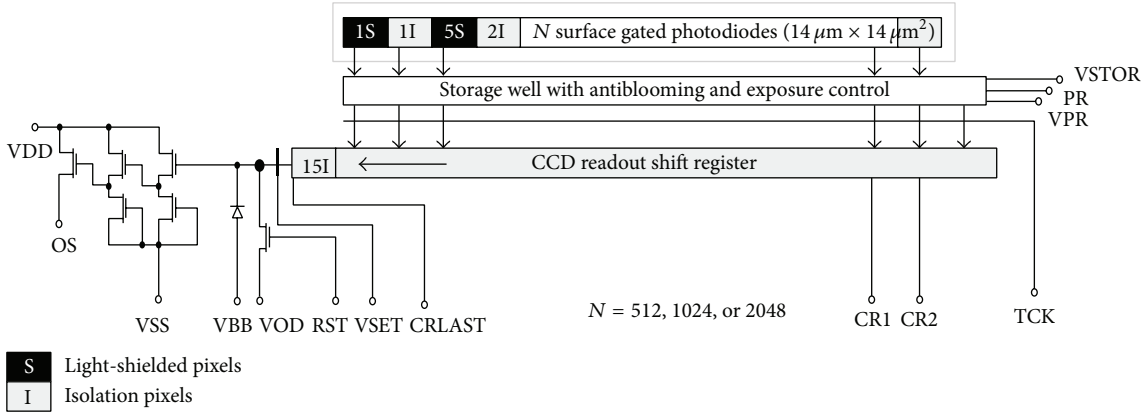


FIGURE 2: Block diagram of DALSA's IL-P3-B linear CCD [7].

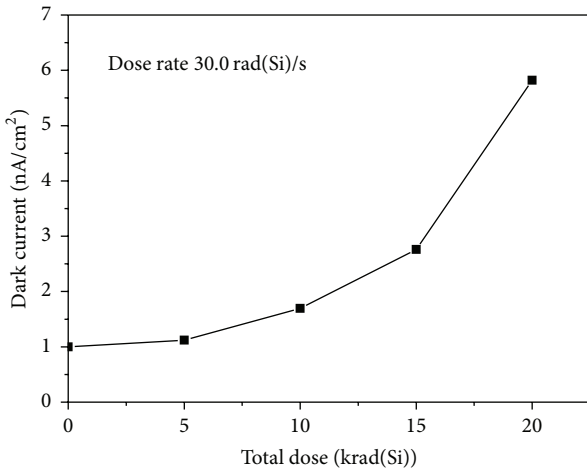


FIGURE 3: Dark current versus the TID at 30.0 rad(Si)/s.

The dark current, μ_I , is expressed as

$$\mu_I = \int_{E_V}^{E_C} G dE_t, \quad (4)$$

$$\mu_I = \frac{\pi}{2} (\sigma_n \sigma_p)^{1/2} v_{th} k D_t T n_i.$$

3.2. Increase of DSNU and PRNU. The CCD readout images include a series of pixel output and vary from pixel to pixel. The inhomogeneities are of no noise which makes the output signal vary in time. The inhomogeneities may only distribute randomly, so it is better to name this effect nonuniformity [5]. Essentially, there are two basic nonuniformities. First, the dark signal is various in different pixels. This effect is called DSNU. Second, the variation of the sensitivity is called PRNU. Both the DSNU and the PRNU of a CCD will be degraded by TID damage.

The DSNU represents the root mean square deviation of all effective pixel outputs of the imaging area in dark environments. As the EMVA1288 standard, the DSNU is given by [8]

$$\mu_{y,\text{dark}} = \frac{1}{MN} \sum_{m=0}^{M-1} \sum_{n=0}^{N-1} y_{\text{dark}} [m] [n],$$

$$s_{y,\text{dark}}^2 = \frac{1}{MN-1} \sum_{m=0}^{M-1} \sum_{n=0}^{N-1} (y_{\text{dark}} [m] [n] - \mu_{y,\text{dark}})^2, \quad (5)$$

$$\text{DSNU} = s_{y,\text{dark}},$$

where M and N are the number of rows and columns of the image, m and n are the row and column indices of the array, $y_{\text{dark}} [m] [n]$ is the mean dark signal of all $[m] [n]$ pixels in all the captured dark images, $\mu_{y,\text{dark}}$ is the mean dark signal of all the captured dark images, and $s_{y,\text{dark}}^2$ is the spatial variance of all the captured dark images.

Figure 4 shows the DSNU increases with increasing TID. When the TID is higher than 10 krad(Si), the DSNU increases remarkably. This is because the TID damage is worse with the accumulation of TID. TID radiation induces an increase not only in the dark signal but also in DSNU. The DSNU is due to the dark signal fluctuations within pixels of the CCDs induced by a fluctuation in the number of generation states. The fluctuation increases with increasing TID. When the TID is lower than 10 krad(Si), the number of generation states is small and has a limited influence on the DSNU.

The PRNU is the nonuniformity of the sensitivity of photo response. The PRNU is defined as a standard deviation relative to the mean value. The PRNU gives the spatial standard deviation of the photo response nonuniformity in % from the mean. As the EMVA1288 standard, the PRNU is given by [8]

$$\mu_{y,50} = \frac{1}{MN} \sum_{m=0}^{M-1} \sum_{n=0}^{N-1} y_{50} [m] [n],$$

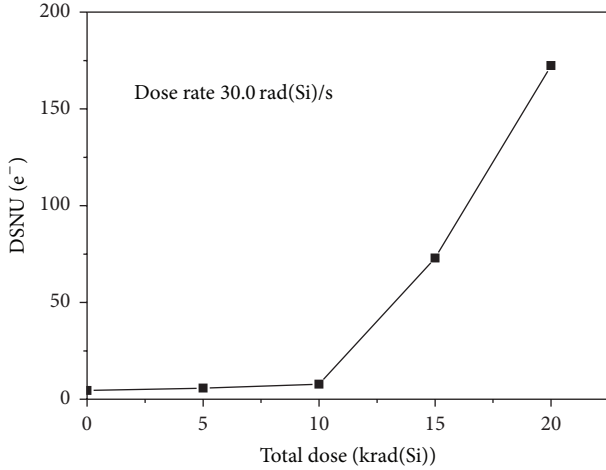


FIGURE 4: DSNU versus the TID at 30.0 rad(Si)/s.

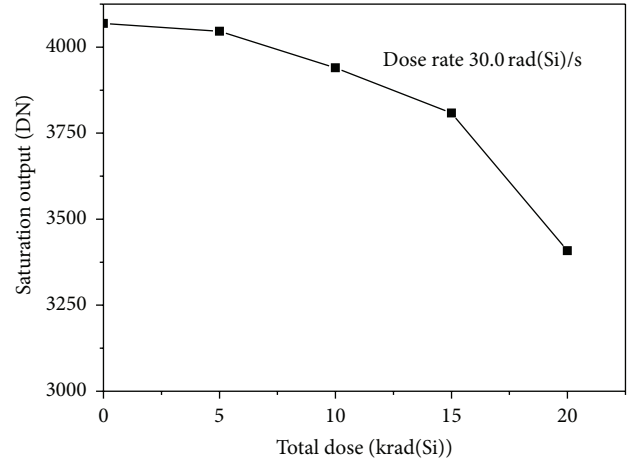


FIGURE 6: Saturation output versus the TID at 30.0 rad(Si)/s.

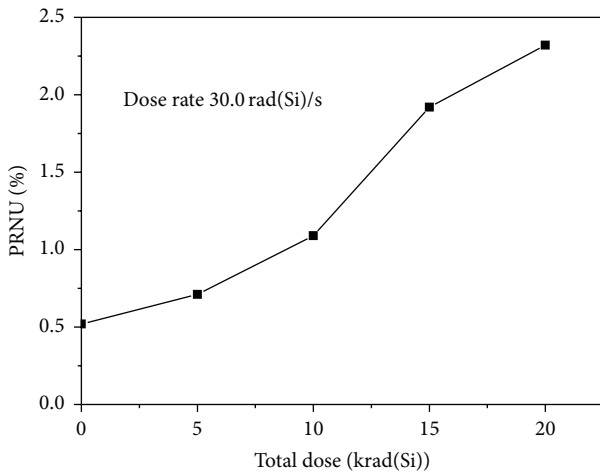


FIGURE 5: PRNU versus the TID at 30.0 rad(Si)/s.

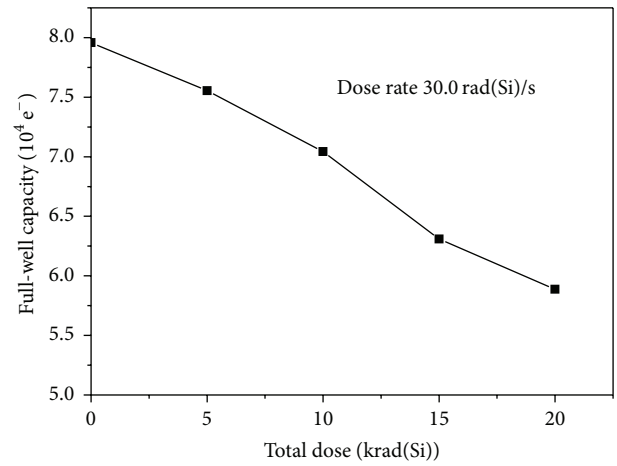


FIGURE 7: Full-well capacity versus the TID at 30.0 rad(Si)/s.

$$s_{y,50}^2 = \frac{1}{MN-1} \sum_{m=0}^{M-1} \sum_{n=0}^{N-1} (y_{50}[m][n] - \mu_{y,50})^2, \quad (6)$$

$$\text{PRNU} = \frac{\sqrt{s_{y,50}^2 - s_{y,\text{dark}}^2}}{\mu_{y,50} - \mu_{y,\text{dark}}} \times 100\%,$$

where M and N are the number of rows and columns of the image, m and n are the row and column indices of the array, $y_{50}[m][n]$ is the mean of all $[m][n]$ pixels in the 50% saturation images, $\mu_{y,50}$ is the mean of the 50% saturation images, and $s_{y,50}^2$ is the spatial variance of 50% saturation images.

Figure 5 shows the PRNU increases with increasing TID. The PRNU increase is caused by the oxide traps and the interface traps induced by TID radiation. These traps can capture the signal charges in the potential well and then emit them, which increases the signal charge fluctuations within pixels of the CCDs. The fluctuation increases with increasing TID, so the PRNU also increases with increasing TID.

3.3. Decrease of Saturation Output and FWC. The saturation output is the maximum output signal with all pixels illuminated to saturation. The saturation output as a function of TID at 30.0 rad(Si)/s is shown in Figure 6. From Figure 6, one can see that the saturation output decreases with increasing TID. When the TID is higher than 10 krad(Si), the saturation output decreases remarkably. The degradation of the saturation output is due to the depth of the potential wells in the shift register region and the imaging region decrease induced by TID damage.

It has been known that the TID damage induces the threshold voltage shift of CCD readout shift register as shown in Figure 2. The threshold voltage shift causes a decrease of the potential well depth. So the saturation output filled in the full potential well also decreases.

The FWC is calculated by dividing the saturation output (DN) by conversion factor (DN/e⁻). The FWC versus the TID at 30.0 rad(Si)/s is shown in Figure 7. From Figure 7, one can see that FWC decreases with increasing TID. This is due to the decrease of saturation output and the increase of conversion

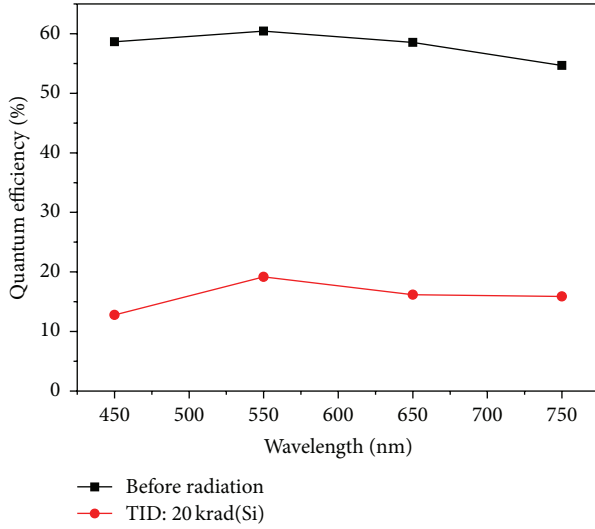


FIGURE 8: QE versus the wavelength before and after 20 krad(Si) radiation.

factor. The experiment results show that the conversion factor increases a little after TID radiation.

3.4. Decrease of QE and Responsivity. QE and spectral responsivity represent how a CCD responds to the impinged photons. TID damage will cause a decrease of QE and spectral responsivity in a CCD. QE is a quantitative parameter that reflects the photon-sensitivity of an image sensor as a function of the wavelength (i.e., the energy) of impinging photons. It is given by [10]

$$QE = \frac{N_{sig}(\lambda)}{N_{ph}(\lambda)}, \quad (7)$$

where N_{sig} is the collected video signal charge, N_{ph} is the number of injected photons, and λ stands for the wavelength.

The QE loss is mainly due to two limitations. The first is the impinging loss which represents the photon loss during the impinging procedures. It includes the loss from the optical system and the absorption and reflection by the structures above the photodiode (e.g., the metal and dielectric layers). In other words, the impinging loss stands for the missing photons that do not make it to the surface of the photosensing region. Secondly, the collection of the photon-generated carriers is not one hundred percent efficient, which thus introduces a QE reduction [10].

The QE versus the wavelength before and after 20 krad(Si) radiation at 30.0 rad(Si)/s is shown in Figure 8. The QE decreases remarkably after 20 krad(Si) radiation. The photon-generated carriers within the depletion region can be collected without any loss because of the existence of the built-in electrical field. However, the carriers generated outside the depletion region may be recombined before diffusing to the depletion region. The threshold voltage shift induced by TID damage causes the deep depletion region decrease, and thus the collected photon-generated carriers decrease. The increase in density of traps induced by TID damage causes

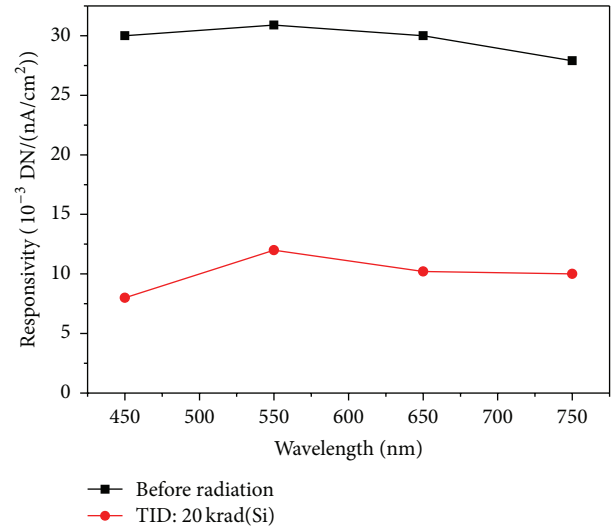


FIGURE 9: Responsivity versus the wavelength before and after 20 krad(Si) radiation.

the impinging loss of photon-generated carriers. So the QE decreases remarkably after 20 krad(Si) radiation.

The responsivity is also used to characterize the photon-sensitivity of a CCD. It is the ratio of photocurrent to optical input power and is given by [10]

$$R = \frac{I_{ph}}{P} = QE \frac{q\lambda}{hc}, \quad (8)$$

where I_{ph} is the photocurrent and P is the optical input power.

The responsivity versus the wavelength before and after 20 krad(Si) radiation at 30.0 rad(Si)/s is shown in Figure 9. The responsivity also decreases remarkably after 20 krad(Si) radiation. From (8), we can conclude that the responsivity degradation mechanisms are similar to the QE.

4. Conclusion

The radiation effects on the DALSA CCD at 30.0 rad(Si)/s were investigated. The behavior of the tested CCD had shown a remarkable degradation after ⁶⁰Co γ -ray radiation. The dark current increases with increasing TID, which is due to the increase in density of traps induced by TID damage. The DSNU and PRNU increase with increasing TID, which is due to the increase of the signal charge fluctuations (both dark and illumination environments) within pixels of a CCD induced by TID damage. When the TID is higher than 10 krad(Si), the dark current, DSNU, and PRNU increase remarkably. This means that the CCD used in the radiation environments where the TID is higher than 10 krad(Si) should consider the serious degradation of the performance.

The saturation output and FWC decrease with increasing TID, which is mainly due to the decrease of the potential well depth in the CCD induced by TID damage. When the TID is higher than 10 krad(Si), the saturation output and FWC decrease remarkably. The QE and responsivity decrease with increasing TID, which is due to the deep depletion region

decrease and the impinging loss of photon-generated carriers induced by TID damage. When the TID is 20 krad(Si), the QE and responsivity decrease remarkably, which induces the remarkable decrease of the photon-sensitivity of a CCD.

In order to study dose rate effects on the CCDs, more radiation experiments and annealing tests on the CCDs will be carried out in the laboratory to compare the degradations under the same total ionizing doses at 0.03, 0.3, and 3.0 rad(Si)/s. More detailed experimental results will be provided.

Competing Interests

The authors declare that they have no competing interests.

Acknowledgments

This work was supported by the National Science Foundation of China (Grants nos. 11305126, 11235008) and the Foundation of State Key Laboratory of China (Grant no. SKLIPR1211).

References

- [1] K. Abe, A. Arodzero, C. Baltay et al., "Design and performance of the SLD vertex detector: a 307 Mpixel tracking system," *Nuclear Instruments and Methods in Physics Research Section A: Accelerators, Spectrometers, Detectors and Associated Equipment*, vol. 400, no. 2-3, pp. 287–343, 1997.
- [2] A. Yamashita, T. Dotani, H. Ezuka, M. Kawasaki, and K. Takahashi, "Performance of the X-ray CCDs aboard the ASCA satellite after 5-year operation in space," *Nuclear Instruments and Methods in Physics Research A*, vol. 436, no. 1-2, pp. 68–73, 1999.
- [3] T. Hardy, R. Murowinski, and M. J. Deen, "Charge transfer efficiency in proton damaged CCDs," *IEEE Transactions on Nuclear Science*, vol. 45, no. 2, pp. 154–163, 1998.
- [4] A. Simone, I. Debusschere, A. Alaerts, and C. Claeys, "Ionizing radiation hardening of a CCD technology," *IEEE Transactions on Nuclear Science*, vol. 39, no. 6, pp. 1964–1973, 1992.
- [5] G. R. Hopkinson, "Radiation-induced dark current increases in CCDs," in *Proceedings of the 2nd European Conference on Radiation and its Effects on Components and Systems (RADECS '93)*, pp. 401–408, St. Malo, France, September 1993.
- [6] Z. Wang, W. Chen, S. Huang, M. Liu, B. He, and J. Sheng, "Degradation of saturation output of the COTS array charge-coupled devices induced by total dose radiation damage," *Nuclear Instruments and Methods in Physics Research Section A: Accelerators, Spectrometers, Detectors and Associated Equipment*, vol. 751, pp. 31–35, 2014.
- [7] Dalsa, Dalsa IL-P3-B image sensors datasheet, 2003.
- [8] European Machine Vision Association (EMVA), "Standard for characterization of image sensors and cameras," EMVA Standard 1288, 2010.
- [9] J. R. Janesick, T. Elliott, and F. Pool, "Radiation damage in scientific charge-coupled devices," *IEEE Transactions on Nuclear Science*, vol. 36, no. 1, pp. 572–578, 1989.
- [10] X. Wang, *Noise in sub-micron CMOS image sensors [Ph.D. dissertation]*, Delft University of Technology, Delft, The Netherlands, 2008.

Research Article

Design and Fabrication of Air-Based 1-3 Piezoelectric Composite Transducer for Air-Coupled Ultrasonic Applications

Cunfu He, Yaoyao Wang, Yan Lu, Yuepeng Liu, and Bin Wu

College of Mechanical Engineering and Applied Electronics Technology, Beijing University of Technology, Beijing 100124, China

Correspondence should be addressed to Yan Lu; lvyan@bjut.edu.cn

Received 20 February 2016; Revised 12 May 2016; Accepted 26 May 2016

Academic Editor: Manel del Valle

Copyright © 2016 Cunfu He et al. This is an open access article distributed under the Creative Commons Attribution License, which permits unrestricted use, distribution, and reproduction in any medium, provided the original work is properly cited.

The air-based 1-3 piezoelectric composite transducers are designed and fabricated in order to solve the acoustic impedance matching problem. Firstly, a finite element model using honeycomb structure as the piezoelectric composite matrix is built to reduce the acoustic impedance of the sensitive element. Three important factors, volume fraction of piezoelectric materials φ , the thickness h , and the size s of the square cross section of piezoelectric column, are examined and verified in simulation. Then, according to the result of simulation, the piezoelectric composites and the air-coupled transducers are fabricated. The honeycomb structures of resin are produced by the method of 3D printing technology, with the volume fraction of air being 30%. The impedance characteristics and the excitation/reception performance of the air-coupled transducers are measured and optimized. Meanwhile, a scanning experiment is carried out to demonstrate the crack detection process in monocrystalline silicon. A_0 mode of Lamb waves is excited and collected. The location and size of the defect will be determined by calculating the correlation coefficients of the received signals and reference signals. Finally, a 15 mm \times 0.5 mm \times 0.5 mm scratch is clearly distinguished.

1. Introduction

Silicon is one of the most important components of solar cells, and the original integrity of silicon wafer affects the photoelectric conversion efficiency and service life significantly. So, a suitable nondestructive testing and evaluation method should be performed to inspect the cracks in silicon wafer.

In many researches, the damage detection for silicon wafer is mainly classified into several methods, which include resonance ultrasonic vibrations [1] and ultrasonic guided waves [2]. With the increasing demand for high-speed inspection, nondestructive inspection modes using ultrasonic guided waves have become a research hotspot. The nondestructive inspection modes can be broadly divided into contact methods and noncontact methods. At present, the methods of noncontact ultrasonic testing are mainly air-coupled ultrasonic testing [3], laser ultrasonic testing [4], and electromagnetic ultrasonic testing [5].

Air-coupled ultrasonic testing avoids the specimen contact in order to wipe the influence of contact conditions and coupling materials. Then, only air will be used as the coupling medium, and the transducer can easily move to make

it possible to do scanning quickly. Air-coupled ultrasonic testing includes penetration detection, pulse-echo testing, and oblique incident detection. Kichou et al. [6] used air-coupled transducers to excite pure Lamb waves in plate. The relationship between the deviation of Lamb wave beam and the inclination angle of specimen is researched. Solodov et al. [7] demonstrated the periodic distribution of Lamb wave amplitudes and phases along the various directions in silicon wafer by air-coupled transducers. Yan et al. [8] investigated the impact of delamination in a carbon-epoxy composite plate. The group velocity of air coupling Lamb waves is extracted to identify the positions of defects. Chakrapani et al. [9] experimentally located the crack in both monocrystalline and polycrystalline silicon wafer with the thickness of 200 μm using linear scanning method by A_0 mode Lamb waves. Liu et al. [10] utilized the air-coupled ultrasonic transducers to generate and receive Lamb waves in composite beams for delamination detection and analyzed the reflection and mode conversion at the ends of lamination defects.

However, the main restriction associated with air coupling method is the large acoustic impedance mismatch at

the transducer/air and air/specimen interfaces, where most of the incident wave will be reflected [5]. When the ultrasound passes through an interface, only a proportion of it can be coupled into the next material. This “proportion” depends on how close the acoustic impedance of these two materials is. The acoustic impedance of traditional piezoelectric ceramic materials is almost $(30\sim 40) \times 10^6$ Rayl, but that of air is only 420 Rayl. So the proportion of the ultrasound that is coupled into the air will be only 0.003%~0.005%.

The active materials, 1-3 type piezoelectric composites, composed of polymer (epoxy resin or polyurethane) and piezoelectric ceramic, can reduce the acoustic impedance significantly. Hence, the transmitted proportion (from transducer to air) can be increased. Generally, the 1-3 type piezoelectric composites possess the following attributes: low density, low acoustic impedance, wide bandwidth, and high electromechanical coupling coefficient. Newnham et al. [11] first put forward the concept of 1-3 piezoelectric composites. Based on their study, extensive researches have been carried out. Hayward and Bennett [12] analyzed the working characteristic of 1-3 piezoelectric composite transducers by finite element method. Hladky-Hennion and Decarpigny [13] observed the influence of geometrical parameters on 1-3 piezoelectric composites by establishing a cycle model. Bhardwaj [14] firstly proposed the prototype of air-based piezoelectric composites sensors, using honeycomb structure or foam material as the substrate to reduce the density and acoustic impedance.

To sum up, in this paper, air-based 1-3 piezoelectric composites air-coupled transducer will be introduced and evaluated. Firstly, the structure of piezoelectric composites is manipulated. Secondly, 3D finite element models are created to analyze the performance of air-based 1-3 piezoelectric composites. Then, the transducers based on 1-3 piezoelectric composites are fabricated with the honeycomb structures of resin which are produced by 3D printing. Also, the excitation and reception performance are tested. Finally, these transducers will be applied in the crack detection by generating and receiving Lamb waves.

2. 3D Simulations of 1-3 Piezoelectric Composites

2.1. 1-3 Piezoelectric Composites and Their Finite Element Model (FEM). As shown in Figure 1, conventional 1-3 piezoelectric composites are composed of piezoelectric columns, which are mounted inside the polymer parallelly and periodically. The structure can reduce the density and decrease the acoustic impedance effectively. This will close the impedance between piezoelectric transducer and the air, so as to let more ultrasound through.

In order to reduce the acoustic impedance of the piezoelectric composites significantly, air-based 1-3 piezoelectric composites should be induced. The structure and components of air-based 1-3 piezoelectric composites are shown in Figure 2. Using honeycomb structure as a matrix of piezoelectric composites, the piezoelectric columns are embedded in the cellular structure. The honeycomb structure acts as a

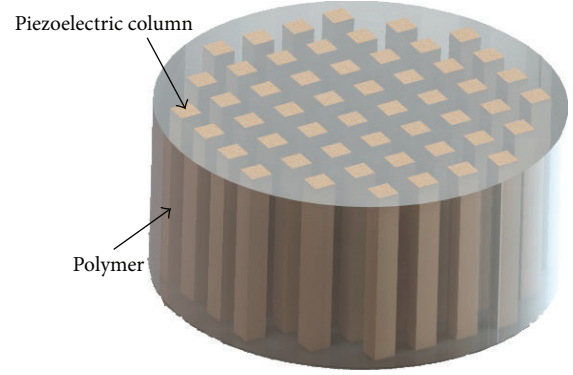


FIGURE 1: Conventional 1-3 piezoelectric composites.

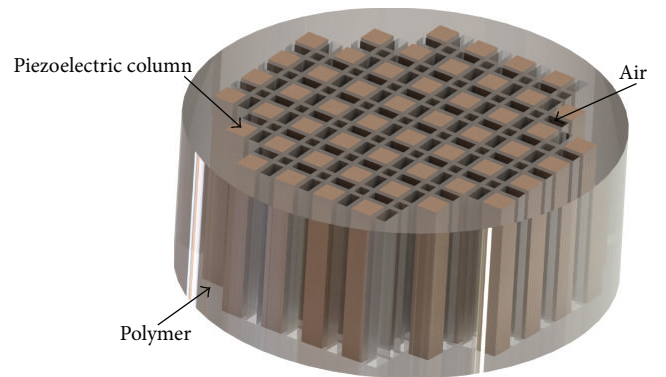


FIGURE 2: Air-based 1-3 piezoelectric composites.

skeleton to support the piezoelectric column. However, the air gap (instead of the filling polymer in Figure 1) reduces the density and the acoustic impedance efficiently. Thus, the air becomes the main part of the composite matrix. And this is where the “air base” comes from.

According to 1-3 piezoelectric composites thickness-mode oscillation theory [15], the acoustic impedance of 1-3 piezoelectric composites can be formulated by

$$\bar{Z} = (\bar{c}_{33}\bar{\rho})^{1/2}, \quad (1)$$

where \bar{Z} , \bar{c}_{33} , and $\bar{\rho}$ are the generalized acoustic impedance, elastic constants, and density, respectively. \bar{c}_{33} and $\bar{\rho}$ of 1-3 piezoelectric composites are determined by the volume fraction and the original elastic constants and density of each own phase. Compared with the conventional 1-3 piezoelectric composites, the air-based 1-3 piezoelectric composites use honeycomb structure as a matrix, which will inevitably reduce the acoustic impedance. For example, when $\varphi = 40\%$, epoxy 30%, and air 30%, we can obtain the generalized acoustic impedance which equals $1.28 \times 10^7 \text{ kg}\cdot\text{m}^{-2}\cdot\text{s}$, while the conventional one equals $1.37 \times 10^7 \text{ kg}\cdot\text{m}^{-2}\cdot\text{s}$. It shows a 7% decrease. Therefore, at the same PZT volume fraction, the acoustic impedance of air-based 1-3 piezoelectric composites is lower than that of epoxy-based 1-3 piezoelectric composites.

TABLE 1: Material parameters of PZT-5H.

ρ kg/m ³	$c, 10^{10}$ N/m ²						$e, C/m^2$			ϵ/ϵ_0	
	c_{11}	c_{12}	c_{13}	c_{33}	c_{44}	c_{66}	e_{33}	e_{31}	e_{15}	ϵ_{11}	ϵ_{33}
7500	12.6	7.95	8.41	11.7	2.3	2.35	23.3	-6.5	17	1700	1470

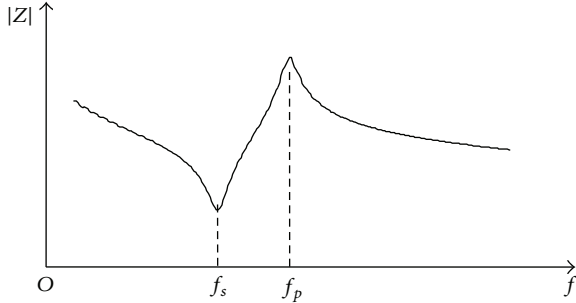


FIGURE 3: Typical characteristic impedance curve of piezoelectric materials.

When an electrical signal is applied to the piezoelectric materials, the equivalent impedance of the piezoelectric element will change along with the exciting frequency. The characteristic impedance curve of piezoelectric materials is shown in Figure 3. The minimum of this curve corresponds to the series resonant frequency f_s , while the maximum of impedance represents the parallel resonant frequency f_p .

In this research, the electromechanical coupling coefficient K_t and the mechanical quality factor Q_m are selected as the critical factor to evaluate the performance of the piezoelectric composites. K_t is a quantity that measures the conversion efficiency between electrical energy and acoustic energy in piezoelectric materials. For thickness vibration mode of 1-3 piezoelectric composites, the electromechanical coupling coefficient K_t can be formulated by

$$K_t^2 = \frac{\pi f_s}{2 f_p} \tan\left(\frac{\pi f_p - f_s}{2 f_p}\right). \quad (2)$$

Q_m is a quantity that measures the wastage of energy overcoming the internal friction when the piezoelectric materials resonate. Usually, this part of energy turns out to be heat. The mechanical quality factor Q_m can be formulated by

$$Q_m = \frac{f_p^2}{2\pi f_s |Z| C^T (f_p^2 - f_s^2)}, \quad (3)$$

where $|Z|$ is the minimum of the resonant impedance; C^T is the free capacitance. Accordingly, when Q_m is greater, more energy turns into mechanical oscillation.

Air-based 1-3 piezoelectric composites are formed by the same structural unit in a certain periodical arrangement. In this repeatable unit, there exist two symmetrical planes, as shown in Figure 4. One-quarter of the unit is called a cell. If symmetrical boundary conditions are set to the finite element model, actually, the performance of the air-based 1-3 piezoelectric composites can be obtained by only one cell

TABLE 2: Material parameters of epoxy resin.

	$\rho, \text{kg/m}^3$	$c_T, \text{m/s}$	$c_L, \text{m/s}$	ϵ/ϵ_0
CY1301/HY1300	1140	1140	2370	4

model. In order to study the performance of 1-3 piezoelectric composites, PZT-5H is selected as the piezoelectrics, while epoxy resin is the polymer matrix. The material parameters are shown in Tables 1 and 2. The 3D FE simulations are carried out using COMSOL Multiphysics (COMSOL Inc., Sweden), with symmetrical boundary conditions. The finite element model of one cell of air-based 1-3 piezoelectric composites is illustrated in Figure 4. In FE model, the volume fraction ϕ of PZT is gradually increased from 10% to 60% with the interval of 10%, the cross-sectional area s of the piezoelectric square column is increased from 1 mm \times 1 mm to 3 mm \times 3 mm, with the side length stepping by 0.5 mm, and the thickness h of piezoelectric column is increased from 5 mm to 10 mm, with the interval of 1 mm. The element chose a 3-dimensional brick type. The element sizes in length (x direction), in width (y direction), and in thickness (z direction) are all 0.2 mm, approximately 1/10 wavelength. The scanning frequency ranges from 50 kHz to 500 kHz, with the interval of 1 kHz.

2.2. Influence of PZT Volume Fraction ϕ . In the composite material, the content of piezoelectrics directly affects the piezoelectric properties. With the increase of volume fraction of PZT, the piezoelectric constant and dielectric constant of composite material will increase. Meanwhile, the acoustic impedance of the composite material will also increase. So a suitable volume fraction of PZT should be optimized to balance the piezoelectric constant/dielectric constant and the acoustic impedance.

In the finite element model of piezoelectric composite, the thickness h and the cross-sectional area s (red area) of the piezoelectric column are 10 mm and 1 mm \times 1 mm. The volume fraction of PZT ϕ is gradually increased from 10% to 60% with the interval of 10%, while keeping the volume fraction of air 30%, as shown in Figure 5.

The simulation results are shown in Figures 6 and 7. With the increase of volume fraction ϕ of the PZT, the electromechanical coupling coefficient K_t of 1-3 piezoelectric composites will gradually increase, while the mechanical quality factor Q_m will gradually decrease. When volume fraction ϕ of the PZT is 40%~60%, the electromechanical coupling coefficient K_t tends to be stable and maximum, which means this electromechanical conversion efficiency is optimized. But the mechanical quality factor Q_m changes slightly and is much lower than PZT-5H. Meanwhile, at the same volume fraction, the electromechanical coupling

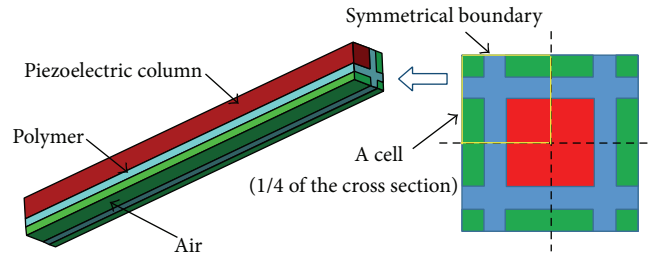


FIGURE 4: A quarter cycle finite element model of 1-3 piezoelectric composite.

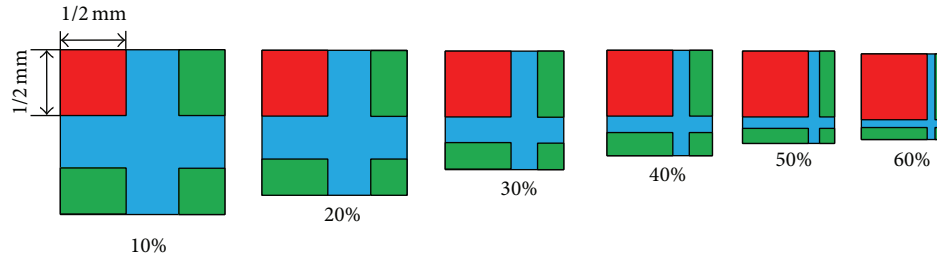


FIGURE 5: Increase of PZT volume fraction φ .

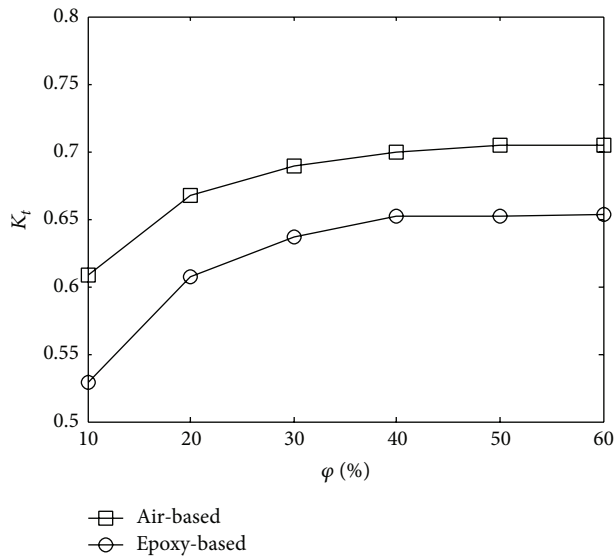


FIGURE 6: Influence of the PZT volume fraction on the electromechanical coupling coefficient.

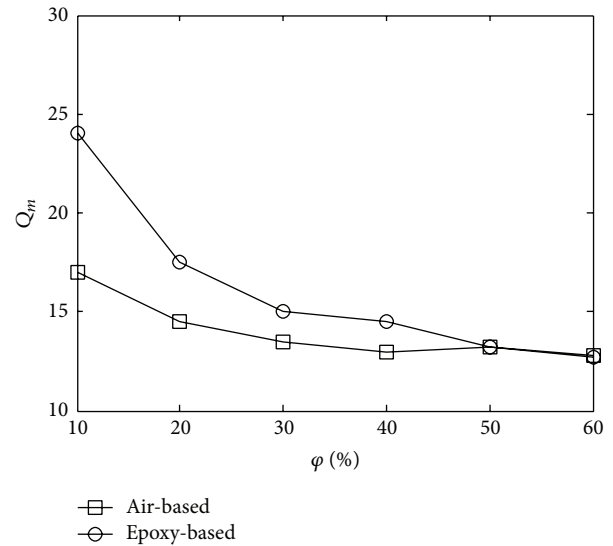


FIGURE 7: Influence of the PZT volume fraction on the mechanical quality factor.

coefficient K_t of air-based 1-3 piezoelectric composites is greater than that of epoxy-based 1-3 piezoelectric composites for almost 10%. The volume fraction of 40% for PZT is selected to ensure both high electromechanical conversion efficiency and low acoustic impedance.

2.3. Influence of PZT Cross-Sectional Area s . In the finite element model, the thickness h and the volume fraction φ of PZT are 10 mm and 40%. The cross-sectional area s of the piezoelectric square column is gradually increased from 1 mm \times 1 mm to 3 mm \times 3 mm, with the side length stepping by 0.5 mm, as shown in Figure 8.

The relationship between the electromechanical coupling coefficient K_t and the cross-sectional area s is shown in Figure 9. The change of s of PZT has little impact on K_t . And the electromechanical conversion efficiency of air-based 1-3 piezoelectric composites is greater than that of epoxy-based ones. The influence of the cross-sectional area s on the mechanical quality factor Q_m is shown in Figure 10. The change of s of PZT also shows little impact on Q_m .

In the composite material, the PZT cross-sectional area s mainly affects the vibration mode. In general, for piezoelectrics, the vibration mode includes thickness vibration mode and lateral vibration mode [16]. Generally, the greater

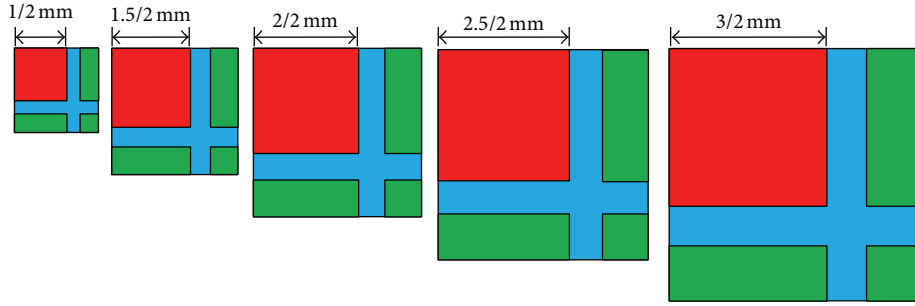
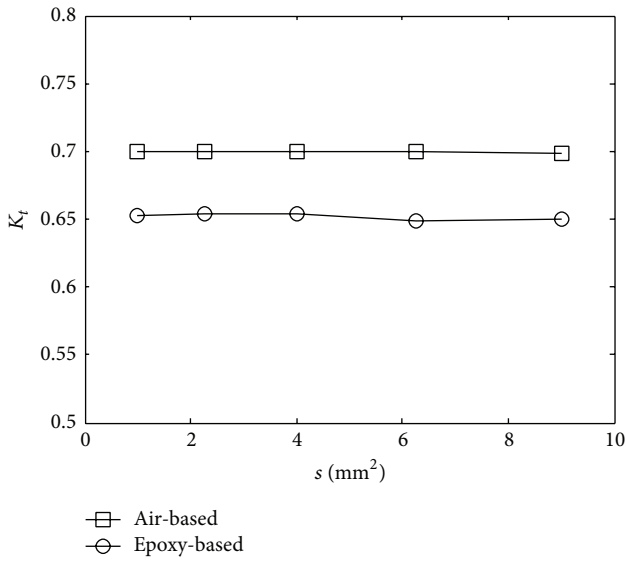
FIGURE 8: Increase of PZT cross-sectional area s .

FIGURE 9: Influence of the PZT cross-sectional area on the electromechanical coupling coefficient.

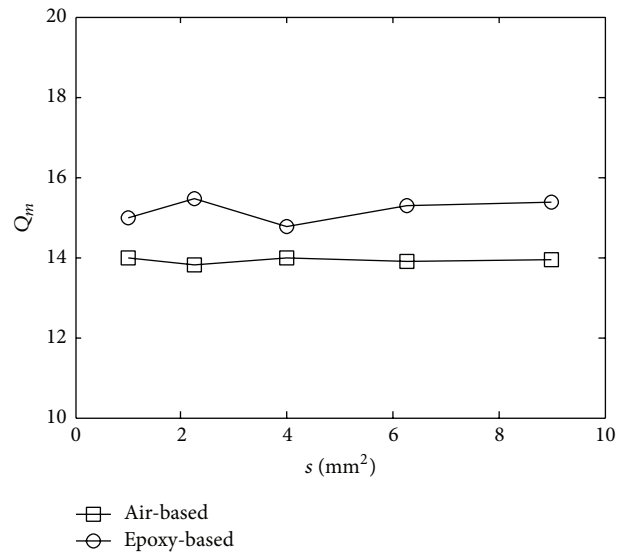


FIGURE 10: Influence of the PZT cross-sectional area on the mechanical quality factor.

the thickness electromechanical coupling coefficient, the stronger the thickness vibration mode; the greater the planar electromechanical coupling coefficient, the stronger the lateral vibration mode. For 1-3 piezoelectric composites, when the PZT cross-sectional area is larger, which means the larger aspect ratio (side length/thickness), the lateral vibration mode will affect the thickness vibration mode significantly, leading to the fact that the thickness vibration mode will be limited. So, it is important to fabricate “long and thin” PZT column. Considering both the processing procedures and the cost, the cross-sectional area of $1 \text{ mm} \times 1 \text{ mm}$ is selected for the PZT column.

2.4. Influence of PZT Thickness h . The frequency constant of PZT-5H is $N = 2000 \text{ Hz}\cdot\text{m}$. The relationship between the resonant frequency f_0 of thickness vibration mode and the thickness of PZT h can be formulated by

$$N = f_0 \cdot h. \quad (4)$$

In the finite element model, the cross-sectional area s and the volume fraction φ of PZT are $1 \text{ mm} \times 1 \text{ mm}$ and 40%. The thickness of piezoelectric column is gradually increased from 5 mm to 10 mm, with the interval of 1 mm.

As is shown in Figures 11 and 12, the electromechanical conversion efficiency K_t and the mechanical quality factor Q_m both vary slightly with the increase of the thickness of PZT h . However, when the volume fraction of PZT φ is constant, with the increase of the PZT thickness h , the center frequency of air-coupled 1-3 piezoelectric composites is almost linearly decreasing, as is shown in Figure 13. Therefore, according to the desired center frequency, the appropriate thickness of the piezoelectric composites should be designed.

According to the results of the above simulation analysis, the volume fraction of PZT is $\varphi = 40\%$ to ensure the optimal electromechanical conversion efficiency and to keep the low acoustic impedance. The side length of PZT column is $a = 1 \text{ mm}$ to limit the lateral vibration mode. The thickness of the sensitive element is $h = 10 \text{ mm}$ to ensure the center frequency of the air-coupled transducers to be about 200 kHz.

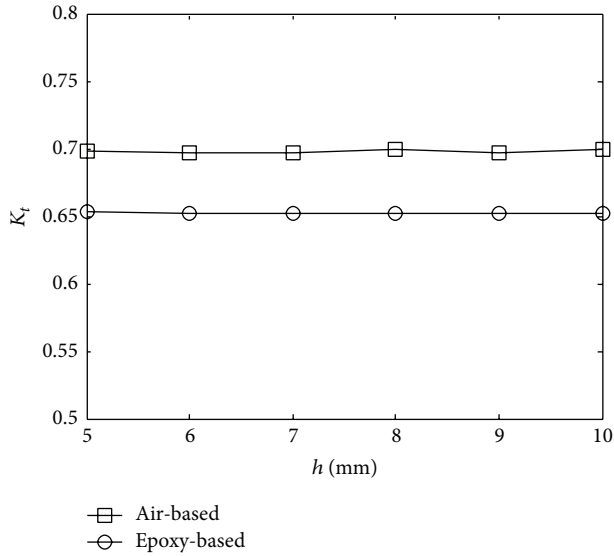


FIGURE 11: Influence of the ceramic thickness on the electromechanical coupling coefficient.

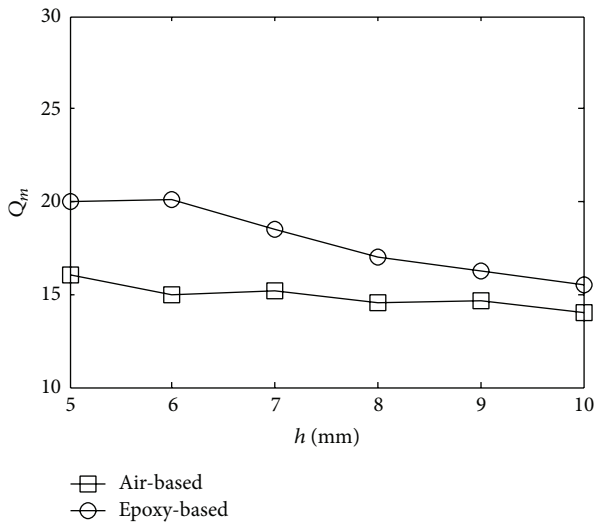


FIGURE 12: Influence of the ceramic thickness on the mechanical quality factor.

3. Fabrication and Performance Test of Air-Coupled Transducer

3.1. Air-Coupled Transducer Preparation and Impedance Characteristics Analysis. Since the substrate of the air-based 1-3 piezoelectric composite is intensive honeycomb structure, the traditional mechanical method is not feasible for the fabrication. In this research, the honeycomb structures made of resin are constructed by the method of 3D printing technology, with the 30% volume fraction of air.

The ProJet 3510 SD (3D Systems, USA) 3D printer is used to fabricate the honeycomb structure, with the resin material of VisiJet Crystal. The honeycomb structure is divided into several layers and printed layer by layer. The resolution of the

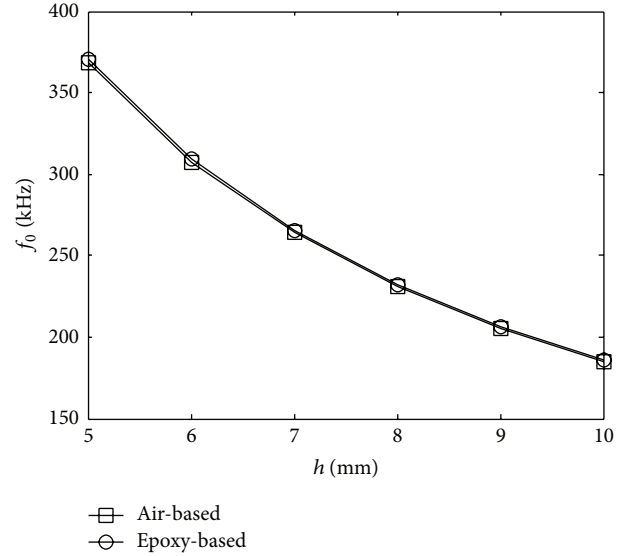


FIGURE 13: Influence of the ceramic thickness on the center frequency.

TABLE 3: Frequency of series resonant and parallel resonant of transducers.

Number	f_s	f_p
1	147.2 kHz	166.1 kHz
2	155.3 kHz	181.2 kHz
3	146.1 kHz	167.9 kHz

3D printer is $32 \mu\text{m}$ to make sure the precision of the structure is at $0.025 \text{ mm} - 0.05 \text{ mm}$. Then, a precise honeycomb structure will be obtained. The piezoelectric columns are manually inserted into the honeycomb structures, both combined by epoxy adhesive. After curing, the upper and bottom surfaces are polished. Then, the gold is sputtered on the two surfaces as electrodes. Finally, when the air-based 1-3 piezoelectric composites are packaged up with the shield, the air-coupled transducer will be complete, as shown in Figure 14. The impedance characteristics of the air-coupled transducers are measured by an impedance analyzer (Agilent 4294A). The results are shown in Figure 15. The characteristic impedance curves of the transducers differ a little. The frequencies of series resonant f_s and parallel resonant f_p , shown in Table 3, are slightly different. Meanwhile, because the aspect ratio of the piezoelectric column is relatively small, the lateral vibration mode is far away from the thickness vibration mode. So, the pure thickness vibration mode is approached.

3.2. Air-Coupled Transducer Performance Test. The air-coupled transducers are tested. The transducer arrangement is shown in Figure 16. The distance between the transmitting transducer and the receiving transducer is 80 mm. The direct wave signals transmitted through the air are detected.

The excitation signal is a 5-cycle 200 kHz sinusoidal tone burst, modulated by a Hanning window. The received signals are shown in Figure 17. As can be seen from the results, the air-coupled transducers can both excite and receive the

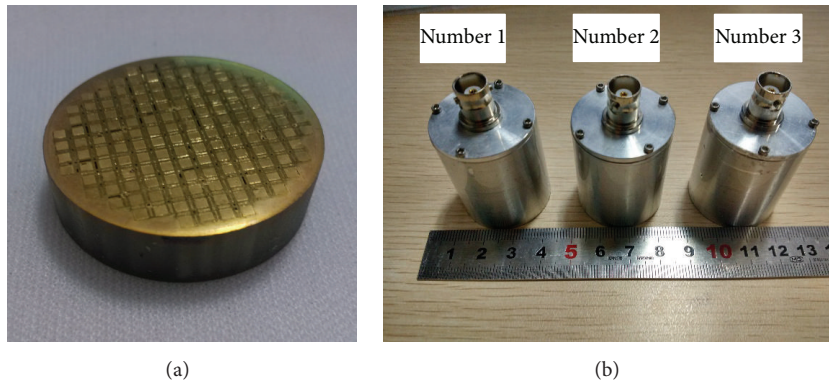


FIGURE 14: Schematic representation of 1-3 piezoelectric composite and air-coupled transducers: (a) air-based 1-3 piezoelectric composite and (b) air-coupled transducers.

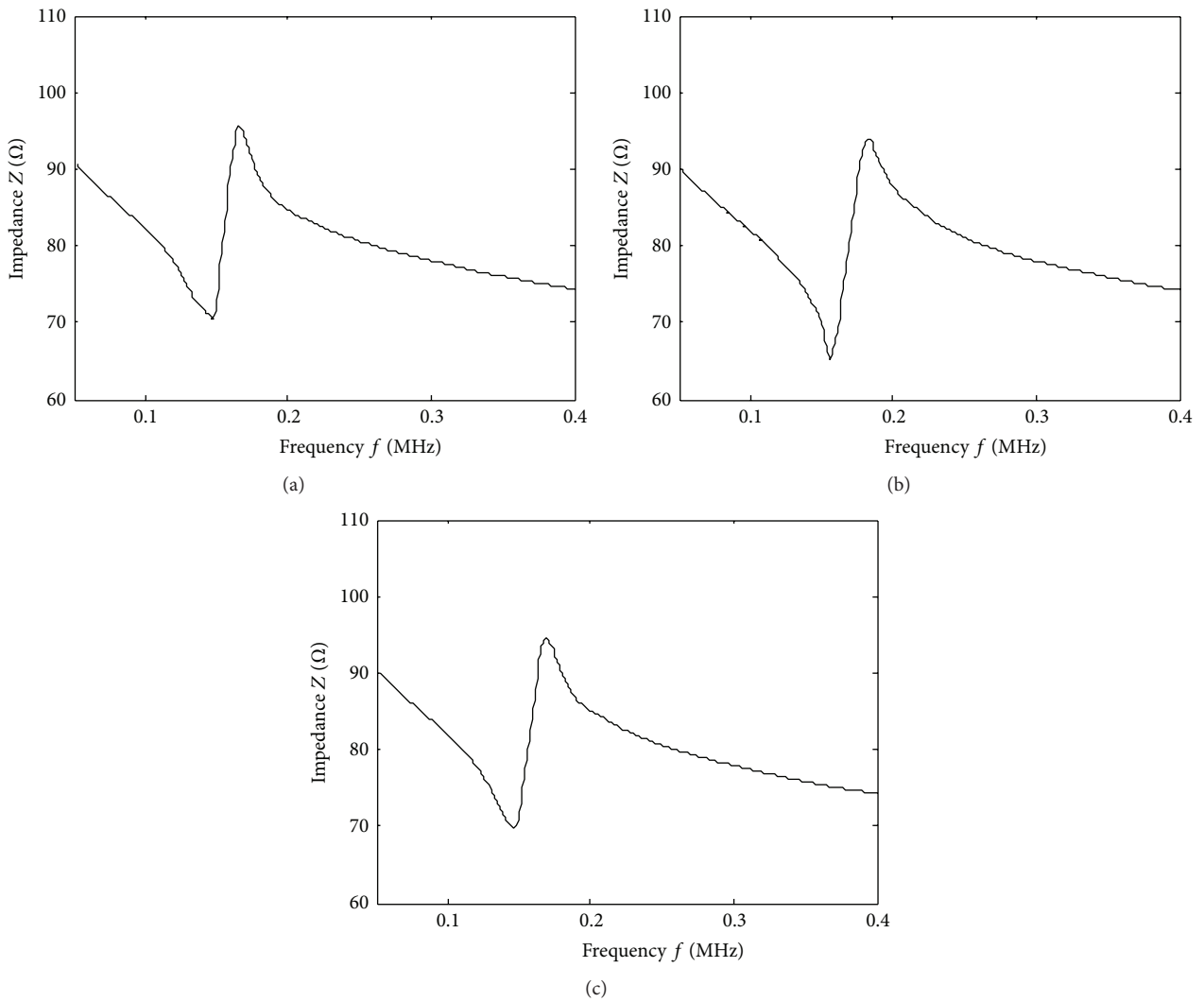


FIGURE 15: Impedance curves of air-coupled transducers: (a) number 1, (b) number 2, and (c) number 3.

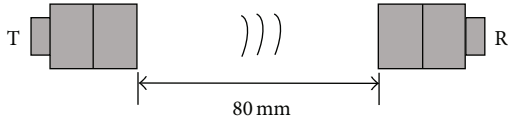


FIGURE 16: Transducer arrangement of testing experiment.

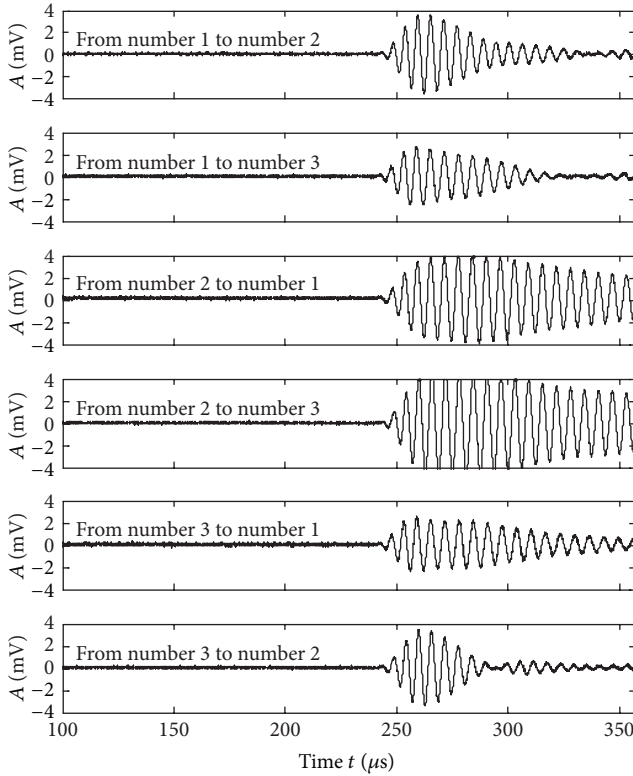


FIGURE 17: Performance test results of air-coupled transducers at 200 kHz.

ultrasound in the air, and the signal-to-noise ratio (SNR) of direct wave signals seems to be very well. According to the received waveform signals, in the subsequent experiment of defect detection, number 3 transducer is selected as transmitter to emit an ultrasonic pulse, while number 2 transducer is selected as receiver.

According to the fabrication and performance test of air-coupled transducer, it is feasible to introduce 3D printing method to fabricate a transducer. However, because all of the air-coupled transducers are handmade, the consistency is not very good. Hence, the excitation and reception performance of air-coupled transducers differ. Meanwhile, as the transducers do not include matching and backing layer, the received waveforms trail a lot.

4. Experiment of Defect Detection

Lamb waves are ultrasonic guided waves formed by the superposition of longitudinal and transverse waves propagating in a plate-like structure in which the thickness is comparable

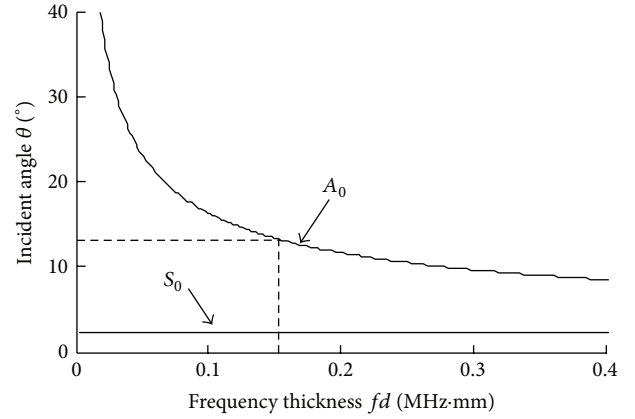


FIGURE 18: Incident angle dispersion curves of Lamb waves along $\langle 110 \rangle$ orientation for monocrystalline silicon wafer.

to the wavelength. Lamb waves can travel relatively long distances with little attenuation in plate structures [17], and they are sensitive to both surface and subsurface discontinuities [18].

The Lamb wave, generated by air-coupled transducers, is introduced into the production and quality control process of monocrystalline silicon, and the final purpose is to determine and detect the defects nondestructively [19]. Due to the center frequency of excitation and the thickness of the plates, different symmetric mode (S_0) and antisymmetric mode (A_0) should be induced. In this case, 200 kHz is chosen as the excitation frequency. The signal received by air-coupled transducer is the leaky wave from the silicon surface. S_0 mode possesses mainly in-plane displacement, whereas out-of-plane displacement is dominant in A_0 mode [20]. Thus, A_0 mode can be easier to be collected with air-coupled ultrasonic transducers. Meanwhile, the wavelength of A_0 mode is shorter than that of S_0 mode at the same frequency.

When ultrasonic waves travel through air and hit the air/plate interface at an angle, both reflected and refracted waves are produced. After multiple reflections and mode conversion, one or more Lamb wave modes are excited. In order to excite Lamb wave at a specific frequency, the incident angle should satisfy Snell's law, formulated by [21]

$$\sin \theta = \frac{c_{\text{air}}}{c_p}, \quad (5)$$

where θ is the incident angle, c_{air} is the velocity of the wave propagating in air, and c_p is the phase velocity of the Lamb wave. As the velocity of air and the phase velocity of Lamb waves are known, incident angle disperse curves of Lamb waves along $\langle 110 \rangle$ direction of monocrystalline silicon can be obtained by solving (5). The results are shown in Figure 18. These curves help in optimizing the orientation of the transmitting and receiving air-coupled ultrasonic transducers. According to the results, the theoretical coincidence incident angle for A_0 mode at 200 kHz should be 13° .

4.1. Air-Coupled Ultrasonic Experiment System. The experimental set-up consists of a high power signal generator,

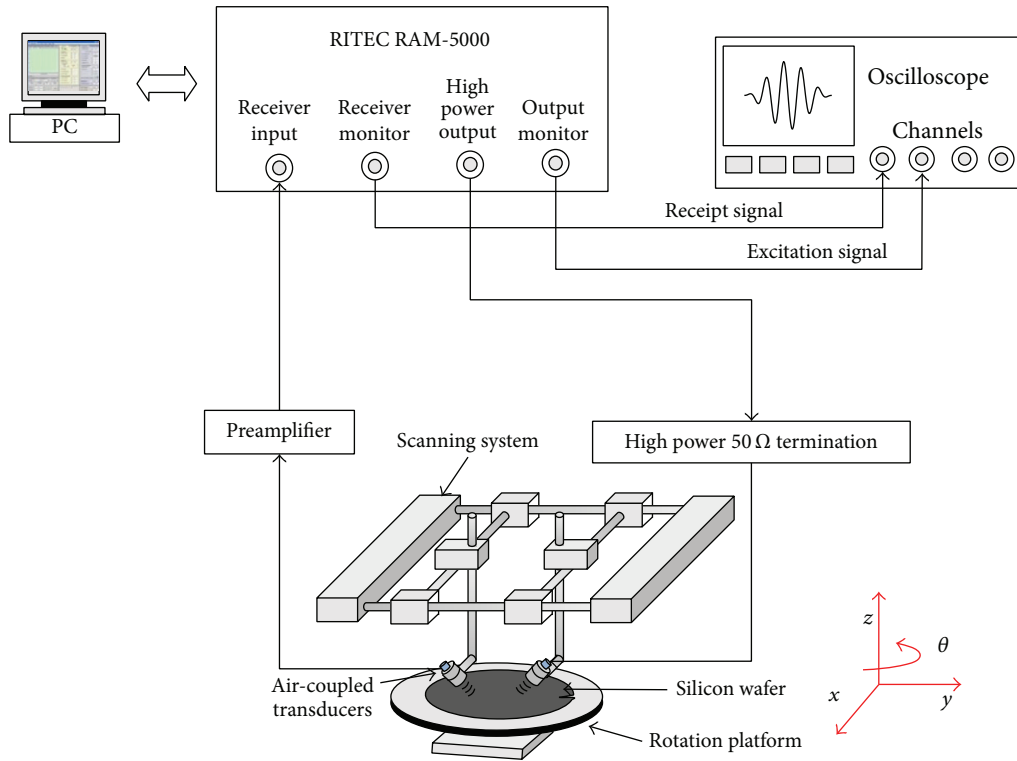


FIGURE 19: The diagram of air-coupled ultrasonic detection system.

a high dB preamplifier, high power $50\ \Omega$ termination, a personal computer, an oscilloscope, and a scanning system. The schematic diagram of experimental set-up is shown in Figure 19. The SNAP RAM-5000 (RITEC, USA) ultrasonic measurement system is used to generate high power tone burst signals for excitation of the transmitting transducer (number 3) and to receive signals from the receiving transducer (number 2) with its preamplifier. The signal is then acquired by an oscilloscope (DPO4054, Tektronix, USA) with a sampling frequency of 50 MHz. A pair of transducer fixtures are used to hold and orient the air-coupled ultrasonic transducers at a special angle for exciting and receiving Lamb waves.

4.2. Specimens. Monocrystalline silicon, shown in Figure 20, is supplied in the form of plate with a crystal orientation of (001), whose diameter is 200 mm and thickness is $725\ \mu\text{m}$, and the size of the crack defect is $15\ \text{mm} \times 0.5\ \text{mm} \times 0.5\ \text{mm}$ with the direction of $\langle 110 \rangle$.

4.3. Experiments and Results. The transmitting transducer and the receiving transducer are arranged in the same side above the silicon wafer surface, with the fixed distance of 80 mm, scanning along the direction of the crack detection. The incident angle of transmitter θ_T kept equal to the receiver θ_R is 13° . The scanning distance is totally 50 mm in step of 2 mm. The excitation signal is also a 5-cycle 200 kHz sinusoidal tone burst modulated by a Hanning window. The signals received at both the defect-free position and defective position are shown in Figure 21.

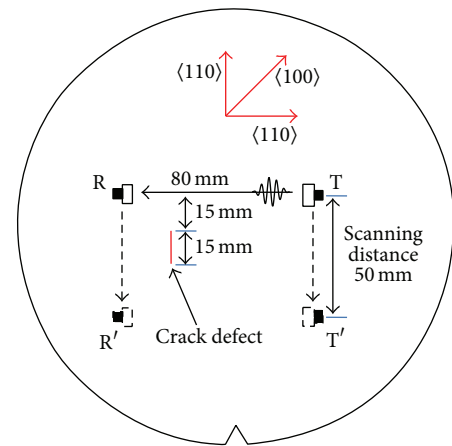


FIGURE 20: Sample of monocrystalline silicon and transducer set-up.

In usual process of defect detection, the amplitude of direct wave that transmits through the defect is used to describe the presence and the size of the defects. In this experiment, the influence of the presence of cracks on the amplitude of signals is not that obvious. So, it is difficult to distinguish the location of the defect accurately based on amplitude characteristics.

However, when Lamb waves propagate through the crack, not only will the amplitude change, but also the phase will shift or distort. The correlation coefficient of the received signal and the reference signal is calculated to extract the

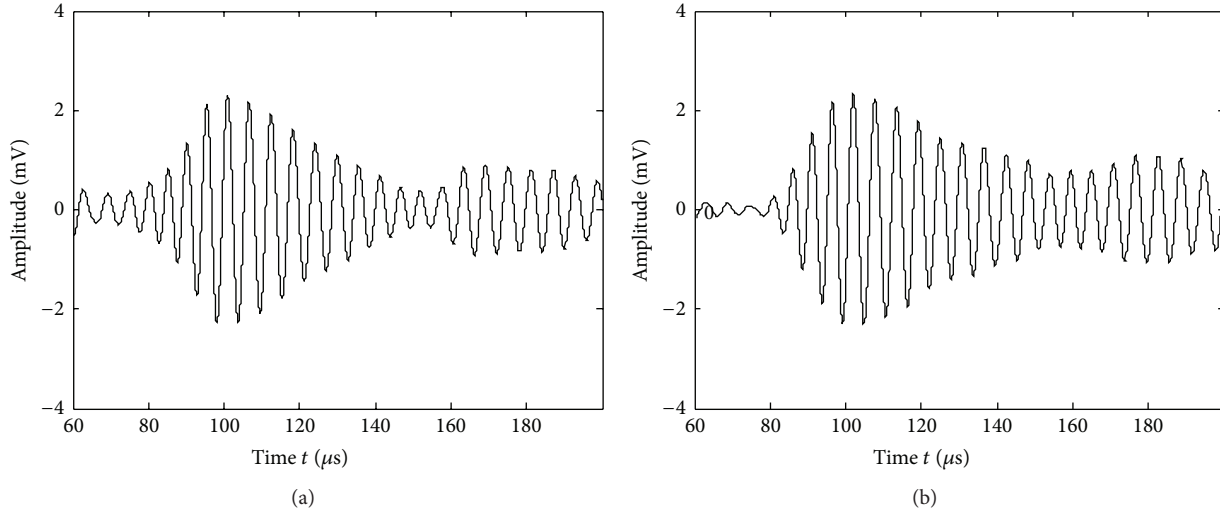


FIGURE 21: Received signals for (a) defect-free position and (b) defective position.

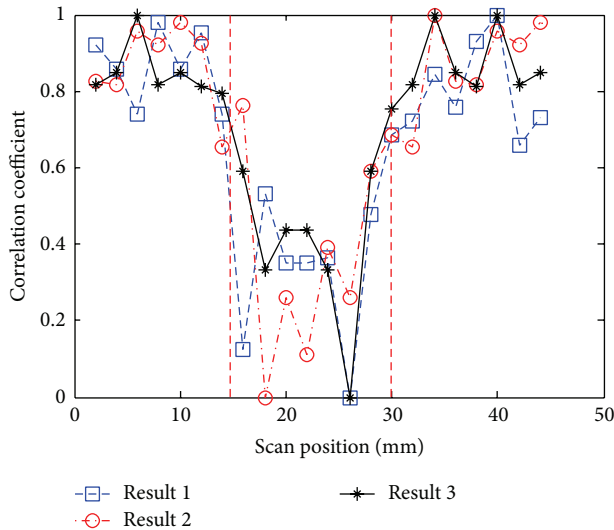


FIGURE 22: Correlation coefficient between reference signals and reception signals.

influence of the crack on the signals [22]. The rectangular window is used to intercept the received signals of Lamb wave, and the signal of defect-free position is used as reference signal. The correlation coefficients of all the received signals and reference signal are calculated and established the corresponding relationship with the scan position. The results can be seen in Figure 22. The experiment has been implemented for 3 times. All of the results show that the correlation coefficients of the received signals at defective position are lower, which means the waveforms have been distorted when Lamb wave travels across the defect. The correlation coefficient of 0.6 is chosen as the threshold. The defect position determined by this method is conformed with the actual defect position. It proved that the method is feasible in monocrystalline silicon defect detection.

5. Conclusion

In this research, a new structure of air-based 1-3 piezoelectric composites is introduced. The influence of the structural parameters on the performance of air-based 1-3 piezoelectric composites has been investigated through finite element analysis. According to the results of simulation, the air-based 1-3 piezoelectric composites and air-coupled transducers are fabricated with the PZT volume fraction $\varphi = 40\%$; meanwhile, the side length of PZT column $a = 1$ mm and the thickness of the sensitive element $h = 10$ mm. All of the air-coupled transducers can excite and receive the ultrasound in air effectively, and the signal-to-noise ratio (SNR) of direct wave seems to be very well.

Scanning method is used to detect the crack defect in the monocrystalline silicon wafer by Lamb waves. The direct wave of A_0 mode is used to identify the defect. Results reveal that the location and size of the defect can be detected by calculating the correlation coefficient of the received signals and reference signals. It proved that this method is feasible in monocrystalline silicon defect detection.

To sum up, the 3D printed air-based 1-3 piezoelectric composites structures are appropriate to fabricate the air-coupled transducers. They can both reduce the acoustic impedance and enhance the electromechanical conversion efficiency. In future studies, matching/backing layer should be taken into account to improve the performance of air-coupled transducers.

Competing Interests

The authors declare that there are no competing interests regarding the publication of this paper.

Acknowledgments

The work in this paper is financially supported by the National Natural Science Foundation of China (Grant

nos. 11372016 and 51235001) and the Outstanding Young Researcher Program from Organization Department of the CPC Beijing Municipal Committee (Grant no. 2014000020124G038).

References

- [1] A. Belyaev, O. Polupan, W. Dallas, S. Ostapenko, D. Hess, and J. Wohlgemuth, "Crack detection and analyses using resonance ultrasonic vibrations in full-size crystalline silicon wafers," *Applied Physics Letters*, vol. 88, no. 11, Article ID 111907, 2006.
- [2] G. Yun, K.-M. Kim, Y. Roh, Y. Min, J.-K. Lee, and Y. H. Kim, "Comparison of slowness curves of Lamb wave with elastic moduli and crystal structure in silicon wafers," in *Proceedings of the IEEE International Ultrasonics Symposium (IUS '13)*, pp. 1598–1601, IEEE, Prague, Czech Republic, July 2013.
- [3] S.-H. Kee and J. Zhu, "Using air-coupled sensors to determine the depth of a surface-breaking crack in concrete," *Journal of the Acoustical Society of America*, vol. 127, no. 3, pp. 1279–1287, 2010.
- [4] O. Balogun, G. D. Cole, R. Huber, D. Chinn, T. W. Murray, and J. B. Spicer, "High-spatial-resolution sub-surface imaging using a laser-based acoustic microscopy technique," *IEEE Transactions on Ultrasonics, Ferroelectrics, and Frequency Control*, vol. 58, no. 1, pp. 226–233, 2011.
- [5] Z. Zhou and D. Wei, "Progress of air-coupled ultrasonic non-destructive testing technology," *Chinese Journal of Mechanical Engineering*, vol. 44, no. 6, pp. 10–14, 2008.
- [6] H. B. Kichou, J. A. Chavez, A. Turo, J. Salazar, and M. J. Garcia-Hernandez, "Lamb waves beam deviation due to small inclination of the test structure in air-coupled ultrasonic NDT," *Ultrasonics*, vol. 44, pp. e1077–e1082, 2006.
- [7] I. Y. Solodov, R. Stoessel, and G. Busse, "Material characterization and NDE using focused slanted transmission mode of air-coupled ultrasound," *Research in Nondestructive Evaluation*, vol. 15, no. 2, pp. 65–85, 2004.
- [8] F. Yan, E. Hauck, T. M. Pera et al., "Ultrasonic guided wave imaging of a composite plate with air-coupled transducers," in *Review of Progress in Quantitative Nondestructive Evaluation*, pp. 1007–1012, AIP Publishing, 2007.
- [9] S. K. Chakrapani, M. J. Padiyar, and K. Balasubramaniam, "Crack detection in full size Cz-silicon wafers using lamb wave air coupled ultrasonic testing (LAC-UT)," *Journal of Nondestructive Evaluation*, vol. 31, no. 1, pp. 46–55, 2012.
- [10] Z. Liu, H. Yu, C. He, and B. Wu, "Delamination damage detection of laminated composite beams using air-coupled ultrasonic transducers," *Science China: Physics, Mechanics and Astronomy*, vol. 56, no. 7, pp. 1269–1279, 2013.
- [11] R. E. Newnham, D. P. Skinner, and L. E. Cross, "Connectivity and piezoelectric-pyroelectric composites," *Materials Research Bulletin*, vol. 13, no. 5, pp. 525–536, 1978.
- [12] G. Hayward and J. Bennett, "Assessing the influence of pillar aspect ratio on the behavior of 1-3 connectivity composite transducers," *IEEE Transactions on Ultrasonics, Ferroelectrics, and Frequency Control*, vol. 43, no. 1, pp. 98–108, 1996.
- [13] A.-C. Hladky-Hennion and J.-N. Decarpigny, "Finite element modeling of active periodic structures: application to 1–3 piezocomposites," *Journal of the Acoustical Society of America*, vol. 94, no. 2 I, pp. 631–635, 1993.
- [14] M. Bhardwaj, "Piezoelectric transducer with gas matrix," WO2004017369 A2, 2007, 2003.
- [15] W. A. Smith and B. A. Auld, "Modeling 1-3 composite piezoelectrics: thickness-mode oscillations," *IEEE Transactions on Ultrasonics, Ferroelectrics, and Frequency Control*, vol. 38, no. 1, pp. 40–47, 1991.
- [16] T. R. Gururaja, W. A. Schulze, L. E. Cross et al., "Resonant modes of vibration in piezoelectric PZT-polymer composites with two dimensional periodicity," *Ferroelectrics*, vol. 54, no. 1, pp. 183–186, 1984.
- [17] J. L. Rose, "A baseline and vision of ultrasonic guided wave inspection potential," *Journal of Pressure Vessel Technology*, vol. 124, no. 3, pp. 273–282, 2002.
- [18] M.-K. Song and K.-Y. Jhang, "Crack detection in single-crystalline silicon wafer using laser generated Lamb Wave," *Advances in Materials Science and Engineering*, vol. 2013, Article ID 950791, 6 pages, 2013.
- [19] M.-K. Song and K.-Y. Jhang, "Crack detection in single-crystalline silicon wafer using laser generated Lamb wave," *Advances in Materials Science and Engineering*, vol. 2013, Article ID 950791, 6 pages, 2013.
- [20] Z. Su, L. Ye, and Y. Lu, "Guided Lamb waves for identification of damage in composite structures: a review," *Journal of Sound and Vibration*, vol. 295, no. 3–5, pp. 753–780, 2006.
- [21] M. Castaings, P. Cawley, R. Farlow, and G. Hayward, "Single sided inspection of composite materials using air coupled ultrasound," *Journal of Nondestructive Evaluation*, vol. 17, no. 1, pp. 37–45, 1998.
- [22] R. Cepel, K. C. Ho, B. A. Rinker, D. D. Palmer Jr., T. P. Lerch, and S. P. Neal, "Spatial correlation coefficient images for ultrasonic detection," *IEEE Transactions on Ultrasonics, Ferroelectrics, and Frequency Control*, vol. 54, no. 9, pp. 1841–1849, 2007.

Research Article

Development of a Wireless Temperature Sensor Using Polymer-Derived Ceramics

Ran Zhao,¹ Gang Shao,² Ni Li,³ Chengying Xu,⁴ and Linan An¹

¹Department of Materials Science and Engineering, Advanced Materials Processing and Analysis Center, University of Central Florida, Orlando, FL 32816, USA

²School of Materials Science and Engineering, Zhengzhou University, Zhengzhou, Henan 450001, China

³Department of Mechanical and Aerospace Engineering, University of Central Florida, Orlando, FL 32816, USA

⁴Department of Mechanical Engineering, Florida State University, Tallahassee, FL 32310, USA

Correspondence should be addressed to Ni Li; ni.li@ucf.edu and Linan An; lan@mail.ucf.edu

Received 18 January 2016; Revised 16 March 2016; Accepted 29 March 2016

Academic Editor: Gyuhae Park

Copyright © 2016 Ran Zhao et al. This is an open access article distributed under the Creative Commons Attribution License, which permits unrestricted use, distribution, and reproduction in any medium, provided the original work is properly cited.

A temperature sensor has been developed using an embedded system and a sensor head made of polymer-derived SiAlCN ceramics (PDCs). PDC is a promising material for measuring high temperature and the embedded system features low-power consumption, compact size, and wireless transmission. The developed temperature sensor has been experimentally tested to demonstrate the possibility of using such sensors for real world applications.

1. Introduction

Accurate temperature measurements are crucial for many applications, such as chemical processing, power generation, and engine monitoring. As a result, development of temperature sensors has always been a focus of microsensor field. A variety of materials have been studied for temperature sensor applications, for example, semiconducting silicon and silicon carbide. Silicon based sensors are typically used at temperatures lower than 350°C due to accelerated material degradation at higher temperature [1, 2]. Silicon carbide based sensors are better than silicon based sensors in high temperature measurement and can be applied in temperatures up to 500°C [3–5].

Polymer-derived SiAlCN ceramics (PDCs) are another widely studied material that demonstrate properties such as excellent high temperature stability [6] as well as good oxidation/corrosion resistance [7]. PDCs have been considered as a promising material for measuring high temperature [8]. Our early works have showed that PDC sensor head can accurately measure high temperature up to 830°C [9] using data acquisition system from National Instruments. The cost and size of the sensor system must be significantly reduced before it can be deployed for real world applications. In this

paper, we develop a temperature sensor using PDC and an embedded system. Comparing to the National Instruments data acquisition equipment used in the previous paper, the newly developed embedded sensor is much smaller (9.7 dm³ versus 0.3 dm³), lighter (5.97 kg versus 0.19 kg), and cheaper (approximately \$8000 versus \$170). A WiFi module is also added so the temperature measurement can be transmitted wirelessly. The embedded board and WiFi module used in this paper are commercially available. The experiments in this paper demonstrate the possibility of deploying PDC based sensors for real world applications.

2. Fabrication of the PDC Sensor Head

In this study, the PDC sensor head is fabricated by following the procedure reported previously [9]. In brief, 8.8 g of commercially available liquid-phased polysilazane (HTT1800, Kion) and 1.0 g of aluminum-tri-sec-butoxide (ASB, Sigma-Aldrich) are first reacted together at 120°C for 24 hours under constant magnetic stirring to form the liquid precursor for SiAlCN. The precursor is then cooled down to room temperature, followed by adding 0.2 g of dicumyl peroxide (DP) into the liquid under sonication for 30 minutes. DP is the thermal initiator which can lower the solidification

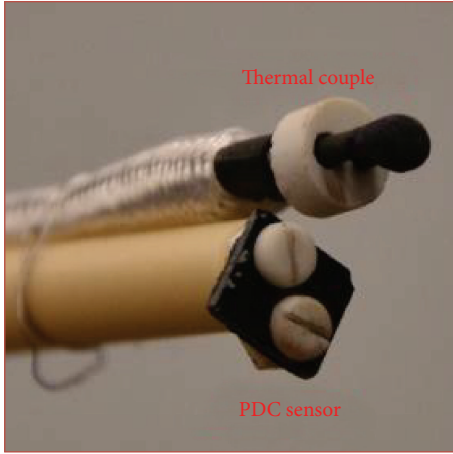


FIGURE 1: PDC sensor head, along with thermal couple for calibration and validation.

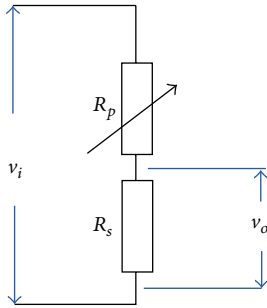


FIGURE 2: Diagram of resistance-to-voltage conversion circuit.

temperature and tailor the electrical properties [10]. The resultant liquid mixture is solidified by heat-treatment at 150°C for 24 hours. The disk-shaped green bodies are then prepared by ball-milling the solid into fine powder of $\sim 1\ \mu\text{m}$ and subsequently uniaxially pressing. A rectangular-shaped sample is cut from the discs and pyrolyzed at 1000°C for 4 hours. The entire fabrication is carried out in high-purity nitrogen to avoid any possible contamination.

Pt wires are attached to the sensor head by two ceramic fasteners on the two mounting holes on the diagonal of the sensor head. To improve the conductivity, both mounting holes are coated with Pt plasma; see Figure 1.

3. Sensor Design and Characterization

3.1. Resistance Conversion Circuit. PDC sensors are resistive sensors whose resistance must be converted to voltage to be picked up by analog to digital converter (ADC). A simple circuit as shown in Figure 2 is designed to serve that purpose. The sensor head is connected in series with a metal film resistor, denoted as R_s , and we have the following equation:

$$R_p = \frac{v_i - v_o}{v_o} R_s, \quad (1)$$

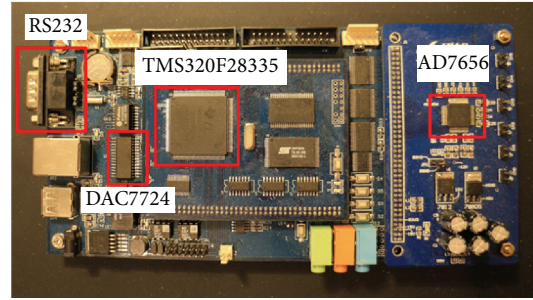


FIGURE 3: Embedded experiment board.

where v_o is the output voltage of the circuit, R_p represents the PDC sensor resistance, and v_i is the voltage supplied to the circuit. In this paper, a resistor of $R_s = 0.998\ \text{k}\Omega$ is used.

3.2. Design of Core of the PDC Sensor. A YX-F28335 embedded experimental board from YanXu (<http://www.adianji.com/>) is used to build the sensor system. The board is equipped with one 16-bit ADC (AD7656 from Analog Device) and one 12-bit digital-analog converter (DAC7724 from Texas Instruments). The picture of the embedded board is shown in Figure 3 with important components highlighted in red boxes. The core of the system is a TMS320F28335 microcontroller from Texas Instruments. TMS320F28335 is a high performance floating-point microcontroller of Texas Instruments' C2000 microcontroller family.

To measure temperature using the PDC sensor, the processor needs to perform the following tasks: (1) supply voltage v_i to the circuit through DAC7724; (2) sample the circuit output v_o using AD7656 and convert the output to temperature measurement; and (3) transmit data to readers from the RS232 port.

The input signal v_i to the conversion circuit is a sinusoidal signal of $\pm 10\ \text{V}$. The sinusoidal signal can bypass the parasitic capacitor in series to the PDC probe. The noise from the furnace coil can also be greatly subdued. The sensor output voltage v_o is approximately sinusoidal as well and its magnitude can be computed using Fast Fourier Transformation (FFT) or curve fitting using recursive least square method (RLSM) [11]. Comparing to FFT, RLSM is more computationally efficient but may have numerical instability because TMS320F28335 only supports IEEE 754 floating-point arithmetic. Here we prefer FFT for fast prototyping purpose because Texas Instruments provides FPU library that performs floating FFT routines on C2000 series microcontroller. Next we explain how the sensor works.

A high-priority interrupt service request (ISR1) based on a CPU timer continues reading a look-up-table and drives the DAC7724 to generate the input signal v_i . The frequency of v_i is controlled by the frequency of ISR1. ISR1 also samples circuit output from AD7656 and adds the data to a 1024-point buffer if there is no FFT running. Once the buffer is filled up, ISR1 stops writing the buffer and the FFT routine starts. The FFT routine is implemented in another slower low-priority interrupt service (ISR2). Once the FFT routine is completed, ISR2 will give ISR1 the permission to clean and write the

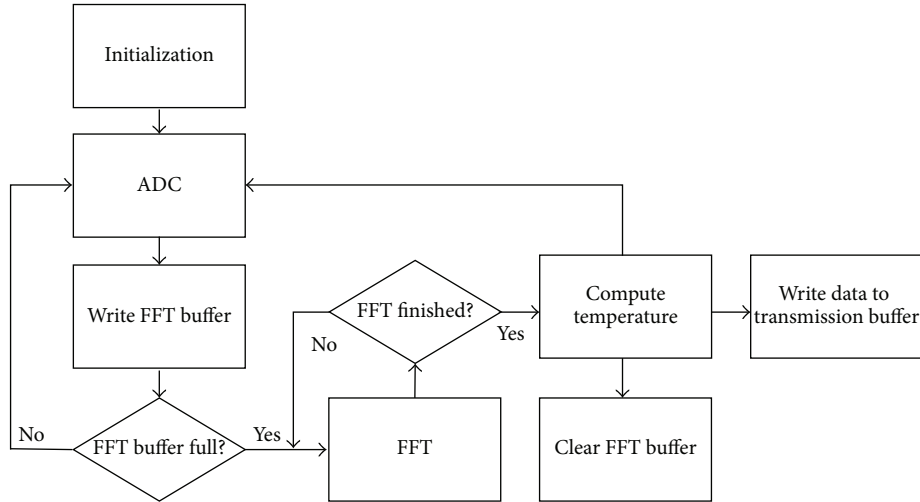


FIGURE 4: Software flowchart.

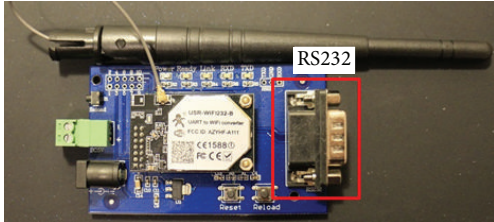


FIGURE 5: WiFi module.

input buffer again. The magnitude from the FFT is used as the circuit output v_o . The software flowchart is shown in Figure 4.

3.3. Wireless Signal Transmission. A WiFi module from Youren Tech (<http://www.usr.cn/>) shown in Figure 5 is connected to the embedded board through a RS-232 port. The computed temperature is written to a data register and then transmitted by the WiFi module automatically. The WiFi module can be wirelessly accessed as a hotspot. Once connected, readers (e.g., PC computers, hand-hold devices) can directly access the data from a virtual serial port simulated by the driver that comes with the WiFi module.

3.4. Auxiliary Measuring System Using Thermal Couple. A K-type thermal couple is used to provide the reference temperature inside the furnace tube, which is used to characterize and verify the performance of the PDC sensor.

4. Results and Discussion

4.1. Sensor Characterization. The temperature-resistance curves of the PDC sensor head were obtained in the furnace setup shown in Figure 6.

The tube furnace (GSL-1100x from MTI) is programmed to raise temperature from 500°C to 850°C and then cool back down to 500°C. To get the steady state measurement of the sensor, the temperature was set to dwell at several plateaus

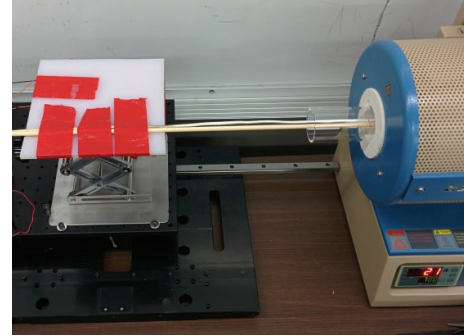


FIGURE 6: Experimental setup for sensor characterization.

during the test and the temperature difference between two consecutive plateaus is 50°C. The furnace program was run twice to check the repeatability of the PDC sensor head. The reference temperature and the output of the PDC sensor are both plotted in Figure 7, where the blue solid line and red dashed line are data from first and second runs, respectively. It is clear that PDC sensor demonstrates good repeatability as the voltage outputs from the two tests are very close.

It should be noted that the reference temperatures used in this paper are not from the furnace but from the external thermal couple placed next to the PDC sensor (Figure 1). This is because the furnace (GSL-1100x from MTI) we used does not have temperature data recording option. The temperature measured by the external thermal couple is about 25°C lower than the readings of the furnace. This measurement difference is consistent and therefore does not affect the sensor calibrations and performance validations.

The resistance of the sensor head should comply with the Thermistor equation [12]:

$$\ln \frac{1}{R_p} = c_1 \frac{1}{T} - c_2, \quad (2)$$

where c_1 and c_2 are constant coefficients, which are experimentally determined using linear optimization. The result

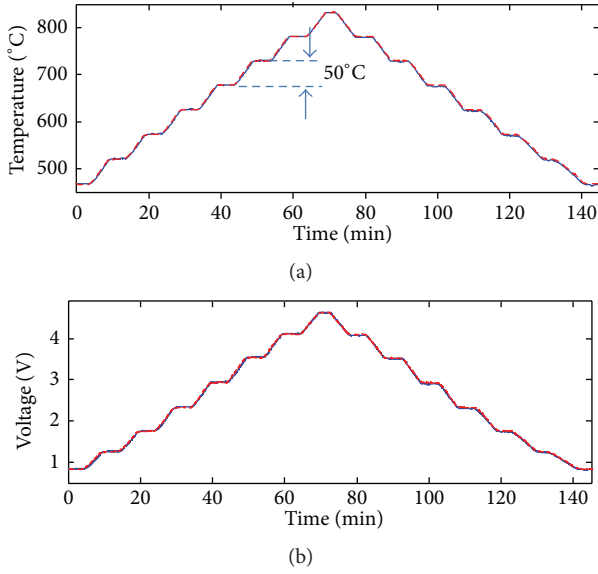


FIGURE 7: (a) Temperature measured by thermal couple and (b) voltage output v_o from the PDC sensor.

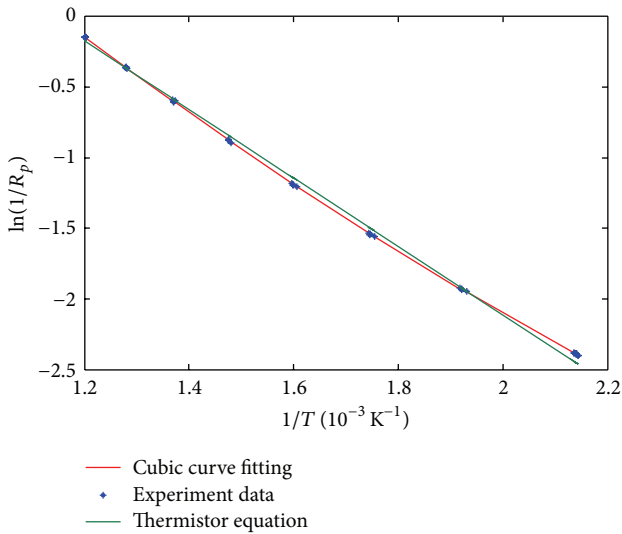


FIGURE 8: Sensor resistance versus temperature in a format of $\ln(1/R_p)$ versus $1/T$.

of the curve fitting is shown in Figure 8 as the green curve.

It is clear that $\ln(1/R_p)$ is only approximately linear to the inverse of temperature and the linear curve fitting is not perfect. To get better results over the entire temperature range, we use a third-order polynomial to replace (2):

$$c_1 \left(\ln \frac{1}{R_p} \right) + c_2 \left(\ln \frac{1}{R_p} \right)^2 + c_3 \left(\ln \frac{1}{R_p} \right)^3 + c_4 = \frac{1}{T}, \quad (3)$$

where c_1 , c_2 , c_3 , and c_4 are constant coefficients and the result is shown in Figure 8 as the red curve. Apparently, the third-order polynomial matches the experiment results better than the linear curve fitting. With the coefficients determined by

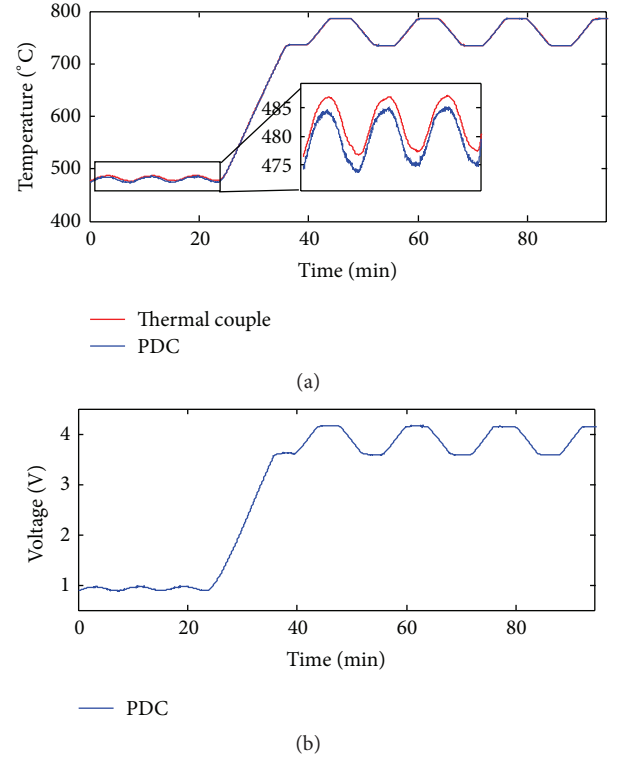


FIGURE 9: Sensor performance validation. (a) Temperatures measured by thermal couple and PDC. (b) Raw voltage signal from PDC circuit.

the numerical optimization, the temperature measurements can be obtained by combining (1) and (3).

4.2. Performance Validation. In this section, we proceed to examine the performance of the sensor. To comprehensively test the performance, two furnace programs are designed. The low temperature program first commands the furnace to dwell at 510°C for 2 minutes and then rise to 520°C in 2 minutes. After that, the program stays at 520°C for 2 minutes and then goes back to 510°C in 2 minutes. The high temperature program first stays at 750°C for 5 minutes, rises to 800°C in 5 minutes, stays at 800°C for 5 minutes, and then cools back down to 750°C in 5 minutes.

The validation test repeats the low temperature program 3 times and then rises to 750°C in 12 minutes and then repeats the high temperature program 3 times. The furnace program is designed to cover both low and high temperatures as well as different temperature change rates. The experimental results are shown in Figure 9. The raw voltage signal shown in Figure 9(b) is used to calculate the corresponding temperature measurement which is compared to data from the external thermal couple shown in Figure 9(a). It is clear that the PDC sensor system can accurately measure temperature at both low and high temperatures. The maximum error is about 2.5°C at low temperature range. This measurement error can be further reduced by fine tuning the calibration experiments and by using better curve fittings that characterize the sensor better.

5. Conclusion

In this paper, a temperature sensor was successfully fabricated using polymer-derived SiAlCN ceramics and an embedded system. Characterization and validation experiments demonstrate excellent performance. More importantly, the low cost and compact size of the sensor make it possible to deploy for actual application.

Our research efforts have also been devoted to building PDC sensors using low-power consumption MSP430 from Texas Instruments and radio frequency identification (RFID) technology to develop battery-less sensors. The results would be presented in our future publications.

Competing Interests

The authors declare that they have no competing interests.

Authors' Contributions

Ran Zhao and Gang Shao contributed equally to this work.

References

- [1] M. Biebl, G. Brandl, and R. T. Howe, "Young's modulus of in situ phosphorus-doped polysilicon," in *Proceedings of the 8th International Conference on Solid-State Sensors and Actuators, and Eurosensors IX*, pp. 80–83, Stockholm, Sweden, Jun 1995.
- [2] G. L. Pearson, W. T. Read Jr., and W. L. Feldmann, "Deformation and fracture of small silicon crystals," *Acta Metallurgica*, vol. 5, no. 4, pp. 181–191, 1957.
- [3] E. A. de Vasconcelos, S. A. Khan, W. Y. Zhang, H. Uchida, and T. Katsube, "Highly sensitive thermistors based on high-purity polycrystalline cubic silicon carbide," *Sensors and Actuators A: Physical*, vol. 83, no. 1–3, pp. 167–171, 2000.
- [4] J. B. Casady, W. C. Dillard, R. W. Johnson, and U. Rao, "A hybrid 6H-SiC temperature sensor operational from 25°C to 500°C," *IEEE Transactions on Components, Packaging, and Manufacturing Technology: Part A*, vol. 19, no. 3, pp. 416–422, 1996.
- [5] J. Yang, "A silicon carbide wireless temperature sensing system for high temperature applications," *Sensors (Switzerland)*, vol. 13, no. 2, pp. 1884–1901, 2013.
- [6] R. Riedel, A. Kienzle, W. Dressler, L. Ruwisch, J. Bill, and F. Aldinger, "A silicoboron carbonitride ceramic stable to 2,000°C," *Nature*, vol. 382, no. 6594, pp. 796–798, 1996.
- [7] Y. Wang, W. Fei, and L. An, "Oxidation/corrosion of polymer-derived SiAlCN ceramics in water vapor," *Journal of the American Ceramic Society*, vol. 89, no. 3, pp. 1079–1082, 2006.
- [8] H. Ryu, Q. Wang, and R. Raj, "Ultra-high temperature semiconductors made from polymer-derived ceramics," *Journal of the American Ceramic Society*, vol. 93, no. 6, pp. 1668–1676, 2010.
- [9] R. Zhao, G. Shao, Y. Cao, L. An, and C. Xu, "Temperature sensor made of polymer-derived ceramics for high-temperature applications," *Sensors and Actuators A: Physical*, vol. 219, pp. 58–64, 2014.
- [10] Y. Wang, L. Zhang, W. Xu et al., "Effect of thermal initiator concentration on the electrical behavior of polymer-derived amorphous silicon carbonitrides," *Journal of the American Ceramic Society*, vol. 91, no. 12, pp. 3971–3975, 2008.
- [11] L. Ljung and T. Söderström, *Theory and Practice of Recursive Identification*, MIT Press, 1983.
- [12] F. J. Hyde, *Thermistors*, Iliffe Books, London, UK, 1971.